Toyohashi University of Technology

Doctor Thesis

Load Swing and Skew Vibration Suppression and Excitation Controls of Crane Systems

(クレーンシステムにおける吊り荷の揺れとねじれ振動抑制および励起制御)

Author
Ho Duc Tho
(ホドゥクトォ)

Supervisors
Prof. Naoki Uchiyama
Prof. Kazuhiko Terashima

Student ID
D155113

Doctor of Philosophy (Engineering)

Systems Engineering Laboratory
Department of Mechanical Engineering

July 2020

Dept. of Mechanical Engineering		ID	155113
Name	Ho Duc Tho		

Supervisors	Prof. Naoki Uchiyama
	Prof. Kazuhiko Terashima

Abstract

Title	**Load Swing and Skew Vibration Suppression and Excitation Controls of Crane Systems.**

The transportation of heavy and hazardous payloads from and to various places, such as harbors, factories, shipyards, is mainly carried out by cranes. All types of cranes share a common structure, i.e., the payload is suspended under a trolley or a boom tip by flexible ropes. Therefore, the pendulum-like motion of the payloads, which is referred to as vibration, is induced when actuators start to exert accelerations on the payloads through ropes. In fact, there are two types of vibrations existing in crane systems. The first type is swing vibration, which occurs when the payload position is changed. The second type is skew vibration, and it happens when the payload orientation is adjusted. The swing vibration is spherical pendulum-like, whereas the skew vibration is torsional pendulum-like. The central concept of crane control is to manipulate these vibrations as our wish to suit different engineering purposes. Thus, a number of new control schemes and refined algorithms were established in this dissertation to address both skew and swing vibration control problems of cranes. The current common school of thought views the vibration as a harmful phenomenon that needs to be eliminated, which is why the vibration suppression control is a widely studied subject in many literatures. However, in fact, the vibration might be undesirable for some applications but favorable for others (e.g., bulk material transportation described in Chapter 6). Hence, crane control should be perceived from the points of view of both *vibration suppression control* and *vibration excitation control*.

Part I of this dissertation focuses on the skew vibration control of crane systems. To solve the robust control problem of the skew transfer process in the presence of parametric uncertainties, two robust controllers were proposed. First, an integral sliding mode controller was established. A coupled integral siding function was introduced to inject the skew vibration information into the control law to drive the payload to a desired skew angle while effectively damping the vibration. The reaching phase as found with the conventional sliding mode controllers was also canceled, so the robustness can be achieved from the beginning of time. Second, a dynamic output feedback H_∞ controller was also applied to the system for comparison with the integral sliding mode control. The robust stability condition of the H_∞ controller was performed using the μ-synthesis with a structure singular value criterion, whereas the Lyapunov indirect method was employed for the integral sliding mode controller. For both schemes, an optimization routine based on the metaheuristic particle swarm optimization mechanism was established, and it adopted the robust stability conditions with regard to each controller as the nonlinear constraints. With the proposed optimization procedure, the minimization of a desirable performance index and robust stabilization of the closed-loop system was simultaneously guaranteed in a single framework. Based on a random

simulation and the experimental results, the integral sliding mode controller showed its superiority over the H_∞ control, and hence it is the preferable candidate for actual implementation on the real-size system in use at the harbor. A switched optimal controller was subsequently introduced to improve transport productivity. The novelty of such an approach is that the energy consumption can be reduced without trading-off the sub-optimal transfer time. The basic idea is to use a binary actuator—an electro-mechanical clutch—to intelligently disengage the connection between the motor and the payload during motion so that the payload can continue to rotate only with its own momentum. Two solutions, namely particular and general schemes, were proposed. Physical constraints of the actuator, including bounded velocity and bounded acceleration, were explicitly taken into account. Both simulation and experimental results were provided to demonstrate the effectiveness of the proposed switched optimal control system. In addition, comparisons with the no-switched time-optimal, input shaping, and integral sliding mode controllers were also presented.

Part II of the dissertation deals with the swing vibration control problem of cranes. First, minimum-time zero-vibration S-curve commands were established for an overhead crane. Based on a position baseline S-curve, which is generated from a bang-off-bang acceleration profile, two approaches were proposed to build the vibration suppression capability: embedding and shaping methods. In both schemes, the baseline S-curve was parameterized to establish minimum-time optimization problems in which the maximum velocity and maximum acceleration of the actuator are explicitly taken into consideration. Minimum-time solutions were successfully obtained. Also, online trajectory generation can be achieved using the proposed approach. In comparison with other relevant studies, the minimum-time S-curve commands were faster. Second, a model reference input shaping control was formulated for a nonlinear luffing dynamics of a rotary crane system with a time-varying rope length. The newly established technique is able to completely suppress the residual vibration for a highly nonlinear time-varying system. The fundamental idea is to match the real vibration of the system with a reference oscillation, by which an exact zero vibration suppression can be achieved for the actual system. Standard input shaping control designs cannot possess such a quality. Finally, a vibration excitation control scheme was introduced for an overhead crane system in the context of bulk material transportation where the transferred materials can be dropped/discharged while in the air. In order to exploit such a unique feature, a new concept, named tossing control methodology, was introduced to enhance transportation productivity. A specific type of tossing controller that relies on the phenomenon of linear resonance was proposed to induce oscillation in a periodically increasing amplitude. It was shown that the resonance-based tossing control can reduce the transfer time up to 26.5% compared with the well-known minimum-time swing suppression controller—the fastest member of the swing suppression control group—under similar requirements of bulk material transportation, conditions, and actuator constraints. Thus, it was found that the vibration suppression control is not always the best option in every situation.

Contents

Chapter 1

Introduction

Transportation is usually defined as an action to move humans, animals, and goods from one location to another. The mankind' first means of transportation involved walking, running, and swimming. Later, various animals had been used to carry and transport heavy objects at a faster speed. However, due to the strength and endurance limits of biological bodies, the modern transportation mostly relies on mechanical tools, structures, and machines, which are able to operate in diverse environments such as air, land, water, and space. Some typical transport machines/structures can be listed as follows: fix-wing aircraft and helicopters (air), cars and trains (land), vessels and submarines (water), and spacecraft and space shuttle (space). These machines considerably free humans from hard, menial, and dull work. The transportation enables trade between people regardless of geographical distance, which is crucial for the development of civilizations.

It is widely accepted that cranes are one of the most important means of transportation in various places, including factories, shipyards, construction sites, and especially harbors, as they are needed for transferring heavy and hazardous materials between different locations within the workspace. The 21st century witnessed a revolution in the maritime industry, in which containerization played a key role. Every year, billion tons of merchandise and containers are transported by sea, and it is generally accepted that more than 90% of the global trade belongs to seaborne commerce. In order to transload such an enormous and annually increasing amount of goods, crane systems are getting larger in size and in lifting capacity. They are also being designed to operate at much higher productivity rates than before so as to shorten the transloading time. As a result, the transportation cost can significantly be reduced. The main focus factor in the pursuit of improving the productivity of cranes is the oscillation of the payload around its equilibrium. The vibration phenomenon is a natural characteristic of every

crane and it is elaborated in Section 1.2. The central idea here is to control that vibration in order to suit and adhere to different engineering purposes. At present, mainstream research focuses on the vibration suppression control, where the vibration is seen as an unwanted phenomenon that needs to be eliminated. However, the vibration might be undesirable for some applications but favorable for others (e.g., bulk material transportation described in Chapter 6). Therefore, crane vibration control should also be understood in the sense of vibration excitation control, not just in the direction of vibration suppression control. Due to its significance in fostering both theory and application advancements, the vibration control of cranes attracted considerable attention from both control theorists and control engineers. The last 50 years have seen a tremendous interest and effort in modeling and control of crane systems. It is therefore necessary to review common crane types and their vibration control techniques.

1.1 Crane categorization

Cranes are the machines that can lift and lower loads, by means of ropes and pulleys, and move the load horizontally. It is primarily used for lifting heavy loads, which are beyond the normal capacity of a human, and transport them to other places [1]. There are many types of cranes, e.g., overhead crane, boom crane, tower crane, telescopic crane, level luffing crane, crawler crane, floating crane, etc. However, conceptually, cranes can be classified into two main categories depending on their structures: gantry cranes and rotary cranes. They are different in the sense that, in gantry cranes, all main motions are linear, whereas rotary cranes can perform at least one rotary motion.

1.1.1 Gantry cranes

Gantry cranes are commonly used in factories, warehouses, and shipyards, where they usually work in a three-dimensional configuration. The trolley can move along the Y-axis rail, which has a linear motion on the X-axis rail, as shown in Fig. 1.1. These motions are called trolley and gantry motions, respectively. The payload is attached to the hook below the trolley by ropes, and its height can be adjusted along the vertical axis by a hoisting motion, which is the motion of extending or retracting the rope. By incorporating the three aforementioned linear motions, the payload can be transferred to any point within the workspace. Since all the motions of the gantry crane are perpendicular to each other, they can be best described in the Cartesian coordinate. Gantry cranes mainly work in a two-dimensional configuration (trolley motion is the primary one) at harbors, where they are specialized in handling containers. For this reason, they are called container cranes. Instead of using a conventional

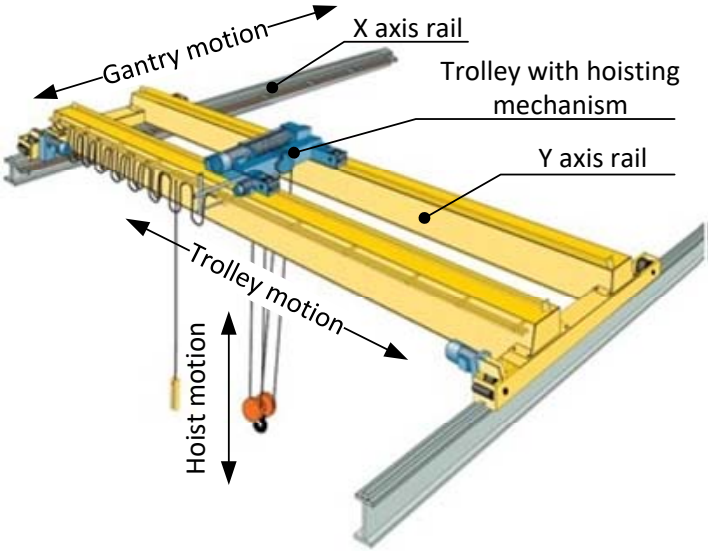

FIGURE 1.1: A three-dimensional gantry crane.[1]

hook, container cranes are equipped with a device called spreader, which is used to grip the container more efficiently by means of a twistlock mechanism.

1.1.2 Rotary cranes

Rotary cranes are characterized by the rotary motion of at least one actuator, and they can be divided into two types: boom cranes, which are commonly used in shipyards, and tower cranes, which are frequently seen at construction sites. In these cranes, the load-line attachment point undergoes rotation, but another degree of freedom may exist for this point. In boom crane systems, this point moves vertically, whereas it moves horizontally in tower cranes. The cable and load are treated as a spherical pendulum with a two-degree-of-freedom sway.

Boom cranes, as shown in Fig. 1.2, are naturally described in spherical coordinates, where a boom rotates about both perpendicular and parallel axes with respect to the ground. This type of crane has three main motions: slewing, luffing, and hoisting. The payload is supported using a suspension cable at the end of the boom. Generally, boom cranes have main advantage of handling loads in compression. As a result, they are typically more compact than bridge or tower cranes with similar load-carrying capacities.

[1]Source: https://www.craneservicesystems.com

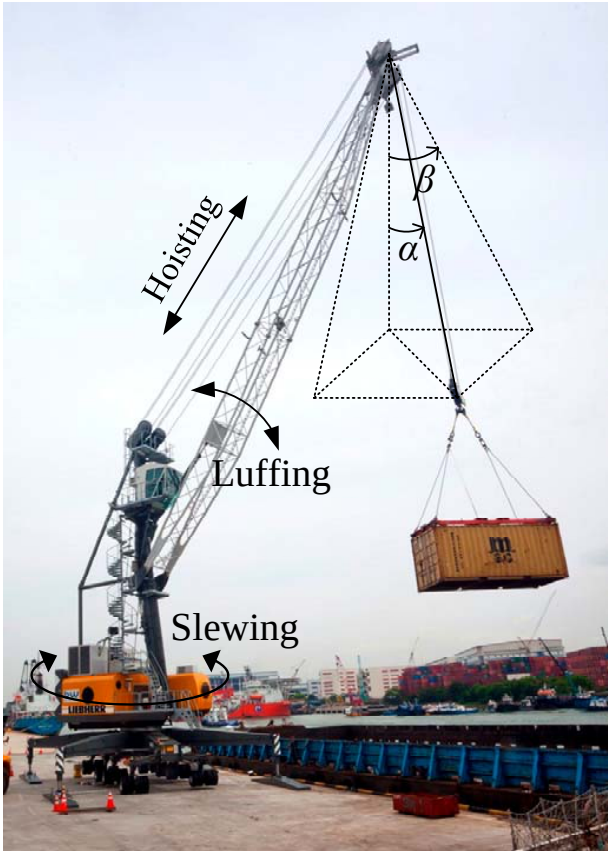

FIGURE 1.2: A boom crane at a harbor.[2]

Tower cranes are most naturally described in cylindrical coordinates, where a horizontal jib arm rotates around a vertical tower. As shown in Fig. 1.3, a tower crane moves the payload within the workspace using three motions: slewing, trolley, and hoisting. The payload is suspended under the trolley by cables, which radially moves along the jib arm. Tower cranes are commonly used in the construction of multi-story buildings, and they have the advantage of having a small footprint-to-workspace ratio.

1.2 Swing and skew oscillations in cranes

1.2.1 Swing oscillation

All crane types share a common structure, where the payload is suspended under the trolley (in gantry and tower cranes) or under the boom tip (in boom cranes) by flexible ropes. Such a design is adopted

[2]Source: https://www.liebherr.com

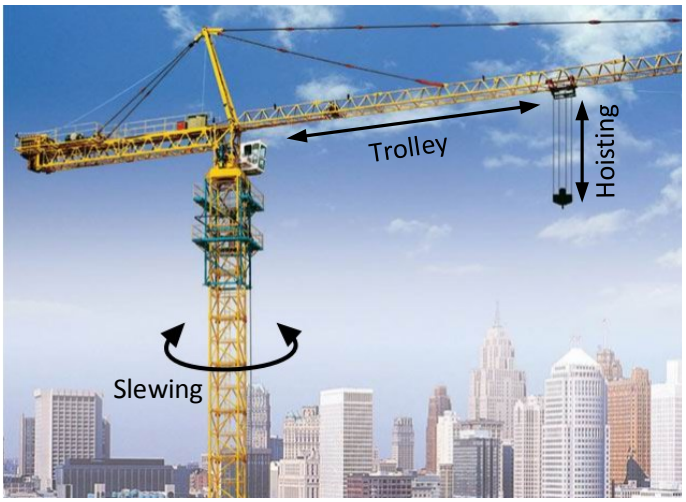

FIGURE 1.3: A tower crane at a construction site.[3]

because altitude of the payload needs to be changed in a large range, which might reach up to 40–50 meters in some cranes. Therefore, a cable-driven structure is more suitable than a rigid-arm one for large-scale systems like cranes. Since ropes are flexible, the payload behaves like a spherical pendulum when it is transferred from one point to another, as shown in Fig. 1.2. This pendulum-like motion is referred to as the *swing oscillation* of cranes, and it can be decomposed into two swing angles: α and β in a spherical coordinate system whose origin is attached to the boom tip. Due to the swing oscillation, the payload does not stop at the designated position after the transfer, but rather oscillates around that point if no control action is imposed.

1.2.2 Skew oscillation

In every crane, three fundamental motions (i.e., gantry + trolley + hoist in gantry cranes, slew + luff + hoist in boom cranes, and slew + trolley + hoist in tower cranes) can only control the *position* of the payload. To further adjust the payload's *orientation*, cranes need to be equipped with an additional skew adjustment device. In fact, the skew orientation control of a payload plays an important role in crane systems. For example, the payload's center of gravity G of the overhead crane system shown in Fig. 1.4 arrived at the correct position without any oscillation. However, when the target orientation is taken into account, the transferring process is said to be incomplete since there exists a skewing mismatch angle γ between the payload's orientation and its desirable pose. Therefore, it is essential to rotate the payload at a skew angle of γ along the Z-axis in the counter-clockwise direction so as

[3]Source: https://www.simscrane.com

to accomplish the transferring task. A similar issue is also encountered in boom crane systems in use at harbors, where the skew orientation of the container has to be adjusted to comply with that of the truck or vessel.

In practice, there are two types of mechanisms currently being used for controlling the skew orientation of the payload, namely the indirect and direct types. The indirect mechanism is usually utilized in container cranes, where a sophisticated four-rope configuration is used in conjunction with a spreader [2–4]. Four actuators are equipped to independently control the length of each rope so that full orientations of the payload, namely trim-list-skew angles, can be controlled. However, in this type of mechanism, the maximum skewing angle can only be adjusted up to a few degrees in both clockwise and counter-clockwise directions. Therefore, the flexibility of the skew adjustment is very limited. The second kind of skewing control mechanism is illustrated in Fig. 1.4, where a two-rope configuration in combination with a simple device called a *rotary hook* is used. In contrast to the indirect type, the rotary hook device is not designed to control the rope lengths. Alternatively, it directly controls the skewing orientation of the payload using a servo motor that is mounted inside the device. As shown in the zooming area in Fig. 1.4, the payload is directly attached to the motor shaft, and the entire suspended load is hung below the trolley through two flexible ropes. By using this kind of direct mechanism, the skewing orientation can be controlled to any desired value (> 360 degrees). However, along with the above advantage, after reaching the desired angle, the payload continues to oscillate rather than stop at the designated skew angle due to the law between inertia force and rope tensions.

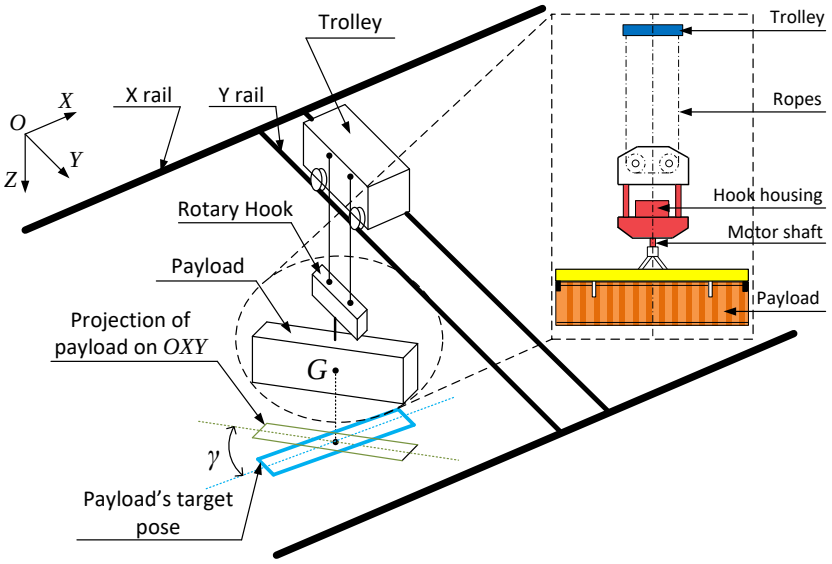

FIGURE 1.4: Necessity of the payload orientation control in an overhead crane system. To adjust the payload's skew orientation, the direct mechanism with an aid of the rotary hook device is employed.

To sum up, the swing oscillation of the payload is induced by the point-to-point transfer, whereas the skew oscillation is resulted mainly from the orientation adjustment of cranes.

1.3 Overview of cranes' vibration controls

We know from Section 1.2 that both swing and skew oscillations exist in crane systems. As a consequence, two major themes prevail in the current literature: swing vibration control and skew vibration control. The prominent challenge in the vibration control of cranes is the underactuated characteristic of the system (i.e., the number of control inputs is less than that of the control outputs) as well as the presence of uncertainties and disturbances. Two survey papers [5] and [6] have provided a sufficiently comprehensive summary of the dynamics and swing vibration suppression controls of cranes, where the latter is relatively more recent than the first one. Since the accumulative literature is too vast to list every single detail of all the made efforts on the topic, only the most notable and commonly used techniques are subsequently reviewed. Even though the structures of different crane systems are quite distinctive, the control techniques, which are successfully established on one crane type, are generally supposed to be applicable on others, of course, after some modifications or simplifications.

1.3.1 Swing vibration controls

As previously discussed, one must rely on the objective and context of each given application to determine if one should use the swing suppression control or the swing excitation control. In general, the swing suppression control must be used to transfer large blocks for safety, and the swing excitation control should be appropriately employed in the case of transporting bulk material (e.g., sand, cement, etc.) so as to shorten the transfer time (see Chapter 6).

1.3.1.1 Swing suppression control

In this case, the swing oscillation is seen as a harmful factor to the system, so it needs to be suppressed. The swing suppression control can be classified into two main categories: feedback and feedforward controls. These types can be combined to obtain a 2-DOF control system for improving control performance.

Feedback controls

Feedback control techniques are rich in the literature, which lend themselves many key developments of the control theory field. Therefore, in the primitive era, linear controls were intensively utilized [7–9]. Among them, one of the earliest works can be traced to Hazlerigg [10], where a lead compensator was utilized to damp the payload and compensate for random disturbance forces acting on it. The conflict between a good swing damping and the external disturbance rejection can be compromised by simply introducing an additional outer feedback loop that takes the error between the actual payload position and its reference as the input. Yoshida and Kawabe [7] applied a saturating control law that guaranteed a specific upper bound of a quadratic performance index. Furthermore, the control input constraint was also ensured. Lee et al. [11] proposed a cascade control system for a three-dimensional overhead crane in which the position servo control and the anti-swing loop were designed based on loop-shaping and root locus techniques, respectively. Sawodny et al. [12] utilized a pole placement controller to suppress the vibration of an automated gantry crane, which showed good performance through both simulations and experiments. Uchiyama [13] proposed a linear robust control method for a boom crane. The controller only partially used state feedback, and it was endowed with an integrator to reduce the position tracking error. In addition, the control system was robust against the rope length uncertainties. Recently, Mori and Tagawa [14] introduced a transfer-function-based controller for an overhead crane. To account for the limited acceleration, a linear parameter varying model with an acceleration limit was established. Experimental results were shown to be satisfactory. Nevertheless, most of the linear control laws require linearized models. Therefore, they may not be suitable candidates for high-performance overhead crane systems in which the usage of nonlinear models is necessary. As a result, modern crane controls steered toward the nonlinear control techniques, where the second method of Lyapunov was being centralized.

The feedback linearization and differential-flatness-based methodology [15, 16], which aims at transforming nonlinear models to linear ones so as to utilize the well-established linear controls, were also widely applied [17–20]. Tuan et al. [19] employed a partial feedback linearization technique for a three-dimensional overhead crane, where the total control law consisted of stabilizing control components of both actuated and unactuated subsystems. Qian et al. [21] established a learning-based partial feedback linearization technique for an offshore boom crane. The unknown periodic disturbances caused by the sea heaves were estimated and compensated in the control law. The main disadvantage of the feedback linearization method lied in the fact that it is not robust to the parametric uncertainties and unmodeled dynamics. In order to deal with such circumstances, sliding mode-based controls [22–24], adaptive controls [25–28], and energy and passivity-based nonlinear controls [29–32] are preferable. Almutairi et al. [23] proposed a first-order sliding mode controller for a three-dimensional overhead

crane, where the key point is to inject the swing oscillation to the sliding function to deal with the underatuation of the system. Simulation results were provided. Chen et al. [33] introduced an adaptive control law for a tower crane system. Unlike the sliding mode control scheme, the swing information was naturally integrated into the parameter adaptation law. Recently, Sun et al. [34] formulated a nonlinear controller for a dual boom crane. The proposed method eliminated the need for velocity sensors or implicit differentiation, which is sensitive to measurement noises. Furthermore, the actuator constraints were explicitly taken into account in the design process. Other new developments in model predictive control have promptly been applied to crane systems [35–38]. Also, intelligence controls, which are based on fuzzy logic and neural networks have also been successfully implemented to overhead crane systems [39–42].

Feedforward controls

Unlike the feedback controls counterpart, feedforward controllers do not need to use the information of swing oscillations for vibration suppression. This plan-and-run feature makes the implementation of feedforward control schemes to real systems easy and simple since it does not require a complex sensor structure. However, the robustness of feedforward controls is not comparable to that of feedback schemes under the presence of uncertainties and especially under harsh disturbances. In the case that only mild uncertainties and disturbances affecting the system, feedforward controls have proven to be very effective for achieving a transportation without residual vibration. There are three main techniques in the feedforward control category: input shaping, optimal control, and motion planning.

Input shaping [43–50] is perhaps the most widely used technique in the feedforward vibration control. Its basic idea is to intelligently modulate the original reference command by convolving with a sequence of impulses called input shaper. The input shaper is designed in a way that the induced vibration by all impulses is self-canceled. If an input shaper causes no vibration, its convolution with any reference command also results in a zero-vibration for the system. The study of Singer et al. [44] is among the first ones to apply the input shaping control to a crane system. Since then, input shaping has been a promising method for suppressing sway motions in crane systems. Singhose et al. [46] reported that input shaping control results in a considerable reduction in both residual and transient oscillations, even when the hoisting distance is a large percentage of the cable length. Lawrence and Singhose [51] proposed two new input shapers that suit the slewing motion of a tower crane. It was shown that the improved input shapers outperformed the standard zero-vibration, zero-vibration-derivative, and unity-magnitude input shapers. Both simulation and experimental results were provided. In [52], a multi-mode specified insensitivity input shaper was implemented to a laboratory double-pendulum tower crane. Recently, Ramli et al. [53] attempted to use an artificial neural network (ANN) trained by

particle swarm optimization to modify the unity-magnitude zero-vibration input shaper online and to deal with the change in the rope length and payload mass uncertainties. The ANN was actually used as a nonlinear multivariate regression method, whose training data was taken from a given list of optimal unity-magnitude input shapers for different rope lengths and payload mass values. An improvement was demonstrated through experimental results in comparison with standard input shapers.

Optimal control originated in the 17th century, and its foundation is based on the calculus of variation, whose pioneers are among the greatest mathematicians of all time, including Leonhard Euler, Joseph-Louis Lagrange, and Karl Weierstrass. In 1956, this field was revolutionized by Lev Pontryagin with his Minimum Principle, which gave necessary conditions for optimality in the presence of state and/or input constraints [54–57]. Instead of minimizing the given functional over an admissible function space, by the Pontryagin Minimum Principle (PMP), the problem at hand can be converted to a pointwise optimization problem for the Hamiltonian function, which is much easier to solve. For some simple dynamical systems, the PMP can provide analytical solution. However, in most cases where we need to deal with complex nonlinear systems, computational techniques have to be employed. When formulating an algorithm to solve the optimal control problem, we need to ensure that the algorithm must be convergent, and that the converged solution must satisfy the imposed optimality condition by the PMP. In this line of research, Sakawa and Shindo [58] proposed an efficient algorithm for solving the optimal control of container cranes with both state and input constraints. The method is based on both first-order differential dynamic programming and the PMP. Simulation results on a real-size container crane were provided. Auernig and Troger [59] reported a time-optimal control scheme of a container crane for both force and position control configurations. The neccesary conditions for optimality with actuator constraints were first introduced, and then suitable values of co-state variables were selected. Also, active and inactive constraints were rationally considered in the numerical computation process. Terashima el al. [60] performed a computational optimal control algorithm on a rotary crane using the straight transfer transformation method. The luffing and slewing motion were coordinated to transfer the payload in a way that the projection of the payload trajectory on the horizontal plane is in a straight line. All the three motions of the rotary crane, including the slewing, luffing, and hoisting, were simultaneously considered. A free-terminal-state and fixed-terminal-time optimal control problem was solved using an iterative procedure with the Davidon–Fletcher–Powell update rule for the search direction. Simulation and experimental results were presented, and they properly resembled each other. Apart from the schemes using the PMP, a different method that can also solve the universal optimal control problem is the one that bases on the nonlinear or linear programming techniques. The system is discretized to formulate and solve linear/nonlinear programs using optimization solvers [61–64]. In general, this method is less accurate, and it requires more computational effort than the

methods that use the PMP, with which the "shape" of the optimal control input can be foreseen, and thus we know more information on what the actual optimal input solution should look like.

In the motion planning method, it is common to assume a specific class of control inputs that will be applied to the system. From the necessary conditions for vibration-free transportation, essential constraints on the assumed control input (e.g., rising time, falling time, magnitude of each period) need to be determined [65–71]. In comparison with the optimal control approach, which can result in universal optimal solutions, the motion planning method can only provide local solutions for a particular class of control inputs. However, analytical solutions can usually be obtained when the motion planning method is used. Thus, it does not require high computational effort as much as the optimal control technique. Moreover, control input and state constraints can also be conveniently incorporated in the design process. Meckl and Arestides [65] proposed a S-curve position command generated from a bang-off-bang acceleration profile to suppress vibration for flexible systems. The excitation energy of the input forcing function was minimized using frequency analysis. Uchiyama et al. [68] introduced a simplified model of a rotary crane system that includes significant centrifugal and Coriolis force terms. This simple model allowed the analytical solutions of the differential equations of the model to be derived. Then, a trigonometric S-curve trajectory of the slewing motion was designed such that the vibration at the end of transportation should be zero. Satisfactory experimental results were provided. Chen et al. [72] established a time-optimal off-line trajectory planning method and a tracking control scheme for an overhead crane. The B-spline trajectory was parameterized with unknown parameters to establish a static optimization problem in which the cost function was the total transfer time. Several constraints, including actuator limitations and maximum allowable swing angles, were taken into account. Both simulation and experimental results were presented. Using an overhead crane, Wu and Xia [61] compared the performances of various motion planning methods in both time-efficiency and energy-efficiency criteria. In [71], a discrete-time command profile was proposed using finite step segments that matched steps of the discrete command signal to those of the control hardware. In contrast to the above studies, the jerk-limited S-curve trajectory of [69, 70] was established in the jerk level for damped and undamped flexible systems. Most of the motion planning methods utilized linear models in their designs. To directly employ the original nonlinear models of cranes so as to enhance the control performance, the differential flatness-based approach can be used [73–76]. Cranes are known to be flat systems in which the flat outputs are the vertical and horizontal positions of the payload. Therefore, the motions can be first planned for the payload position, and then the flat inputs can easily be derived based on simple algebraic relations connecting the flat outputs and the inputs. There are two main disadvantages in the differential flatness-based motion planning. First, the input trajectory must be smooth. From the PMP, we know that the time-optimal controller

(of a linear system with only input constraints) is of a bang-bang type, which is not even continuous. Therefore, the resultant trajectory of the flatness-based method is generally slower than that of other methods, such as input shaping and especially optimal control. This disadvantage is significant in the case of real-size cranes where the natural period of the system is large. The second drawback of the differential flatness-based motion planning approach is that embedding robustness with respect to parametric uncertainties into the planning trajectory is not straightforward.

1.3.1.2 Swing excitation control

In the current literature, the swing oscillation is often seen as an undesirable property. As a result, there are almost no studies on the topic of swing excitation control. In Chapter 6 of this thesis, it is shown that, in the context of bulk material transportation, the swing excitation control can significantly reduce the transfer time compared with the minimum-time vibration suppression controller—the fastest member of the vibration suppression control group.

1.3.2 Skew vibration controls

Skew oscillation is mostly unfavorable in crane systems because the skew adjustment is only necessary in the case of large block transfers. Therefore, vibration suppression is the sole objective that needs to be considered in the skew vibration control. In comparison with the well-established swing vibration suppression control (see Section 1.3.1.1), there have only been a few studies that paid attention to designing skew vibration suppression controllers. In other words, the current mainstream only focuses on the payload position control to suppress the swing oscillation. There is a serious lack of considerations in the payload skew orientation control in which the skew oscillation exists. A brief literature review of the skew vibration suppression control is given below, and further details are mentioned in Chapters 2 and 3. Moreover, this thesis focuses on the direct mechanism type with the aid of a rotary hook device to obtain full flexibility in controlling the payload's skew angle (see Section 1.2.2).

The very first work on modeling and designing automatic controllers for the rotary hook system should be credited to [77]. A nonlinear model of the rotary hook system was formulated in conjunction with the development of two controller types, namely time-optimal and state feedback control, based on a simplified double integrator plant. Full-scale experiments were conducted to verify the performance of the state feedback controller, and the controller gains were chosen based on trial and error. Terashima and Suzuki [78] established an innovative autonomous 3D crane system consisting of path planning and obstacle avoidance algorithms considering the rotary motion of the payload. This study only

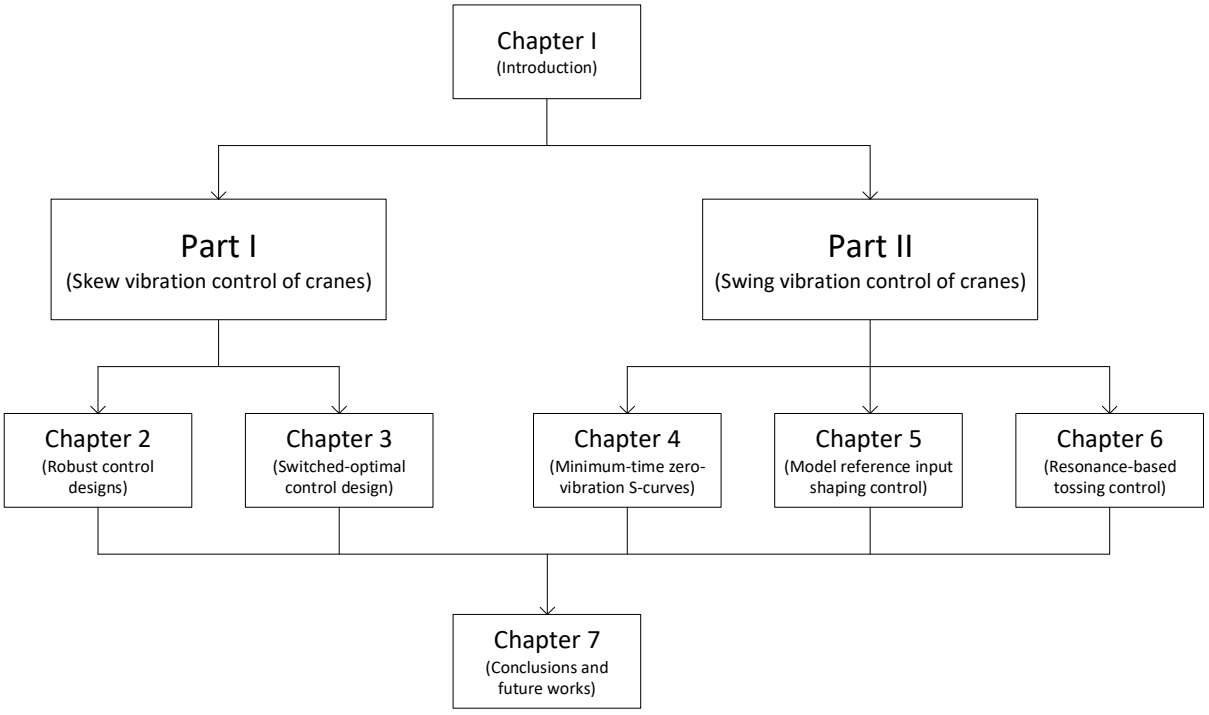

FIGURE 1.5: Structure of the thesis.

emphasized the potential method and its extension for solving the path generation problem. In other words, the skew oscillation suppression was not considered to an elaborate degree. Sawodny et al. [12] introduced a linear model of a rotating system whose function is similar to that of the rotary hook device. A 2-DOF controller was designed based on the pole placement technique. Experimental results showed that the tracking error and vibration damping capability of the proposed controller were satisfactory. Nevertheless, the nonlinear model needs to be further developed and employed to enhance the control performance as well as to extend the feasible operating region. Recently, Schaper et al. [79] proposed a 2-DOF skew control with a novel trajectory controller that consists of both state feedback and model predictive control feedforward paths. The performance of the control system was validated with test drives using a full-size mobile harbor boom crane.

1.4 Objectives and outline of the thesis

The objective of this thesis is to solve several new practical control problems related to both skew and swing vibration controls of cranes. These problems arise from the industrial demand, which makes them practically important. This thesis aims at creatively applying the control theory foundation to

solve unanswered control problems and improve the existing solutions in crane control. The main content of the thesis is organized into two parts whose structure is illustrated in Fig. 1.5.

Part I of this thesis is devoted to the skew vibration (suppression) control of crane systems, and it comprises of Chapters 2 and 3, whose brief summaries are elaborated below.

- Chapter 2 solves the robust control problem for the vibration-free skew transfer process of cranes in the presence of parametric uncertainties. Two robust controllers are proposed: a nonlinear integral sliding mode control (ISMC) and a dynamic output feedback sub-optimal H_∞ control. The robust stability of each controller was obtained using two different techniques: Lyapunov-based method for the nonlinear ISMC and μ-synthesis for the H_∞ controller. These robust stability conditions were then included in an optimization process in which the metaheuristic particle swarm optimization mechanism was utilized to optimize a control criterion. Thus, the minimization of the desired performance index and the robust stabilization of the closed-loop system can simultaneously be guaranteed in a single framework.

- Chapter 3 pursues a solution to the time-optimal control problem to enhance the transfer productivity of the skew rotation system in cranes. A computational optimal control scheme based on a conjugate gradient method was applied, which monotonically converges to a (local) optimal solution. Meanwhile, the optimality condition resulting from the PMP was satisfied. The main idea of Chapter 3 is to use an additional binary actuator, especially an electro-mechanical clutch, to reduce energy consumption without trading-off the sub-optimal transfer time. By intelligently switching on and off the binary actuator, unnecessary energy usage can significantly be reduced, since in a specific interval, the payload can rotate by its own momentum. As a result, a switched optimal control problem must be addressed. The experimental results showed that, under a similar minimum transfer time, the switched optimal control system was able to reduce energy consumption by 25.49% and 61.70% in the medium and long transfer cases compared with the no-switched optimal control system, respectively.

Part II of the thesis deals with the swing vibration control problem of cranes. In the first two chapters (Chapters 4 and 5), some new results are presented to improve the performance of the existing swing vibration control methods, and they are all feedforward types. In Chapter 6, a swing excitation control problem was first proposed in the context of the bulk material transportation of an overhead crane system. Then, it was solved using a resonance-based controller. Both simulation and experimental results are provided in Chapter 4 and Chapter 6, whereas only simulation results are given in Chapter 5. A brief summary of Chapters 4–6 of Part II is given as follows.

- Chapter 4 establishes minimum-time zero-swing-vibration S-curve commands (in the position level) for an overhead crane. The actuator limits, including the maximum velocity and acceleration, were explicitly taken into account in the design process. Based on a parameterized bang-off-bang acceleration profile, two methods were proposed to build the swing suppression capability. The first one is an embedding method that directly injects the essential terminal conditions for swing-free transportation into the baseline S-curve command. The other one is a shaping method inspired by the input shaping technique. Minimum-time solutions were successfully obtained by solving constrained (discrete) nonlinear programs. An online trajectory generation can be achieved using the proposed approach.

- Chapter 5 formulates a model reference input shaping control for a luffing dynamics of a rotary crane system with a time-varying rope length. Unlike Chapter 4 in which a linear model was utilized, the newly established input shaping technique in Chapter 5 can completely suppress the swing oscillation for a highly nonlinear time-varying system. The fundamental idea is to match the real swing oscillation of the nonlinear time-varying crane with that of a linear time-invariant reference system on which the standard input shaping is applied.

- Chapter 6 introduces a new concept of swing excitation control in crane systems, which is named tossing control. Bulk material transport has a unique feature that can be exploited, i.e., the transferred material can be dropped or discharged while in the air. This allows the relaxation of the terminal zero swing angle as found with the swing suppression control. To realize the tossing control requirement, a resonance-based tossing controller is proposed to induce oscillation with a periodically increasing amplitude. It was then evidently demonstrated that the resonance tossing control is capable of breaking the time limitation of the minimum-time swing suppression control—the fastest member of the swing suppression control group.

Finally, Chapter 7 draws the conclusions and the possible future developments of the thesis.

1.5 Contributions of the thesis

This thesis presents several original contributions to solve new problems relevant to both skew and swing vibration controls in cranes. Since all the chapters are quite distinct, each chapter' contribution is separately elaborated as follows.

Skew vibration (suppression) control:

- The robust control problem of the uncertain skew transfer process in cranes was not addressed in the current literature. This problem is solved in Chapter 2 using two robust controllers whose gains or weighting coefficients are automatically tuned using the particle swarm optimization mechanism to ensure both robust stability and control performance. Especially, a new coupled integral sliding function is proposed for the nonlinear ISMC to inject the swing oscillation information into the resultant control law as well as to cancel the reaching phase as found with conventional sliding mode controllers.

- Using a binary actuator, a novel switched optimal control system was established for the skew transfer process of cranes in Chapter 3. The proposed method was able to significantly reduce the total energy consumption compared to no-switched control schemes, including the no-switched optimal control, input shaping control, and nonlinear ISMC. The basic idea is to impose upon the conservation of angular momentum to make the payload rotate with its own inertia over a specific period of time.

Swing vibration control:

- A minimum-time zero-vibration solution of the class of bang-off-bang acceleration inputs subject to both maximum velocity and maximum acceleration constraints is proposed for an overhead crane in Chapter 4, which fills a gap in the literature. The proposed minimum-time trajectory is considerably faster than related studies in the literature which use the same class of inputs.

- A new design of a model reference input shaping controller for a luffing dynamics of a rotary crane system is introduced in Chapter 5. The newly established technique is able to completely suppress the residual swing oscillation for a highly nonlinear time-varying system. This is not a trivial result compared with the conventional input shaping control design.

- It is shown in Chapter 6 that the swing suppression control is not always the best option in every circumstance. One example exists in the bulk material transportation where the zero terminal swing angle constraint is not necessary. This allows us to use the swing excitation control rather than the swing suppression control to further reduce the transfer time so as to improve the transport productivity. In fact, the results in Chapter 6 demonstrate the possibility of breaking the time limitation of the minimum-time swing suppression control—the fastest controller in the swing suppression control family—by using a resonance-based swing excitation control.

Part I

Skew Vibration Control of Cranes

Chapter 2

Robust Control Designs

In this chapter, a robust nonlinear Integral Sliding Mode Control (ISMC) is proposed as a vibration controller for the payload's skew rotation process of a boom crane to cope with parametric uncertainties in the system parameters. By using the indirect Lyapunov method, algebraic inequality constraints for the ISMC gains are formulated to ensure the robust stability of the closed-loop system under the sliding mode and in a context where the reaching phase is completely eliminated. Moreover, a robust output feedback H_∞ control is introduced as a benchmark to compare with the nonlinear ISMC. Specifically, μ-synthesis is utilized to establish the robust stabilization for the H_∞ controller. An optimization routine based on the meta-heuristic Particle Swarm Optimization (PSO) mechanism is established, which adopts the robust stability conditions with regard to each controller as the nonlinear constraints. By means of the proposed optimization procedure, minimization of desirable performance index and robust stabilization of the closed-loop system are guaranteed simultaneously in a single framework. Through both random simulation and experimental results, ISMC shows its superiority to the H_∞ control, hence ISMC is the preferable candidate for actual implementation on the real-size system in use at the harbor.

2.1 Introduction

In Section 1.2.2, the importance of the skew adjustment process is demonstrated on an overhead crane. Another example is subsequently given in the case of a boom crane system working at the harbor. Skew mismatch between the container and the truck is often encountered in practice. For an example, as shown in Fig. 2.1a, the boom crane must rotate the container at a skew angle of α in order to place on the truck properly. If the landing angle of the container is not precise or oscillated, four oval holes

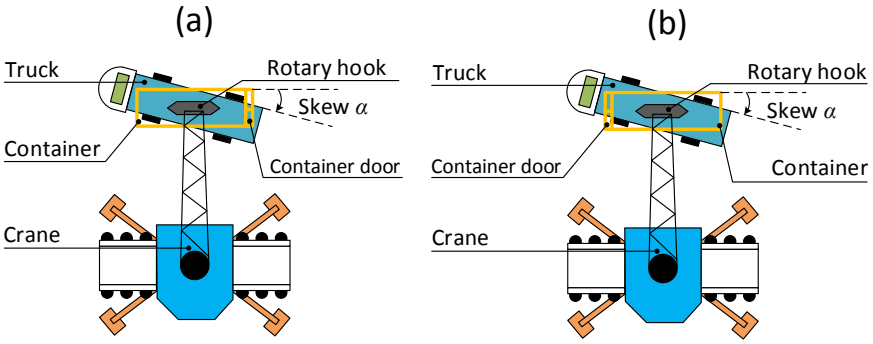

FIGURE 2.1: Necessity of the container skew angle correction. In the left figure, the container should be rotated α degrees clockwise, whilst in the right figure, the container should be turned $180^\circ - \alpha$ degrees in counter-clockwise direction to make the container door at the rear end of the truck.

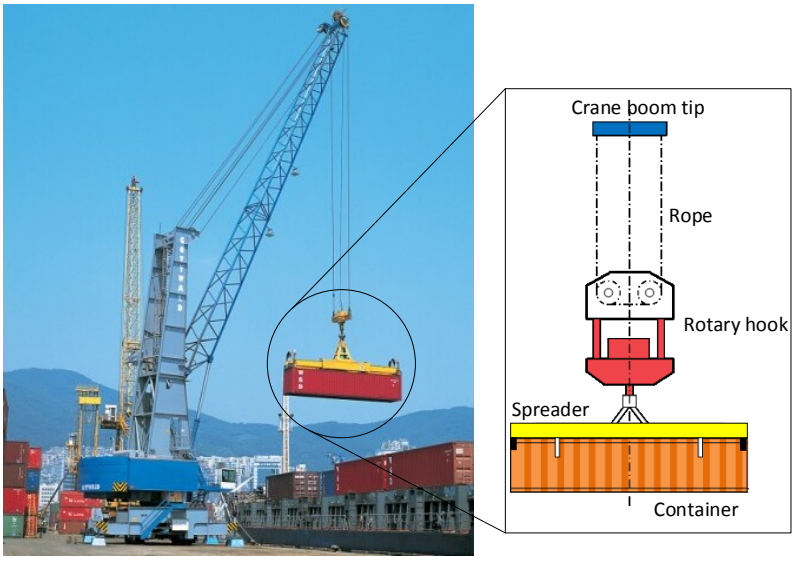

FIGURE 2.2: Boom crane equipped with a rotary hook device at the harbor.[1]

in the corners of container cannot be inserted to the twistlocks fitted on the truck, and therefore the loading/unloading process cannot be completed. Furthermore, in the case described in Fig. 2.1b, the container skew angle must be corrected by an amount of $180^\circ - \alpha$ with the purpose of making the container door locate at the rear end of the truck. In fact, in a transloading cycle, it takes significant time for the crane operator to manually suppress the residual oscillation of the container at the end of skew rotation.

In contrast with a complex trolley-spreader system used in the gantry crane which allows the container orientation can be adjusted in either trim, list, or skew angles [4], in reality, the boom crane system utilizes a simple device called rotary hook to rotate the container to any desired skew angle. The

[1]Source: https://www.konecranes.com

structure of a rotary hook system is described in Fig. 2.2, where the spreader grips the container by a twistlock mechanism and is also connected with a motor shaft which is mounted inside the housing of the rotary hook. Finally, the rotary hook device is hung below the crane boom tip by ropes. Note that the rotary hook device only enables the boom crane to adjust the skew angle of the container, however it can be arbitrary (> 360 degrees). Nevertheless, after the rotation of the motor shaft drives the payload to the desired angle, a large residual oscillation will appear because the whole system (including payload and rotary hook device) has large inertia, low damping ratio and is suspended by flexible ropes. In reality, because the rotary hook is an under-actuated system (i.e., the number of actuators is less than the number of control outputs), the crane operator must possess substantial skill and experience to perform multi-tasks simultaneously (i.e., driving the payload to the desired skew angle and suppressing the residual skew oscillation), and as a consequence, the transfer process is not particularly time efficient. Therefore in order to significantly reduce the workload on the crane operator as well as the duty cycle time of the transshipment, an automatic controller should be developed for the rotary hook system.

Despite urgent requirements from the harbor industry and in contrast to the well-established swing suppression controls, there are only a few studies paying attention to design payload skew vibration suppression controllers. In [77], modeling of the rotary hook system is derived, in conjunction with the development of two controller types: open-loop time optimum control and closed-loop state feedback control. However, the system natural frequency is assumed to be known in the design process, therefore unrealistic in practice. The robustness of controllers are not sufficiently mentioned in the above study. Recently, Schaper et al. [79] proposed a 2-DOF skew control with a novel trajectory tracking controller which consists of both feed-forward and feedback paths. A state feedback control law is utilized to compensate any deviation of the system outputs to the generated reference trajectory. The performance of control system is verified with a test drive on a full-size mobile harbor crane. Nevertheless, none of aforementioned studies thoroughly consider the robustness of controllers with respect to the parametric uncertainties.

The actual specification of the rotary hook system in use at the harbor is characterized by wide parametric uncertainties. Therefore, without a robustness consideration, the controller will likely cause instability to the closed-loop system. The sliding mode control is known to be one of the most powerful tool to deal with uncertain systems. In a conventional sliding mode controller, the reaching phase exists, over which the convergence of controlled variables to their references cannot be claimed. For this reason, the system should be forced to slide on the designated sliding surface in the very beginning of time, which leads to the development of ISMC in this chapter. Since its first introduction in [80], ISMC has been developed in various forms and applications [81–90]. In [91], a synthesized

ISMC is proposed for controlling systems with both matched and unmatched uncertainty. The sliding mode exists at the beginning, hence the system can reinforce the robustness against perturbations more than other conventional SMC. Xu et al. [92] have employed the ISMC proposed in [91] to an under-actuated unicycle vehicle. The comparison results between a LQR controller with nonlinear compensation and the ISMC have been conducted. The experimental results of [92] is reported in [93], where the ISMC consists of a state feedback nominal control law and switching terms. However, the robust stability analysis of closed-loop system under sliding mode in the presence of parametric uncertainties is not considered to an elaborated degree in the above researches.

H_∞ robust control is one of the most elegant fashion to treat the uncertainties in a dynamical system [94–97]. Therefore, in order to draw a comprehensive capability of the robust control theory in practical application, H_∞ controller will be introduced as a representative of linear method to compare with the nonlinear ISMC. The conclusion of comparative study will suggest the preferable approach should be utilized for the rotary hook system. Along with the rapid development of fundamental theory, numerous practical applications employing the robust H_∞ controller are reported [98–102]. However, the major stumbling block in the design process of H_∞ controller lies on the fact that there is not a specific rule/procedure for choosing appropriate weighting functions. At the moment, the weighting functions selection is mainly based on trial and error with the rule of thumb being simply that the gains of weighting functions on tracking errors and disturbance attenuations should be high in the low-frequency region (i.e., in the form of low-pass filter) and the opposite way is applied for the gain of weighting functions on measurement noises or unmodeled dynamics [103–107].Especially, in order to achieve a satisfactory control performance and robustness for a system which has large parametric uncertainties such as rotary hook, it would be very exhausting and time consuming if only trial and error strategies are performed.

To address the remaining problems in the above discussions, the following contributions are presented in the chapter. Firstly, the robust stability analysis of ISMC in the presence of parametric uncertainties is systematically established. By using the indirect Lyapunov method, algebraic inequality constraints of ISMC gains are exploited to guarantee the robustness of the closed-loop system in the context where the reaching phase is eliminated. Secondly, to draw a fair comparison between ISMC and H_∞ control, a new optimization routine is proposed. Parameters of each controller will be automatically obtained by the optimization procedure to ensure both minimization of one desirable performance index and the closed-loop robust stability conditions in a unified framework.

The remainder of this chapter is organized as follows. In Section 2.2, a mathematical model of the rotary hook system is provided and validated on the experimental testbed. Next, an ISMC law

is formulated and robust stability analysis of the closed-loop system is carried out in Section 2.3. Moreover, an optimization routine using particle swarm mechanism for the ISMC gains is proposed which employs the robust stability conditions as nonlinear constraints. In Section 2.4, a robust output feedback sub-optimal H_∞ control is configured and designed, therein weighting matrices are optimized to obtain both minimization of performance index and robust stabilization. The superiority of ISMC to the H_∞ control is shown by random simulation results and explained thoroughly in Section 2.5. Experimental studies of the robust controllers are provided in Section 2.6. It is later shown that performances of controllers are satisfactory without any gains tuning activity. Finally, some conclusions will be discussed in Section 2.7.

2.2 Mathematical modeling validation

2.2.1 Mathematical model

This section provides a brief description on modeling of the rotary hook system which consists of a rotary hook device, payload, ropes, and boom tip. The skew residual oscillation of the rotary hook system resulting from the rotation of payload is depicted in Fig. 2.3, where $\varphi(t)$ denotes the relative angle between the load and the hook, whilst $\theta(t)$ represents the absolute angle between the hook versus x axis. Table 2.1 provides the definitions of all system parameters. The mathematical modeling of rotary hook system is given as follows

$$\ddot{\theta} = f + bu, \tag{2.1}$$

where

$$f = \frac{1}{I_L + I_H + \dfrac{mR^4 \sin^2\theta}{a^2}} \times \left[\frac{-mR^2 \sin\theta}{a} \left(\frac{R^4 \dot{\theta}^2 \sin^2\theta}{a^3} + \frac{R^2 \dot{\theta}^2 \cos\theta}{a} + g \right) - c\dot{\theta} \right]$$

$$b = \frac{I_L}{I_L + I_H + \dfrac{mR^4 \sin^2\theta}{a^2}}$$

$$u = \ddot{\varphi},$$

and $a = \left(l^2 - 2R^2\left(1 - \cos\theta\right)\right)^{1/2}$ is the holonomic constraint due to inelastic rope. Linearized model of the rotary hook system, which will be employed in the H_∞ controller design process, is described

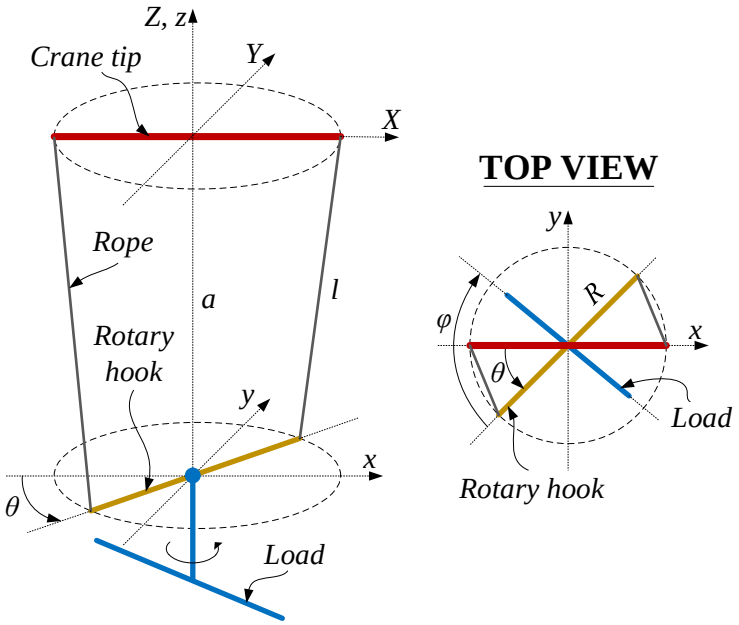

FIGURE 2.3: Modeling of the skew rotation system.

TABLE 2.1: Parameters of the uncertain skew rotation system.

Symbol	Description	Variation range
I_L	Inertia of the payload (kgm^2)	[2.64, 41.89]
I_H	Inertia of the hook (kgm^2)	[1, 1.5]
m	Total mass of the load and the hook (kg)	[77.39, 207]
R	Skewing radius (m)	0.25
l	Rope length (m)	[2.5, 5.5]
c	Friction coefficient (Ns/rad)	[0.1, 0.5]
g	Gravity acceleration (m/s^2)	9.81

by the following linear differential equation:

$$\ddot{\theta} = \frac{-mgR^2}{l\,(I_L + I_H)}\theta - \frac{c}{I_L + I_H}\dot{\theta} + \frac{I_L}{I_L + I_H}u. \tag{2.2}$$

Note that the system has only one control input (i.e., $\ddot{\varphi}$ generated by a servo motor) and two control outputs (i.e., $\varphi \rightarrow \varphi_d$ and $\theta \rightarrow 0$ where φ_d is the reference skew angle of the payload). The under-actuated characteristic of the rotary hook system makes the ISMC implementation not straightforward, however it becomes trivial in the H_∞ controller design process.

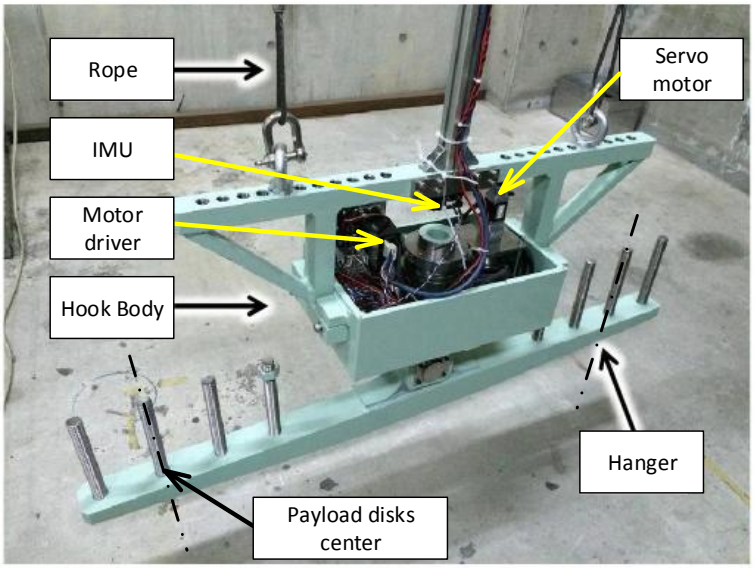

FIGURE 2.4: Experimental testbed structure. The payload mass and inertia can be adjusted by adding/reducing the number of payload disks installed on the hanger. The rope can be changed manually to a different length. Moreover, the angle $\varphi(t)$ can be measured by the encoder attached at the end of servo motor. A high accuracy 9-DOF IMU is utilized to measure the angle $\theta(t)$.

2.2.2 Experimental apparatus

Structure of the experimental testbed is illustrated in Fig. 2.4. The control input limitation provided by the servo motor is given as $|u|_{\max} = 0.5$ rad/s^2. In order to verify the effectiveness and robustness of the proposed controllers, the experimental apparatus is designed in such a way that the system parameters can be varied accordingly. The variation ranges of all system parameters are given in Table 2.1. Note that, the nominal values of total mass m, payload inertia I_L, hook inertia I_H, viscous damping c, and rope length l are chosen at the average of their variation intervals and are denoted as $\hat{m}$, $\hat{I}_L$, $\hat{I}_H$, $\hat{c}$, and $\hat{l}$ respectively. Generally, all of the actual system parameters cannot be measured in practice thus the robust controllers should be designed to have sufficient robustness under parametric uncertainty conditions described in Table 2.1. It should be clarified that "maximum case" refers to the case where the maximum number of payload disks are installed on the hanger thus m and I_L achieve their maximum values, similarly "minimum case" refers to the case that none of payload disk is installed hence m and I_L adopt their minimum values (in above discussed cases, all other parameters remain at their nominal values), and finally "nominal case" corresponds to the case that all of system parameters are at their nominal values.

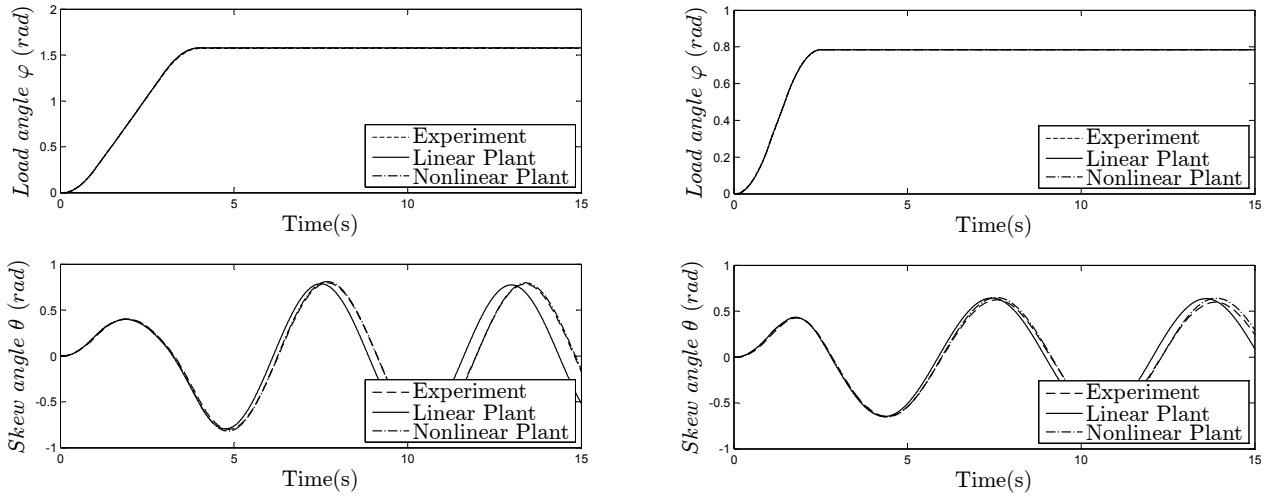

FIGURE 2.5: Model validation in the nominal case (left) and in the maximum case (right): the experiment data have a strong agreement with the nonlinear model (2.1) whilst there are significant lags in hook skew angle $\theta(t)$ between experiment data and the linear model (2.2).

2.2.3 Modeling validation

The rotary hook modeling will be validated in two cases: nominal and maximum case. In these cases, the amplitude of the hook skew angle $\theta(t)$ is sufficiently large which violates the assumption for derivation of the linearized model (2.2), hence advantage of the nonlinear model (2.1) can be revealed. In each case, the actual parameters of the experimental testbed will be feed for both nonlinear model (2.1) and linear model (2.2) in the simulations. The model validation results are shown in Fig. 2.5. It is observed that the nonlinear model (2.1) surpasses the linear model (2.2) in describing the dynamic of the rotary hook system, and this advantage will benefit the performance of ISMC which employs the nonlinear model (2.1) in comparison with the H_∞ controller which utilizes the linear model (2.2).

2.3 Robust integral sliding mode control design

2.3.1 Control law design and robust stability analysis

Without loss of generality, the tracking problem is considered in this chapter. Denoting the reference trajectory of the payload angle as $\varphi_d(t)$, thus the tracking error term can be expressed as $e(t) =$

$\varphi(t) - \varphi_d(t)$. The coupled integral sliding function is proposed as follows

$$\sigma = \beta_1 \dot{e} + \beta_2 e + \int_0^t \left(\beta_3 e(\tau) + \beta_4 \theta(\tau)\right) d\tau + \beta_5 \theta + \beta_6, \tag{2.3}$$

where $\beta_1, \ldots, \beta_6 \in \mathbb{R}$ and they will be bounded in the robust stability analysis process (see Theorem 1). By adding the constant term β_6 into the sliding function, it is expected to completely cancel the reaching phase (i.e., force the system to slide on the sliding surface at the very beginning of time), therefore the constraint $\sigma(t = 0) = 0$ should be satisfied which implies that

$$\beta_6 = -\beta_1 \dot{e}(0) - \beta_2 e(0) - \beta_5 \theta(0). \tag{2.4}$$

Note that all initial conditions of the system at the beginning of the motion can be always measured by the sensors (see Section 2.2.2), thus the value of β_6 in (2.4) can be easily established. By letting $\dot{\sigma} = -K\text{sgn}(\sigma)$ where K is a strictly positive real number satisfying $K > |\beta_1||\ddot{\varphi}_d|_{\max} + \eta$ and $\eta > 0$ (η can be arbitrarily small), the sliding mode control law can be obtained as

$$u_I = -\beta_1^{-1} \left(\beta_2 \dot{e} + \beta_3 e + \beta_4 \theta + \beta_5 \dot{\theta} + K\text{sgn}\left(\sigma\right)\right). \tag{2.5}$$

In order to verify the ability of the control law (2.5) in maintaining the sliding mode, a conventional Lyapunov function $V = \frac{1}{2}\sigma^2$ is employed, hence we have $\dot{V} = \dot{\sigma}\sigma \leq -\eta|\sigma|$. Therefore the sliding condition is ensured [108, p. 280], and as a consequence, the sliding surface $\sigma = 0$ becomes an invariant set. Note that with the choice of β_6 as in (2.4) and the usage of the sliding mode control law (2.5), the system will be attracted to the invariant set $\sigma = 0$ at $t = 0$ thus the reaching phase is actually eliminated.

Next, robust stability analysis of the proposed ISMC will be carried out. Since the sliding surface $\sigma = 0$ is coupled thus under the sliding mode, the convergence of tracking error $e(t)$ and skew angle $\theta(t)$ to their references, cannot be ensured automatically, especially with the presence of parametric uncertainties in the system parameters. Therefore, the following theorem will be proposed.

Theorem 1. For the under-actuated rotary hook system described by (2.1), by using the sliding mode control law (2.5) with an integral sliding function (2.3), the sufficient condition for all controlled variables to asymptotically converge to their references (i.e., $\varphi \to \varphi_d$, $\dot{\varphi} \to \dot{\varphi}_d$, $\theta \to 0$, $\dot{\theta} \to 0$) regardless of parametric uncertainties in all system parameters is

$$\beta_1 > 0, \beta_2 > 0, \beta_3 > 0, \beta_4 > 0, \beta_5 > 0, \beta_2\beta_4 - \beta_3\beta_5 > 0.$$

Proof. On the sliding surface $\sigma = 0$, the equation $\dot{\sigma} = 0$ also holds, hence by defining the state variables as $x_1 = \theta$, $x_2 = \dot{\theta}$, $x_3 = \varphi - \varphi_d$, $x_4 = \dot{\varphi} - \dot{\varphi}_d$, the closed-loop system under sliding mode is governed as follows

$$\begin{cases} \dot{x}_1 = x_2 \\ \dot{x}_2 = f - b\beta_1^{-1}(\beta_4 x_1 + \beta_5 x_2 + \beta_3 x_3 + \beta_2 x_4) \\ \dot{x}_3 = x_4 \\ \dot{x}_4 = -\beta_1^{-1}(\beta_4 x_1 + \beta_5 x_2 + \beta_3 x_3 + \beta_2 x_4). \end{cases} \tag{2.6}$$

It is observed that when the integral sliding surface (2.3) is used, under the sliding mode, the closed-loop system (2.6) remains the same order with the original system (2.1). Next, define the state vector as $\boldsymbol{x} = [x_1 \;\; x_2 \;\; x_3 \;\; x_4]^\top$, linearized model of the nonlinear autonomous system (2.6) around the equilibrium point $\boldsymbol{x} = 0$ can be described as

$$\dot{\boldsymbol{x}} = \boldsymbol{A}\boldsymbol{x}, \tag{2.7}$$

where

$$\boldsymbol{A} = \begin{bmatrix} 0 & 1 & 0 & 0 \\ -\mu_1 & -\mu_2 & -\mu_3 & -\mu_4 \\ 0 & 0 & 0 & 1 \\ -\beta_1^{-1}\beta_4 & -\beta_1^{-1}\beta_5 & -\beta_1^{-1}\beta_3 & -\beta_1^{-1}\beta_2 \end{bmatrix}, \tag{2.8}$$

therein $\mu_1 = \omega_n^2 + \bar{b}\beta_1^{-1}\beta_4$, $\mu_2 = c_N + \bar{b}\beta_1^{-1}\beta_5$, $\mu_3 = \bar{b}\beta_1^{-1}\beta_3$, $\mu_4 = \bar{b}\beta_1^{-1}\beta_2$, where $c_N = c/\left(I_L + I_H\right)$, $\bar{b} = I_L/(I_L + I_H)$, and $\omega_n^2 = (mgR^2)/(l(I_L + I_H))$.

The characteristic equation of the linear system (2.7) is determined as $\det\left(\lambda \boldsymbol{I} - \boldsymbol{A}\right) = 0$, which yields

$$\lambda^4 + h_1\lambda^3 + h_2\lambda^2 + h_3\lambda + h_4 = 0, \tag{2.9}$$

where

$$\begin{aligned} h_1 &= \mu_2 + \beta_1^{-1}\beta_2 \\ h_2 &= \mu_1 + \mu_2\beta_1^{-1}\beta_2 + \beta_1^{-1}\beta_3 - \mu_4\beta_1^{-1}\beta_5 \\ h_3 &= \mu_1\beta_1^{-1}\beta_2 + \mu_2\beta_1^{-1}\beta_3 - \mu_3\beta_1^{-1}\beta_5 - \mu_4\beta_1^{-1}\beta_4 \\ h_4 &= \mu_1\beta_1^{-1}\beta_3 - \mu_3\beta_1^{-1}\beta_4. \end{aligned}$$

According to the Hurwitz stability criterion, sufficient condition for the uncertain linear system (2.7) to be asymptotically stable is given by

$$\begin{cases} h_i > 0 \qquad (i = 1, \ldots, 4) \\ h_1 h_2 - h_3 > 0 \\ h_1 h_2 h_3 - h_3^2 - h_1^2 h_4 > 0. \end{cases} \tag{2.10}$$

It is straightforward to show that, by choosing $\beta_1 > 0$, $\beta_2 > 0$, $\beta_3 > 0$, $\beta_4 > 0$, $\beta_5 > 0$, and $\beta_2\beta_4 > \beta_3\beta_5$, all of inequalities in (2.10) will be satisfied. Therefore, based on the indirect (or linearization) Lyapunov method [108, p. 55], the nonlinear autonomous system (2.6) is asymptotically stable at the equilibrium point $\boldsymbol{x} = 0$, thus the proof now can be completed. □

Remark 1. The integral term in the sliding function (2.3) is essential in the sense that it will ensure both load angle φ and load speed $\dot{\varphi}$ to track the reference trajectory (i.e., $\varphi \to \varphi_d$ and $\dot{\varphi} \to \dot{\varphi}_d$) simultaneously. To clarify this claim, consider the case that the integral term does not involve in the sliding function (2.3) (i.e., $\beta_3 = \beta_4 = 0$), which yields

$$\sigma = \beta_1 \dot{e} + \beta_2 e + \beta_5 \theta + \beta_6, \tag{2.11}$$

where β_6 still follows the constraint (2.4) in order to cancel the reaching phase. Therefore, the control law (2.5) now can be described by (2.12)

$$u_I = -\beta_1^{-1} \left(\beta_2 \dot{e} + \beta_5 \dot{\theta} + K \mathrm{sgn}(\sigma) \right). \tag{2.12}$$

It is easily to show that the control law (2.12) will maintain the system (2.1) to slide on the sliding surface $\sigma = 0$ (here, σ refers to (2.11)) in the very beginning of time. However, in this case, the closed-loop system under the sliding mode reduces the order and is minimally realized by

$$\dot{\boldsymbol{x}}_r = \boldsymbol{F} \boldsymbol{x}_{\boldsymbol{r}}, \tag{2.13}$$

where $\boldsymbol{x_r} = [\theta \;\; \dot{\theta} \;\; \dot{\varphi} - \dot{\varphi}_d]^\top$ and

$$\boldsymbol{F} = \begin{bmatrix} \dot{\theta} \\ f - b\beta_1^{-1} \left(\beta_5 \dot{\theta} + \beta_2 (\dot{\varphi} - \dot{\varphi}_d) \right) \\ -\beta_1^{-1} \left(\beta_5 \dot{\theta} + \beta_2 (\dot{\varphi} - \dot{\varphi}_d) \right) \end{bmatrix}.$$

By performing the remaining steps similarly to the proof of *Theorem 1*, the constraints on β_1, β_2, and β_5 can be obtained to guarantee the robust stability of the closed-loop system (2.13). Consequently,

$\boldsymbol{x_r}$ approaches zero asymptotically, namely $\theta \rightarrow 0$, $\dot{\theta} \rightarrow 0$, and $\dot{\varphi} \rightarrow \dot{\varphi}_d$. As a result, the control law (2.12) is only able to track the velocity of reference trajectory (i.e., only ensures $\dot{\varphi} \rightarrow \dot{\varphi}_d$). Note that the control law (2.12) cannot be used when the load reference is in a step form (i.e., in the case that $\dot{\varphi}_d = 0$). From above discussions, obviously, the tracking performance of the control law (2.5) (with integral sliding surface) will outperform to the control law (2.12) whose integral term is absent in the sliding surface. It should be emphasized that the method in this chapter results in the algebraic inequality constraints for ISMC gains, which is different from LMI constraints formulated in [109]. Note that, the LMI optimization would sometimes fail to provide a feasible solution if the relevant weighing terms are not chosen appropriately.

Remark 2. To reduce the chattering in the control signal, the signum function $\text{sgn}(\sigma)$ in (2.5) should be replaced by a saturation function $\text{sat}(\sigma)$ which is defined in (2.14), therein ε is a constant related to the thickness of the boundary layer [108]

$$\text{sat}(\sigma) = \begin{cases} 1 & \text{if} \quad \sigma/\varepsilon > 1 \\ -1 & \text{if} \quad \sigma/\varepsilon < -1 \\ \sigma/\varepsilon & \text{if} \quad |\sigma/\varepsilon| < 1. \end{cases} \tag{2.14}$$

Remark 3. In order to ensure the payload motion sufficiently smooth, a 3$^{\text{rd}}$ order reference trajectory $\varphi_d(t)$ is proposed as in (2.15), by which the first and second derivatives of $\varphi_d(t)$ are ensured continuous.

$$\varphi_d(t) = \begin{cases} \dfrac{2\psi}{3t_f}t^3 + \varphi(0), & t \in \mathbb{T}_1 \\ \dfrac{-2\psi}{3t_f}t^3 + \psi t^2 - \dfrac{\psi t_f}{4}t^2 + \dfrac{\psi t_f^2}{48} + \varphi(0), & t \in \mathbb{T}_2 \\ \dfrac{2\psi}{3t_f}t^3 - 2\psi t^2 + 2\psi t_f t - \dfrac{13}{24}\psi t_f^2 + \varphi(0), & t \in \mathbb{T}_3 \\ \varphi_f, & t \in \mathbb{T}_4, \end{cases} \tag{2.15}$$

where $t_f = \sqrt{8\left[\varphi_f - \varphi(0)\right]/\psi}$, $\mathbb{T}_1 = [0,\ t_f/4)$, $\mathbb{T}_2 = [t_f/4,\ 3t_f/4)$, $\mathbb{T}_3 = [3t_f/4,\ t_f)$, and $\mathbb{T}_4 = [t_f, +\infty)$. In (2.15), φ_f is the final target angle (i.e., $\varphi(t_f) = \varphi_f$) and

$$\psi = \begin{cases} |\ddot{\varphi}_d|_{\max} & , \text{if } \varphi_f > \varphi(0) \\ -|\ddot{\varphi}_d|_{\max} & , \text{if } \varphi_f \leq \varphi(0). \end{cases} \tag{2.16}$$

By choosing φ_f and $|\ddot{\varphi}_d|_{\max}$, the reference trajectory is established. To this end, $\varphi_d(t)$ described in (2.15) is employed for all simulation and experiment studies with $\varphi_f = 90$ degrees (or $\pi/2$ rads) and

$|\ddot{\varphi}_d|_{\max} = |u|_{\max} = 0.5$ rad/s^2. Furthermore, without loss of generality, the system initial conditions are assumed as $\varphi(0) = 0$ (rad), $\dot{\varphi}(0) = 0$ (rad/s), $\theta(0) = 0$ (rad), and $\dot{\theta}(0) = 0$ (rad/s) hereafter, namely the system motion begins from rest.

2.3.2 Optimization of the ISMC gains

Two control objectives should be achieved for the concerning system: driving the payload to desired skew angle and suppressing the skew vibration simultaneously. Performance of each controller in accomplishing two aforementioned targets is measured by *settling time* t_{set} and *vibration suppression time* t_{sup}. The settling time t_{set} is defined as the time for the response curve of the payload angle $\varphi(t)$ to reach and maintain within a range $\zeta\%$ of the final target angle φ_f, namely

$$t_{set} = \min\{t : (1 - \zeta \text{sgn}(\varphi_f))\varphi_f < \varphi(t + \Delta_t) < (1 + \zeta \text{sgn}(\varphi_f))\varphi_f, \forall \Delta_t > 0\}, \tag{2.17}$$

where $\zeta\%$ is chosen as 1%. Moreover, the vibration suppressing time is expressed as

$$t_{sup} = \min\left\{t : |\theta(t + \Delta_t)| < |\theta(t)| \leq \theta_{tol},\ \forall \Delta_t > 0\right\}, \tag{2.18}$$

where θ_{tol} is selected as 0.25 degree. At the time when both (2.17) and (2.18) are satisfied, the transfer process is said to be completed. That instant is termed as the *complete time* which is simply defined as follows

$$t_{comp} = \max\{t_{set}, t_{sup}\}. \tag{2.19}$$

The complete time will be used as the performance index in the optimization routine.

In theory, it is preferable to evaluate the complete time t_{comp} at each possible combination of the uncertain parameters. However, an infinite computation of the performance index will be generated. Therefore, in the optimization procedure, three cases will be considered when all of the system parameters are at their: (1) minimum boundaries, (2) maximum boundaries, (3) average of the variation ranges (see Table 2.2). The complete time of each above-mentioned case is denoted as $(t_{comp})_j$, $(j = 1, 2, 3)$ respectively.

TABLE 2.2: Three cases whose complete times are evaluated in the optimization routines.

Case	Values of the system parameters
(1)	$I_L = 2.64$, $I_H = 1$, $m = 77.39$, $R = 0.25$, $l = 2.5$, $c = 0.1$
(2)	$I_L = 41.89$, $I_H = 1.5$, $m = 207$, $R = 0.25$, $l = 5.5$, $c = 0.5$
(3)	$I_L = 22.27$, $I_H = 1.25$, $m = 142.2$, $R = 0.25$, $l = 4$, $c = 0.3$

Now, the optimization problem of the ISMC gains is described as follows

$$\begin{aligned} \min_{\beta_i, K} \quad & J = \max\left\{(t_{comp})_j\right\},\ j = 1,2,3 \\ s.t. \quad & \beta_i > 0 \quad (i = 1, \ldots, 5) \\ & \beta_2\beta_4 > \beta_3\beta_5 \\ & K > \beta_1 \left|\ddot{\varphi}_d\right|_{\max}. \end{aligned} \tag{2.20}$$

It is noted that the constraint terms in (2.20) are reflected by the robust stability conditions of closed-loop system posed in Theorem 1. Therefore, the proposed optimization routine simultaneously considers the control system performance and the robust stabilization in a single framework.

Since the optimization problem (2.20) is generally non-smooth therefore the traditional gradient-based techniques [110] are usually inapplicable. Moreover, these methods often result in local extremums hence undesirable solutions might be reported. Recently, Genetic Algorithm (GA) [111] and Particle Swarm Optimization (PSO) [112], which are among of population-based methods have been received considerable attentions due to theirs ability in solving the global searching problems without making assumptions in differentiability as well as continuity of the search space. In the modern heuristic optimization theory, PSO algorithm is relatively newer than the GA. Moreover, in comparison with GA, many superior properties of PSO are acknowledged: faster convergence rate and lower computational time [113, 114]. Therefore, the PSO algorithm will be employed to solve the non-traditional and non-smooth optimization problem (2.20). However, the configuration described in (2.20) is not suitable for the PSO mechanism, thus (2.20) will be converted to the nonlinear-constraint-free optimization problem (2.21) by augmenting an additional penalty term as follows

$$\begin{aligned} \min_{\beta_i, K} \quad & J = \max\left\{(t_{comp})_j\right\} + \underbrace{\kappa^\top \boldsymbol{\Omega} \kappa}_{\text{Penalty term}},\ j = 1,2,3 \\ s.t. \quad & \beta_i > 0 \quad (i = 1, \ldots, 5) \\ & K > 0, \end{aligned} \tag{2.21}$$

Algorithm 1: Optimization procedure for the ISMC gains.

Step 1 Obtain a particle $(\beta_1, \ldots, \beta_5, K)$ from the PSO mechanism, go to Step 2.

Step 2 If $\beta_2\beta_4 \leq \beta_3\beta_5$ or $K \leq \beta_1 \left|\ddot{\varphi}_d\right|_{\max}$, then go to Step 3, otherwise go to step 4.

Step 3 The robust stabilization cannot be drawn, hence set $J = +\infty$ and go to Step 5.

Step 4 Evaluate $\left(t_{comp}\right)_{j=1,2,3}$, set $J = \max\{\left(t_{comp}\right)_j\}$ and go to Step 5.

Step 5 Repeat Step 1 – Step 4 until the PSO mechanism is converged.

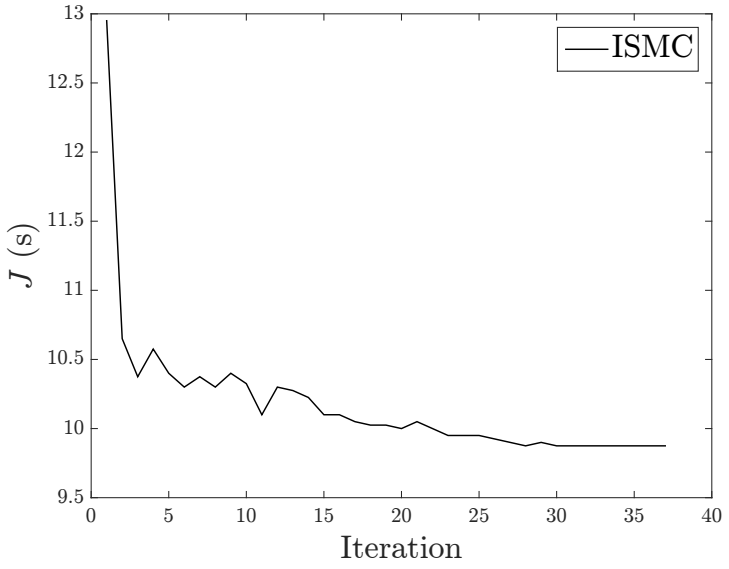

FIGURE 2.6: Cost function history over iteration of ISMC gains optimization.

where $\kappa = [\beta_2\beta_4 - \beta_3\beta_5 \quad K - \beta_1 \left|\ddot{\varphi}_d\right|_{\max}]^\top$, $\mathbf{\Omega} = \mathrm{diag}(\omega_1, \omega_2)$, and

$$\omega_1 = \begin{cases} 0 & , \text{ if } \beta_2\beta_4 > \beta_3\beta_5 \\ +\infty & , \text{ if } \beta_2\beta_4 \leq \beta_3\beta_5, \end{cases}$$

$$\omega_2 = \begin{cases} 0 & , \text{ if } K > \beta_1 \left|\ddot{\varphi}_d\right|_{\max} \\ +\infty & , \text{ if } K \leq \beta_1 \left|\ddot{\varphi}_d\right|_{\max}. \end{cases}$$

It is noted that whenever the constraints covered by the penalty term in (2.21) are violated, the value of the cost function J is infinity which indicates that the particle is "unhealthy" and it will be excluded from consideration of the future swarm. The PSO mechanism provided by *particleswarm* routine in the Global Optimization Toolbox of MATLAB is utilized. Algorithm 1 is given to solve the optimization problem (2.21).

The optimization result is shown in Fig. 2.6. After 37 iterations, the solution of (2.21) is converged at $\beta_1 = 1.988$, $\beta_2 = 10.258$, $\beta_3 = 0.0058$, $\beta_4 = 14.136$, $\beta_5 = 1.058$, and $K = 3.726$ with the minimum cost function is $J_{\min} = 9.85$ seconds. The optimization time is 8519 seconds on a personal computer with 2.5-GHz Intel Core i5-3210M and 8GB of RAM.

Remark 4. The computational time is defined as the preparation time to compute the controller for a given configuration *in the actual implementation*. Although the optimization process for the ISMC gains requires a long time to compute (i.e., 8195 seconds), it is not counted as the preparation time in the actual implementation. The reason is that the optimized gains of the ISMC is computed one and only one time beforehand in the simulation. These optimized gains are afterward used for any given configuration in the actual implementation of the controller. Therefore, the ISMC does not need any preparatory computational time. Alternatively, the ISMC retrieves data from the sensors in real-time to do the necessary computations, because it is a feedback controller. On the other hand, for each given configuration, the optimal control and the input shaping control (see Chapter 3) require long preparation times to compute the control input of the entire operation, since they belong to the feed-forward control category, which is unlike the ISMC. In summary, since the control gains of the ISMC are optimized offline, such a long optimization time is not an issue. A similar conclusion can be made for the H_∞ controller in Section 2.4.

2.4 Robust H_∞ control design

2.4.1 Output feedback sub-optimal H_∞ control configuration

The uncertain transfer functions between the control input u and two control outputs φ and θ are described in (2.22) and (2.23) respectively. To draw the distinction, in the case of H_∞ controller, the notation u will be replaced by u_∞ hereafter.

$$G_1(s) = \frac{\Phi(s)}{U(s)} = 1/s^2 \tag{2.22}$$

$$G_2(s) = \frac{\Theta(s)}{U(s)} = \frac{I_L}{(I_L + I_H)\, s^2 + cs + \dfrac{mgR^2}{l}}. \tag{2.23}$$

It is worth mentioning that the parametric uncertainties in the system parameters only enters $G_2(s)$, whilst $G_1(s)$ is simply a double integrator. The nominal system which is utilized in the H_∞ control

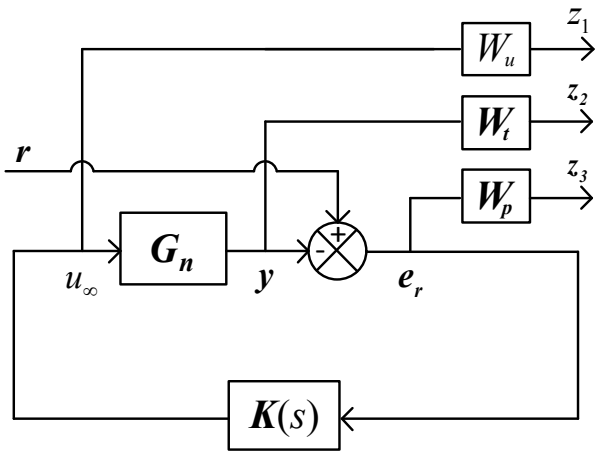

FIGURE 2.7: The closed-loop system augmented with weighting matrices: $\boldsymbol{W_p}$ on tracking errors, $\boldsymbol{W_t}$ on control outputs, and W_u on control input.

design process is given as $\boldsymbol{G_n} = [G_1 \quad G_{n2}]^\top$, where nominal subsystem G_{n2} of the uncertain transfer function G_2 can be obtained by substituting the nominal system parameters $\hat{m}$, $\hat{I}_L$, $\hat{I}_H$, $\hat{c}$, and $\hat{l}$ into corresponding uncertain parameters in (2.23).

Fig. 2.7 illustrates the closed-loop system augmented by weighting matrices $\boldsymbol{W_p}$, $\boldsymbol{W_t}$, W_u on tracking errors $\boldsymbol{e_r}$, control outputs $\boldsymbol{y}$, and control input u_∞ respectively. Note that $\boldsymbol{r} = [\varphi_d \quad 0]^\top$, $\boldsymbol{y} = [\varphi \quad \theta]^\top$, and $\boldsymbol{e_r} = \boldsymbol{r} - \boldsymbol{y}$. The objective of sub-optimal H_∞ controller $\boldsymbol{K}(s)$ is to internally stabilize the closed-loop system whilst make the H_∞ norm of transfer matrices between the interest variables z_1, $\boldsymbol{z_2}$, $\boldsymbol{z_3}$ and the exogenous input $\boldsymbol{r}$ less than a predefined positive value γ. Mathematically, it is written as

$$\underset{\text{stabilizing}}{\boldsymbol{K}(s)} \; : \left\| \begin{matrix} \boldsymbol{W_p S_o} \\ W_u \boldsymbol{K S_o} \\ \boldsymbol{W_t T_o} \end{matrix} \right\|_\infty < \gamma. \tag{2.24}$$

In (2.24), the output complementary sensitivity matrix is denoted as $\boldsymbol{T_o} = \boldsymbol{G_n K} \left(\boldsymbol{I} + \boldsymbol{G_n K}\right)^{-1}$. The output sensitivity matrix $\boldsymbol{S_o}$ is given as $\boldsymbol{S_o} = \boldsymbol{I} - \boldsymbol{T_o}$.

The main problem in optimizing the weighting matrix $\boldsymbol{W_p}$, $\boldsymbol{W_t}$, and W_u to ensure both minimization of performance index and closed-loop robust stability will be discussed in Section 2.4.3.

Remark 5. Since $G_1(s)$ is simply a double integrator hence it has two poles lying on the imaginary axis which violates the very first assumption of the sub-optimal H_∞ controller solution [94, p. 270]. To deal with this issue, the poles of the original system are shifted away from imaginary axis by using

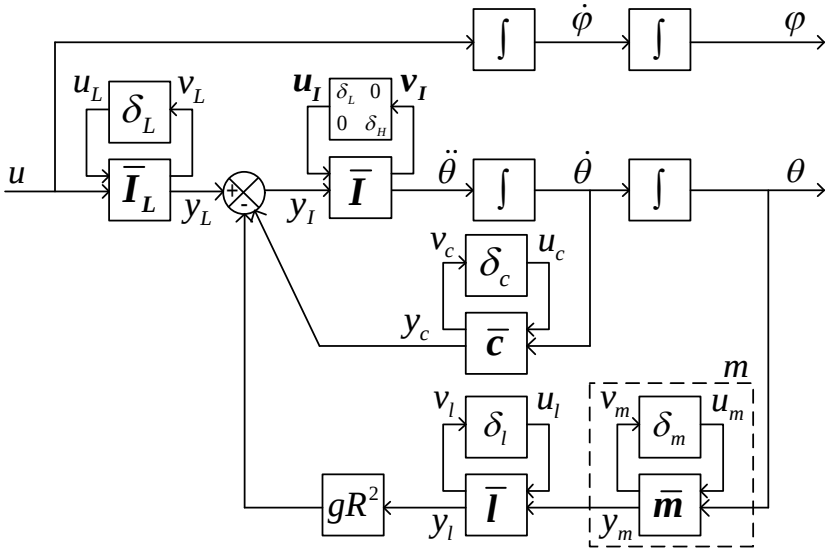

FIGURE 2.8: The uncertain rotary hook system modeled by structured uncertainties. The normalized uncertainty $\delta_m, \delta_L, \delta_H, \delta_l, \delta_c$ (i.e., $-1 \leq \delta_m, \delta_L, \delta_H, \delta_l, \delta_c \leq 1$) are pulled out of nominal parts by LFT method. Based on Table 2.1, the variation percentage p_m, p_L, p_H, p_l, p_c of total mass, payload inertia, hook inertia, rope length, and viscous damping are 45.6%, 88.1%, 20%, 37.5% and 66.67% respectively.

the following bilinear transformation [115]

$$s(\tilde{s}) = \frac{\tilde{s} + p_1}{1 + \tilde{s}/p_2}, \tag{2.25}$$

where the function $s(\tilde{s})$ maps the imaginary axis in the s-plane into the circle in the complex $\tilde{s}$-plane having diameter $[-p_1 \ -p_2]$. The H_∞ controller will be designed in the $\tilde{s}$-plane and afterward, it is shifted back to s-plane. Here, $p_1 = -15$ and $p_2 = -0.002$ are chosen.

2.4.2 Uncertainty modeling and robust stability formulation

In order not to overestimate the uncertainties in the system, the parametric uncertainties are modeled as a structured perturbation. Robust stability of the closed-loop system is then established by using μ-synthesis.

Fig. 2.8 illustrates the uncertain rotary hook system, where each element in the block diagram of the uncertain rotary hook system will be decomposed into a nominal part and a normalized uncertainty part based on the Linear Fractional Transformation (LFT) technique [94, p. 165]. As an example, for the uncertain block m in Fig. 2.8, it can be written that $m = \hat{m}\,(1 + \delta_m p_m)$, where $\hat{m}$ and p_m are the nominal value and variation percentage of m respectively. By letting

$m = \bar{\boldsymbol{m}}_{\boldsymbol{22}} + \bar{\boldsymbol{m}}_{\boldsymbol{21}}\delta_m \left(\boldsymbol{I} - \bar{\boldsymbol{m}}_{\boldsymbol{11}}\delta_m\right)^{-1} \bar{\boldsymbol{m}}_{\boldsymbol{12}}$, the uncertain block m can be represented in the sense of an upper LFT as $m = F_U\left(\bar{\boldsymbol{m}}, \delta_m\right)$ where $\bar{\boldsymbol{m}} = \begin{bmatrix} 0 & \hat{m} \\ p_m & \hat{m} \end{bmatrix}$. In the similar manner, the nominal components of all uncertain blocks in Fig. 2.8 are given by

$$\bar{\boldsymbol{I}} = \frac{-1}{\hat{I}_L + \hat{I}_H} \begin{bmatrix} \hat{I}_L p_L & \hat{I}_H p_H & -1 \\ \hat{I}_L p_L & \hat{I}_H p_H & -1 \\ \hat{I}_L p_L & \hat{I}_H p_H & -1 \end{bmatrix}, \; \bar{\boldsymbol{I}}_{\boldsymbol{L}} = \begin{bmatrix} 0 & \hat{I}_L \\ p_L & \hat{I}_L \end{bmatrix}, \; \bar{\boldsymbol{c}} = \begin{bmatrix} 0 & \hat{c} \\ p_c & \hat{c} \end{bmatrix}, \; \bar{\boldsymbol{l}} = \begin{bmatrix} -p_l & 1/\hat{l} \\ -p_l & 1/\hat{l} \end{bmatrix}. \tag{2.26}$$

By pulling out all of normalized uncertainties, the uncertain rotary hook system now can be expressed in an upper LFT $F_U\left(\boldsymbol{G_s}, \boldsymbol{\delta}\right)$, therein $\boldsymbol{\delta} = \operatorname{diag}\left(\delta_L, \delta_L, \delta_H, \delta_c, \delta_l, \delta_m\right)$ and the nominal plant $\boldsymbol{G_s}$ is established as follows. As shown in Fig. 2.8, denote $x_{1s} = \varphi$, $x_{2s} = \dot{\varphi}$, $x_{3s} = \theta$, $x_{4s} = \dot{\theta}$, $\boldsymbol{v_I} = [v_{I_1} \;\; v_{I_2}]^\top$, $\boldsymbol{u_I} = [u_{I_1} \;\; u_{I_2}]^\top$, $y_1 = \varphi$, and $y_2 = \theta$, the nominal plant $\boldsymbol{G_s}$ can be expressed as in (2.27).

$$\begin{bmatrix} \dot{x}_{1s} \\ \dot{x}_{2s} \\ \dot{x}_{3s} \\ \dot{x}_{4s} \\ \hline v_L \\ v_{I_1} \\ v_{I_2} \\ v_c \\ v_l \\ v_m \\ \hline y_1 \\ y_2 \end{bmatrix} = \left[\begin{array}{cccccccccccc} 0 & 1 & 0 & 0 & 0 & 0 & 0 & 0 & 0 & 0 & 0 \\ 0 & 0 & 0 & 0 & 0 & 0 & 0 & 0 & 0 & 0 & 1 \\ 0 & 0 & 0 & 1 & 0 & 0 & 0 & 0 & 0 & 0 & 0 \\ 0 & 0 & -\frac{\hat{m}gR^2}{\hat{l}(\hat{I}_L+\hat{I}_H)} & -\frac{\hat{c}}{\hat{I}_L+\hat{I}_H} & \frac{p_L}{\hat{I}_L+\hat{I}_H} & -\frac{\hat{I}_L p_L}{\hat{I}_L+\hat{I}_H} & -\frac{\hat{I}_H p_H}{\hat{I}_L+\hat{I}_H} & -\frac{p_c}{\hat{I}_L+\hat{I}_H} & \frac{p_l gR^2}{\hat{I}_L+\hat{I}_H} & -\frac{p_m gR^2}{\hat{l}(\hat{I}_L+\hat{I}_H)} & \frac{\hat{I}_L}{\hat{I}_L+\hat{I}_H} \\ 0 & 0 & 0 & 0 & 0 & 0 & 0 & 0 & 0 & 0 & \hat{I}_L \\ 0 & 0 & -\frac{\hat{m}gR^2}{\hat{l}(\hat{I}_L+\hat{I}_H)} & -\frac{\hat{c}}{\hat{I}_L+\hat{I}_H} & \frac{p_L}{\hat{I}_L+\hat{I}_H} & -\frac{\hat{I}_L p_L}{\hat{I}_L+\hat{I}_H} & -\frac{\hat{I}_H p_H}{\hat{I}_L+\hat{I}_H} & -\frac{p_c}{\hat{I}_L+\hat{I}_H} & \frac{p_l gR^2}{\hat{I}_L+\hat{I}_H} & -\frac{p_m gR^2}{\hat{l}(\hat{I}_L+\hat{I}_H)} & \frac{\hat{I}_L}{\hat{I}_L+\hat{I}_H} \\ 0 & 0 & -\frac{\hat{m}gR^2}{\hat{l}(\hat{I}_L+\hat{I}_H)} & -\frac{\hat{c}}{\hat{I}_L+\hat{I}_H} & \frac{p_L}{\hat{I}_L+\hat{I}_H} & -\frac{\hat{I}_L p_L}{\hat{I}_L+\hat{I}_H} & -\frac{\hat{I}_H p_H}{\hat{I}_L+\hat{I}_H} & -\frac{p_c}{\hat{I}_L+\hat{I}_H} & \frac{p_l gR^2}{\hat{I}_L+\hat{I}_H} & -\frac{p_m gR^2}{\hat{l}(\hat{I}_L+\hat{I}_H)} & \frac{\hat{I}_L}{\hat{I}_L+\hat{I}_H} \\ 0 & 0 & 0 & \hat{c} & 0 & 0 & 0 & 0 & 0 & 0 & 0 \\ 0 & 0 & \hat{m}/\hat{l} & 0 & 0 & 0 & 0 & 0 & -p_l & p_m/\hat{l} & 0 \\ 0 & 0 & \hat{m} & 0 & 0 & 0 & 0 & 0 & 0 & 0 & 0 \\ 1 & 0 & 0 & 0 & 0 & 0 & 0 & 0 & 0 & 0 & 0 \\ 0 & 0 & 1 & 0 & 0 & 0 & 0 & 0 & 0 & 0 & 0 \end{array}\right] \begin{bmatrix} x_{1s} \\ x_{2s} \\ x_{3s} \\ x_{4s} \\ \hline u_L \\ u_{I_1} \\ u_{I_2} \\ u_c \\ u_l \\ u_m \\ \hline u \end{bmatrix} \tag{2.27}$$

Finally, the uncertain rotary hook system in the LFT form will be plugged into the closed-loop system to conduct the robust stability analysis. In Fig. 2.9, the plant $\boldsymbol{P}$ can be established by using *sysic* command of MATLAB to interconnect the H_∞ controller $\boldsymbol{K}(s)$ with the nominal plant $\boldsymbol{G_s}$ in a closed-loop fashion.

Theorem 2 (Small SSV theorem [96, p. 28])**.** Let $\boldsymbol{P}(s)$ denote the transfer matrix of the nominal plant $\boldsymbol{P}$ and assuming $\boldsymbol{P}(s)$ is stable, define the Struture Singular Value (SSV) of $\boldsymbol{P}$–$\boldsymbol{\delta}$ closed-loop system shown in Fig. 2.9 as

$$\mu_{\boldsymbol{\delta}}(\boldsymbol{P}(s)) = \sup_{\omega \in \mathbb{R}^+} \left[\min_{\delta \in \boldsymbol{\delta}} \left\{ \bar{\sigma}(\delta) : \det(\boldsymbol{I} - \boldsymbol{P}(j\omega)\delta) = 0 \right\} \right]^{-1},$$

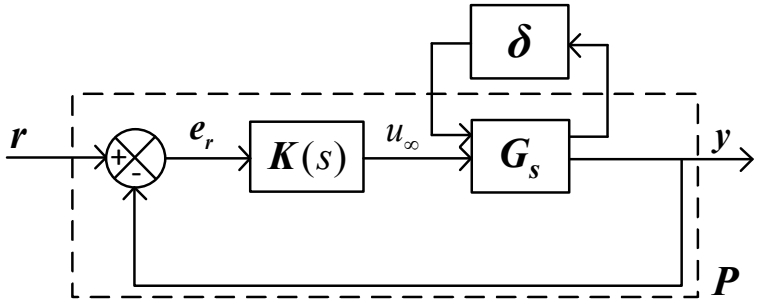

FIGURE 2.9: The uncertain rotary hook system, which is modeled by a structured uncertainty $\boldsymbol{\delta}$ and a nominal plant $\boldsymbol{G_s}$, is plugged into the loop.

where $\bar{\sigma}(\delta)$ represents the largest singular value of the matrix δ, then the perturbed system illustrated in Fig. 2.9 is robustly stable, with respect to $\boldsymbol{\delta}$, if and only if $\mu_{\boldsymbol{\delta}}(\boldsymbol{P}(s)) < 1$.

In Theorem 2, the SSV $\mu_{\boldsymbol{\delta}}(\boldsymbol{P})$ cannot be computed exactly [116]. However, the lower bound and upper bound of $\mu_{\boldsymbol{\delta}}(\boldsymbol{P})$ can be satisfactorily estimated. Therefore, the robust stability condition posed in Theorem 2 can be replaced as $\bar{\mu}_{\boldsymbol{\delta}}(\boldsymbol{P}) < 1$, where $\bar{\mu}_{\boldsymbol{\delta}}(\boldsymbol{P})$ is the upper bound of $\mu_{\boldsymbol{\delta}}(\boldsymbol{P})$. The *mussv* routine of MATLAB Robust Control Toolbox is employed to numerically compute $\bar{\mu}_{\boldsymbol{\delta}}(\boldsymbol{P})$. At this point, H_∞ sub-optimal control design configuration for the nominal plant and the robust stability for the uncertain closed-loop system are formulated. In the next section, an optimization routine is proposed to obtain a H_∞ controller which achieves both desirable performance index and robust stabilization in one framework.

2.4.3 Optimization setup and result

The weighting matrices $\boldsymbol{W_p}$, $\boldsymbol{W_t}$, and W_u described in the Section 2.4.1 are configured as follows

$$\boldsymbol{W_p} = \begin{bmatrix} \dfrac{a_1}{s+a_2} & 0 \\ 0 & \dfrac{b_1}{s+b_2} \end{bmatrix}, \ \boldsymbol{W_t} = \begin{bmatrix} \dfrac{c_1}{s+c_2} & 0 \\ 0 & \dfrac{d_1}{s+d_2} \end{bmatrix}, \ W_u = \rho, \tag{2.28}$$

where $\rho,\ a_i,\ b_i,\ c_i > 0,\ (i = 1, 2)$. In similar to the optimization routine of ISMC gains (Section 2.3.2), the performance index is chosen as $J = \max\{(t_{comp})_j\}$, $j = 1, 2, 3$, where $(t_{comp})_j$ is the complete time of the j^{th} case shown in Table 2.2. By considering the robust stability condition, the constrained

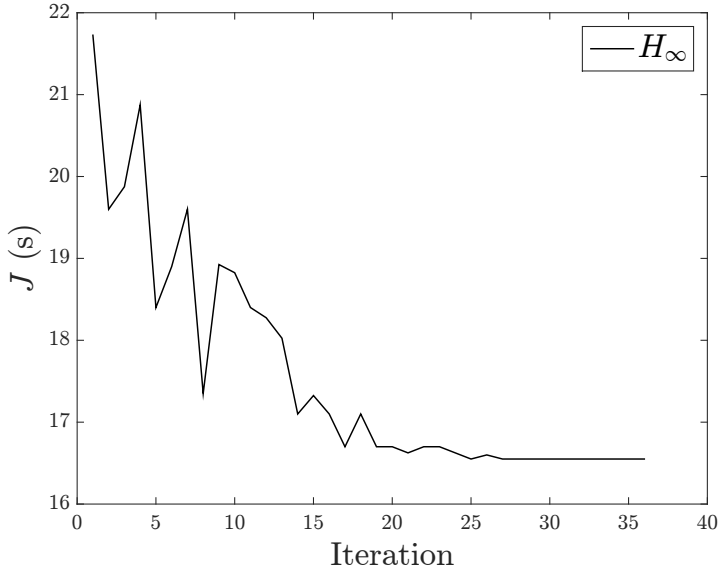

FIGURE 2.10: Cost function over iteration of the weighting matrices optimization for the H_∞ control.

optimization problem is posed as follows

$$\begin{aligned} \min_{a_i,b_i,c_i,d_i,\rho} \quad & J = \max\left\{(t_{comp})_j\right\},\ j = 1,2,3 \\ \text{s.t.} \quad & \rho > 0, a_i > 0, b_i > 0, c_i > 0, d_i > 0,\ (i = 1,2) \\ & \bar{\mu}_{\boldsymbol{\delta}}(\boldsymbol{P}) < 1. \end{aligned} \tag{2.29}$$

Since (2.29) is not appropriate for the PSO mechanism, it will be converted to a nonlinear-constraint-free optimization problem as shown in (2.30)

$$\begin{aligned} \min_{a_i,b_i,c_i,d_i,\rho} \quad & J = \max\left\{(t_{comp})_{j=1,2,3}\right\} + \overbrace{\omega_\infty \left(\bar{\mu}_{\boldsymbol{\delta}}(\boldsymbol{P}) - 1\right)^2}^{\text{Penalty term}} \\ \text{s.t.} \quad & \rho > 0, a_i > 0, b_i > 0, c_i > 0, d_i > 0,\ (i = 1,2), \end{aligned} \tag{2.30}$$

where

$$\omega_\infty = \begin{cases} 0 & \text{, if } \bar{\mu}_{\boldsymbol{\delta}}(\boldsymbol{P}) < 1 \\ +\infty & \text{, if } \bar{\mu}_{\boldsymbol{\delta}}(\boldsymbol{P}) \geq 1. \end{cases}$$

In (2.30), when a particle violates the nonlinear constraint $\bar{\mu}_{\boldsymbol{\delta}}(\boldsymbol{P}) < 1$, the cost function J will be set to infinity which forces the PSO routine to discard that particle from future swarm evaluation. Note

Algorithm 2: Optimization procedure for the weighting matrices of the H_∞ control.

Step 1 Obtain a particle (ρ, a_i, b_i, c_i, d_i), $i = 1, 2$ from the PSO mechanism *particleswarm* and go to Step 2.

Step 2 Based on the configuration (2.24), design the sub-optimal H_∞ controller by *hinfsyn* routine of MATLAB in $\tilde{s}$-plane. Shifting the resultant H_∞ controller back to the s-plane by inversion of the bilinear transformation (2.25), go to Step 3.

Step 3 Establish the closed-loop system (shown in Section 2.4.2). Computing $\bar{\mu}_{\boldsymbol{\delta}}(\boldsymbol{P})$ by *mussv* routine. If $\bar{\mu}_{\boldsymbol{\delta}}(\boldsymbol{P}) < 1$ then go to Step 4, otherwise go to Step 5.

Step 4 Evaluate $(t_{comp})_{j=1,2,3}$, set $J = \max\{(t_{comp})_j\}$ and go to Step 6.

Step 5 The robust stabilization cannot be drawn, hence set $J = +\infty$ and go to Step 6.

Step 6 Repeat Step 1 – Step 5 until the PSO mechanism is converged.

that if the robust stability of the H_∞ control and the ISMC are satisfied by their optimum solutions, the cost function J corresponding to the ISMC in (2.21) and to the H_∞ control in (2.30) are similar. Algorithm 2 is provided to solve the optimization problem (2.30).

Fig. 2.10 shows the optimization result of the Algorithm 2. After 36 iterations, the solution converges at $a_1 = 1.114$, $a_2 = 0.0045$, $b_1 = 6.211$, $b_2 = 50.369$, $c_1 = 29.403$, $c_2 = 1.701$, $d_1 = 20.781$, $d_2 = 1.031$, and $\rho = 0.0088$ with the optimized cost function is $J_{min} = 16.52$ seconds. The optimization time is 21943 seconds on a personal computer with 2.5-GHz Intel Core i5-3210M and 8GB of RAM. The detail comparison between two optimized results of the H_∞ controller and ISMC is given in Section 2.5. The 7^{th} order H_∞ controller $\boldsymbol{K}(s)$ corresponding to the optimized weighting matrices is given in (2.31).

$$\boldsymbol{K}(s) = \begin{bmatrix} \dfrac{67.626(s+15)(s+1.53)(s+0.9394)(s+0.005248)(s+0.002926)(s^2+0.2408s+0.923)}{(s+14.98)(s+1.922)(s+0.9823)(s+0.6724)(s+0.006547)(s^2+22.36s+317.8)} \\ \dfrac{-230.63(s+15)(s+1.53)(s+0.9394)(s-0.8811)(s+0.00842)(s-0.0004701)}{(s+14.98)(s+1.922)(s+0.9823)(s+0.6724)(s^2+22.36s+317.8)} \end{bmatrix}^\top \tag{2.31}$$

In practice, the order of $\boldsymbol{K}(s)$ should be reduced as smallest as possible. The controller order reduction will be carried out by means of the command *reduce* of MATLAB, in which the balanced model truncation via square root method is employed. Denote the reduced order controller of $\boldsymbol{K}(s)$ as $\boldsymbol{K_r}(s)$. The order of $\boldsymbol{K_r}(s)$ will be chosen based on the H_∞ norm of additive model error (i.e., $||\boldsymbol{K}(s) - \boldsymbol{K_r(s)}||_\infty$). According to Table 2.3, the lowest order of $\boldsymbol{K_r}(s)$ can be chosen as 5^{th}. The

TABLE 2.3: Additive error of the controller order reductions

	Order of $\boldsymbol{K_r}(s)$				
	2	3	4	**5**	6
$\|\|\boldsymbol{K}(s) - \boldsymbol{K_r}(s)\|\|_\infty$	1.352	0.059	0.011	$\mathbf{2.67 \times 10^{-4}}$	2.66×10^{-4}

state space form of the resultant controller $\boldsymbol{K_r}(s)$ is given as below

$$\begin{cases} \dot{\boldsymbol{x}}_{\boldsymbol{\infty}} = \boldsymbol{A}_{\boldsymbol{\infty}}\boldsymbol{x}_{\boldsymbol{\infty}} + \boldsymbol{B}_{\boldsymbol{\infty}}\boldsymbol{e_r} \\ u_\infty = \boldsymbol{C}_{\boldsymbol{\infty}}\boldsymbol{x}_{\boldsymbol{\infty}} + \boldsymbol{D}_{\boldsymbol{\infty}}\boldsymbol{e_r}, \end{cases} \tag{2.32}$$

where

$$\begin{aligned}
\boldsymbol{A}_{\boldsymbol{\infty}} &= \begin{bmatrix} -11.180 & 13.885 & 0 & 0 & 0 \\ -13.885 & -11.180 & 0 & 0 & 0 \\ 0 & 0 & -15.075 & 0 & 0 \\ 0 & 0 & 0 & -1.907 & 0 \\ 0 & 0 & 0 & 0 & -0.697 \end{bmatrix} \\
\boldsymbol{B}_{\boldsymbol{\infty}} &= \begin{bmatrix} 10.426 & 12.849 & -0.670 & -0.389 & -0.202 \\ -39.019 & -43.910 & 2.425 & 1.714 & 0.604 \end{bmatrix}^\top \\
\boldsymbol{C}_{\boldsymbol{\infty}} &= \begin{bmatrix} -72.642 & -63.246 & -2.322 & 1.662 & 0.629 \end{bmatrix} \\
\boldsymbol{D}_{\boldsymbol{\infty}} &= \begin{bmatrix} 67.626 & -230.628 \end{bmatrix} \\
\boldsymbol{e_r} &= \begin{bmatrix} \varphi_d - \varphi & -\theta \end{bmatrix}^\top .
\end{aligned}$$

The structured singular value of the uncertain closed-loop system is given for the reduce order controller $\boldsymbol{K_r}(s)$ by Fig. 2.11, in which it can be recognized that $\bar{\mu}_{\boldsymbol{\delta}}(\boldsymbol{P}) < 1$. Furthermore, by means of (2.24), $\boldsymbol{K_r}(s)$ internally stabilizes the nominal plant $\boldsymbol{P}$ hence according to Theorem 2, the uncertain closed loop system is robustly stable. Note that, in the experiment, the H_∞ control law u_∞ formed by (2.32) can be solved by any fixed-step ODE solver. Furthermore, the state space representation of the controller $\boldsymbol{K_r}(s)$ should be in a canonical form to reduce the mathematical operations of the on-board computational process.

It is worth mentioning that in order to directly take the parametric uncertainties account into the robust control design process, one can use μ-synthesis (see [94, 96]). However, the μ-controller resulted from a heuristic D-K iteration process often has very high order. Even if the controller order reduction

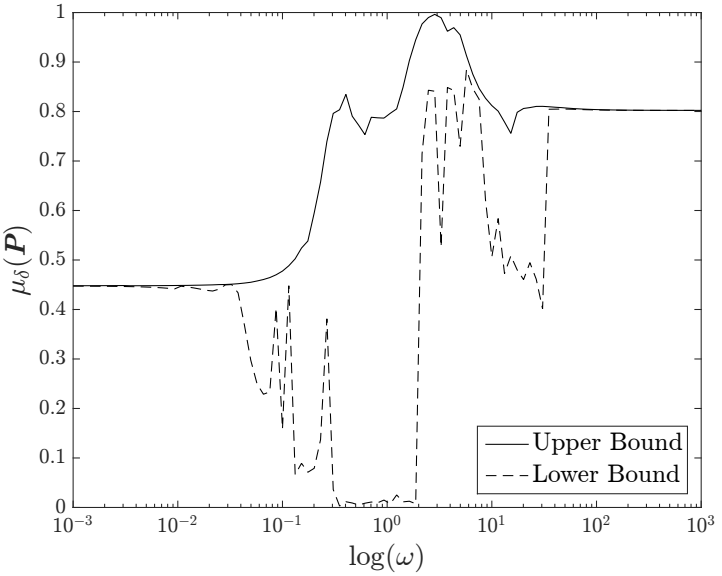

FIGURE 2.11: Structured singular value of the $\boldsymbol{P}$–$\boldsymbol{\delta}$ closed-loop system corresponding to the reduced order H_∞ controller $\boldsymbol{K_r}(s)$.

is conducted, the complexity of μ-controller cannot be afforded in our low-cost oriented experimental apparatus, thus it is not a suitable candidate in practice.

2.5 Discussions and simulation results

Two optimized results of ISMC and H_∞ controller are summarized in Table 2.4. It is observed that $J_{\min}$ in the case of ISMC (9.85 seconds) is much lower than the case of H_∞ controller (16.52 seconds). Therefore, the performance of ISMC is superior to the H_∞ controller. This fact can be explained as follows. Firstly, ISMC guarantees the system responses to track not only their reference trajectories but also the velocity of reference trajectories (i.e., ensures $\varphi \to \varphi_d$, $\theta \to 0$ *and* $\dot{\varphi} \to \dot{\varphi}_d$, $\dot{\theta} \to 0$, see Theorem 1). On the other hand, output feedback H_∞ controller only guarantees outputs of the system to follow their references (i.e., only ensures $\varphi \to \varphi_d$ and $\theta \to 0$). Secondly, the robust stability condition presented by SSV in the case of H_∞ control could be more conservative than ISMC case since SSV cannot computed exactly (only lower and upper bound can be obtained). From the above explanations, obviously, ISMC outperforms the output feedback sub-optimal H_∞ controller.

The optimization time of the ISMC gains (8195 seconds) is also much smaller than the H_∞ control case (21967 seconds). It can be easily explained by the fact that in the H_∞ control case, numerical computations of both H_∞ controller and SSV upper bound $\bar{\mu}_{\boldsymbol{\delta}}(\boldsymbol{P})$ are required which significantly

TABLE 2.4: Optimization and random simulation results of ISMC and H_∞ control

			ISMC	H_∞ control
Optimization result	$J_{\min}$		**9.85 s**	16.52 s
	Computation time		**8195 s**	21967 s
Random sim. result	t_{comp}	Mean	**9.97 s**	15.80 s
		Std. deviation	0.631 s	**0.328 s**

The sampling time in simulations is 28 ms.

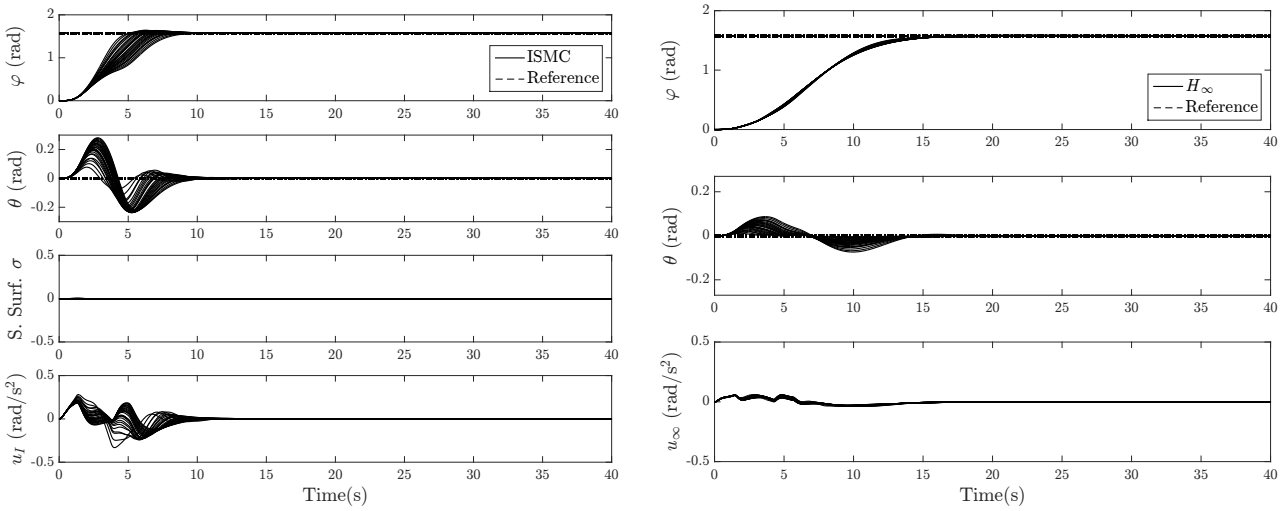

FIGURE 2.12: Random simulation result of the ISMC (left) and the H_∞ controller (right). It is observed that ISMC performs faster than the H_∞ control in completing the transfer process.

lengthen the overall process, whereas the control law as well as the robust stability conditions of ISMC are given analytically.

In reality, the system parameters are generally unknown hence it is reasonable to conduct a random simulation to evaluate the performance of robust controllers in uncertain condition. Specifically, 30 random sets of system parameters will be utilized. These sets of system parameters are randomly sampled within the domains given in Table 2.1, and thus the simulation study could be realized in the manner of the Monte Carlo framework. The control performance of the ISMC and the H_∞ controller will be accessed by both mean value and standard deviation of the complete time t_{comp}. The simulation results of ISMC and H_∞ controller are shown in Fig. 2.12 where the 3$^{\text{rd}}$ order reference trajectory in (2.15) is employed (with $\varphi_f = 90$ degrees and $|\ddot{\varphi}_d|_{\max} = 0.5$ rad/s^2). Note that in the experiments, due to the limitation of hardware computational speed, the sampling time in the case of ISMC and H_∞ controller are 28 ms and 57 ms respectively. Therefore, to draw a fair comparison, the simulation

studies of all controllers will be conducted in both 28 ms and 57 ms sampling time. Nevertheless, the results are same between two cases (i.e., 28 ms and 57 ms). Table 2.4 summarizes the mean values and standard deviations of complete time for both controllers.

As shown in Table 2.4, in agreement with the previous conclusion, ISMC outperforms the H_∞ control in the random simulation study according to the mean of t_{comp}. However, it is observed that the standard deviation of t_{comp} in the case of H_∞ control (0.328s) is only half of the ISMC case (0.631s) which shows that H_∞ control seems more consistent in ensuring the control performance for various cases. Nevertheless, this fact actually brings disadvantage to the H_∞ control. As our observation, the lower the payload inertia is, the faster the ISMC law pushes the payload to track the reference trajectory since in these cases, physically, the payload can be easily braked without a large overshoot.

Because ISMC performs faster transfer time thus in comparison with the H_∞ control, a larger vibration peak and control signal are observed. However, it is not a matter since our highest priority is to drive the payload to the target angle and suppress the vibration as fast as possible, which is reflected by the choice of t_{comp} as the performance index in the optimization routines (see (2.21) and (2.30)).

2.6 Experimental results

The designed robust controllers now will be applied on the experimental apparatus in three cases: minimum, nominal and maximum case. The control structures of both ISMC and H_∞ controller are implemented in the C environment. The Motion Designer software platform provided by TAMAGAWA SEIKI CO., LTD is utilized to compose the executing C code. Note that the controller gains of ISMC used in the simulation will be directly employed on the experimental testbed, in the other words, there is not any gains tuning process in our experiments. Moreover, in order to solve the ODE equations set (2.32) to obtain the H_∞ control law u_∞, a second order Runge-Kutta fixed-step ODE solver (or Heun method) [117] will be employed. It is recommended that, with such a long sampling period when the H_∞ controller is implemented (i.e., 57 ms), high order Runge-Kutta solver should not be used because they require interpolation values of measurement data which may be very inaccurate.

It is observed that the experimental results of the ISMC (Fig. 2.13) have strong agreements with the simulation results in all cases. Moreover, despite the fluctuation in the control input, the sliding functions are kept inside the neighborhood of zero bounded by the designated boundary layer with a thickness of ε. Due to the effect of inertia, peak of the skew vibration $\theta(t)$ is smallest in the minimum case and largest in the maximum case, which adheres to the common physical sense.

TABLE 2.5: Complete time of ISMC and H_∞ control in the experiments.

		ISMC	H_∞ control
t_{comp}	Minimum case	**9.67 s**	14.76 s
	Nominal case	**11.03 s**	15.34 s
	Maximum case	**8.24 s**	15.21 s

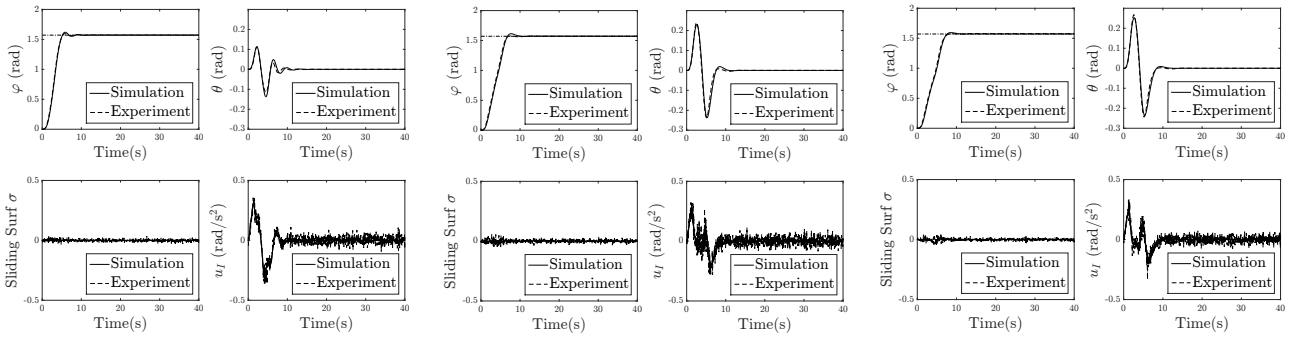

FIGURE 2.13: Experimental result of the ISMC in the: minimum case (left), nominal case (middle), and maximum case (right). Experimental data are in complete agreements with the simulation results.

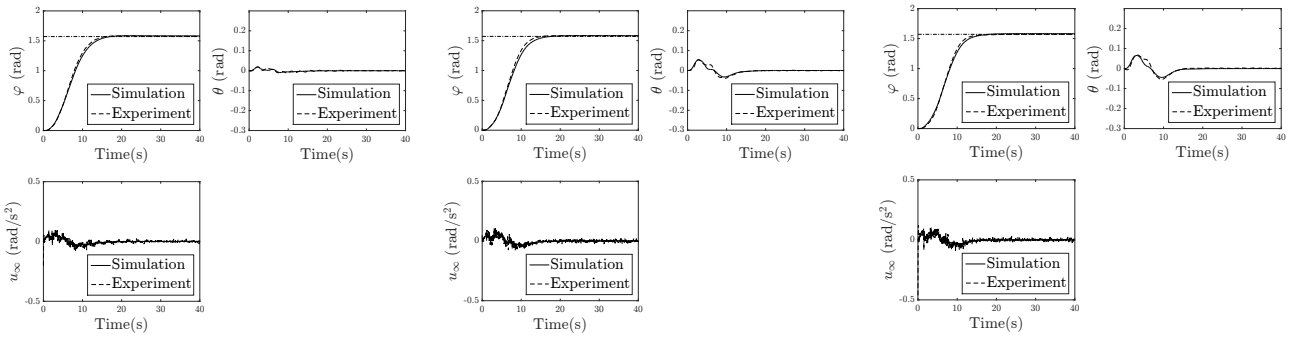

FIGURE 2.14: Experimental result of the H_∞ controller in the: minimum case (left), nominal case (middle), and maximum case (right). Some variations between the experimental data and the simulations are observed.

In contrast to ISMC, there are slight differences between the experimental and simulation results in the case of H_∞ controller (Fig. 2.14). In detail, the experiment response curve of the load angle $\varphi(t)$ always perform some variations compared with the simulation. The reason possibly comes from the accumulated error in the ODE fixed-step solver computational process. In particular, the solution of ODEs set (2.32) at the time instant $t_0 + h$ (h is sampling period) can be written as $\boldsymbol{x_\infty}(t_0 + h) = \boldsymbol{x_\infty}(t_0) + \gamma h$, where γ is weighted average slope approximation [117]. Therefore, the solution at the time instance $t_0 + h$ is dependent on the solution of previous time step t_0, hence if the sampling period h is large, the accumulated error can be considerable even if the fluctuation in the measurement data

and control input are small.

Table 2.5 summarizes the complete time of ISMC and H_∞ controller in the experiment studies. It is observed that t_{comp} of ISMC are much smaller in all cases. Therefore, ISMC shows its superiority to the H_∞ controller not only in the simulation but also in the practical implementation.

In the experimental results, the control signal of ISMC is more fluctuated than the H_∞ controller. It can be explained by the fact that in practice, there always exist modeling errors caused by actuator dynamic omittance, gear hysteresis, etc., hence the switching control term in the ISMC law (2.5) is activated to compensate such mentioned errors.

Remark 6. The skew dynamical behavior of the payload is explained as follows. During the transfer process, the payload exhibits the skew oscillation in both cases, i.e., with and without the controllers. The reason is that the system is underactuated and the load inertia cannot be negligible. However, without the vibration controllers, the skew oscillation continues when the payload reaches its target skew angle (see Fig. 2.5). On the other hand, if the vibration controllers are employed, the residual skew oscillation is completely suppressed when the payload approaches its desire skew reference. This also demonstrates the effectiveness of the proposed ISMC and H_∞ controllers.

2.7 Summary

In this chapter, a robust nonlinear ISMC and a robust linear output feedback H_∞ controller have been proposed for an under-actuated rotary hook system in order to deal with parametric uncertainties in the system parameters. By eliminating the reaching phase, dynamic ambiguity in the transient state forwarding to the sliding mode can be avoided completely. Robust stability of each controller is investigated thoroughly. Optimization routines are proposed for both ISMC and H_∞ controller, which adopt the robust stability conditions of the closed-loop system as the nonlinear constraints. To be able to solve the nonlinear constraint optimization problem by a particle swarm mechanism, penalty functions are augmented to the original cost function. By means of the proposed algorithm, the control performance and robust stabilization can be achieved simultaneously in a single framework. Through both simulation and experimental results, ISMC shows its superiority to the H_∞ control. Specifically, H_∞ controller requires much larger computational resources than ISMC because of the fixed-step ODE solver operation. Moreover, the performance of ISMC is better than H_∞ controller in the experimental studies hence it is concluded that ISMC is the preferable candidate for actual implementation on the real rotary hook system in use at harbor.

Chapter 3

Switched Optimal Control Design

This chapter pursues a time-optimal skew transfer process with no-vibration and less energy consumption, so nonlinear optimal control schemes are proposed. The main objective is to reduce energy consumption of the system without trading-off the sub-optimal transfer time. The novel idea is to use a binary actuator—an electro-mechanical clutch in particular—to intelligently disengage the connection between the motor and the payload during the motion such that the payload can continue rotating only by its own momentum. As a result, a switched optimal control problem must be realized. Two solutions, namely particular and general schemes are proposed in the chapter, where physical constraints of the actuator including bounded velocity and bounded acceleration are explicitly taken into account. Both simulation and experimental results are provided to prove the effectiveness of the proposed optimal control systems. The established schemes can be directly applied to transfer the payload to a desirable skew orientation without any residual oscillation, or can be utilized as a sub-optimal-time reference trajectory planner of the skewing control module in either overhead or rotary crane systems. Furthermore, the hybrid rotation process presented in this chapter, which is driven by the engaging/disengaging event of the clutch, can be served as a theoretical benchmark for any newly established switched optimal control method.

3.1 Introduction

In most existing studies, including the robust control designs presented in Chapter 2, a sub-optimal-time transfer process (subject to the physical constraints of a real rotary hook device) was not considered, and hence transfer productivity is not optimum. Furthermore, the feedback controllers always

require a sophisticated and expensive sensor system. For those reasons, in this chapter, feedforward control schemes based on the nonlinear optimal control technique will be formulated to obtain a low-cost control system while maintaining a precise skew transferring and an effective residual oscillation suppression. The problem in saving energy without sacrificing the sub-optimal transferring time will be elaborately considered by employing the switched optimal control approach with the aid of a binary actuator, which is an electro-mechanical clutch.

In the literature, a clutch is usually used in the vehicle transmission control [118–121]. The main functionality of the clutch in a powertrain system is to allow the car to both change speed and to completely stop without turning off the engine. However, in contrast to the existing researches, this chapter will introduce a new application aspect of the electro-mechanical clutch, which is installed inside the rotary hook device, in reducing energy consumption for the skew transferring process of crane systems.

In this chapter, indoor application for the overhead crane system is adopted as the context in which the rotary hook system is employed hence external disturbances can be neglected. Simple operations of the clutch, namely engaging and disengaging, will result in a hybrid system dynamic which can be obtained by the Euler-Lagrange approach. The key idea is to disengage the clutch and turn off the motor simultaneously in a specific interval during the transferring process such that the payload can travel only by its own inertial movement. In order to find appropriate switching instants at which the clutch is disengaged or engaged as well as the optimal control input during the actuated intervals, a switched optimal control approach is utilized. To solve the problem, both particular and general solutions are proposed. A particular solution is established by imposing specific state constraints at the switching instants so that the original problem can be transformed to the no-switched domain. On the other hand, the general solution views the switched optimal control problem in its original perspective, namely both switching instants and control inputs need to be optimized. In comparison with the general solution, the particular solution provides better control performance and computational efficiency. By employing the switched optimal control system, the energy consumptions are reduced up to 25.49% and 61.70% in the medium and long transferring cases respectively, *without any influence on the sub-optimal transferring time obtained in the no-switched optimal control scheme.*

The remainders of this chapter are organized as follows. Section 3.2 introduces the internal structure of the rotary hook device with an electro-mechanical clutch as well as the experimental apparatus. In Section 3.3, modeling of the hybrid rotary hook system is established in theory and validated in experiments. A brief review of the clipping-off Conjugate Gradient (CG) method is given in Section 3.4. Section 3.5 formulates an optimal control scheme for the no-switched system in which the clutch is

engaged during the entire transferring process. Switched optimal controls are then presented in Section 3.6 with both particular and general solutions. Section 3.7 provides simulation and experimental results of the switched optimal control system. Discussions and comparisons between switched and no-switched scenarios in terms of transferring time and energy consumption are given in Section 3.8. Moreover, input shaping and integral sliding mode controls are also applied on the system to highlight advantages of the switched optimal control system. Finally, some conclusions and future works are presented in Section 3.9.

3.2 Structure of the switched skew rotation system with an electro-mechanical clutch

Fig. 3.1 shows the internal structure of the rotary hook system with an electro-mechanical clutch. The clutch is comprised of two parts. The rotor (upper part) is connected with the servo motor shaft and the armature (lower part) is attached to a transmission gear system whose end of effector is the payload. When the current is applied, the clutch is engaged which means that the upper and lower portions are connected with each other thus the servo motor can transmit the motion to the payload. On the other hand, removing the current will cause two parts of the clutch to separate, hence the payload cannot be actuated by the servo motor—the clutch is said to be in the disengaging state. In this case, the system is constituted of two autonomous subsystems, namely the hook device and the payload. If the initial absolute velocity of the payload in the disengaging period is not identical to zero then the payload will continue rotating relying upon its own momentum, whereas the hook keeps oscillating with a higher natural frequency than in the engaging case due to the reduction of overall moment of inertia. In order to verify the effectiveness of the proposed control schemes, an experimental apparatus is built, whose configuration is illustrated in Fig. 3.2. The actuator is a TAMAGAWA TS4738 servo motor equipped with a 100:1 gearbox. The incremental encoder attached at the end of the motor has a resolution of 2048 pulses/rev. For safety reasons as well as according to the motor and gear transmission ratio specifications, the maximum speed of the servo motor is given by $v^m_{\max} = 2000$ rpm $= 209.44$ rad/s and the limitation torque of the servo motor actuating on the payload is $\tau_{\max} = 6.6$ (Nm). Note that when the clutch is disengaged, the position of the payload cannot be measured by the encoder attached at the end of servo motor. Therefore, an auxiliary encoder with a resolution of 2048 pulses/rev is installed to retrieve the rotation information of the payload in the disengaging state.

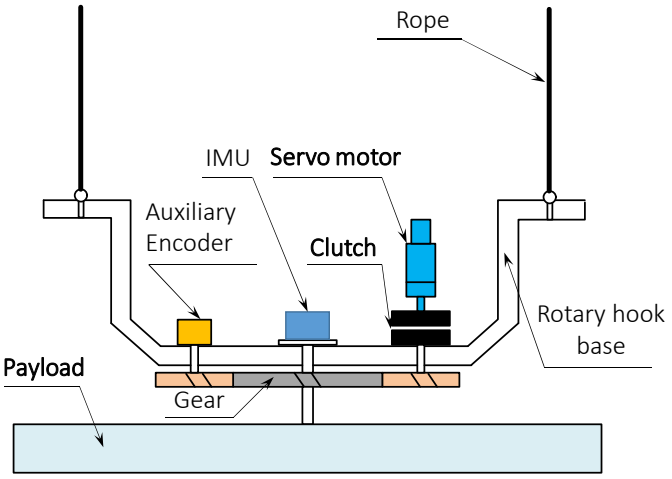

FIGURE 3.1: Internal structure of the rotary hook system with a clutch.

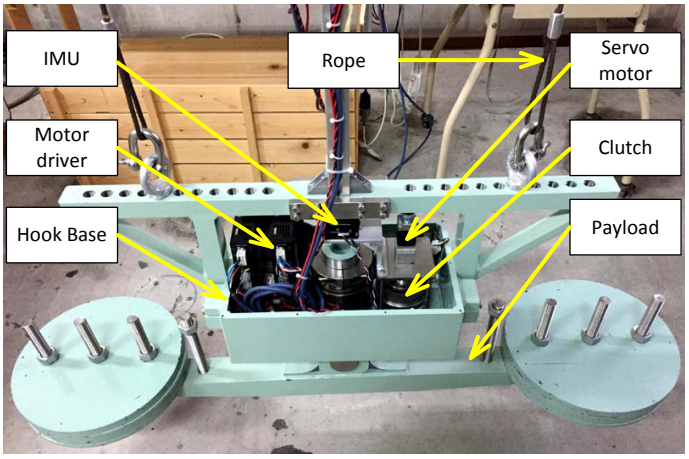

FIGURE 3.2: Experimental testbed configuration with a clutch. In a similar way to Chapter 2, a high accuracy 9-DOF IMU is utilized to measure the skew oscillation angle $\theta(t)$. The relative angle $\varphi(t)$ are measured by means of the encoders.

3.3 Mathematical modeling of the switched skew rotation process

3.3.1 Mathematical modeling

This section is devoted to formulating a modeling of the rotary hook system which consists of a rotary hook device *equipped with a clutch*, payload, ropes, and crane tip. The skew residual oscillation resulting from the rotation of the payload is depicted in Fig. 3.3, where $\varphi(t)$ denotes the relative angle between the payload and the hook, whereas $\theta(t)$ and $\gamma(t)$ represent the absolute angles between the hook and the payload versus x axis respectively. Note that two control objectives, namely driving

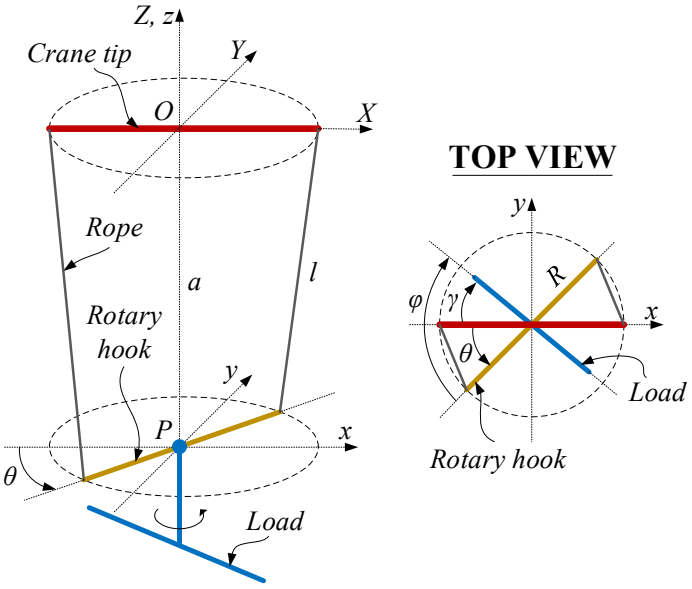

FIGURE 3.3: Modeling of the rotary hook system.

TABLE 3.1: Parameters of the miniature rotary hook system.

Symbol	Description	Value
I_L	Inertia of the payload (kgm^2)	16.5
I_H	Inertia of the hook (kgm^2)	1.25
m	Total mass of the load and the hook (kg)	142.2
R	Skewing radius (m)	0.25
l	Rope length (m)	4
g	Gravity acceleration (m/s^2)	9.81

the payload to a reference skew angle γ_d ($\gamma(t) \to \gamma_d$ and $\dot{\gamma}(t) \to 0$) without any vibration ($\theta(t) \to 0$ and $\dot{\theta}(t) \to 0$) are utilized to establish the cost functionals in the subsequent optimal control designs. Note that, when the clutch is engaged, the system dynamics is identical to which has been introduced in Section 2.2 of Chapter 2. The difference only occurs when the clutched is disengaged. However, to make the content of this chapter self-contained, some details of Section 2.2 in Chapter 2 are also presented here. Table 3.1 describes the definitions of all system parameters used in this chapter.

In Fig. 3.3, P refers to the conjunction point of the load and the hook. Denote the length of OP line as a. The steel ropes are assumed to be inelastic thus following holonomic constraint must hold

$$a^2 = l^2 - 2R^2(1 - \cos\theta). \tag{3.1}$$

The total kinetic energy of the system comprises of the rotation energies of the payload and the hook as well as the translation energy of the overall mass along the vertical direction. Therefore, it can be written by

$$T = \frac{1}{2} I_L \dot{\gamma}^2 + \frac{1}{2} I_H \dot{\theta}^2 + \frac{1}{2} m \dot{a}^2. \tag{3.2}$$

The potential energy of the system is given as

$$V = -mga. \tag{3.3}$$

Therefore, the Lagrangian function can be established by

$$L = T - V = \frac{1}{2} I_L \dot{\gamma}^2 + \frac{1}{2} I_H \dot{\theta}^2 + \frac{1}{2} m \dot{a}^2 + mga. \tag{3.4}$$

The generalized coordinate vector of the system is chosen as $\boldsymbol{q} = [\gamma(t) \quad \theta(t)]^\top$. Applying the Euler-Lagrange equation on the first generalized coordinate $\theta(t)$ yields

$$\frac{d}{dt}\left(\frac{\partial L}{\partial \dot{\theta}}\right) - \frac{\partial L}{\partial \theta} = 0. \tag{3.5}$$

Note that $\gamma(t) = \varphi(t) - \theta(t)$. By developing (3.5) using (3.1) and (3.4), it can be obtained that

$$\left(I_H + \frac{mR^4 \sin^2\theta}{a^2}\right)\ddot{\theta} = -\frac{mR^2 \sin\theta}{a}\left(\frac{R^4 \dot{\theta}^2 \sin^2\theta}{a^3} + \frac{R^2}{a}\dot{\theta}^2 \cos\theta + g\right) + I_L \ddot{\gamma}. \tag{3.6}$$

Denote $\tau(t)$ as the net torque exerting on the payload. Employing the Euler-Lagrange equation on the actuated generalized coordinate $\gamma(t)$ results in

$$\frac{d}{dt}\left(\frac{\partial L}{\partial \dot{\gamma}}\right) - \frac{\partial L}{\partial \gamma} = \tau. \tag{3.7}$$

By developing (3.7), the second dynamic equation can be adopted. By (3.4), following results can be easily obtained

$$\frac{d}{dt}\left(\frac{\partial L}{\partial \dot{\gamma}}\right) = I_L \ddot{\gamma}, \quad \frac{\partial L}{\partial \gamma} = 0. \tag{3.8}$$

Substituting (3.8) into (3.7), it can be obtained that

$$I_L \ddot{\gamma} = \tau. \tag{3.9}$$

It is noted that one can either use the acceleration $\ddot{\gamma}(t)$ or the torque $\tau(t)$ as the control input for the system since they just relate to each other through a constant I_L. However, the problematic frictional forces presented in $\tau(t)$ can be avoided by choosing the acceleration $\ddot{\gamma}(t)$ as the control input. Therefore, the system dynamic during the engaging period of the clutch is described by (3.6) in which the control input is the acceleration $\ddot{\gamma}(t)$ generated from the servo motor.

When the clutch is disengaged, there are two subsystem motions exist, namely the free-running payload and the free-oscillating hook device. Note that the clutch is placed at the motor output shaft (see Fig. 3.1), thus it is safe to assume that the friction acting on the payload during the disengaging period is sufficiently small because the gearbox attached to the servo motor is the only high frictional source. Therefore, the torque acting on the payload is zero, namely $\tau = 0$, hence the free motion of the payload during the disengaging period of the clutch is governed by

$$I_L \ddot{\gamma} = 0. \tag{3.10}$$

Note that (3.10) is equivalent to the result of angular momentum conservation principle, and it is only used when the clutch is disengaged. Since the payload inertia I_L does not vary with time; hence, from (3.10), the payload will travel with a constant angular velocity. In addition, the free oscillating movement of the rotary hook device can be depicted by substituting (3.10) into (3.6).

It is worth mentioning that from (3.9), by neglecting the friction forces, one can easily compute $u_{\max}$ as $u_{\max} := |\ddot{\gamma}|_{\max} = \tau_{\max}/I_L = 0.4$ (rad/s^2). Furthermore, denote the speed of the servo motor as $\dot{\varphi}_m(t)$ ($|\dot{\varphi}_m(t)| \leq v^m_{\max} = 209.44$ (rad/s)). Based on the transmission ratio of the gearbox and the auxiliary gear system (see Fig. 3.1), it holds that $\dot{\varphi} = \dot{\varphi}_m/r_g$ ($r_g = 400$) when the clutch is engaged. Therefore $v_{\max} := |\dot{\varphi}|_{\max} = v^m_{\max}/r_g = 0.524$ (rad/s) during the engaging state of the clutch. Note that when the clutch is disengaged, generally $\dot{\varphi} \neq \dot{\varphi}_m/r_g$.

In summary, the state of the electro-mechanical clutch, that is to say engaging and disengaging, will determine the dynamic of the switched rotary hook system which falls into either of the following configurations

$$\text{Engaging: } \begin{cases} \ddot{\gamma} = u \\ \ddot{\theta} = f(\theta, \dot{\theta}) + b(\theta)u, \end{cases} \tag{3.11}$$

$$\text{Disengaging: } \begin{cases} \ddot{\gamma} = 0 \\ \ddot{\theta} = f(\theta, \dot{\theta}), \end{cases} \tag{3.12}$$

where

$$f(\theta,\dot{\theta}) = \frac{1}{I_H + \dfrac{mR^4\sin^2\theta}{a^2}}\left[-\frac{mR^2\sin\theta}{a}\left(\frac{R^4\dot{\theta}^2\sin^2\theta}{a^3} + \frac{R^2\dot{\theta}^2\cos\theta}{a} + g\right)\right], \tag{3.13}$$

$$b(\theta) = \frac{I_L}{I_H + \dfrac{mR^4\sin^2\theta}{a^2}}. \tag{3.14}$$

Note that the nonlinear system (3.12) which describes the free motions of the load and the hook is always autonomous since no control input can be applied when the clutch is disengaging.

Remark 7. No-switched system refers to the configuration of the rotary hook system in the context where the clutch is engaged in entire transferring process. On the other hand, the switched system corresponds to the case that the clutch is disengaged at least once during the motion.

Remark 8. The only dimension that can be directly controlled by the servo motor is related to the relative angle $\varphi(t)$, namely $\dot{\varphi}(t)$ and $\ddot{\varphi}(t)$, thus the chosen control input $u(t) = \ddot{\gamma}(t)$ must be regarded as a virtual quantity. In the actual experiment, the virtual optimal control input will be replaced by a profile of the payload's relative speed $\dot{\varphi}(t)$ which is obtained in the simulation. In the other words, the feed-forward speed command will be generated by the simulating trajectory of $\dot{\varphi}(t)$. More specifically, once the optimal profile of the virtual control input $\ddot{\gamma}(t)$ is found, it can be plugged into (3.6) to numerically compute $\dot{\theta}(t)$ by any ODE solver (e.g., 4^{th} Runge-Kutta method). In addition, $\dot{\gamma}(t)$ can be adopted by integrating $\ddot{\gamma}(t)$. Therefore, one can compute the profile of $\dot{\varphi}(t)$ by using the relation $\dot{\varphi}(t) = \dot{\gamma}(t) + \dot{\theta}(t)$. The actual velocity command to the servo motor can be easily obtained by using $\dot{\varphi}_m = r_g\dot{\varphi}$ where $r_g = 400$.

Remark 9. The backlash phenomenon is inevitable when gear systems are used, and it can affect the measurement accuracy of the encoders. However, crane systems generally do not require particularly high positioning accuracy, and therefore it is not necessary to perform measures to compensate for the backlash phenomenon.

3.3.2 Modeling validation

In order to verify the correctness of the established mathematical modeling of the hybrid nonlinear rotary hook system, experimental validations are conducted in the following cases

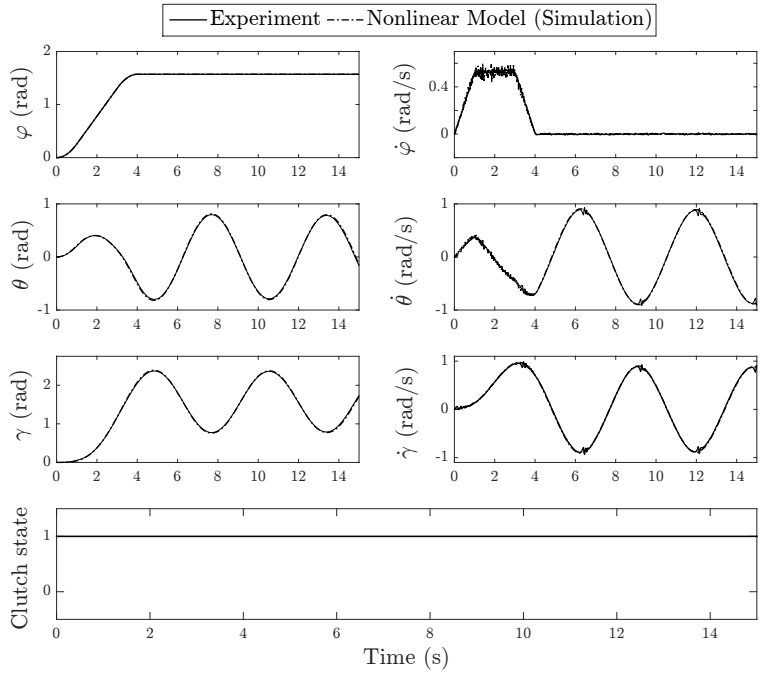

FIGURE 3.4: Model validation in the scenario of Case 1: no-switched system.

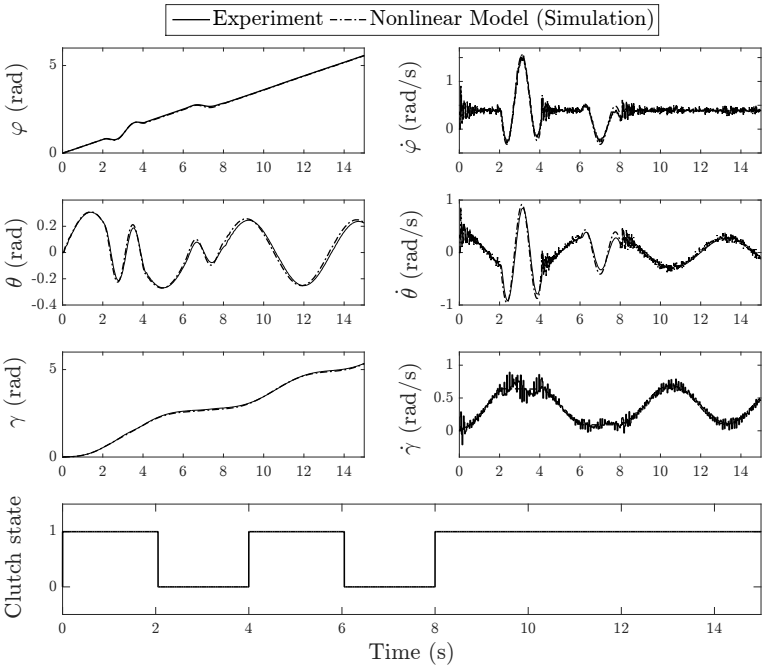

FIGURE 3.5: Model validation in the scenario of Case 2: switched system, switching period is 2 seconds.

- Case 1: The clutch is engaged in the entire process, namely the no-switched system dynamic is put into consideration.

- Case 2: During the transferring process, the clutch is engaged and disengaged alternatively at an interval of 2 seconds. By means of this experiment, the established switched system dynamic can be verified.

In all cases, the actual system parameters of the experimental testbed given in Table 3.1 will be utilized for the nonlinear models (3.11) and (3.12) in the simulations. A reference velocity profile of $\dot{\varphi}_m(t)$ is fed to the servo motor and all of system states are measured. Specifically, in Case 1 where the no-switched system is examined, a trapezoidal trajectory of $\dot{\varphi}_m(t)$ is employed. Moreover, in Case 2 where the switched system is under consideration, motion of the servo motor is kept constantly at 1500 rpm. Meanwhile, the clutch is engaged and disengaged alternatively with a period of 2 seconds.

Results of the model validation in two cases are shown in Fig. 3.4 and Fig. 3.5 respectively. In each figure, "0" value of the clutch state graph indicates the disengaging interval whereas "1" implies the engaging period of the clutch. Note that the measurement data in Fig. 3.5 is more fluctuated than Fig. 3.4 of the no-switched case. This observation can be explained as follows. In Case 2, for the sake of consistency, the payload position information is entirely measured by the auxiliary encoder whereas in Case 1, these data can be obtained by the encoder attached at the end of the servo motor. Furthermore, the noise level of the auxiliary encoder is much heavier than the encoder of the servo motor due to effect of the motor gearbox.

It is recognized that in all cases, experimental data strongly agrees with the mathematical model given in (3.11) and (3.12). Therefore it can be concluded that the formulated modeling accurately describes the dynamic behavior of the switched rotary hook system. Note that as shown in Fig. 3.5, the reduction of the payload velocity $\dot{\gamma}(t)$ during the disengaged stage of the clutch (2 - 4 seconds and 6 - 8 seconds) is very small. It indicates that the small friction coefficient assumption is reasonable. In the real application, the internal structure of the hook device is placed inside a closed shield, which protects it from effects of the environment. Therefore, the friction of the system could be guaranteed small without a frequent maintenance.

At this point, the mathematical modeling of the hybrid rotary hook system is successfully established. The optimal control designs for both no-switched and switched systems will be discussed in Sections 3.5 and 3.6 respectively. In practice, the physical constraints of the actuator must taken into account, thus in this chapter, both control input and state constraints will be considered in the optimal control formulations. Generally, it is almost impossible to obtain an analytical solution of the constrained optimal control problem for a nonlinear system except in some simple cases [55, 56, 122]. Therefore, a numerical method will be adopted.

3.4 Preliminary of the clipping-off conjugate gradient method

In the domain of numerical approaches to solve a constrained optimal control problem, direct [123–125] and indirect [126–128] methods can be found in the literature. However, the indirect techniques always result in a faster convergence rate and better cost performance index [122, 129], thus it will be employed in this chapter. Quintana and Davison [128] introduced a novel conjugate gradient method in conjunction with a clipping-off operator to effectively solve the bounded optimal control problem. This technique elegantly incorporates the classical conjugate gradient method (for solving an unconstrained optimization problem) and the clipping-off operator to enforce the local optimizer satisfying the necessary condition of optimality subjected to the control input constraints. For the sake of convenience in following presentations, the algorithm of [128] will be briefly reviewed in this section.

Consider the following class of nonlinear systems

$$\dot{\boldsymbol{x}}(t) = \boldsymbol{f}(\boldsymbol{x}, \boldsymbol{u}), \quad \boldsymbol{x}(t_0) = \boldsymbol{x_0}, \tag{3.15}$$

where $\boldsymbol{f}$ is a nonlinear n-dimensional vector function of n-dimensional state vector $\boldsymbol{x}$ and r-dimensional control input $\boldsymbol{u} = [u_1 \quad \dots \quad u_r]^\top$ (i.e., $\boldsymbol{f} \in \mathbb{R}^n$, $\boldsymbol{x} \in \mathbb{R}^n$, $\boldsymbol{u} \in \mathbb{R}^r$). Denote t_0 and t_f as the initial and terminal time respectively, which are assumed to be known. The optimal control problem with a fixed terminal time t_f is given as

$$\begin{aligned} \min_{\boldsymbol{u}} \quad & J(\boldsymbol{u}) = \phi(\boldsymbol{x}(t_f), t_f) + \int_{t_0}^{t_f} L(\boldsymbol{x}, \boldsymbol{u}) dt \\ \text{s.t.} \quad & \dot{\boldsymbol{x}} = \boldsymbol{f}(\boldsymbol{x}, \boldsymbol{u}) \\ & \boldsymbol{u} \in \Omega, \end{aligned} \tag{3.16}$$

therein the admissible control set Ω is defined as

$$\Omega \triangleq \{u_j : |u_j| \leq u_{\max}\}, j = 1, 2, \dots, r. \tag{3.17}$$

Denote H as the Hamiltonian function

$$H(\boldsymbol{x}, \boldsymbol{\lambda}, \boldsymbol{u}) \triangleq \boldsymbol{\lambda}^\top \boldsymbol{f}(\boldsymbol{x}, \boldsymbol{u}) + L(\boldsymbol{x}, \boldsymbol{u}), \tag{3.18}$$

where the n-dimensional costate vector $\boldsymbol{\lambda}(t)$ must satisfy

$$\dot{\boldsymbol{\lambda}}(t) = -\left(\frac{\partial H}{\partial \boldsymbol{x}}\right)^{\top} \text{ and } \boldsymbol{\lambda}(t_f) = \left(\frac{\partial \phi(\boldsymbol{x}(t_f), t_f)}{\partial \boldsymbol{x}(t_f)}\right)^{\top}. \tag{3.19}$$

In (3.16), $\phi\left(\boldsymbol{x}(t_f), t_f\right)$ is the component related to the terminal condition, whereas $L(\boldsymbol{x}, \boldsymbol{u})$ is corresponding to the accumulating cost performance of the system as the time proceeding. Note that (3.16) is a general optimal control problem, which is only used for a purpose of briefly reviewing the CG gradient method. Concrete optimal control problems for the no-switched and switched rotary hook system are posed in (3.21), (3.27), and (3.31).

Let $\boldsymbol{g}(t) = (\partial H/\partial \boldsymbol{u})^{\top} = [\partial H/\partial u_1 \ \ \ldots \ \ \partial H/\partial u_r]^{\top} \triangleq [g_1(t) \ \ \ldots \ \ g_r(t)]^{\top}$, following control input constraints must be fulfilled in order to guarantee the necessary condition for optimal solution [130]

$$\begin{cases} u_j = u_{\max} & \text{if } \dfrac{\partial H}{\partial u_j} < 0 \\ -u_{\max} \leq u_j \leq u_{\max} & \text{if } \dfrac{\partial H}{\partial u_j} = 0 \ , \quad j = 1, \ldots, r. \\ u_j = -u_{\max} & \text{if } \dfrac{\partial H}{\partial u_j} > 0 \end{cases} \tag{3.20}$$

Basically, the clipping-off CG method of [128] iteratively compute the control input $\boldsymbol{u}$ from an initial guess until a local optimum solution is reached. The key point is that the search direction of each iteration is forced to be conjugate to all previous search directions, which makes it more efficient than the steepest descent method since additional information can be obtained. Moreover, the resultant local minimizer of (3.16) will satisfy all of the necessary conditions for optimality given in (3.19) and (3.20). Further details are greatly explained in [128]. It is highly recommended for interest readers.

3.5 Optimal control of no-switched system

In this section, an optimal control scheme will be formulated for the rotary hook system when the clutch is always kept engaged during the transferring process. Two control objectives, namely driving the payload to the desired skew angle and suppressing the skew oscillation simultaneously (i.e., forcing $\gamma(t) \to \gamma_d$, $\dot{\gamma}(t) \to 0$, $\theta(t) \to 0$, and $\dot{\theta} \to 0$) are the basics to establish the cost functional. A fixed terminal time optimal control problem is firstly formulated and then a sub-optimal-time solution can be obtained by gradually reducing the terminal time through a bisection method.

3.5.1 Problem formulation and algorithm

Denote a state vector of the control system as $\boldsymbol{x} = [x_1 \;\; x_2 \;\; x_3 \;\; x_4]^\top = [\gamma(t) \;\; \dot{\gamma}(t) \;\; \theta(t) \;\; \dot{\theta}(t)]^\top$. Note that the system is assumed to start from rest, namely $\boldsymbol{x}(t_0) = 0$. By taking the physical limitations of the servo motor including the maximum velocity $v_{\max}$ and maximum acceleration $u_{\max}$ into account, the optimal control problem for the no-switched rotary hook system can be posed as

$$\begin{aligned} \min_u \; & J = \omega_1 \left(x_1(t_f) - \gamma_d\right)^2 + \omega_2 x_2^2(t_f) + \omega_3 x_3^2(t_f) + \omega_4 x_4^2(t_f) \\ \text{s.t. } & \dot{\boldsymbol{x}} = \boldsymbol{f}(\boldsymbol{x}) + \boldsymbol{b}(\boldsymbol{x})u, \quad \boldsymbol{x}(t_0) = 0 \\ & (x_2 + x_4)^2 \le v_{\max}^2 \\ & |u| \le u_{\max}. \end{aligned} \tag{3.21}$$

In (3.21), t_f is a fixed terminal time and it will be determined by Algorithm 3. The weighting coefficients are chosen as $\omega_1 = \ldots = \omega_4 = 10^6$. As discussed in Section 3.2, $u_{\max} = |\ddot{\gamma}|_{\max} = 0.4$ (rad/s^2) and $v_{\max} = |\dot{\varphi}|_{\max} = |x_2 + x_4|_{\max} = 0.524$ (rad/s). The system modeling in the engaging state of the clutch given by (3.11) is employed, thus

$$\boldsymbol{f}(\boldsymbol{x}) = [x_2 \;\; 0 \;\; x_4 \;\; f]^\top \text{ and } \boldsymbol{b}(\boldsymbol{x}) = [0 \;\; 1 \;\; 0 \;\; b]^\top, \tag{3.22}$$

where f and b terms are given in (3.13). Note that the optimal control problem (3.21) is involved by both control input and state constraints. As discussed in Section 3.4, control input constraint can be efficiently solved by the clipping-off CG method. To eliminate the state constraint, the original cost functional J will be augmented by a step penalty function. The state-constraint-free optimal control problem of the no-switched rotary hook system can be further described as

$$\begin{aligned} \min_u \quad & J_s = J + \underbrace{\int_{t_0}^{t_f} k_1 \phi_1^2 dt}_{\text{Penalty term}} \\ \text{s.t.} \quad & \dot{\boldsymbol{x}} = \boldsymbol{f}(\boldsymbol{x}) + \boldsymbol{b}(\boldsymbol{x})u, \quad \boldsymbol{x}(t_0) = 0 \\ & |u| \le u_{\max} \\ & \phi_1 = v_{\max}^2 - (x_2 + x_4)^2 \\ & k_1 = \begin{cases} 0 & \text{if } \phi_1 \ge 0 \\ \mu_1 & \text{if } \phi_1 < 0, \end{cases} \end{aligned} \tag{3.23}$$

Algorithm 3: Bisection method to solve the sub-optimal-time problem.

Step 1 Let $t_f = \gamma_d/(\alpha v_{\max})$, $a_1 \leftarrow 0$, and $a_2 \leftarrow t_f$. Obtaining the optimal control input $u^\star(t_f)$. If $J_s(u^\star, t_f) < J_{tol}$ then to step 2, otherwise go to step 3.

Step 2 Let $t_f \leftarrow (a_1 + a_2)/2$. Retrieving $u^\star(t_f)$. If $J(u^\star, t_f) < J_{tol}$ then $a_2 \leftarrow t_f$, otherwise $a_1 \leftarrow t_f$, go to Step 4.

Step 3 Let $a_1 \leftarrow a_2$, $a_2 \leftarrow 2a_2$, and $t_f \leftarrow a_2$. Calculating $u^\star(t_f)$. If $J_s(u^\star, t_f) > J_{tol}$ then repeat Step 3, otherwise go to Step 2.

Step 4 If $a_2 - a_1 > \Delta_t$ then go to Step 2. Otherwise, go to Step 5.

Step 5 If $J_s(t_f = a_1) < J_{tol}$ then $t_f \leftarrow a_1$, otherwise $t_f \leftarrow a_2$. Output $u^\star(t_f)$ as the optimal control input corresponding to the sub-optimal transferring time t_f.

where $\mu_1 = 10^6$. Note that the penalty coefficient k_1 is activated whenever the state constraint associated with ϕ_1 is violated.

Remark 10. It is easy to reduce the energy consumption of the transferring process by adding the control input to the integral term of (3.23). However, it is well-known that such treatment will significantly lengthen the transferring time. In the other words, an unfavorable trade-off will be encountered. Alternatively, Section 3.6 will propose a method to save energy of the overall process without influencing the sub-optimal transferring time by employing the switched optimal control approach.

Denote $u^\star(t_f)$ as the resultant optimal control input of (3.23) with respect to the fixed terminal time t_f. The sub-optimal-time control problem can be solved by extending (3.23) through a bisection method [60] by means of Algorithm 3. Note that $u^\star(t_f)$ in Algorithm 3 is always obtained by the clipping-off CG method shown in Section 3.4.

In Algorithm 3, α relates to the initial value of the terminal time t_f. Typically, it can be chosen that $\alpha = 0.5$. Moreover, J_{tol} specifies the requirements corresponding to the transfer accuracy, residual vibration suppression, and state constraint assurance. With the large weighting coefficients ($\omega_1 = \ldots = \omega_4 = 10^6$), it can be heuristically chosen that $J_{tol} = 1$ to sufficiently fulfill the control performance. The terminated condition of Algorithm 3 is determined by the tolerance Δ_t which regards to the minimum distance between two consecutive trial terminal time points. Here, $\Delta_t = 0.1$ second is adopted. It is important to remark that the initial guess of the optimal control input for the present terminal time t_f should be taken from that of the previous successive iteration. Such choice can significantly reduce the computational effort.

TABLE 3.2: Computation results of the no-switched optimal controls.

Case	$\min(t_f)$	J_s	Compt. time	$\max(-\phi_1(t))$
$\gamma_d = 30°$	3.13 s	0.6651	35.1 s	0.0170
$\gamma_d = 90°$	5.06 s	0.8060	61.7 s	0.0093
$\gamma_d = 180°$	7.97 s	0.4165	85.2 s	0.0072

Compt. time: Computational time.

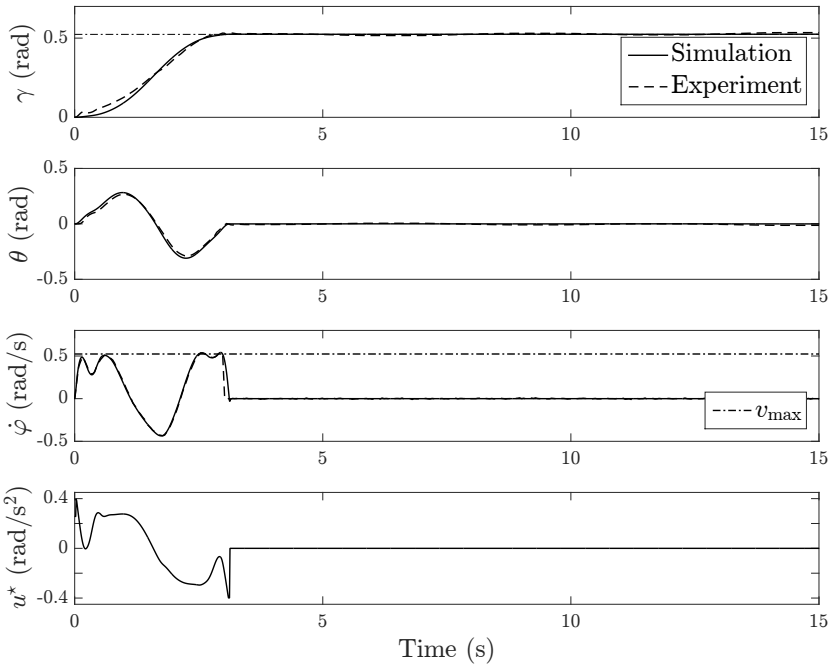

FIGURE 3.6: Simulation and experimental results in the short transferring case ($\gamma_d = 30$ degs): no-switched optimal control scenario.

3.5.2 Simulation and experimental results

By employing Algorithm 3, optimal control with both input and state constraints will be computed for three cases: short ($\gamma_d = 30$ degrees), medium ($\gamma_d = 90$ degrees), and long transferring case ($\gamma_d = 180$ degrees). An initial guess of the optimal control input in the clipping-off CG algorithm is given by $u(t) = 0, t_0 \leq t \leq t_f$. The computation is conducted on a personal computer with 2.5-GHz Intel Core i5-3210M and 8 GB of RAM. The computational results for all cases are summarized in Table 3.2. Note that the clipping-off CG method is restarted every 2 iterations.

The simulation and experimental results in three cases are shown in Figs. 3.6–3.8 respectively. It can be recognized that with the computed optimal control inputs, the payload accurately reaches

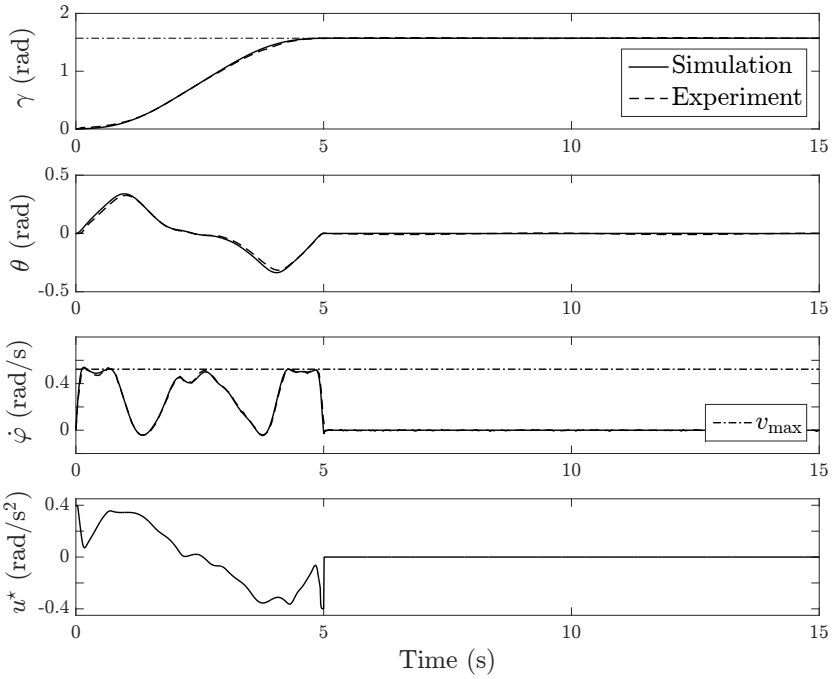

FIGURE 3.7: Simulation and experimental results in the medium transferring case ($\gamma_d = 90$ degs): no-switched optimal control scenario.

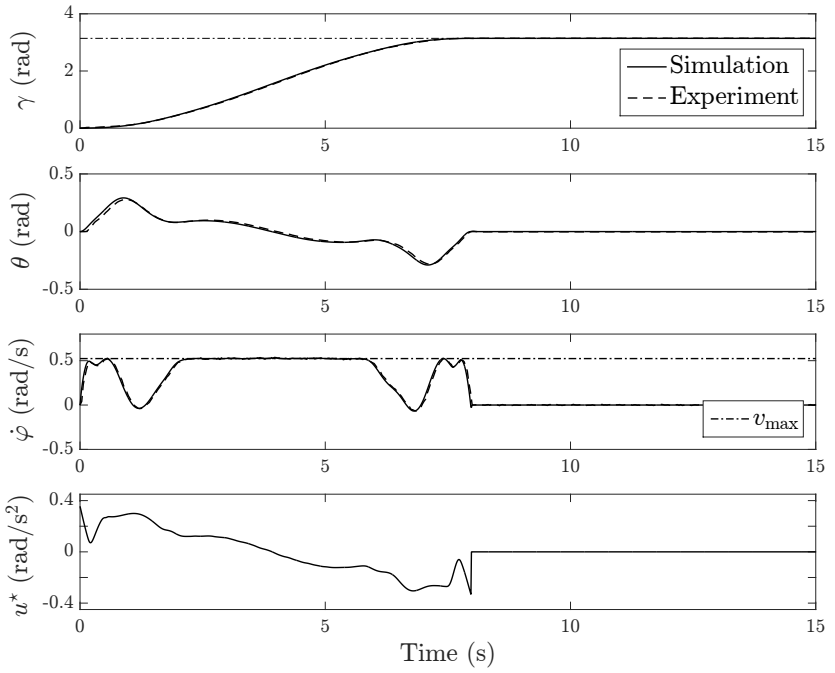

FIGURE 3.8: Simulation and experimental results in the long transferring case ($\gamma_d = 180$ degs): no-switched optimal control scenario.

the desired skew angle as well as the skew oscillation nearly vanishes after the motion. Both control input and state constraints are sufficiently assured by the resultant optimal solutions. Therefore, it is concluded that effectiveness of the proposed no-switched optimal control system is verified.

3.6 Optimal control of switched system

3.6.1 Motivation and problem formulation

Consider the motor speed profile $\dot{\varphi}(t)$ of the long transferring case as shown in Fig. 3.8, one can recognize that the motor speed residents on its upper constraint in the middle of transferring process. The motor must maintain a constant maximum speed during this uniform interval, thus the energy is considerably consumed. Therefore, the basic idea is to remove the above-mentioned undesirable interval by imposing upon the movement generated by the inertia of the payload itself. Specifically, consider the free motion of the payload subsystem when the clutch is disengaged as in (3.12), namely $\ddot{\gamma}(t) = 0$ whose solution is $\dot{\gamma}(t) =$ constant. It is recognized that the motion of payload in this case has the same property with the unfavorable interval encountered in the no-switched optimal control solution. In the other words, motion of the motor should be replaced by the inertial movement of the payload by disengaging the clutch in a specified period of the entire transferring process to reduce the energy consumption.

By the above observation, the whole time span $\mathbb{T} = \{t : t \in [t_0 \;\; t_f]\}$ of the payload motion can be divided into three sub-intervals: $\mathbb{T}_1 = \{t : t \in [t_0 \;\; t_1]\}$, $\mathbb{T}_2 = \{t : t \in [t_1 \;\; t_2]\}$, and $\mathbb{T}_3 = \{t : t \in [t_2 \;\; t_f]\}$. In the first interval $\mathbb{T}_1$, the control input generated by the motor is applied to accelerate the payload until the time variable t reaches the time instant t_1. At t_1, the clutch is disengaged in the second interval $\mathbb{T}_2$ to force the payload travel with a constant speed only by its own inertia. Finally, in the third interval $\mathbb{T}_3$, the clutch is engaged again, the control input is put into operation to complete the entire motion. By means of the above discussion, subsystems and their activated intervals can be described as

$$\begin{array}{lll} \text{Subsystem 1:} & \dot{\boldsymbol{x}} = \boldsymbol{f}_1(\boldsymbol{x}) + \boldsymbol{b}_1(\boldsymbol{x})u_1 & , t \in \mathbb{T}_1. \\ \text{Subsystem 2:} & \dot{\boldsymbol{x}} = \boldsymbol{f}_2(\boldsymbol{x}) & , t \in \mathbb{T}_2. \\ \text{Subsystem 3:} & \dot{\boldsymbol{x}} = \boldsymbol{f}_3(\boldsymbol{x}) + \boldsymbol{b}_3(\boldsymbol{x})u_3 & , t \in \mathbb{T}_3. \end{array} \tag{3.24}$$

In (3.24), $\boldsymbol{f}_1(\boldsymbol{x}) = \boldsymbol{f}_2(\boldsymbol{x}) = \boldsymbol{f}_3(\boldsymbol{x}) = \boldsymbol{f}(\boldsymbol{x})$ and $\boldsymbol{b}_1(\boldsymbol{x}) = \boldsymbol{b}_3(\boldsymbol{x}) = \boldsymbol{b}(\boldsymbol{x})$, where $\boldsymbol{f}(\boldsymbol{x})$ and $\boldsymbol{b}(\boldsymbol{x})$ are given in (3.22). Note that the subsystem 2 is an autonomous system without control input.

Here, there are two switching instants, namely t_1 and t_2 hence it can be termed as a 2-switched control system. Obviously, one can generate N-switched system by engaging and disengaging the clutch N times in which $N = 2k$ ($k \in \mathbb{N}^+$) since at the end of the transferring process, the clutch must be in the engaging state. However, a large number of switchings within a short time possibly cause damage to the clutch. Therefore, a 2-switched control system is reasonably adopted in practice. Note that, the speed profile $\dot{\varphi}(t)$ of Fig. 3.8 obtained in the no-switched scenario is only employed for a purpose of illustrating the underlying motivation. In the other words, the switching instants as well as the optimal control input for the switched system will be computed in light of the particular solution (Section 3.6.2) or the general solution (Section 3.6.3).

Remark 11. For a mechanical system, physically, it is not feasible to reduce both maneuver time and energy consumption simultaneously. Therefore, the best circumstance can be expected is that, by using the switched optimal control system, the sub-optimal transferring time is reserved whereas the energy consumption is reduced in comparison with the no-switched scenario. In order to reflect such understanding, two above-mentioned objectives are distributed into three sub-intervals of the transferring process. Specifically, the goal in retaining the sub-optimal transferring time and suppressing the residual vibration will be carried out by two intervals, namely acceleration and deceleration stages. Note that, in these two stages, the clutch is engaged so that the computed optimal control input can be applied; hence, the energy is consumed. On the other hands, the objective in reducing the energy consumption is shaped into the free-run interval, in which the clutch is disengaged and the payload travels by its own angular momentum generated by the previous acceleration stage; therefore, no energy consumption happens in the free-run interval. By combining three aforementioned sub-intervals, the main purpose in retaining the sub-optimal transferring time, suppressing the residual vibration, and reducing the energy consumption can be achieved.

At this point, it is recognized that in conjunction to the task in computing optimal control inputs for the actuating intervals, one must determine two switching instants t_1 and t_2 at which the clutch is disengaged and engaged respectively. One solution to this problem is to impose specific state constraints at the first switching instant t_1 so that the original switched optimal control problem can be transformed to the no-switched domain, which leads to the particular solution. On the other hands, if the system state at t_1 and t_2 are allowed to be free then the switching instants need to be optimized, which results in the general solution. Overview and relation between two types of solutions are illustrated in Fig. 3.9.

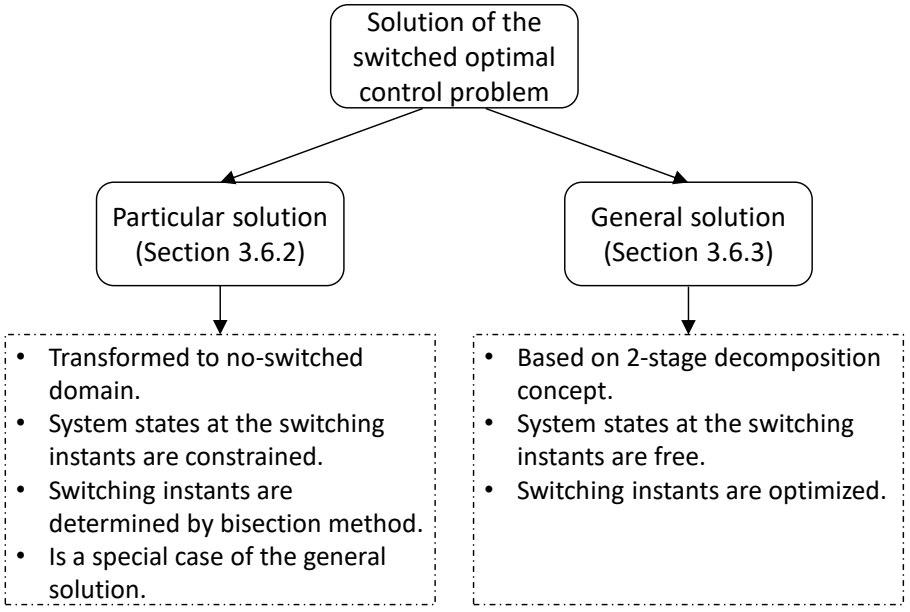

FIGURE 3.9: Two solutions of the switched optimal control problem.

3.6.2 Particular solution

The basic concept of the particular solution is to artificially impose the state constraints (3.25) at the switching instant t_1

$$\dot{\gamma}(t_1) = v_{\max},\ \theta(t_1) = 0,\ \dot{\theta}(t_1) = 0. \tag{3.25}$$

The constraint (3.25) applies for the case that the reference angle $\gamma_d > 0$. For $\gamma_d < 0$, $\dot{\gamma}(t_1) = -v_{\max}$ should be made. However, the two above cases are symmetric. Thus it only needs to compute the optimal control input for one case, the other can be obtained by sign reverse. A graphical illustration of the particular solution is shown in Fig. 3.10. The optimal trajectory of the payload speed $\dot{\gamma}(t)$ is partitioned into three intervals: acceleration, free-run, and deceleration, with a set of state constraints at the end of acceleration stage. Note that, in the particular solution, the control input of jth interval will be denoted as $\tilde{u}_j$ $(j = 1, 3)$ whose optimums are $\tilde{u}_j^\star(t)$.

In order to further explain the choice of the constraints made in (3.25), recall the subsystem dynamic when the clutch is disengaged as follows

$$\begin{cases} \ddot{\gamma}(t) &= 0 \\ \ddot{\theta}(t) &= f\left(\theta(t), \dot{\theta}(t)\right). \end{cases} \tag{3.26}$$

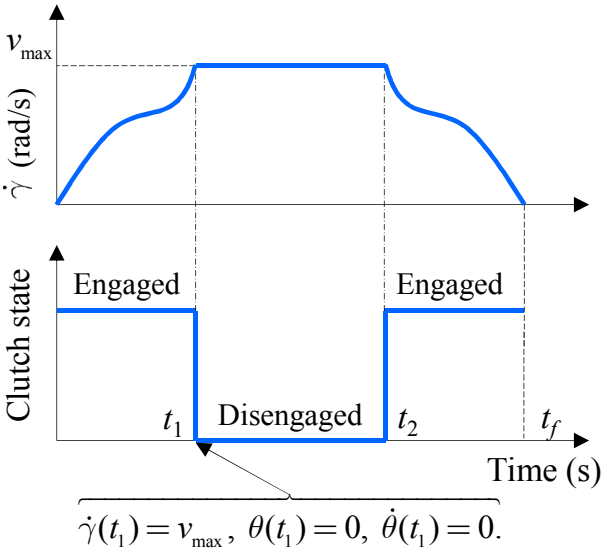

FIGURE 3.10: Particular solution: profile of the payload speed $\dot{\gamma}(t)$ with specified state constraints at the switching instant t_1.

According to (3.25) and (3.26), it is guaranteed that $\dot{\gamma}(t_2) = v_{\max},\ \theta(t_2) = 0$, and $\dot{\theta}(t_2) = 0$. Therefore, when the bounded optimal control input $\tilde{u}_1^\star$ is found in the acceleration interval in order to bring the system from the initial condition to the intermediate state specified in (3.25), then the optimal control input $\tilde{u}_3^\star$ of the deceleration stage can be simply flipped and sign reversed. Note that, by (3.25), thus $\dot{\varphi}(t_1) = \dot{\gamma}(t_1) + \dot{\theta}(t_1) = v_{\max} + 0 = v_{\max}$. This means that the motor will use its maximum velocity at the end of the acceleration stage to "throw" the payload.

By pre-specifying the system states at the switching instant t_1 by (3.25), the optimal control problem for the switched system can be now reduced to the following problem of finding the bounded optimal control input for the acceleration stage which is actually no-switched:

$$\min_{\tilde{u}_1} \quad J_p = \phi_p\left(\boldsymbol{x}(t_1)\right) + \underbrace{\int_{t_0}^{t_1} k_1 \phi_1^2 dt}_{\text{penalty term}} \tag{3.27}$$

$$\text{s.t.} \quad \dot{\boldsymbol{x}} = \boldsymbol{f}_1(\boldsymbol{x}) + \boldsymbol{b}_1(\boldsymbol{x})\tilde{u}_1, \quad \boldsymbol{x}(t_0) = 0$$

$$|\tilde{u}_1| \leq u_{\max}$$

$$\phi_p = \omega_2 \left(x_2(t_1) - v_{\max}\right)^2 + \omega_3 x_3^2(t_1) + \omega_4 x_4^2(t_1)$$

$$\phi_1 = v_{\max}^2 - \left(x_2 + x_4\right)^2$$

$$k_1 = \begin{cases} 0 & \text{if } \phi_1 \geq 0 \\ \mu_1 & \text{if } \phi_1 < 0, \end{cases}$$

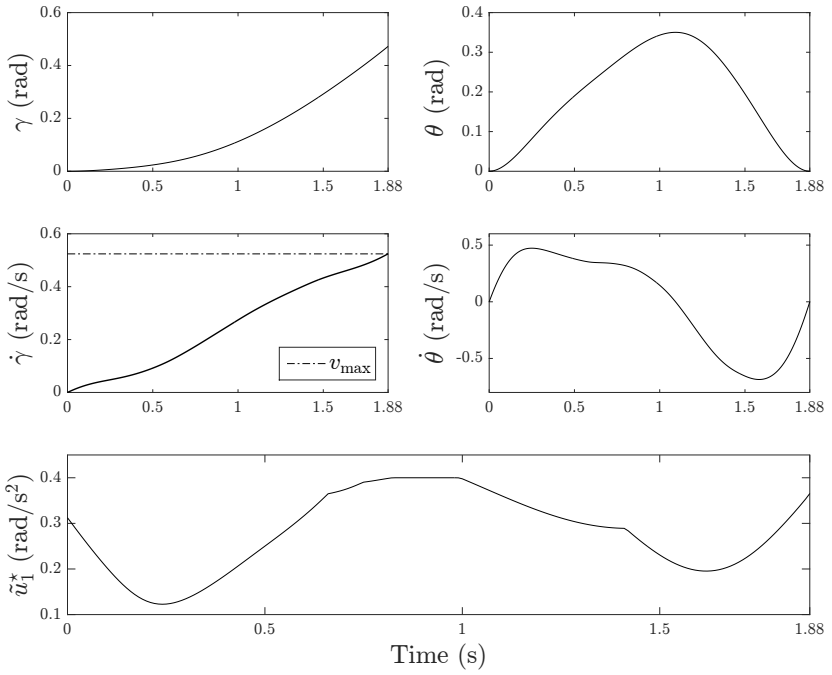

FIGURE 3.11: Control input and state trajectories at the optimum obtained by the particular solution.

where ϕ_1 is associated with the state constraint due to the maximum of the servo motor speed. The weighting coefficients are similar to those used in the no-switched scenario, namely $\omega_2 = \omega_3 = \omega_4 = \mu_1 = 10^6$. The optimal control problem (3.27) can be solved by means of the conventional clipping-off CG method described in Section 3.4, where the initial guess of the optimal control input is chosen as $\tilde{u}_1^0(t) = u_{\max}$, $\forall t \in \mathbb{T}_1$.

The switching instant t_1 is specified as the sub-optimal time which is successfully found such that $\exists \tilde{u}_1^\star(t_1) : J_p(\tilde{u}_1^\star(t_1)) < J_{tol}$ by using the bisection method in a similar manner with Algorithm 3. Note that the starting value of t_1 in the bisection iteration can be chosen as $v_{\max}/u_{\max}$. Once the optimal control input $\tilde{u}_1^\star(t)$ and the first switching instant t_1 are found, the second switching instant t_2 can be automatically determined by

$$t_2 = \frac{\gamma_d - 2\iint_0^{t_1} \tilde{u}_1^\star(t)dt}{v_{\max}} + t_1. \tag{3.28}$$

The computation is conducted on a personal computer with 2.5-GHz Intel Core i5-3210M and 8 GB of RAM. It takes 24.6 seconds for the particular solution to converge at the optimum. The optimal

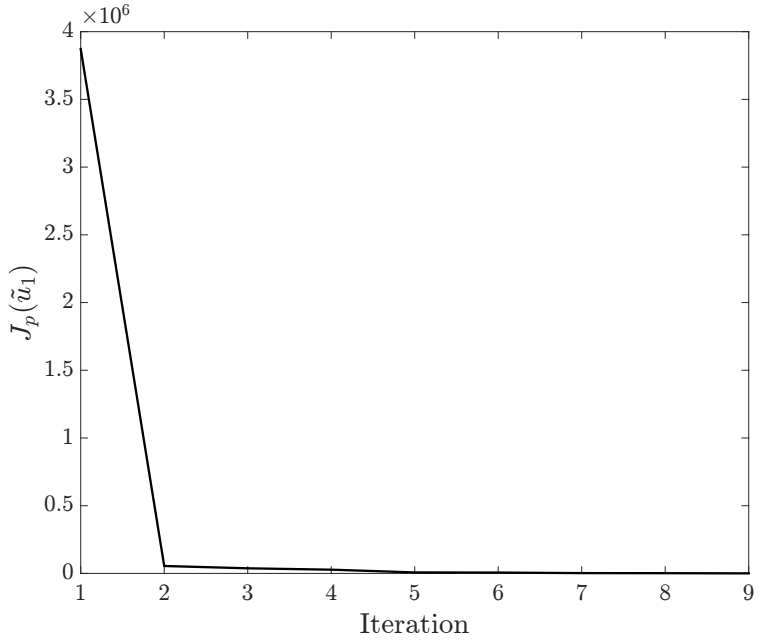

FIGURE 3.12: Cost function history over iterations of the particular solution at the resultant switching instant $t_1 = 1.88$ seconds.

control input $\tilde{u}_1^\star(t)$ and the correspondent state trajectories are shown in Fig. 3.11. The resultant sub-optimal switching instant and cost functional are given as $t_1^\star = 1.88$ seconds and $J_p(\tilde{u}_1^\star(t_1^\star)) = 0.2571$ respectively. From Fig. 3.11, one can easily compute the profile of $\dot{\varphi}(t)$ which is then fed to the servo motor as a velocity command. The implementation of the switched optimal control system using the particular solution is provided in Section 3.7. The cost functional history over iterations at $t_1 = 1.88$ seconds is shown in Fig. 3.12. It can be observed that the clipping-off CG method improves the cost functional of the initial guess $J_p(\tilde{u}_1^0) = 3.87 \times 10^6$ to the optimum $J_p(\tilde{u}_1^\star) = 0.2571$ in only a few iterations. The requirements of the control performance is fulfilled since $J_p(\tilde{u}_1^\star) < J_{tol}$, $(J_{tol} = 1)$. Consequently, the particular solution is feasible to solve the switched optimal control problem for the rotary hook system.

Remark 12. Since the acceleration and deceleration intervals are explicitly partitioned in the particular solution hence one needs to determine the lower bound of γ_d for which the particular solution is applicable. This lower bound of is given as

$$\underline{\gamma_d} = 2 \iint_0^{t_1} \tilde{u}_1^\star(t) dt. \tag{3.29}$$

Algorithm 4: General solution of the switched optimal control problem for the rotary hook system by means of the two-stage decomposition concept.

Step 1 Set the incremental index $i = 0$. Choose an initial switching instants vector $\boldsymbol{t}^0 = [t_1^0 \;\; t_2^0]^\top$.

Step 2 -Stage (a)- Solving the optimal control problem for the system with respect to the switching instant vector $\boldsymbol{t}^i$. Obtain $J_g(\boldsymbol{t}^i)$. Go to step 3.

Step 3 -Stage (b)- By using $J_g(\boldsymbol{t}^i)$, update the switching instants vector by solving the following constrained optimization problem

$$\min_{0<t_1<t_2<t_f} \quad J_g(t_1, t_2) \tag{3.30}$$

By means of a nonlinear programming method, the switching instants can be updated. Denote the updated value of $\boldsymbol{t}^i$ as $\boldsymbol{t}^{i+1}$. If the nonlinear programmer converges to a local optimum then terminate. Otherwise, let $i = i + 1$ and repeat step 2.

Based on the optimal control input $\tilde{u}_1^\star$ shown in Fig. 3.11, it can be numerically computed as $\underline{\gamma_d} = 49.8$ degrees. Implication of the lower bound $\underline{\gamma_d}$ is given in the Section 3.8. Note that for any target skewing angle γ_d satisfying the condition $\gamma_d > \underline{\gamma_d}$ then the optimal solution shown in Fig. 3.11 can be reusable. The only parameter that needs to be recomputed is the switching instant t_2 which can be easily obtained by (3.28).

In summary, the total optimal control input for the whole transferring process in the case of the particular solution is denoted as $\tilde{u}^\star(t)$, in which $\tilde{u}^\star(t) = \tilde{u}_1^\star(t)$ $(t \in \mathbb{T}_1)$, $\tilde{u}^\star(t) = 0$ $(t \in \mathbb{T}_2)$, and $\tilde{u}^\star(t) = \tilde{u}_3^\star(t)$ $(t \in \mathbb{T}_3)$.

3.6.3 General solution

As noted in Remark 12, the particular solution is only applicable when the reference skewing angle is sufficiently large, namely $\gamma_d > \underline{\gamma_d} = 49.8$ degrees. Therefore, in this section, an attempt is made to derive a general solution to overcome the above-mentioned limitation of the particular solution. In order to do so, the state constraints (3.25) at the switching instant t_1 will be nullified and the switching instants will be optimized. Note that, to draw a distinction with the particular solution, the control input of jth interval in the general solution will be denoted as u_j $(j = 1, 3)$ whose optimums are $u_j^\star(t)$.

Now, the switching instants optimization problem arises together with the common problem in computing the bounded optimal control input with state constraints. As usual, to eliminate the state

constraint, a step penalty function is employed. Therefore, the optimal control problem with a fixed terminal time for the switched rotary hook system is stated as follows

$$\min_{u_1,u_3,t_1,t_2} J_g = \phi_g\left(\boldsymbol{x}(t_f)\right) + \underbrace{\int_{t_0}^{t_f} L(\boldsymbol{x})dt}_{\text{Penalty term}} \tag{3.31}$$

s.t.

$$\dot{\boldsymbol{x}} = \begin{cases} \boldsymbol{f}_k(\boldsymbol{x}) + \boldsymbol{b}_k(\boldsymbol{x})u_k, & \text{if } t \in \mathbb{T}_k \ (k = 1, 3) \\ \boldsymbol{f}_k(\boldsymbol{x}), & \text{if } t \in \mathbb{T}_k \ (k = 2) \end{cases}, \quad \boldsymbol{x}(t_0) = 0$$

$$\phi_g\left(\boldsymbol{x}(t_f)\right) = \omega_1\left[x_1(t_f) - \gamma_d\right]^2 + \omega_2 x_2^2(t_f) + \omega_3 x_3^2(t_f) + \omega_4 x_4^2(t_f)$$

$$L(\boldsymbol{x}) = k_1\phi_1^2$$

$$|u_1| \leq u_{\max}, \ |u_3| \leq u_{\max}$$

$$\phi_1 = v_{\max}^2 - (x_2 + x_4)^2$$

$$k_1 = \begin{cases} 0 & \text{if } \phi_1 \geq 0 \\ \mu_1 & \text{if } \phi_1 < 0, \end{cases}$$

In (3.31), the weighting coefficients are $\omega_1 = \ldots = \omega_4 = \mu_1 = 10^6$. As can be seen from (3.31), one needs to compute not only bounded optimal control inputs with state constraints but also the optimal switching instants t_1 and t_2. For this reason, a general solution to (3.31) will be formulated based on a concept of two-stage decomposition, namely optimal control seeking stage (stage (a)) and optimal switching instants seeking stage (stage (b)) [131, 132]. In stage (a), switching instants are assumed to be fixed thus the main task is to compute the bounded optimal control input with state constraints. By means of this stage, one can obtain the cost functional J_g corresponding to the current switching instants. In stage (b), the switching instants are updated by employing the cost functional J_g obtained in stage (a) through any constrained nonlinear programming technique. The conceptual procedure is illustrated in Algorithm 4. Details of both stage (a) and stage (b) will be briefly explained as follows. To solve stage (b), the interior point technique provided by the *fmincon* routine of MATLAB will be straightforwardly employed. However, in order to solve stage (a) in which the control input constraints present, an extension of the clipping-off CG method needs to be further developed to suit for the nonlinear switched system context. In the first step, necessary conditions for a control input to be optimal in respect of a switched system with known switching instants must be formulated. In [131], such necessary conditions are derived only for a switched system without control input constraints. In this chapter, it will be extended for a switched system with bounded control

inputs by means of Lemma 2 (Appendix A). Based on Lemma 2, an extended clipping-off CG scheme is proposed in Algorithm 5 of the same appendix. By using Algorithm 5, the switched optimal control problem, subject to the fixed switching instants posed in stage (a), can be solved. The convergence analysis of Algorithm 5 is given in Appendix B.

In the general solution, the sub-optimal transferring time can also be achieved by extending the fixed terminal time switched optimal control problem (3.31) by using the bisection method in a similar manner to Algorithm 3. However, one cannot expect a faster transferring time compared with the no-switched control system (see Remark 11). Therefore, it is rational to utilize the successive sub-optimal transferring time found in the no-switched optimal control solution shown in the Section 3.5 as the target terminal time for the general solution.

Now, it is ready to solve the switched optimal control problem (3.31) by the general solution. As the above discussions, the target terminal time t_f for the switched control system is given by the successive sub-optimal transferring time found in the no-switched scenario, e.g., $t_f = 5.06$ seconds for the medium transferring case ($\gamma_d = 90$ degrees) and $t_f = 7.97$ seconds in the long transferring case ($\gamma_d = 180$ degrees). To start the procedure, initial guesses of the necessary terms are given as

$$
\begin{aligned}
&u_1^0(t) = u_{\max}, \forall t \in \mathbb{T}_1 \text{ and } u_3^0(t) = -u_{\max}, \forall t \in \mathbb{T}_3.\\
&\boldsymbol{t}^0 = \left[t_1^0,\ t_2^0\right]^\top = \left[t_f/3,\ 2t_f/3\right]^\top.
\end{aligned}
$$

Let $\boldsymbol{u}^0(t) = \left[u_1^0(t),\ u_2^0(t)\right]^\top$ and denote the resultant optimal control input of the general solution as $\boldsymbol{u}^\star(t) = \left[u_1^\star(t),\ u_2^\star(t)\right]^\top$. In the medium transferring case, it takes more than 40 minutes (in 42 iterations) for the general solution given by Algorithm 4 to converge. The optimized switching instants are achieved as $\boldsymbol{t}^\star = \left[t_1^\star,\ t_2^\star\right]^\top = \left[1.72,\ 3.48\right]^\top$ seconds. The cost functional is improved from initial value $J_g\left(\boldsymbol{u}^0(t), \boldsymbol{t}^0\right) = 7.2 \times 10^4$ to the local minimum $J_g\left(\boldsymbol{u}^\star(t), \boldsymbol{t}^\star\right) = 289.2$. Note that the converged solution cannot satisfy the required performance since $J_g\left(\boldsymbol{u}^\star(t), \boldsymbol{t}^\star\right) > J_{tol} = 1$. Similar situations are encountered in the short and long transferring cases.

Following discussions are provided to clarify the unsatisfactory results obtained by the general solution. Firstly, the undesirable performance index can be explained by the fact that both clipping-off CG method in the stage (a) and nonlinear programming in the stage (b) only result in local optimum, thus the converged cost functional $J_g\left(\boldsymbol{u}^\star(t), \boldsymbol{t}^\star\right)$ is conservative. Secondly, the long computational time is due to the switching instants optimization (stage (b)), which significantly increase the computational burden since the stage (a) must be restarted all over again in each iteration when the switching instants are updated.

TABLE 3.3: Computational results of the particular solution for the switched control system.

Case	SW instants	Transfer time	Compt. time
$\gamma_d = 90°$	$t_1 = 1.88$ s $t_2 = 3.07$ s	4.95 s	24.6 s
$\gamma_d = 180°$	$t_1 = 1.88$ s $t_2 = 6.06$ s	7.94 s	24.6 s

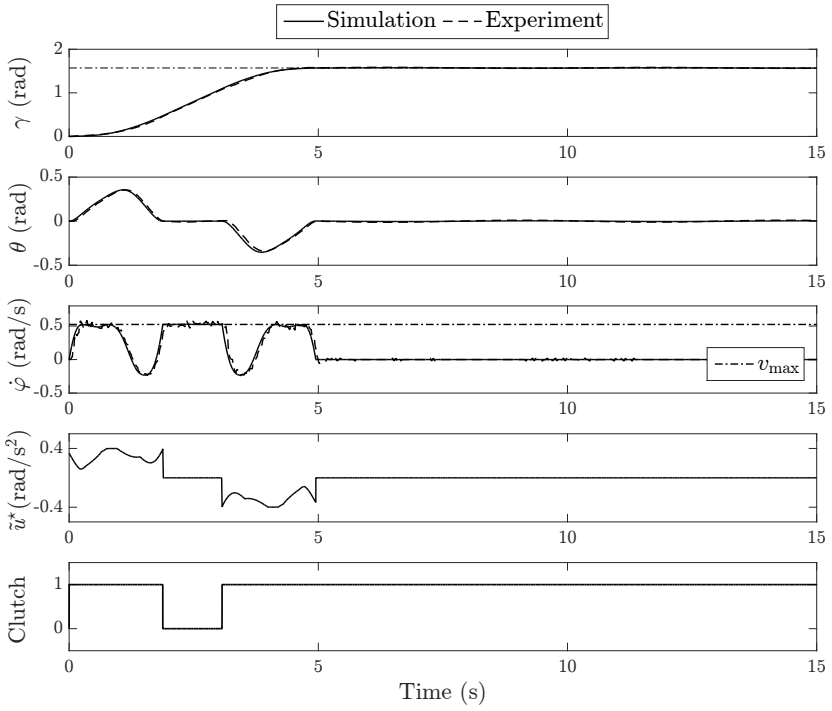

FIGURE 3.13: Simulation and experimental results of the switched control system in the medium transfer. In the clutch graph, "1" denotes the engagement whereas "0" represents the disengagement.

From the above unsatisfactory result of the proposed general solution in the chapter, it opens some possibilities in improving the performance of the general solution to extend the feasibility of energy saving by using the switched optimal control system in practice.

3.7 Experimental results of the switched control system

Effectiveness of the switched optimal control system is now verified on the experimental apparatus. Two cases, namely medium transferring ($\gamma_d = 90$ degrees) and long tranferring ($\gamma_d = 180$ degrees),

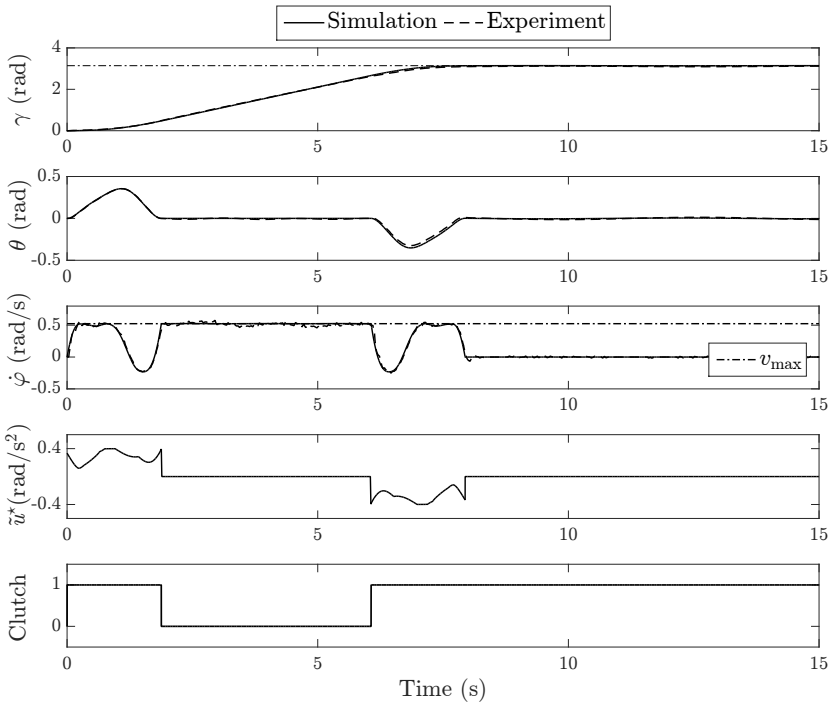

FIGURE 3.14: Simulation and experimental results of the switched control system in the long transfer. In the clutch graph, "1" denotes the engagement whereas "0" represents the disengagement.

will be validated in the experiments. By means of the particular solution, computational results are given in the Table 3.3. It is worth mentioning that during the free-run interval, namely when clutch is disengaged, the motor is actually turned off.

Experimental results of the switched control system are shown in Fig. 3.13 and Fig. 3.14. Note that in each figure, the clutch state are presented in which "1" and "0" represent the engaging and disengaging configuration respectively. It is recognized that the experimental results in all cases are in total agreement with the simulation results. The payload precisely arrives at the desired skew angle whilst the skew oscillation is nearly suppressed at the end of the motion. Therefore, performance of the switched optimal control system employing the particular solution is confirmed.

3.8 Comparison between switched and no-switched control systems

In this section, two scenarios namely switched and no-switched control systems will be compared in terms of the transferring time and overall energy consumption. The actual energy consumption of the servo motor will be employed to quantitatively access the energy usage of each control system.

Specifically, the power utilized by the servo motor is given by $P(t) = \tau_m \dot{\varphi}_m(t)$, where $\tau_m(t)$ is the motor torque. Furthermore, $\tau_m(t)$ is related to the actual motor current $i_m(t)$ by a torque constant $k_t = 0.0152$ (Nm/A), therefore $P(t) = k_t i_m(t)\dot{\varphi}_m(t)$. Energy consumption of the servo motor is just an integration of the power over the operating time, namely

$$E = k_t \int_0^{t_f} i_m(t)\dot{\varphi}_m(t)dt\Big|_{i_m(t)\dot{\varphi}_m(t)\geq 0}. \tag{3.32}$$

Note that the regions where $P(t) = k_t i_m(t)\dot{\varphi}_m(t) < 0$ are the regenerative braking intervals. In these intervals, the power flows back to the system and a dumped resistor is used to dissipate this power into heat. Therefore, the motor does not use energy hence the regenerative braking periods are excluded in (3.32). In the experiments, the actual current $i_m(t)$ and the velocity $\dot{\varphi}_m(t)$ are measured for each switched/no-switched control system. Therefore, the energy consumption E for each controller can be numerically computed by (3.32).

In the experimental studies, the transferring time t_c is defined as the time instant which satisfies two conditions: a) the response curve of the payload's absolute angle $\gamma(t)$ reaches and maintains within a range $\zeta\%$ of the final target angle γ_d, b) the vibration nearly vanishes; that is to say

$$t_c = \min\left\{t : \forall \Delta_t > 0 \text{ s.t. (3.34) and (3.35) are fufilled}\right\}. \tag{3.33}$$

The conditions (3.34) and (3.35) are defined as follows

$$(1 - \zeta \text{sgn}(\gamma_d))\gamma_d < \gamma(t + \Delta_t) < (1 + \zeta \text{sgn}(\gamma_d))\gamma_d, \tag{3.34}$$

$$|\theta(t + \Delta_t)| < |\theta(t)| \leq \theta_{tol}. \tag{3.35}$$

Here, it is chosen that $\zeta = 1\%$, $\theta_{tol} = 1$ degree. Note that "sgn" represents a usual signum function. Comparative results between the switched and no-switched optimal controls in the medium and long transferring cases are shown in Fig. 3.15 and Fig. 3.16 respectively. Their transferring times and energy consumptions are summarized in Table 3.4. According to Table 3.4, the switched optimal control system is able to retain the sub-optimal transferring times provided by the no-switched optimal solution. For instance, in the long transferring case ($\gamma_d = 180^\circ$), the sub-optimal transferring time of the switched and no-switched schemes are 7.91 seconds and 7.93 seconds respectively. Furthermore, when the switched optimal control system is employed, the energy consumption is respectively reduced up to 25.49% and 61.70% in the medium and long transferring cases compared with the no-switched

TABLE 3.4: Transferring time and energy consumption of switched and no-switched control systems.

		Trans. time t_c	Energy E	Comp. time
$\gamma_d = 90°$	**SW**[a]	**4.83 s**	**3.04 J**	**24.6 s**
	NSW[b]	4.89 s	4.08 J	61.7 s
	IS[c]	5.78 s	3.82 J	4.2 s
	ISMC[d]	6.91 s	3.37 J	—
$\gamma_d = 180°$	**SW**	**7.91 s**	**3.11 J**	**24.6 s**
	NSW	7.93 s	8.12 J	85.2 s
	IS	11.74 s	7.10 J	5.4 s
	ISMC	10.61 s	7.18 J	—

[a] Switched optimal control,
[b] No-switched optimal control,
[c] Input shaping control,
[d] Integral sliding mode control.
— Real Time.

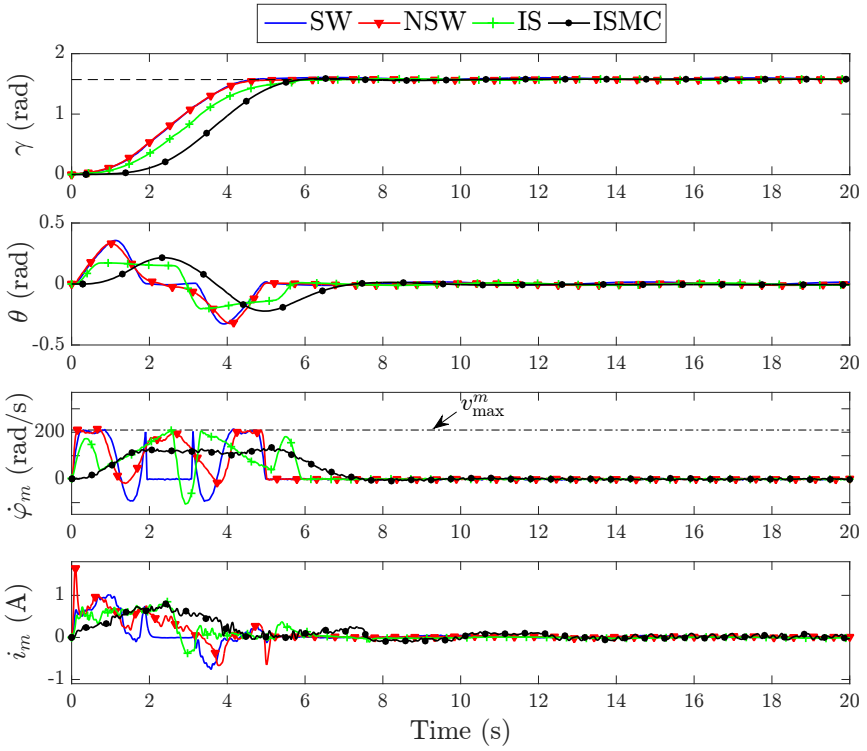

FIGURE 3.15: Comparative experimental results of the switched optimal, no-switched optimal, input shaping, and integral sliding mode controllers ($\gamma_d = 90°$).

counterpart. Therefore, our purpose in *saving energy* for the rotary hook system is achieved *without any influence to the total transferring time* by employing the switched optimal control approach.

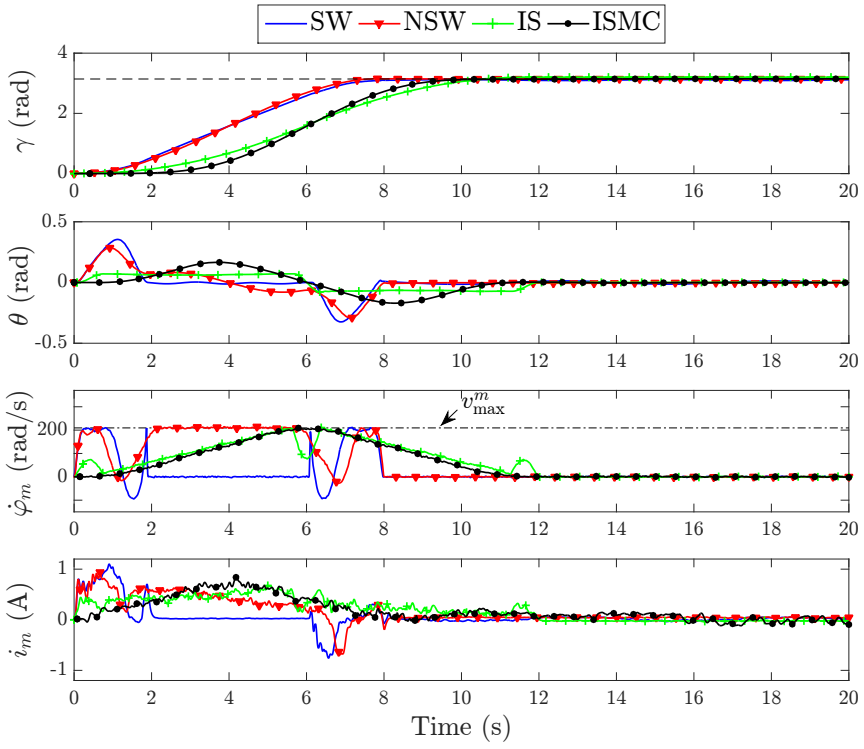

FIGURE 3.16: Comparative experimental results of the switched optimal, no-switched optimal, input shaping, and integral sliding mode controllers ($\gamma_d = 180°$).

It should be noted that the particular solution is only applicable when the target skew angle γ_d satisfies the condition that $\gamma_d > \underline{\gamma_d}$, namely γ_d needs to be sufficiently large. Therefore, in practice, no-switched and switched optimal control systems will be used in a complementary manner. For the short transferring cases, namely $\gamma_d < \underline{\gamma_d} = 49.8$ degrees, no-switched scenario is put into operation. Otherwise, the switched optimal control system will take place to reduce the energy consumption. Such operation is rational since in the short transferring contexts, the amount of energy saving is not significant. Furthermore, in these cases, switching within a small period of time will possibly causes damage to the clutch.

In order to clarify the effectiveness of the proposed switched optimal control scheme in reducing both transferring time and energy consumption, feed-forward Input Shaping (IS) control and Integral Sliding Mode Control (ISMC) are intentionally applied in the context where the clutch is entirely engaged during the motion. The ISMC is used in an exact manner to Chapter 2 whereas in the input shaping scheme, the fastest ZV input shaper [46] is employed. Since the damping ratio of the rotary hook system is not considered, magnitude A_i and time location τ_i $(i = 1, 2)$ of each impulse in the ZV input

shaper are given as follows

$$\begin{bmatrix} A_i \\ \tau_i \end{bmatrix} = \begin{bmatrix} 0.5 & 0.5 \\ 0 & \dfrac{\pi}{\omega_n} \end{bmatrix}, \tag{3.36}$$

where ω_n denotes the angular natural frequency of the system. By linearizing the nonlinear system (3.6) around the equilibrium point, it can be found that $\omega_n = \sqrt{mgR^2/(l \times I_H)}$ and by using the values in Table 3.1, it can be obtained that $\omega_n = 4.175$ (rad/s). Therefore, the ZV input shaper in (3.36) is now specified. In order to ensure a smooth motion, following second order trajectory is planned as the original command for the input shaping control

$$r_{IS}(t) = \begin{cases} \dfrac{4\gamma_d}{\rho^2}\dfrac{t^2}{2} & \text{if } 0 \le t \le \rho/2 \\ \dfrac{\gamma_d}{\rho^2}\left(-2t^2 + 4\rho t - \rho^2\right) & \text{if } \rho/2 \le t \le \rho \\ \gamma_d & \text{if } t \ge \rho. \end{cases} \tag{3.37}$$

In (3.37), ρ regards to the terminal time at which the reference trajectory $r_{IS}(t)$ reaches the target skew angle γ_d. By gradually reducing ρ in a similar manner to the bisection method shown in Algorithm 3, the smallest transferring time (in case of the input shaping control) subjected to the state constraint $|\dot{\varphi}(t)| \le v_{\max}$ and the control input constraint $|u(t)| \le u_{\max}$ can be achieved. Note that the starting value of ρ in the bisection iteration can be chosen as $2\gamma_d/v_{\max}$.

The experimental results of the input shaping control and ISMC are shown in Figs. 3.15–3.16 for the medium and long transferring case respectively. The transferring time, energy consumption, and computational time of all control methods are aggregated in Table 3.4. It can be seen that by using the switched optimal control system, when $\gamma_d = 90^\circ$, the transferring time and energy consumption are respectively reduced up to 16.4% and 20.4% compared to IS control, whereas those are 30.1% and 9.8% in the case of ISMC. Similarly, when $\gamma_d = 180^\circ$, the switched optimal control system saves 32.6% and 56.2% in the transferring time and energy consumption compared to IS control, whilst 25.4% and 56.7% are obtained in the case of ISMC. Note that the energy reduction percentage does not depend on the torque constant k_t. In summary, it is concluded that the proposed switched optimal controller performs a faster transferring process with a smaller energy consumption.

It should be remarked that the optimal controllers proposed in this chapter are actually feed-forward schemes. Therefore, if the working environment is surrounded by various sources of disturbances such as wind, collision, etc., the proposed optimal controllers can serve as a sub-optimal-time reference

trajectory planner for combining with a feedback controller in a 2-DOF control system to enhance overall performance. Furthermore, in the case that system parameters do not significantly vary, namely the parametric uncertainties are small, the proposed scheme is proved to be an effective method to reduce both transferring time and energy consumption for the payload's skew rotation system.

3.9 Summary

In this chapter, nonlinear dynamic of a hybrid rotary hook system is formulated in theory and validated in experiments. Two types of optimal control systems, namely switched and no-switched, are proposed to drive the payload to a desirable skew orientation without any residual vibration. The novelty of the switched optimal controller lies in the fact that it is able to reduce energy consumption without trading-off the sub-optimal transferring time. The key point is to use an electro-mechanical clutch to generate a free motion of the payload imposing upon its own inertial movement. To resolve the switched optimal control problem, both general and particular solutions are proposed in which the particular solution is shown to be advantageous over the general solution. The basic idea of the particular solution is to transform the original switched optimal control problem to the no-switched domain by imposing the state constraints at the switching instants. In comparison to other candidates, namely input shaping and integral siding mode controllers, the proposed switched optimal control scheme shows its advantages in reducing both transferring time and energy consumption. Effectiveness of the optimal control systems are demonstrated on an experimental apparatus and their validities have been shown.

Part II

Swing Vibration Control of Cranes

Chapter 4

Minimum-time Zero Vibration S-curve Command Designs

In the previous two chapters, skew vibration controllers were formulated. The rest of this thesis will focus on the swing vibration control designs. In particular, this chapter introduces minimum-time S-curve commands to realize vibration-free transportation for an overhead crane in the presence actuator limits. S-curve commands are ubiquitous in servo drives owing to their simplicity and smoothness. Nevertheless, they need to be adapted for use in flexible systems, where the problem of residual vibration must be addressed. This chapter proposes a simple motion planning method for the vibration-free transfer process of an overhead crane using S-curve commands. Based on a position baseline S-curve, which is generated from a bang-off-bang acceleration profile, two approaches are proposed to build the vibration suppression capability. One is an embedding method that injects the essential terminal conditions for vibration-free transportation into the baseline S-curve command without altering its original form. The other is a shaping method inspired from the input shaping technique. In both schemes, the baseline S-curve is parameterized to establish minimum-time optimization problems, in which maximum velocity and maximum acceleration of the actuator are explicitly taken into consideration. The minimum-time solutions are successfully obtained by solving constrained (discrete) nonlinear programs. An online trajectory generation can be realized using the proposed approach. Both simulation and experimental results are given to verify the effectiveness of the proposed method.

4.1 Introduction

Overhead cranes are widely considered the most important means of transportation in various places such as factories, harbors, etc. to transfer heavy payloads point-to-point within the workspace. The payload is suspended under the trolley by rope and its height can be adjusted by a hoisting motion. The trolley actuator relocates the payload. This is always a linear motion, and for this reason, the overhead crane is usually described in a Cartesian coordinate. As the rope is flexible, the payload exhibits residual vibration during and after transportation. This undesirable oscillation significantly reduces the safety and productivity of the overhead crane system in practice. Consequently, the control objectives for this system are bringing the trolley to its destination and suppressing the swing movement of the payload. This is a challenging task since the overhead crane is an underactuated system—it has only one control input (trolley actuation) and two control outputs. Therefore, considerable interests were mounting on the vibration control for the overhead crane system. They can be classified into two main categories: feedback and feedforward controls. These types can be combined to obtain a 2-DOF control system to improve control performance.

An extensive background can be found in the feedback control category. Naturally, the vibration control of overhead cranes has evolved along with the development of control theory. New designs of the linear controls and model predictive controls have been promptly employed on the overhead cranes [12, 14, 37, 38, 133]. Feedback linearization and differential-flatness based methodology [16], which aims at transforming a nonlinear model to a linear one to utilize well-established linear controls, have also been widely applied [19, 20]. The main disadvantage of the feedback linearization method is that it is not robust to parametric uncertainties and unmodeled dynamics. In order to deal with such circumstances, sliding-mode based controls [23, 24], adaptive controls [25, 27, 28, 134], energy and passivity based nonlinear controls [33, 135, 136] are preferable. Intelligence—fuzzy and neural network—controls have also been successfully implemented on crane systems [76, 137, 138]. To sum up, feedback control techniques show excellent properties in handling parametric uncertainties and external disturbances. However, they demand a sophisticated and costly sensor structure that requires regular maintenance, and thus feedback controllers are still not popular in practical cranes. In numerous contexts, feedforward controls are preferable in industry due to their simplicity and ease of implementation, as well as no additional measurement system being required.

Minimum-time trajectory planning is a crucial means to enhance transportation productivity of overhead crane systems. To obtain a universal minimum-time Zero Vibration (ZV) reference trajectory in the presence of both state and control input constraints, one can employ indirect [59, 60] or direct methods [63, 64, 71, 139]. Indirect approaches utilize the necessary condition for time-optimality based

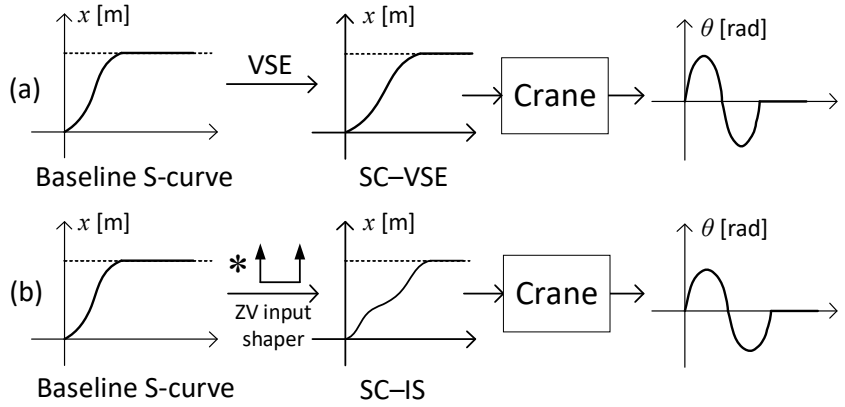

FIGURE 4.1: Description of the embedding (a) and the shaping (b) methods. The operator $*$ denotes the convolution between two signals.

on the Pontryagin Minimum Principle, whereas direct methods discretize the system to formulate and solve linear/nonlinear programs by means of optimization solvers. However, the above-mentioned techniques require high computational effort, and thus they can barely generate motion trajectories in an online fashion. To address this issue, one can limit the attention to a certain class of control inputs and establish an analytical minimum-time solution for that class. In this way, an online trajectory generation can be achieved. The class of bang-off-bang acceleration control inputs [65, 140, 141] is the most basic and commonly used in industrial servo drives compared to other classes such as B-splines [72], trigonometric [68, 140], jerk-limited [70], etc. In [65], a S-curve position command generated from a bang-off-bang acceleration profile was proposed to suppress vibration for a flexible system. The excitation energy of the input forcing function was minimized by using frequency analysis. Unfortunately, the actuator limits were omitted in the design process. Recently, [140] proposed a three-segment (i.e., bang-off-bang) acceleration profile and its modified versions for a 2D overhead crane. A geometric approach, based on the system phase portrait, is employed to derive vibration suppression conditions for the S-curve profile. [141] introduced a similar approach as [140] and extended those results by considering a family of acceleration profiles in a stair form. A minimum-time solution, however, was not considered in the above-mentioned studies. In summary, to date, none of the existing studies have solved the minimum transferring time problem for ZV S-curve commands generated from the class of bang-off-bang acceleration profiles under restrictions imposed by actuator limitations.

The present study aims to obtain a low-cost crane system with enhanced productivity, while maintaining a precise payload positioning and the vibration suppression capability. Therefore, in response to the previous discussions, this chapter will establish minimum-time solutions for the ZV S-curve position commands for an overhead crane system considering both maximum velocity and maximum

acceleration of the actuator. In this chapter, the S-curve command is understood in the position level and it is created from a bang-off-bang acceleration trajectory. Two approaches will be introduced to enable the S-curve to admit the vibration cancellation capability. The embedding method directly injects the vibration suppression conditions at the end of maneuver into the baseline S-curve command. Consequently, the resultant S-curve command—named S-curve–Vibration Suppression Embedded (SC–VSE)—has internal constraints on the duration of acceleration, uniform, and deceleration intervals that strongly relate to the natural frequency of the system. On the other hand, the shaping method does not impose those internal constraints on the baseline S-curve but will use some add-on tools to modulate the original (baseline/unshaped) S-curve command to gain vibration-free transportation. The most well-known add-on—ZV input shaper [44, 46, 49]—will be employed to convolute with the baseline S-curve. For clarification, the resultant S-curve command of the shaping method is termed S-curve–Input Shaped (SC–IS). Illustrations of the embedding and the shaping methods are shown in Fig. 4.1. In the SC–VSE establishment, the conditions of zero residual vibration are deficient, which leads to an underdetermined issue (see Section 4.3.1). This matter is resolved together with the minimum transferring time problem by formulating constrained discrete nonlinear programs (see Sections 4.3.2–4.3.3). The main challenge is to obtain a global optimal solution of those optimization problems in closed form, with which the computational effort is low, and thus online command generation can be realized. In addition, the design of the baseline S-curve command for the SC–IS scheme—to fulfill both minimum-time and actuator limits requirements—is not a trivial task because the convolution process may change the shape as well as the magnitude of the baseline S-curve. As a result, the main difficulty needing to be solved in the minimum-time SC–IS case is to enumerate all feasible shaped families, which is the crucial step to establish a sequence of optimization problems (see Section 4.4.1).

To sum up, in comparison with previous studies, the contributions of this thesis are as follows:

1. The minimum-time solution of the class of bang-off-bang acceleration inputs subject to both maximum velocity and maximum acceleration constraints is resolved, which fills a gap in the literature. Therefore, compared with the related studies in [140] and [141], the proposed ZV reference trajectory is faster.

2. The proposed minimum-time ZV motion profile can be easily computed online, which is a strong advantage compared to universal minimum-time solutions (e.g., in [59, 64]).

3. When infinite actuator limits are allowed, this chapter shows that the SC–VSE is only *two* times slower than a discontinuous command formed by a step function and the ZV input shaper (or SC–IS in equivalence), not *four* times as suggested by [67].

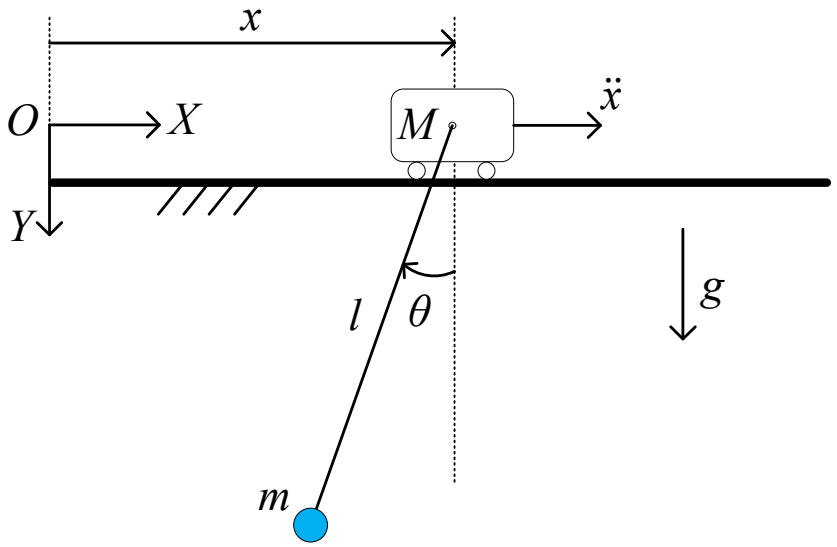

FIGURE 4.2: Mathematical model of the overhead crane system.

4.2 Problem formulation

Swinging motion of the payload resulted from the trolley actuation is illustrated in Fig. 4.2, in which $x(t)$ (m) and $\theta(t)$ (rad) are the trolley position and the swing angle. The net force driving the trolley is denoted as $F(t)$. Furthermore, m (kg), M (kg), l (m), and g (= 9.81 m/s^2) represents the payload mass, trolley mass, rope length, and gravitational acceleration respectively. The following assumptions are made to establish the dynamical model of the overhead crane system: the payload is considered as a point mass, the rope is assumed to be a rigid rod, and the air resistance to the payload could be negligible. Note that, the rigid rope assumption is reasonable and it is commonly used in the literature due to the fact that the elasticity modulus of the wire rope is very high. In other words, the axial elasticity effect of the rope is minor and could be negligible. The Euler–Lagrange method will be employed to establish the system dynamic. From Fig. 4.2, horizontal and vertical positions of the payload can be computed by

$$x_p(t) = x(t) - l\sin\theta(t) \tag{4.1}$$

$$y_p(t) = l\cos\theta(t). \tag{4.2}$$

By differentiating (4.1) and (4.2), horizontal and vertical velocities of the payload are

$$\dot{x}_p(t) = \dot{x}(t) - l\dot{\theta}(t)\cos\theta(t) \tag{4.3}$$

$$\dot{y}_p(t) = -l\dot{\theta}(t)\sin\theta(t). \tag{4.4}$$

The total kinetic energy of the system comprises translation energies of the trolley and the payload, and thus it can be written by

$$\mathcal{K} = \frac{1}{2}M\dot{x}^2 + \frac{1}{2}m\left(\dot{x}_p^2 + \dot{y}_p^2\right). \tag{4.5}$$

The potential energy of the system is given as $\mathcal{V} = -mgy_p$. Therefore, the Lagrangian function can be established by

$$\mathcal{L} = \mathcal{K} - \mathcal{V} = \frac{1}{2}M\dot{x}^2 + \frac{1}{2}m\left(\dot{x}_p^2 + \dot{y}_p^2\right) + mgl\cos\theta. \tag{4.6}$$

The Euler–Lagrange equation applying to the actuated coordinate $x(t)$ and the unactuated coordinate $\theta(t)$ reads:

$$\frac{d}{dt}\left(\frac{\partial\mathcal{L}}{\partial\dot{x}}\right) - \frac{\partial\mathcal{L}}{\partial x} = F. \tag{4.7}$$

$$\frac{d}{dt}\left(\frac{\partial\mathcal{L}}{\partial\dot{\theta}}\right) - \frac{\partial\mathcal{L}}{\partial\theta} = 0. \tag{4.8}$$

By developing (4.7) and (4.8) using (4.3), (4.4) and (4.6), the mathematical model of the overhead crane system is governed by

$$(M+m)\,\ddot{x} - ml\ddot{\theta}\cos\theta + ml\dot{\theta}^2\sin\theta = F \tag{4.9}$$

$$l\ddot{\theta} + g\sin\theta = \cos\theta\ddot{x}. \tag{4.10}$$

From (4.9) and (4.10), it is recognized that one can either use $F(t)$ or $\ddot{x}(t)$ as the control input. For the motion planning task, $\ddot{x}(t)$ is the more appropriate choice for the following reasons: i) the problematic frictional forces presented in $F(t)$ can be avoided, ii) the first and second integration of $\ddot{x}(t)$ will result in the velocity $\dot{x}(t)$ and the position $x(t)$ commands, which can be easily realized by ubiquitous servo drives, iii) the system dynamic is only dependent on the rope length l, which can be easily measured in practice. Therefore, the dynamical equation (4.10) is employed in the control design, in which the control input is $\ddot{x}(t)$. Note that, by choosing such a control signal, it is assumed that the servo motor can satisfactorily track the planned reference trajectory, which is an ordinary requirement for most industrial servo drives. Since the control input is chosen to be $\ddot{x}(t)$, (4.10) is the only dynamical equation considered in the subsequent control design and analysis. By using the small angle approximation [72, 140, 141], (4.10) can be linearized as

$$l\ddot{\theta}(t) + g\theta(t) = \ddot{x}(t). \tag{4.11}$$

From (4.11), the angular natural frequency ω_0 (rad/s) and the natural period T (s) of the overhead crane system are given by $\omega_0 = \sqrt{g/l}$ and $T = 2\pi/\omega_0$. Note that the model (4.11) will be employed to design the minimum-time SC–VSE and the minimum-time SC–IS in Section 4.3 and Section 4.4 respectively. Throughout this chapter, it is assumed that the payload starts from rest, namely $x(0) = \dot{x}(0) = \theta(0) = \dot{\theta}(0) = 0$ [68, 70, 140, 141]. Moreover, to realize a vibration-free transportation, the following terminal conditions must be fulfilled:

$$x(t_f) = x_r,\ \dot{x}(t_f) = 0,\ \theta(t_f) = 0,\ \dot{\theta}(t_f) = 0. \tag{4.12}$$

In (4.12), x_r (m) is the reference value of the trolley position. Without loss of generality, x_r is a positive constant, namely $x_r > 0$. The terminal time t_f will be minimized to enhance the transportation productivity (see Section 4.3 and Section 4.4).

The following maximum velocity and acceleration constraints of the actuator must be strictly kept:

$$|\dot{x}(t)| \leq v_{\max}, \quad |\ddot{x}(t)| \leq a_{\max}, \tag{4.13}$$

where $v_{\max} > 0$ and $a_{\max} > 0$. In the following section, the minimum-time SC–VSE will be formulated.

4.3 Design of the minimum-time SC–VSE

In this section, by embedding the conditions in (4.12) for vibration-free transportation into the baseline S-curve, the SC–VSE can be formed. It will be later shown that the no-residual-swing conditions $\theta(t_f) = \dot{\theta}(t_f) = 0$ are deficient, which leads to an underdetermined issue. This can be solved together with the minimum-time problem by establishing constrained discrete nonlinear programs. Simulation results are provided for various maneuvers with different values of $v_{\max}$ and $a_{\max}$ to verify the proposed minimum-time solution.

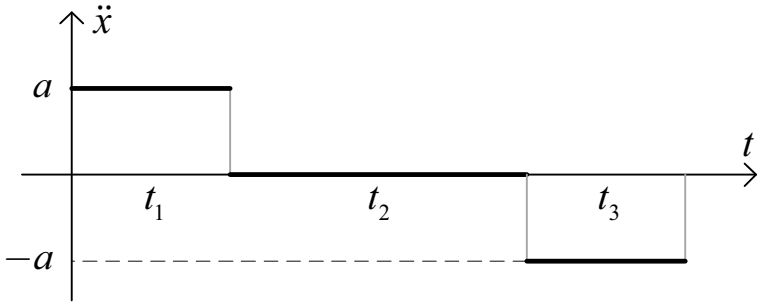

FIGURE 4.3: Parameterized bang-off-bang acceleration profile of the trolley.

The position baseline S-curve trajectory is generated by integrating twice the bang-off-bang acceleration profile as depicted in Fig. 4.3. This piece-wise continuous function can be expressed by[1]

$$\ddot{x}(t) = \begin{cases} a, & 0 \le t < t_1 \\ 0, & t_1 \le t < t_1 + t_2 \\ -a, & t_1 + t_2 \le t \le t_f \ (:= t_1 + t_2 + t_3)\,. \end{cases} \tag{4.14}$$

In (4.14), all of the parameters a, t_1, t_2, and t_3 are unknowns, whose pre-conditions are given as $0 < a \le a_{\max}$, $t_1 > 0$, $t_2 \ge 0$, and $t_3 > 0$. Furthermore, it is easy to see that the baseline S-curve obtained from (4.14) reaches its highest velocity ($= at_1$) at $t = t_1$. Therefore, the maximum velocity constraint $|\dot{x}(t)| \le v_{\max}$ becomes $at_1 \le v_{\max}$. The following subsection will establish additional constraints for these unknown variables to actively gain a vibration-free transferring process.

4.3.1 Embedding vibration-free transportation conditions

By exploiting the vibration-free transportation condition (4.12), essential constraints on a, t_1, t_2, and t_3 can be further obtained. First, response of the system (4.11) under the action of the control input (4.14) will be derived.

During the acceleration interval, namely $0 \le t < t_1$, by substituting $\ddot{x}(t) = a$ into (4.11) and solving the second-order differential equation with a constant excitation, the following result is obtained:

$$\begin{aligned} \theta(t) &= \frac{a}{g}\left(1 - \cos\omega_0 t\right), & \dot{\theta}(t) &= \frac{a\omega_0}{g}\sin\omega_0 t \\ x(t) &= 0.5at^2, & \dot{x}(t) &= at. \end{aligned} \tag{4.15}$$

Similarly, when $t_1 \le t < t_1 + t_2$ (i.e., uniform interval), $\ddot{x}(t) = 0$ holds. Therefore

$$\begin{aligned} \theta(t) &= \frac{a}{g}\left[\cos\left(\omega_0\left(t - t_1\right)\right) - \cos\omega_0 t\right] \\ \dot{\theta}(t) &= -\frac{a\omega_0}{g}\left[\sin\left(\omega_0\left(t - t_1\right)\right) - \sin\omega_0 t\right] \\ x(t) &= at_1 t - 0.5at_1^2 \\ \dot{x}(t) &= at_1. \end{aligned} \tag{4.16}$$

[1] Although the acceleration profile of the motion is only piece-wise continuous, the resultant position S-curve command is continuously differentiable. Consequently, the motion's smoothness is ensured.

Finally, when $t_1 + t_2 \leq t \leq t_f$ (i.e., deceleration interval), $\ddot{x}(t) = -a$. Hence

$$\begin{aligned}
\theta(t) &= \frac{a}{g}\left[\sum_{i=1}^{2}\cos\left(\omega_0\left(t-\sum_{j=1}^{i}t_j\right)\right)-\cos\omega_0 t-1\right]\\
\dot{\theta}(t) &= \frac{-a\omega_0}{g}\left[\sum_{i=1}^{2}\sin\left(\omega_0\left(t-\sum_{j=1}^{i}t_j\right)\right)-\sin\omega_0 t\right]\\
x(t) &= -\frac{1}{2}at^2+a\left(2t_1+t_2\right)t-a\left(t_1^2+t_1t_2+\frac{1}{2}t_2^2\right)\\
\dot{x}(t) &= a\left(-t+2t_1+t_2\right).
\end{aligned} \tag{4.17}$$

From (4.17), the zero velocity condition of the trolley at t_f—$\dot{x}\left(t_f\right) = 0$—gives $a\left(-t_f + 2t_1 + t_2\right) = 0$, which can be easily developed to $t_f - 2t_1 - t_2 = 0$ since $a > 0$. Note that $t_f = t_1 + t_2 + t_3$; thus, $t_1 = t_3$. This means that the duration of the acceleration and deceleration periods must be similar. Using this result, the condition on the target trolley position, namely $x\left(t_f\right) = x_r$, can be exploited as

$$at_1\left(t_1+t_2\right) = x_r. \tag{4.18}$$

The condition of zero swing angle at t_f can be further developed by setting $\theta\left(t_f\right) = 0$ (in (4.17)). Consequently, it yields

$$\cos\left(\omega_0\left(t_1+t_2\right)\right)+\cos\omega_0 t_1 = 1+\cos\left(\omega_0\left(2t_1+t_2\right)\right). \tag{4.19}$$

Using the cosine sum-to-product trigonometric identity $\cos p + \cos q = 2\cos\left(\left(p+q\right)/2\right)\cos\left(\left(p-q\right)/2\right)$ on the left-hand-side (LHS) and $\cos 2p = 2\cos^2 p - 1$ on the right-hand-side (RHS) of (4.19) results in

$$\cos\left(\frac{\omega_0\left(2t_1+t_2\right)}{2}\right)\left[\cos\left(\frac{\omega_0 t_2}{2}\right)-\cos\left(\frac{\omega_0\left(2t_1+t_2\right)}{2}\right)\right] = 0. \tag{4.20}$$

Let $\mathbb{N}^+$ represent the set of positive integers. The solution of (4.20) can be found as

$$\begin{cases} t_1 = k_1 T \\ t_1 + t_2 = k_1 T \\ 2t_1 + t_2 = \left(k_1 - 0.5\right)T \end{cases}, \quad k_1 \in \mathbb{N}^+. \tag{4.21}$$

Lastly, to ensure the zero swing rate condition $\dot{\theta}\left(t_f\right) = 0$, from (4.17), it needs

$$\sin\left(\omega_0\left(t_1+t_2\right)\right)+\sin\omega_0 t_1 = \sin\left(\omega_0\left(2t_1+t_2\right)\right). \tag{4.22}$$

The solution of (4.22) can be similarly obtained as follows:

$$\begin{cases} t_1 = k_2 T \\ t_1 + t_2 = k_2 T \ , \ \ k_2 \in \mathbb{N}^+. \\ 2t_1 + t_2 = k_2 T \end{cases} \tag{4.23}$$

In sum, the zero residual vibration conditions $\theta(t_f) = \dot{\theta}(t_f) = 0$ can be obtained by subsuming (4.21) and (4.23). By using the set associative, commutative, and distributive laws [142], the subsumption of (4.21) and (4.23) leads to either of the following cases:

$$t_1 = k_1 T, \ k_1 \in \mathbb{N}^+ \tag{4.24}$$

$$\text{or } t_1 + t_2 = k_2 T, \ k_2 \in \mathbb{N}^+. \tag{4.25}$$

According to the above analysis, two equations $\theta(t_f) = 0$ and $\dot{\theta}(t_f) = 0$ are reduced to a single equation—either (4.24) or (4.25). Therefore, there are now only two equations ((4.18)&(4.24) or (4.18)&(4.25)) to solve for the three unknowns a, t_1, and t_2, which is clearly an underdetermined problem. Furthermore, the actuator limits represented by $v_{\max}$ and $a_{\max}$ must be taken into account. In order to resolve the above-mentioned underdetermined issue, the common strategy in the literature is to fix a specific quantity and utilize the constraints $|\dot{x}(t)| \leq v_{\max}$ and $|\ddot{x}(t)| \leq a_{\max}$ to determine the value of a. For instance, Sun et al. [140] set k_1 (in (4.24)) to $k_1 = 1$, namely $t_1 = T$. Then, a is calculated by $a = v/T$ where the velocity of the uniform interval v is determined by $v = \min\{v_{\max}, Ta_{\max}, x_r/T\}$. In contrast, Hoang et al. [141] fixed $v = v_{\max}$ and varied the index k_1 until the maximum acceleration constraint is fulfilled. These solutions, however, do not guarantee a time-optimal choice (see comparative results in Section 4.3.5). Therefore, constrained discrete nonlinear programs will be established to solve both underdetermined and time-optimal problems while ensuring that the actuator limits are complied with. The results of these optimization problems are admitted in closed form, and thus no intensive computation is required. The following subsection will discuss the optimal solution for the first case (i.e., $t_1 = k_1 T, \ k_1 \in \mathbb{N}^+$).

4.3.2 Case I of SC–VSE: $t_1 = k_1 T, \ k_1 \in \mathbb{N}^+$

To begin, the essential equality and inequality constraints needing to be taken into account are summarized as follows: 1) trajectory constraints: $t_1 > 0$ and $t_2 \geq 0$, 2) actuator limits: $0 < a \leq a_{\max}$ and $at_1 \leq v_{\max}$, and 3) vibration-free transportation conditions: $t_1 = k_1 T$, $k_1 \in \mathbb{N}^+$ and $at_1(t_1 + t_2) = x_r$ (see Section 4.3.1). By considering all of the above constraints and taking the total transferring time

t_f as the cost function, the following optimization problem can be established:

$$\begin{aligned} \min_{a,t_1,t_2} \quad & t_f = 2t_1 + t_2 \\ \text{s.t.} \quad & at_1\left(t_1 + t_2\right) = x_r \\ & t_1 = k_1 T \left(k_1 \in \mathbb{N}^+\right),\ t_2 \geq 0 \\ & 0 < a \leq a_{\max},\ at_1 \leq v_{\max}. \end{aligned} \tag{4.26}$$

Note that (4.26) is a discrete nonlinear program since t_1 can only be a multiple of the natural period T, whereas a and t_2 are continuous. Eliminating the two variables t_1 and t_2 using two equalities, (4.26) becomes the following mixed nonlinear–integer program:

$$\begin{aligned} \min_{a,k_1} \quad & t_f = k_1 T + \frac{x_r}{ak_1 T} \\ \text{s.t.} \quad & k_1 \in \mathbb{N}^+ \\ & 0 < a \leq a_{\max},\ a \leq \frac{x_r}{\left(k_1 T\right)^2},\ a \leq \frac{v_{\max}}{k_1 T}. \end{aligned} \tag{4.27}$$

In (4.27), the inequality constraint $a \leq x_r/\left(k_1 T\right)^2$ is a result of the condition $t_2 \geq 0$ in (4.26) applied to $t_2 = x_r/\left(ak_1 T\right) - k_1 T$. For a fixed k_1, (4.27) is actually a quasi-linear program, i.e., the original nonlinear optimization problem (4.27) can be converted to a linear one through a suitable variable substitution (see the proof of Lemma 1). Denote a set $\Delta\left(k_1\right)$ as below

$$\Delta(k_1) = \left\{ k_1 T,\ \frac{x_r}{k_1 T a_{\max}},\ \frac{x_r}{v_{\max}} \right\}. \tag{4.28}$$

In the first step, the optimal solution of (4.27) is established for each $k_1 \in \mathbb{N}^+$ by the following lemma:

Lemma 1. Consider the mixed nonlinear–integer optimization problem (4.27). For a fixed k_1 ($k_1 \in \mathbb{N}^+$), the minimizer $a^\dagger(k_1)$ and the optimum cost function $t_f^\dagger\left(k_1\right)$ of (4.27) are given by

$$a^\dagger(k_1) = \frac{x_r}{k_1 T \max \Delta\left(k_1\right)} \text{ and } t_f^\dagger\left(k_1\right) = k_1 T + \max \Delta\left(k_1\right).$$

Proof. By assigning $z = x_r/\left(ak_1 T\right)$, the original nonlinear program (4.27) can be transformed to a linear optimization problem (4.29), where $\mathbb{R}^+$ is the set of positive real numbers.

$$\begin{aligned} \min_{z \in \mathbb{R}^+} \quad & t_f = k_1 T + z \\ \text{s.t.} \quad & z \geq k_1 T,\ z \geq \frac{x_r}{k_1 T a_{\max}},\ z \geq \frac{x_r}{v_{\max}}. \end{aligned} \tag{4.29}$$

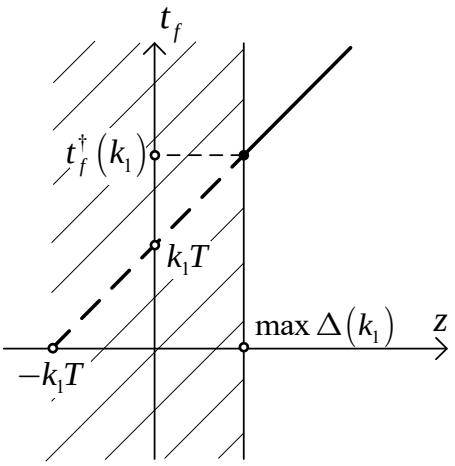

FIGURE 4.4: Optimal solution of the linear optimization problem (4.29).

It can be seen that the feasible region of (4.29) is $z \geq \max\Delta(k_1)$, so based on Fig. 4.4, the minimizer of (4.29) is $z^\dagger = \max\Delta(k_1)$ and $t_f^\dagger = k_1T + z^\dagger$. Using the relation $z = x_r/(ak_1T)$ leads to the results $a^\dagger(k_1) = x_r/(k_1T\max\Delta(k_1))$ and $t_f^\dagger(k_1) = k_1T + \max\Delta(k_1)$. This completes the proof. □

In fact, through Lemma 1, the first step will provide all local minima of the optimization problem (4.27), which are infinite in number. In the second step, these local minima will be compared to each other to determine the global optimum one. The result of the second step is summarized in Theorem 3.

Theorem 3. The global minimizer $k_1^\star$ and $a^\star$ of the mixed nonlinear–integer program (4.27) are

$$k_1^\star = \begin{cases} 1 & \text{if } \bar{k}_1 = 1 \\ \bar{k}_1 & \text{if } \bar{k}_1 > 1 \;\&\; \mu < 0 \\ \bar{k}_1 - 1 & \text{if } \bar{k}_1 > 1 \;\&\; \mu \geq 0 \end{cases}; \; a^\star = \frac{x_r}{k_1^\star T \max\Delta(k_1^\star)},$$

in which $\mu = T + \max\Delta(\bar{k}_1) - \max\Delta(\bar{k}_1 - 1)$. The pivotal index is $\bar{k}_1 = 1$ if $\max\Delta(1) \neq x_r/(Ta_{\max})$. Otherwise, namely $\max\Delta(1) = x_r/(Ta_{\max})$, $\bar{k}_1$ is given by

$$\bar{k}_1 = \max\left\{k_1 \in \mathbb{N}^+ : \max\Delta(k_1) = \frac{x_r}{k_1 T a_{\max}}\right\} + 1.$$

Moreover, the global minimum cost function is

$$t_f^\star(k_1^\star) = k_1^\star T + \max\Delta(k_1^\star).$$

Proof. Based on the condition of the pivotal index $\bar{k}_1$, the proof is divided into two cases: $\max\Delta(1) \neq x_r/(Ta_{\max})$ and $\max\Delta(1) = x_r/(Ta_{\max})$ as follows.

A. Case 1: $\max \Delta(1) \neq x_r/(Ta_{\max})$

Since $\max \Delta(1) \neq x_r/(Ta_{\max})$, it is true that either $\max \Delta(1) = T$ or $\max \Delta(1) = x_r/v_{\max}$. In the case $\max \Delta(1) = T$, it holds that $T \geq x_r/v_{\max}$ and $T \geq x_r/(Ta_{\max})$. Therefore, $x_r/v_{\max} \leq T < 2T < \ldots$ and $\ldots < x_r/(2Ta_{\max}) < x_r/(Ta_{\max}) \leq T < 2T < \ldots$, and thus $\max \Delta(k_1) = k_1 T$, which by Lemma 1 results in

$$t_f^{\dagger}(k_1) = k_1 T + \max \Delta(k_1) = k_1 T + k_1 T = 2k_1 T. \tag{4.30}$$

From (4.30), since $k_1 \in \mathbb{N}^+$, $t_f^{\dagger}(k_1 = 1) < t_f^{\dagger}(k_1 = 2) < t_f^{\dagger}(k_1 = 3) < \ldots$. Consequently, $k_1^{\star} = 1$.

For the remaining case, namely $\max \Delta(1) = x_r/v_{\max}$, the result $x_r/v_{\max} \geq x_r/(Ta_{\max})$ holds. As a consequence, $x_r/v_{\max} \geq x_r/(Ta_{\max}) > x_r/(2Ta_{\max}) > \ldots$. Therefore, $\max \Delta(k_1) = \max\{k_1 T,\, x_r/v_{\max}\}$ can be obtained. From that, for every $n \in \mathbb{N}^+$

$$\begin{aligned} &t_f^{\dagger}(k_1 = 1 + n) - t_f^{\dagger}(k_1 = 1) \\ &= nT + \max\left\{(1+n)T, \frac{x_r}{v_{\max}}\right\} - \frac{x_r}{v_{\max}}. \end{aligned} \tag{4.31}$$

From (4.31), if $\max\{(1+n)T,\, x_r/v_{\max}\} = x_r/v_{\max}$, then $t_f^{\dagger}(k_1 = 1+n) - t_f^{\dagger}(k_1 = 1) = nT > 0$. Otherwise, $\max\{(1+n)T,\, x_r/v_{\max}\} = (1+n)T$, and the result $t_f^{\dagger}(k_1 = 1+n) - t_f^{\dagger}(k_1 = 1) = nT + (1+n)T - x_r/v_{\max}$ holds. But in this circumstance, $\max\{(1+n)T,\, x_r/v_{\max}\} = (1+n)T$, hence $(1+n)T \geq x_r/v_{\max}$; therefore, $t_f^{\dagger}(k_1 = 1+n) - t_f^{\dagger}(k_1 = 1) \geq nT > 0$. Consequently, it is concluded that when $\max \Delta(1) = x_r/v_{\max}$, the result $k_1^{\star} = 1$ is also true. Summarizing from the above arguments, $k_1^{\star} = 1$ whenever $\max \Delta(1) \neq x_r/(Ta_{\max})$.

B. Case 2: $\max \Delta(1) = x_r/(Ta_{\max})$

Flow of the proof for this case is briefly explained as follows. First, it will be proven that the local minimum transferring times $t_f^{\dagger}(k_1)$ (see Lemma 1) is a strictly decreasing sequence with respect to k_1 when $k_1 \leq \bar{k}_1 - 1$. Second, it will be shown that the sequence $t_f^{\dagger}(k_1)$ strictly increases for $\bar{k}_1 \leq k_1 < +\infty$. Finally, among $t_f^{\dagger}(k_1 = \bar{k}_1 - 1)$ and $t_f^{\dagger}(k_1 = \bar{k}_1)$, the smaller one is the global minimum.

Subcase 1: $k_1 \leq \bar{k}_1 - 1$ $(k_1 \in \mathbb{N}^+)$

By definition (see Theorem 3)

$$\bar{k}_1 - 1 = \max\left\{k_1 \in \mathbb{N}^+ : \max \Delta(k_1) = \frac{x_r}{k_1 T a_{\max}}\right\}. \tag{4.32}$$

From (4.32), it can be seen that $\bar{k}_1 \geq 2$. Moreover, $\max \Delta(\bar{k}_1 - 1) = x_r / \left((\bar{k}_1 - 1) T a_{\max}\right)$. From this, it can be obtained that

$$\frac{x_r}{\left(\bar{k}_1 - 1\right) T a_{\max}} \geq \frac{x_r}{v_{\max}} \tag{4.33}$$

$$\frac{x_r}{\left(\bar{k}_1 - 1\right) T a_{\max}} \geq \left(\bar{k}_1 - 1\right) T. \tag{4.34}$$

The inequality (4.33) results in $x_r/(Ta_{\max}) > x_r/(2Ta_{\max}) > \ldots > x_r/\left((\bar{k}_1 - 1)Ta_{\max}\right) \geq x_r/v_{\max}$. Furthermore, (4.34) gives $x_r/(Ta_{\max}) > x_r/(2Ta_{\max}) > \ldots > x_r/\left((\bar{k}_1 - 1)Ta_{\max}\right) \geq (\bar{k}_1 - 1)T > (\bar{k}_1 - 2)T > \ldots > 2T > T$. Therefore, $\max \Delta(k_1) = x_r/(k_1 T a_{\max})$. Since $k_1 = 0$ is not a legitimate index, $t_f^\dagger(k_1 = 0) = +\infty$ is defined for the sake of convenience. Therefore, $t_f^\dagger(k_1) - t_f^\dagger(k_1 - 1)\Big|_{k_1=1} < 0$. In the case that $k_1 \geq 2$, by using Lemma 1, it yields

$$\begin{aligned} &t_f^\dagger(k_1) - t_f^\dagger(k_1 - 1) = \\ &k_1 T + \frac{x_r}{k_1 T a_{\max}} - (k_1 - 1)T - \frac{x_r}{(k_1 - 1)T a_{\max}}. \end{aligned} \tag{4.35}$$

The result of (4.35) can be simplified to

$$t_f^\dagger(k_1) - t_f^\dagger(k_1 - 1) = T - \frac{x_r}{k_1(k_1 - 1)T a_{\max}}. \tag{4.36}$$

Since $\max \Delta(k_1) = x_r/(k_1 T a_{\max})$, $\forall k_1 \leq \bar{k}_1 - 1$, it holds that $x_r/(k_1 T a_{\max}) \geq k_1 T$; therefore, $x_r/(k_1 T a_{\max}) > (k_1 - 1)T$, so $T < x_r/\left(k_1(k_1 - 1)T a_{\max}\right)$. Hence, (4.36) results in $t_f^\dagger(k_1) - t_f^\dagger(k_1 - 1) < 0$. In summary

$$t_f^\dagger(k_1) < t_f^\dagger(k_1 - 1),\ \forall k_1 \leq \bar{k}_1 - 1\ \left(k_1 \in \mathbb{N}^+\right). \tag{4.37}$$

The result in (4.37) implies that the sequence $t_f^\dagger(k_1)$ of local minimum transferring times strictly decreases when $k_1 \leq \bar{k}_1 - 1$.

Subcase 2: $\bar{k}_1 \leq k_1 < +\infty\,(k_1 \in \mathbb{N}^+)$

From the definition of $\bar{k}_1$ (see (4.32)), it is true that $\max \Delta(\bar{k}_1) \neq x_r/(\bar{k}_1 T a_{\max})$, namely $\max \Delta(\bar{k}_1) = \max\left\{\bar{k}_1 T,\ x_r/v_{\max}\right\}$. From this, we have

$$\frac{x_r}{\bar{k}_1 T a_{\max}} \leq \bar{k}_1 T \text{ and } \frac{x_r}{\bar{k}_1 T a_{\max}} \leq \frac{x_r}{v_{\max}}. \tag{4.38}$$

From (4.38), the following results are obtained:

$$\ldots < \frac{x_r}{(\bar{k}_1+1)Ta_{\max}} < \frac{x_r}{\bar{k}_1 Ta_{\max}} \leq \bar{k}_1 T < (\bar{k}_1+1)T < \ldots \tag{4.39}$$

$$\ldots < \frac{x_r}{(\bar{k}_1+1)Ta_{\max}} < \frac{x_r}{\bar{k}_1 Ta_{\max}} \leq \frac{x_r}{v_{\max}}. \tag{4.40}$$

It can be immediately seen from (4.39) and (4.40) that

$$\max \Delta(k_1) = \max \left\{ k_1 T,\ \frac{x_r}{v_{\max}} \right\},\ \forall k_1 \geq \bar{k}_1. \tag{4.41}$$

Therefore, $\forall k_1 \geq \bar{k}_1\ (k_1 \in \mathbb{N}^+)$, by using Lemma 1

$$\begin{aligned} &t_f^\dagger(k_1+1) - t_f^\dagger(k_1) = T \\ &+ \max \left\{ (k_1+1)T,\ \frac{x_r}{v_{\max}} \right\} - \max \left\{ k_1 T,\ \frac{x_r}{v_{\max}} \right\}. \end{aligned} \tag{4.42}$$

From (4.42), two possibilities can be classified: $\max\{k_1 T,\ x_r/v_{\max}\} = k_1 T$ and $\max\{k_1 T,\ x_r/v_{\max}\} = x_r/v_{\max}$. For the first possibility, that is to say, $\max\{k_1 T,\ x_r/v_{\max}\} = k_1 T$, the inequality $x_r/v_{\max} \leq k_1 T < (k_1+1)T$ holds, and thus $\max\{(k_1+1)T,\ x_r/v_{\max}\} = (k_1+1)T$. Therefore, (4.42) becomes

$$t_f^\dagger(k_1+1) - t_f^\dagger(k_1) = T + (k_1+1)T - k_1 T = 2T > 0. \tag{4.43}$$

For the second possibility, that $\max\{k_1 T,\ x_r/v_{\max}\} = x_r/v_{\max}$, (4.42) can be simplified to

$$\begin{aligned} &t_f^\dagger(k_1+1) - t_f^\dagger(k_1) = \\ &T + \max \left\{ (k_1+1)T,\ \frac{x_r}{v_{\max}} \right\} - \frac{x_r}{v_{\max}}. \end{aligned} \tag{4.44}$$

From (4.44), it is not difficult to show that

$$t_f^\dagger(k_1+1) - t_f^\dagger(k_1) \geq T > 0. \tag{4.45}$$

From (4.43) and (4.45), the conclusion is

$$t_f^\dagger(k_1+1) > t_f^\dagger(k_1),\ \forall k_1 \geq \bar{k}_1\ \left(k_1 \in \mathbb{N}^+\right). \tag{4.46}$$

The result of (4.46) implies that the local minimum transferring times $t_f^\dagger(k_1)$ is a strictly increasing sequence with respect to k_1 when $\bar{k}_1 \leq k_1 < +\infty$.

Summarizing the results in (4.37) and (4.46) gives

$$\begin{cases} t_f^\dagger(k_1) < t_f^\dagger(k_1-1), & \forall k_1 \le \bar{k}_1 - 1 \\ t_f^\dagger(k_1) < t_f^\dagger(k_1+1), & \forall k_1 \ge \bar{k}_1 \end{cases}, \; k_1 \in \mathbb{N}^+. \tag{4.47}$$

Therefore, the global optimal index of the mixed nonlinear–integer program (4.27) is the one among $\bar{k}_1 - 1$ and $\bar{k}_1$, which produces a smaller transferring time. Using the result of Lemma 1 results in

$$\begin{aligned} &t_f^\dagger(k_1 = \bar{k}_1) - t_f^\dagger(k_1 = \bar{k}_1 - 1) = \\ &T + \max \Delta(\bar{k}_1) - \max \Delta(\bar{k}_1 - 1). \end{aligned} \tag{4.48}$$

By utilizing the definition of μ in Theorem 3 and (4.48), the conclusion is that when $\mu \ge 0$, namely $t_f^\dagger(k_1 = \bar{k}_1) \ge t_f^\dagger(k_1 = \bar{k}_1 - 1)$, the global optimal index of (4.27) is $k_1^\star = \bar{k}_1 - 1$. Otherwise, namely $\mu < 0$, the result $k_1^\star = \bar{k}_1$ holds. This completes the proof. □

The computation of the global optimal solution (for Case I) based on Theorem 3 should begin from the determination of the pivotal index $\bar{k}_1$, and then μ can be computed. From $\bar{k}_1$ and μ, the global optimum index $k_1^\star$ can be determined. Finally, the optimal acceleration $a^\star$ and the minimum transferring time $t_f^\star\,(k_1^\star)$ can be calculated. The optimal values of t_1 and t_2 are computed by $t_1^\star = k_1^\star T$ and $t_2^\star = t_f^\star - 2t_1^\star$ respectively. Now the global minimum-time solution of SC–VSE in Case I has been established. Next, Case II ($t_1 + t_2 = k_2 T,\; k_2 \in \mathbb{N}^+$) will be investigated.

Remark 13. In the first step of solving the mixed nonlinear–integer program (4.27), it was chosen to find the local minimum for each $k_1 \in \mathbb{N}^+$ rather than for each a. If the latter strategy is employed, the optimization problem needing to be solved in the second step becomes much more complex. Therefore, fixing k_1 first is the more reasonable approach.

4.3.3 Case II of SC–VSE: $t_1 + t_2 = k_2 T,\; k_2 \in \mathbb{N}^+$

In order to draw a distinction with Case I, in Case II, the unknown parameters a, t_1, t_2, and t_f are denoted as $\tilde{a}$, $\tilde{t}_1$, $\tilde{t}_2$, and $\tilde{t}_f$ respectively. Similar to Case I, by gathering all essential trajectory, actuator limits, and vibration-free transportation constraints and taking the total transferring time as

the cost function, the following discrete nonlinear program can be established:

$$\begin{aligned} \min_{\tilde{a},\tilde{t}_1,\tilde{t}_2} \quad & \tilde{t}_f = 2\tilde{t}_1 + \tilde{t}_2 \\ \text{s.t.} \quad & \tilde{a}\tilde{t}_1\left(\tilde{t}_1 + \tilde{t}_2\right) = x_r \\ & \tilde{t}_1 + \tilde{t}_2 = k_2 T \,(k_2 \in \mathbb{N}^+),\ \tilde{t}_1 > 0,\ \tilde{t}_2 \geq 0 \\ & 0 < \tilde{a} \leq a_{\max},\ \tilde{a}\tilde{t}_1 \leq v_{\max}. \end{aligned} \tag{4.49}$$

By using the equality constraints, the two variables $\tilde{t}_1$ and $\tilde{t}_2$ can be eliminated, and thus (4.49) can be transformed into the following mixed nonlinear–integer program:

$$\begin{aligned} \min_{\tilde{a},k_2} \quad & \tilde{t}_f = k_2 T + \frac{x_r}{\tilde{a}k_2 T} \\ \text{s.t.} \quad & k_2 \geq \frac{x_r}{T v_{\max}},\ k_2 \geq \frac{1}{T}\sqrt{\frac{x_r}{a_{\max}}},\ k_2 \in \mathbb{N}^+ \\ & \frac{x_r}{(k_2 T)^2} \leq \tilde{a} \leq a_{\max}. \end{aligned} \tag{4.50}$$

By conducting an analogous procedure to Case I, the solution of the optimization problem (4.50) is stated in Theorem 4. To begin, a new set $\beta(k_2)$ is denoted as follows:

$$\beta(k_2) = \left\{ k_2,\ \frac{x_r}{T v_{\max}},\ \frac{1}{T}\sqrt{\frac{x_r}{a_{\max}}} \right\}. \tag{4.51}$$

Theorem 4. The global optimal solution of the mixed nonlinear–integer program (4.50) is

$$\begin{aligned} k_2^\star &= \min\left\{ k_2 \in \mathbb{N}^+ : \max \beta(k_2) = k_2 \right\} \\ \tilde{a}^\star &= a_{\max}. \end{aligned}$$

Moreover, the global minimum cost function is given by

$$\tilde{t}_f^\star(k_2^\star) = k_2^\star T + \frac{x_r}{k_2^\star T a_{\max}}.$$

Proof. The first step of the proof is to find the local optimal solutions of (4.50) for each $k_2 \in \mathbb{N}^+$ satisfying $k_2 \geq \max\left\{ x_r/(Tv_{\max}),\ (1/T)\sqrt{x_r/a_{\max}}) \right\}$ The second step compares all the local minima provided by the first step (which are infinite in number) to justify the global optimum.

In the first step, for a fixed $k_2 \in \mathbb{N}^+$ satisfying $k_2 \geq \max\left\{ x_r/(Tv_{\max}),\ (1/T)\sqrt{x_r/a_{\max}} \right\}$, by introducing a new variable $\tilde{z} = x_r/(\tilde{a}k_2 T)$, (4.50) can be transformed into the following simple linear

optimization problem:

$$\begin{aligned} \min_{\tilde{z}\in\mathbb{R}^+} \quad & \tilde{t}_f = k_2 T + \tilde{z} \\ \text{s.t.} \quad & \frac{x_r}{k_2 T a_{\max}} \leq \tilde{z} \leq k_2 T. \end{aligned} \tag{4.52}$$

It is easy to show that the minimizer $\tilde{z}^\dagger$ and the minimum cost function $\tilde{t}_f^\dagger$ of (4.52) are $\tilde{z}^\dagger(k_2) = x_r/(k_2 T a_{\max})$ and $\tilde{t}_f^\dagger(k_2) = k_2 T + \tilde{z}^\dagger(k_2)$. Using the relation $\tilde{z} = x_r/(\tilde{a} k_2 T)$ results in $\tilde{a}^\dagger(k_2) = a_{\max}$ and $\tilde{t}_f^\dagger = k_2 T + x_r/(k_2 T a_{\max})$.

Now, the second step can be proceeded by solving the following optimization problem:

$$\begin{aligned} \min_{k_2\in\mathbb{N}^+} \quad & \tilde{t}_f^\dagger(k_2) = k_2 T + \frac{x_r}{k_2 T a_{\max}} \\ \text{s.t.} \quad & k_2 \geq \max\left\{ \frac{x_r}{T v_{\max}},\ \frac{1}{T}\sqrt{\frac{x_r}{a_{\max}}} \right\}. \end{aligned} \tag{4.53}$$

Considering a function $\tilde{t}_f^\dagger(y)$ where $y \in \mathbb{R}^+$, $y \geq \max\left\{ x_r/(T v_{\max}),\ (1/T)\sqrt{x_r/a_{\max}} \right\}$. Taking the first derivative of $\tilde{t}_f^\dagger(y)$ with respect to y results in

$$\frac{d\tilde{t}_f^\dagger(y)}{dy} = T - \frac{x_r}{y^2 T a_{\max}}. \tag{4.54}$$

However, the feasible region of y gives $y \geq (1/T)\sqrt{x_r/a_{\max}}$, and thus $T \geq x_r/\left(y^2 T a_{\max}\right)$. By applying this result on (4.54), $d\tilde{t}_f^\dagger(y)/dy \geq 0$ can be obtained, which means that the function $\tilde{t}_f^\dagger(y)$ monotonically increases with respect to y. By performing the substitution $y = k_2$, it can also be concluded that the function $\tilde{t}_f^\dagger(k_2)$ monotonically increases with respect to k_2. Therefore, the global optimal index $k_2^\star$ of (4.53) is the minimum integer satisfying $k_2^\star \geq \max\left\{ x_r/(T v_{\max}),\ (1/T)\sqrt{x_r/a_{\max}} \right\}$. In the set notation, the above result is equivalent to $k_2^\star = \min\{k_2 \in \mathbb{N}^+ : \max \beta(k_2) = k_2\}$. The proof is therefore completed. □

By using the result of Theorem 4, the global optimal solution of SC–VSE in Case II can be computed. The optimum values of $\tilde{t}_1$ and $\tilde{t}_2$ are determined by $\tilde{t}_1^\star = \tilde{t}_f^\star - k_2^\star T$ and $\tilde{t}_2^\star = 2k_2^\star T - \tilde{t}_f^\star$ respectively.

4.3.4 Comparison between Case I and Case II

Although Case I ($t_1 = k_1 T$) and Case II ($t_1 + t_2 = k_2 T$) will both result in a vibration-free transferring process, they exhibit some fundamentally distinct properties, which will be clarified in the following

discussion. In Case I, by substituting $t_1 = k_1 T$ ($k_1 \in \mathbb{N}^+$) into (4.16), it yields

$$\theta(t) = \dot{\theta}(t) = 0, \ \forall t \in [t_1, t_1 + t_2). \tag{4.55}$$

The condition of (4.55) implies that, in Case I, there is never any residual vibration during the uniform interval (i.e., $t_1 \leq t < t_1 + t_2$). In contrast, no similar property is present in Case II except when the resultant $\tilde{t}_f^\star$ is also a multiple of the natural period T.

The second different property between Case I and Case II can be revealed by letting $v_{\max} \to +\infty$ and $a_{\max} \to +\infty$, namely, when infinite maximum velocity and maximum acceleration are allowed. In such a context, for Case I, the following can be obtained:

$$\lim_{\lambda \to +\infty} \max \left\{ T, \ \frac{x_r}{T a_{\max}}, \ \frac{x_r}{v_{\max}} \right\} = T, \tag{4.56}$$

where λ is defined by $\lambda = \min\{v_{\max}, \ a_{\max}\}$. Therefore, $\lim_{\lambda \to +\infty} \max \Delta(1) = T$. Consequently, according to Theorem 3, $k_1^\star = 1$ as $\lambda \to +\infty$, and hence

$$\lim_{\lambda \to +\infty} t_f^\star(k_1^\star) = T + T = 2T. \tag{4.57}$$

Similarly, for Case II, it can be shown that $\lim_{\lambda \to +\infty} \max \beta(k_2) = k_2$. Therefore, $k_2^\star = 1$ as $\lambda \to +\infty$. As a result, based on Theorem 4

$$\lim_{\lambda \to +\infty} \tilde{t}_f^\star(k_2^\star) = T. \tag{4.58}$$

The results of (4.57) and (4.58) can be interpreted as follows: with infinite velocity and acceleration limits, the minimum transfer time for Case I is twice the natural period T, whereas it only requires one natural period for Case II. In other words, it is not possible to obtain a transfer time less than one natural period in the case of SC–VSE.

The vibration-free transportation using SC–VSE has two candidates: Case I and Case II. Therefore, in practice, the SC–VSE scheme will choose the one which produces a smaller optimal transferring time. For instance, as $v_{\max} \to +\infty$ and $a_{\max} \to +\infty$, it holds that $t_f^\star(\to 2T) > \tilde{t}_f^\star(\to T)$, and thus Case II should be selected. Note that, Singhose et al. [67] stated that the position S-curve (including both triangular and trapezoidal velocity profiles) must be *four* times longer than a command formed by shaping a step function with a ZV input shaper. The previous discussion showed that the above conclusion is not generally true, namely that it is only correct for Case I, but not for Case II. This can be explained as follows. When a step position command is employed as in [67], it automatically implies

TABLE 4.1: Configuration of testcases (TCs).

TC#	$v_{\max}$	$a_{\max}$	Rope length	Natural period
A1	0.25 m/s	0.05 m/s^2	$l = 1.4$ m	$T = 2.37$ s
A2	0.25 m/s	0.1 m/s^2	$l = 1$ m	$T = 2.01$ s
A3	0.5 m/s	0.5 m/s^2	$l = 1.4$ m	$T = 2.37$ s

TABLE 4.2: Computational results of the minimum-time SC–VSE.

TC#	Selection	$a^\star \vert \tilde{a}^\star$	$t_1^\star \vert \tilde{t}_1^\star$	$t_2^\star \vert \tilde{t}_2^\star$	$k_1^\star \vert k_2^\star$	$t_f^\star \vert \tilde{t}_f^\star$
A1	Case I	0.05 m/s^2	4.75 s	3.68 s	$k_1^\star = 2$	13.17 s
A2	Case II	0.1 m/s^2	2.49 s	5.53 s	$k_2^\star = 4$	10.52 s
A3	Case II	0.5 m/s^2	0.84 s	3.90 s	$k_2^\star = 2$	5.59 s

$x_r = 2$ m. Case I: Section 4.3.2, Case II: Section 4.3.3.

that infinite velocity and acceleration can be admitted. The shaping process between a step position command and the ZV input shaper therefore introduces a total transferring time of $T/2$. Under the same conditions, Case II of SC–VSE can be selected, namely that a vibration-free transportation can be guaranteed with a total time of T (see (4.58)), which is only *two* times longer. The shortcoming of [67] stems from the fact that Case II is not fully considered in the analysis/design. In order to clearly verify the above argument, the minimum-time SC–VSE is computed for the following configuration: $l = 1.4$ m ($T = 2.37$ s), $x_r = 1$ m, $v_{\max} = 5$ m/s, and $a_{\max} = 5$ m/s^2 (high maximum velocity and maximum acceleration are allowed). By applying the results from Section 4.3.2 and Section 4.3.3, Case II is finally selected. The optimal solution is $\tilde{t}_1^\star = 0.084$ s, $\tilde{t}_2^\star = 2.289$ s, $\tilde{a}^\star = 5$ m/s^2. The minimum transferring time of SC–VSE is $\tilde{t}_f^\star = 2.458$ s, which is only 2.071 times longer than $T/2$ (less than four times).

4.3.5 Simulation results of the minimum-time SC–VSE

In this section, simulation results of the minimum-time SC–VSE and comparisons with the related studies in [140] and [141] are given. In order to verify the established theoretical results, the simulation study is conducted under various conditions of the actuator limits, i.e., both maximum velocity $v_{\max}$ and maximum acceleration $a_{\max}$ will be varied. The transferring distance is 2 meters ($x_r = 2$ m). Moreover, necessary parameters for all testcases are shown in Table 4.1. The computations are conducted on a personal computer with 2.7-GHz Intel Core i5-4310M and 8 GB of RAM. Computational

results of the minimum-time SC–VSE are aggregated in Table 4.2. On average, it takes 0.013 second to compute the minimum-time SC–VSE for each testcase showing that online computation is feasible.

The simulation results of all testcases are illustrated in Figs. 4.5–4.7. It is recognized that the larger the actuator limits, the smaller the total transferring time would be (with an increment of the peak value of swing angle). In all testcases, the trolley precisely arrives at the desired destination with no vibration after the transfer. Moreover, the maximum velocity and maximum acceleration constraints are strictly complied with. Therefore, the effectiveness of the minimum-time SC–VSE scheme is confirmed.

The proposed minimum-time SC–VSE is now compared to the related studies [140, 141] in the same bang-off-bang acceleration profile family. Note that, to draw a fair comparison, the constraint of maximum allowable swing angle presented in [140] and [141] are relaxed (i.e., setting $\theta_{\text{ub}} = +\infty$ in [140] and $\theta_{\max} = +\infty$ in [141]). The comparative results are shown in Table 4.3 and Figs. 4.5–4.7. It can be seen that the proposed minimum-time SC–VSE provides considerably smaller transfer time than the existing studies. Specifically, it is 6.06 s and 1.95 s faster in testcase A1, 1.46 s and 1.49 s faster in testcase A2, and 0.78 s and 0.78 s faster in testcase A3, in comparison with [140] and [141] respectively. Thus, the proposed min-time SC–VSE showed its advantage in terms of transfer time.

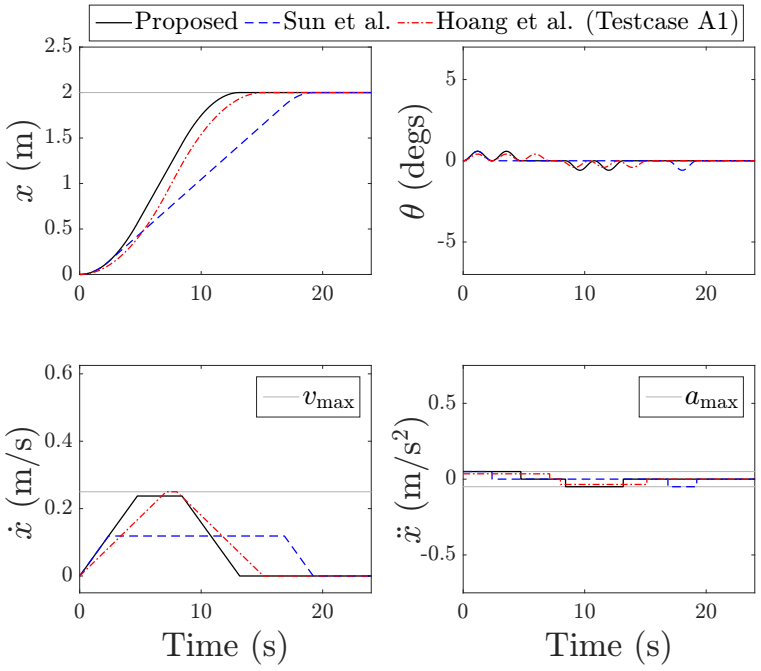

FIGURE 4.5: Simulation result of the minimum-time SC–VSE and its comparison with related studies (testcase A1).

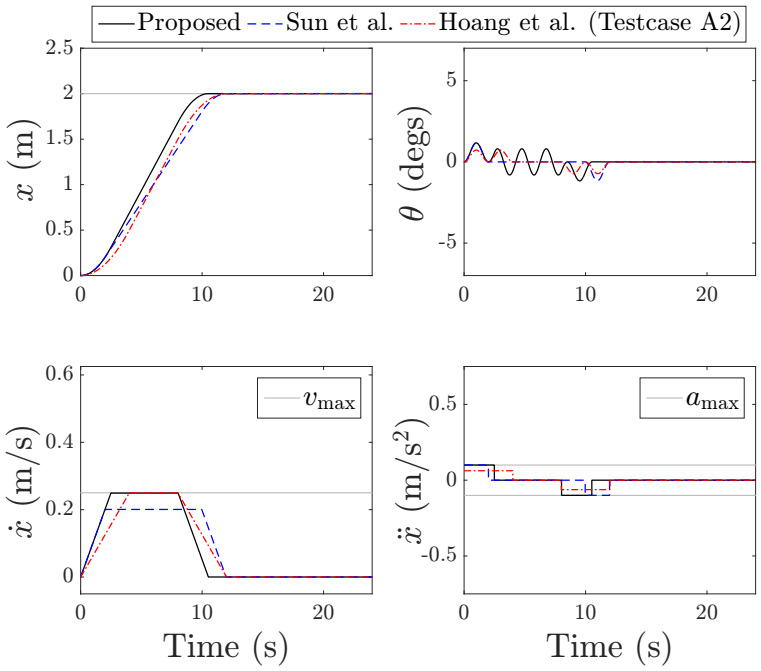

FIGURE 4.6: Simulation result of the minimum-time SC–VSE and its comparison with related studies (testcase A2).

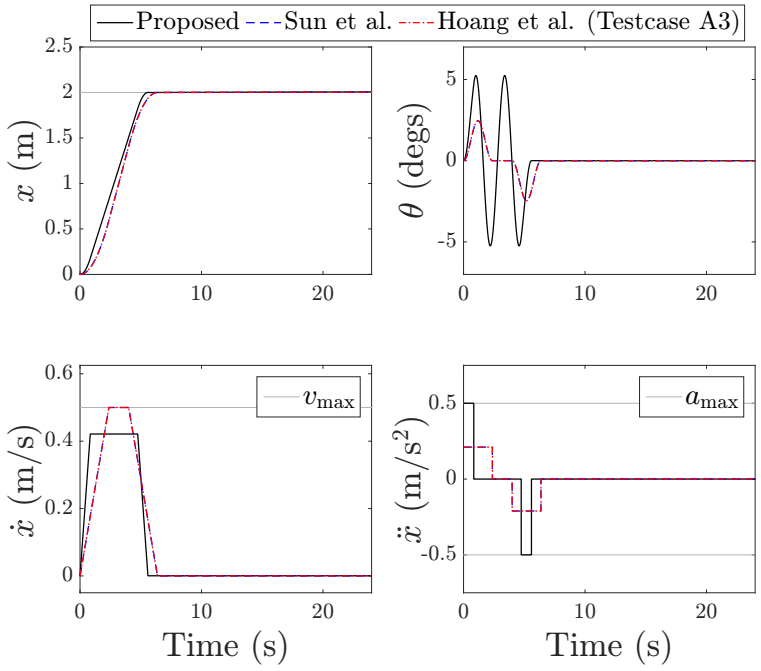

FIGURE 4.7: Simulation result of the minimum-time SC–VSE and its comparison with related studies (testcase A3).

TABLE 4.3: Comparison of the min-time SC–VSE with related studies.

TC#	Transferring time ($x_r = 2$ m)		
	Proposed	Sun et al. [140]	Hoang et al. [141]
A1	**13.17 s**	19.23 s	15.12 s
A2	**10.52 s**	11.98 s	12.01 s
A3	**5.59 s**	6.37 s	6.37 s

4.4 Design of the minimum-time SC–IS

4.4.1 Formulation

In the SC–IS scheme, to gain a vibration-free transportation, the baseline S-curve is modulated by convolving with the well-known ZV input shaper, which is given by [49]

$$I(t) = 0.5\left[\delta(t) + \delta\left(t - T/2\right)\right], \tag{4.59}$$

where $\delta(.)$ is the Dirac's delta generalized function. The position baseline S-curve is still generated by integrating twice the bang-off-bang acceleration profile $\bar{R}(t)$, which takes a similar form of (4.14), that is

$$\bar{R}(t) = \begin{cases} \bar{a}, & 0 \le t < \bar{t}_1 \\ 0, & \bar{t}_1 \le t < \bar{t}_1 + \bar{t}_2 \\ -\bar{a}, & \bar{t}_1 + \bar{t}_2 \le t \le \bar{t}_f \ (:= 2\bar{t}_1 + \bar{t}_2)\,. \end{cases} \tag{4.60}$$

The convolution product between (4.60) and the ZV input shaper will result in a shaped acceleration command, whose double integration is the SC–IS. As a matter of fact, the convolution process will possibly change the shape as well as the magnitude of the original command. Therefore, the present task is to design a baseline function in the form of (4.60), which ensures the resultant shaped command: 1) achieves a minimum transferring time and 2) respects the maximum allowable velocity and acceleration. This design task for the SC–IS scheme is not trivial.

If $\bar{Q}(t)$ is denoted as the shaped acceleration function in time domain, it can be computed by

$$\bar{Q}(t) = \bar{R}(t) * I(t), \tag{4.61}$$

TABLE 4.4: All possibilities of the shaped command $\bar{Q}(t)$ and optimization configurations of the minimum-time SC–IS.

P#	$\bar{Q}(t)$	Optimization Configuration				
		Condition	Acc. Constraint	Vel. Constraint	Equality Constraint	Cost Function
P1	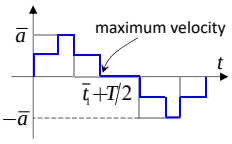	$\bar{t}_1 \geq T/2$ $\bar{t}_2 \geq T/2$	$0 < \bar{a} \leq a_{\max}$	$\bar{a}\bar{t}_1 \leq v_{\max}$		
P2	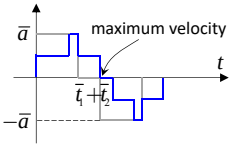	$\bar{t}_1 \geq T/2$ $0 \leq \bar{t}_2 \leq T/2$	$0 < \bar{a} \leq a_{\max}$	$\frac{\bar{a}}{2}\left(2\bar{t}_1 + \bar{t}_2 - \frac{T}{2}\right) \leq v_{\max}$		
P3	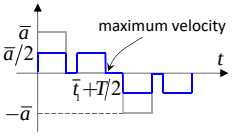	$0 < \bar{t}_1 \leq T/2$ $\bar{t}_1 + \bar{t}_2 \geq T/2$ $\bar{t}_2 \geq T/2$	$0 < \bar{a} \leq 2a_{\max}$	$\bar{a}\bar{t}_1 \leq v_{\max}$	$\bar{a}\bar{t}_1\,(\bar{t}_1 + \bar{t}_2) = x_r$	$\bar{J} = 2\bar{t}_1 + \bar{t}_2 + \frac{T}{2}$
P4	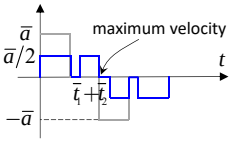	$0 < \bar{t}_1 \leq T/2$ $\bar{t}_1 + \bar{t}_2 \geq T/2$ $0 \leq \bar{t}_2 \leq T/2$	$0 < \bar{a} \leq 2a_{\max}$	$\frac{\bar{a}}{2}\left(2\bar{t}_1 + \bar{t}_2 - \frac{T}{2}\right) \leq v_{\max}$		
P5	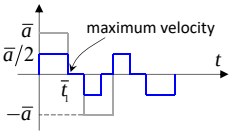	$0 < \bar{t}_1 \leq T/2$ $\bar{t}_1 + \bar{t}_2 \leq T/2$ $2\bar{t}_1 + \bar{t}_2 \geq T/2$	$0 < \bar{a} \leq 2a_{\max}$	$\bar{a}\bar{t}_1 \leq 2v_{\max}$		
P6	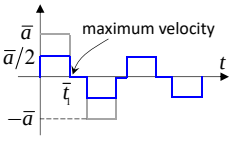	$0 < \bar{t}_1 \leq T/2$ $\bar{t}_1 + \bar{t}_2 \leq T/2$ $2\bar{t}_1 + \bar{t}_2 \leq T/2$	$0 < \bar{a} \leq 2a_{\max}$	$\bar{a}\bar{t}_1 \leq 2v_{\max}$		

Light gray line: unshaped/baseline command $\bar{R}(t)$ (in (4.60)). Bold blue line: shaped command $\bar{Q}(t)$ (in (4.64)).

where $I(t)$ and $\bar{R}(t)$ are given in (4.59) and (4.60) respectively. The operator $*$ denotes the convolution between two signals. In the case of SC–IS scheme, the actual acceleration input feeding to the crane system in (4.11) is $\ddot{\bar{x}}(t) = \bar{Q}(t)$, where $\ddot{x}(t)$ is replaced by $\ddot{\bar{x}}(t)$ to draw a distinction with the SC–VSE technique. To compute $\bar{Q}(t)$ in an explicit form, the Laplace transformation method is employed. The

Laplace transform of the baseline function $\bar{R}(t)$ and the input shaper $I(t)$ can be found as

$$\bar{R}(s) = \frac{-\bar{a}}{s}\left(e^{-s\bar{t}_1} + e^{-s(\bar{t}_1+\bar{t}_2)} - e^{-s(2\bar{t}_1+\bar{t}_2)} - 1\right) \tag{4.62}$$

$$I(s) = 0.5\left(1 + e^{-\frac{T}{2}s}\right). \tag{4.63}$$

Performing the Laplace transform on both sides of (4.61) yields $\bar{Q}(s) = \bar{R}(s)I(s)$. By taking the inverse Laplace transform, $\bar{Q}(t)$ can be calculated by

$$\begin{aligned}\bar{Q}(t) = \frac{\bar{a}}{2}\,[&-H(t-\bar{t}_1) - H(t-\bar{t}_1-\bar{t}_2) - H(t-\bar{t}_1-T/2)\\ &- H(t-\bar{t}_1-\bar{t}_2-T/2) + H(t-2\bar{t}_1-\bar{t}_2)\\ &+H(t-T/2) + H(t-2\bar{t}_1-\bar{t}_2-T/2) + 1]\,,\end{aligned} \tag{4.64}$$

where $H(.)$ is the Heaviside function. According to (4.64) and the anti-symmetrical property of $\bar{Q}(t)$ along the vertical line $t = 0.5\,(\bar{t}_f + T/2)$, all possibilities of $\bar{Q}(t)$ are listed in Table 4.4.

The classification of shaped families P1–P6 in Table 4.4 depends entirely on how large $\bar{t}_1$ and $\bar{t}_2$ of the unshaped command $\bar{R}(t)$ compare with $T/2$ (half of the natural period). For instance, in the case of P1 ($\bar{t}_1 \geq T/2$ and $\bar{t}_2 \geq T/2$), the shaped command $\bar{Q}(t)$ (bold blue line) reserves the maximum magnitude $\bar{a}$ of the baseline function $\bar{R}(t)$ (light gray line). Moreover, the shaped velocity—obtained by integrating $\bar{Q}(t)$—reaches its maximum value $\bar{a}\bar{t}_1$ at $t = \bar{t}_1 + T/2$. On the other hand, in the P4 family, the maximum value of $\bar{Q}(t)$ is reduced to half compared with the original command; the peak of the shaped velocity attains at $t = \bar{t}_1 + \bar{t}_2$ with a magnitude of $0.5\bar{a}(2\bar{t}_1 + \bar{t}_2 - T/2)$. Such a classification is needed because essential inequality constraints generated from the actuator limits $v_{\max}$ and $a_{\max}$ are different for each family of shapes.

For every family P1–P6, by letting the total transferring time of the shaped command as the cost function and collecting all necessary equality and inequality constraints (shown in Table 4.4), an optimization problem can be established to solve for unknowns $\bar{a}$, $\bar{t}_1$, and $\bar{t}_2$. Six nonlinear programs are formulated, and then sequentially solved by the *fmincon* routine of MATLAB. In fact, the optimal solutions of these nonlinear programs can also be analytically obtained by invoking the Karush-Kuhn-Tucker (KKT) optimality condition. However, the present problem has a considerably large number of families, and thus a numerical method is preferable. Finally, the (feasible) optimal solution of the family which produces the smallest transferring time will be chosen as the eventual answer for the minimum-time SC–IS scheme.

TABLE 4.5: Comparative results of the minimum-time SC–IS and the minimum-time SC–VSE.

TC#	Minimum-time SC–IS ($x_r = 1$ m)					Minimum-time SC–VSE ($x_r = 1$ m)					
	Selected family	$\bar{a}^\star$	$\bar{t}_1^\star$	$\bar{t}_2^\star$	$\bar{J}^\star$	Selection	$a^\star \vert \tilde{a}^\star$	$t_1^\star \vert \tilde{t}_1^\star$	$t_2^\star \vert \tilde{t}_2^\star$	$k_1^\star \vert k_2^\star$	$t_f^\star \vert \tilde{t}_f^\star$
A1	P2	0.05 m/s^2	4.47 s	0 s	10.13 s	Case II	0.05 m/s^2	4.21 s	0.53 s	$k_2^\star = 2$	**8.96 s**
A2	P3	0.2 m/s^2	1.00 s	3.98 s	6.99 s	Case II	0.1 m/s^2	2.49 s	1.52 s	$k_2^\star = 2$	**6.50 s**
A3	P5	1 m/s^2	1.00 s	0 s	**3.19 s**	Case II	0.5 m/s^2	0.84 s	1.53 s	$k_2^\star = 1$	3.22 s

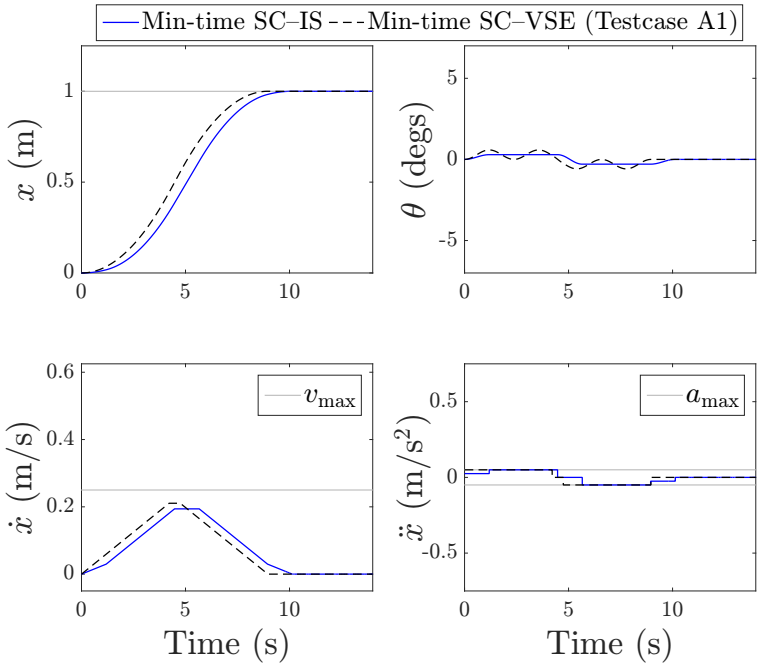

FIGURE 4.8: Simulation result of the minimum-time SC–IS and its comparison with the minimum-time SC–VSE in testcase A1.

4.4.2 Simulation results of the minimum-time SC–IS

In an analogous manner to the SC–VSE scheme, simulation studies of the minimum-time SC–IS are conducted in three testcases with different values of $v_{\max}$ and $a_{\max}$ as shown in Table 4.1. In addition, to facilitate the subsequent experiments in Section 4.5, where the running length of the trolley is limited, the transferring distance is changed to 1 meter (i.e., $x_r = 1$ m). Computational results of the minimum-time SC–IS are summarized in Table 4.5, where $\bar{(.)}^\star$ denotes the resultant optimal value of $\bar{(.)}$. On average, the computational time for each testcase is 0.26 second. Therefore, similar to the minimum-time SC–VSE, the minimum-time SC–IS can also be computed online.

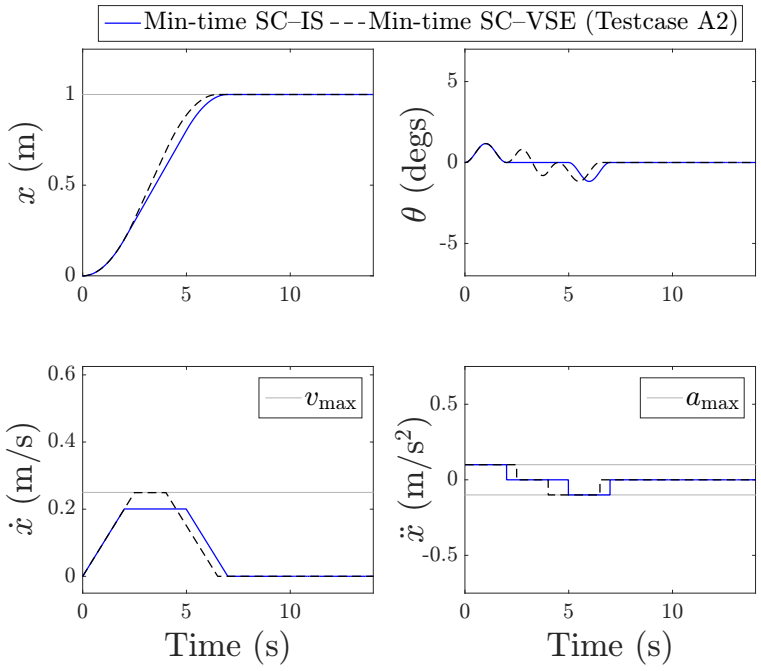

FIGURE 4.9: Simulation result of the minimum-time SC–IS and its comparison with the minimum-time SC–VSE in testcase A2.

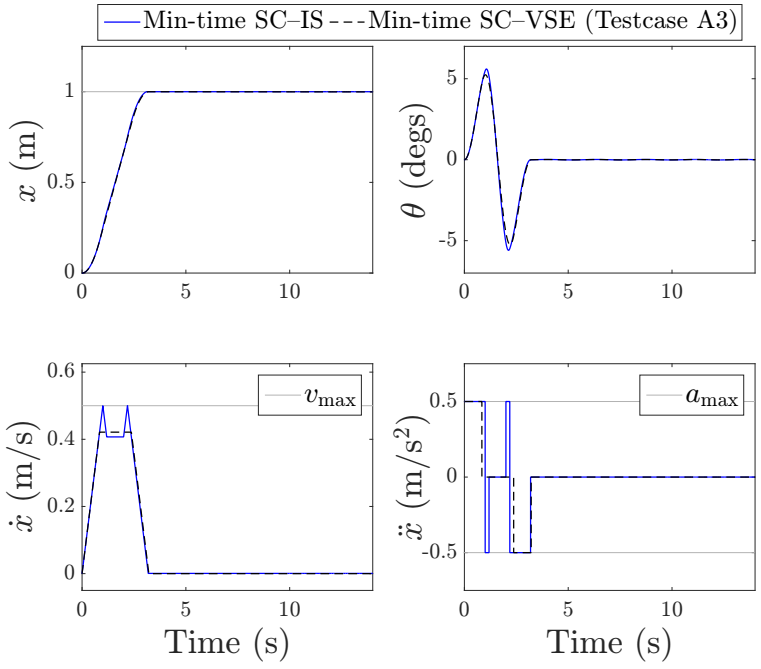

FIGURE 4.10: Simulation result of the minimum-time SC–IS and its comparison with the minimum-time SC–VSE in testcase A3.

Simulation results of the minimum-time SC–IS are depicted in Figs. 4.8–4.10 for all testcases. Like the SC–VSE case, the total transfer time for the SC–IS scheme decreases when the values of $v_{\max}$ and $a_{\max}$ increase. The vibration is suppressed at the end of the transportation. All of the actuator limits are strictly adhered to. Hence, the effectiveness of the minimum-time SC–IS is verified.

4.4.3 A brief comparison between SC–IS and SC–VSE

At the first glance, the SC–IS scheme seems to be a generalization of the SC–VSE. However, it is not true. As a counterexample, no shape family (in Table 4.4) of the SC–IS can produce the SC–VSE in the following configuration: $t_1 + t_2 = 2T$ (Case II), $v_{\max} = 0.5$ m/s, $a_{\max} = 0.05$ m/s^2, $l = 1.4$ m, and $x_r = 1$ m. Thus, the SC–IS does not encompass the SC–VSE in general, namely that they are complementary in relation.

Testcases A1–A2 and testcase A3, respectively, are the instances when the minimum-time SC–VSE results in a faster and longer transferring time compared to the minimum-time SC–IS (see Table 4.5 and Figs. 4.8–4.10). Therefore, in practice, among SC–VSE and SC–IS, it is rational to pick the one which provides a faster transferring time. This is the ultimate choice presented in this chapter. Considering the case that infinite actuator limits are permitted ($v_{\max} \to +\infty$ and $a_{\max} \to +\infty$), it is easy to see that the position baseline S-curve command of the SC–IS scheme comes close to a step function to realize the minimum-time solution. In such a circumstance, the minimum transferring time of the SC–IS scheme approaches $T/2$, where the delay $T/2$ is caused by the ZV input shaper. Therefore, the SC–IS is twice as fast as the SC–VSE when infinite actuator limits are allowed. Thus, the SC–IS will be ultimately chosen.

Remark 14. Since both SC–VSE and SC–IS schemes only utilize the rope length l in their design process, the robustness to parametric uncertainties is not an issue. This can be explained by the fact that the rope length can be easily measured in practice.

Remark 15. The linearized model of a three-dimensional overhead crane system can be decoupled into two independent linear subsystems in x and y directions [143]. Each of them is identical to the model (3), which is used in the designs of the minimum-time ZV S-curve commands. Therefore, the proposed schemes (SC–VSE and SC–IS) can be straightforwardly applied on a three-dimensional overhead crane system.

Remark 16. The simplicity of S-curve commands is not a drawback, but it is actually an advantage when it comes to industrial applications. The reason is that S-curve commands are ubiquitous, and

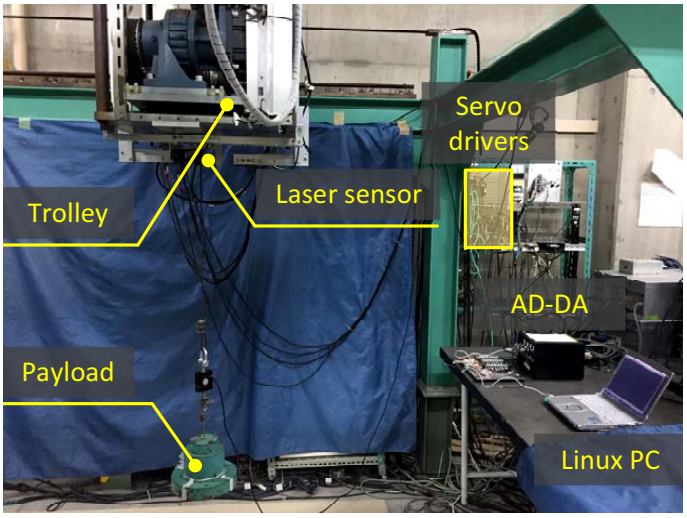

FIGURE 4.11: Structure of the experimental overhead crane system.

they can easily be executed by any industrial servo drives. Moreover, their effectiveness in suppressing the residual vibration has been shown to be satisfactory. Note also that although simplicity is the nature of S-curve commands, obtaining the time-optimal solutions in the presence of actuator constraints is not an easy task (as shown in the theoretical results of Sections 4.3–4.4).

4.5 Experimental results

The proposed motion planning schemes are now implemented on a real overhead crane system, which is illustrated in Fig. 4.11. The actuator is a YASKAWA USAFED-09C2L1K AC servo motor operating in position control mode. MATLAB/Simulink is utilized to compose the program and build the executing file via Real Time Workshop. A Linux PC operates the executing file in real time with a sampling period of 10 ms through Real Time Application Interface (RTAI). Moreover, a pair of laser sensors KEYENCE VG-035 is used to measure the swing angle. Note that, the planned acceleration profile of the minimum-time SC–VSE (or SC–IS) is integrated twice to obtain a reference in the position level. The result is the actual feedforward command feeding to the servo driver to drive the trolley motion via a built-in motor's position controller provided by the motor manufacturer.

Three testcases A1–A3 (see Table 4.1) are employed to compute the minimum-time SC–VSE and the minimum-time SC–IS. Following the discussion in Section 4.4.3, among SC–VSE and SC–IS, the one which produces a smaller transferring time will be chosen. Hence, based on the computational results in Table 4.5, the minimum-time SC–VSE is chosen for testcases A1 and A2, and the minimum-time SC–IS is selected for testcase A3.

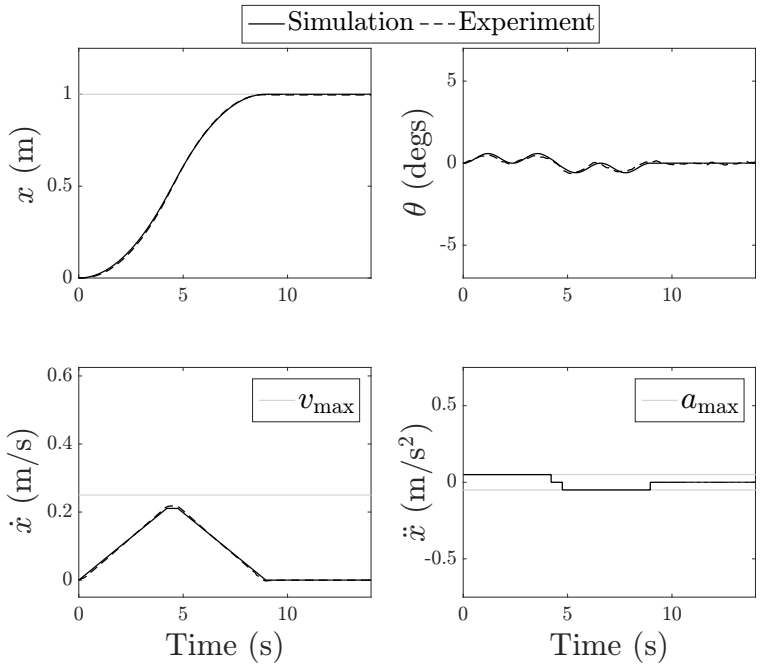

FIGURE 4.12: Experimental result in testcase A1 (the minimum-time SC–VSE is chosen). Simulation and experimental results are in a complete agreement.

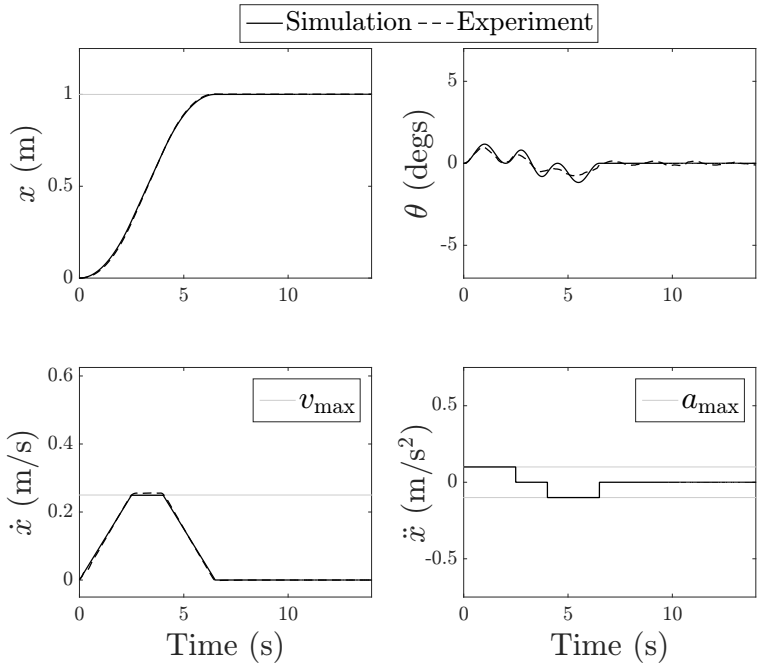

FIGURE 4.13: Experimental result in testcase A2 (the minimum-time SC–VSE is chosen). Simulation and experimental results are in a complete agreement.

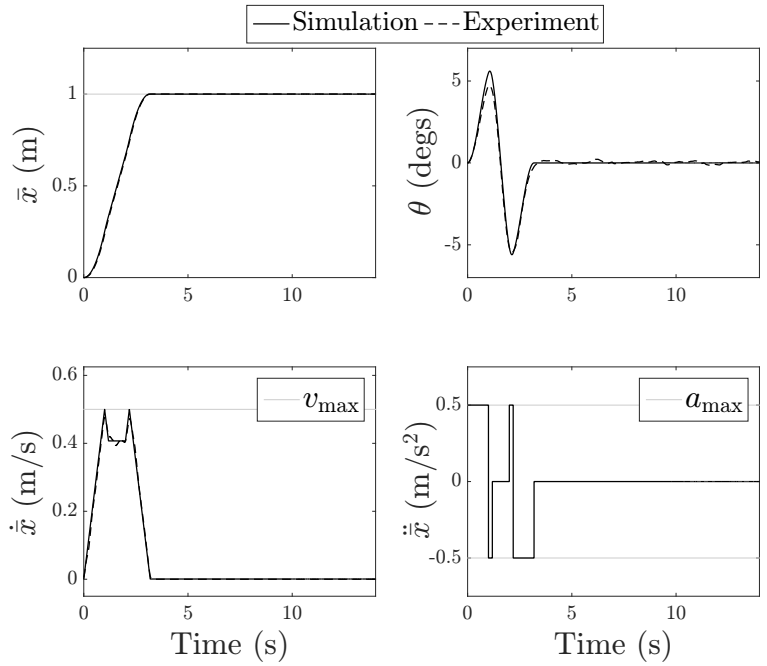

FIGURE 4.14: Experimental result in testcase A3 (the minimum-time SC–IS is chosen). Simulation and experimental results are in a complete agreement.

Figs. 4.12–4.14 depict the experimental results. In all testcases, it can be seen that the trolley precisely reaches the desired destination while the vibration is nearly suppressed. Moreover, the maximum velocity and maximum acceleration constraints of the actuator are strictly complied with. The experimental results strongly agree with the simulation results, which verifies the correctness of the entire modeling and control design process. Therefore, the effectiveness of the proposed method is strongly confirmed. Note that, there are slight differences between the simulations and the experimental results due to the following: i) some physical factors (e.g., air friction, payload's inertia) are neglected in the model of the overhead crane system, ii) the actual rope lengths in practice are slightly different from those used in the simulations because of small measurement errors, and iii) small tracking errors of the computed position commands exist in the experiments (see subfigure x of Figs. 4.12–4.14). Nevertheless, the differences are minor and the performances of the proposed minimum-time ZV S-curve commands have been demonstrated. Thus, such an issue is not critical.

4.6 Summary

In this chapter, minimum-time S-curve commands were proposed to obtain vibration-free transportation of an overhead crane system. In order to build the vibration suppression capability, two techniques

were systematically established, on the basis of a parameterized baseline S-curve command. The first method directly embedded the terminal conditions of vibration-free transportation into the baseline function, whereas the second method employed the input shaping methodology. Minimum-time solutions were formulated for both schemes by solving constrained (discrete) nonlinear optimization problems, in which maximum velocity and maximum acceleration of the actuator were elaborately considered. A comparison with related studies verified the advantage of the proposed minimum-time S-curve command in terms of transfer time, and thus the transportation productivity was enhanced. It was also shown that the online command generation is feasible with the proposed schemes. Both simulation and experimental results were provided to clarify the effectiveness of the proposed methods and they are in a complete agreement.

Chapter 5

Model Reference Input Shaping Control

In Chapter 4, two motion planning methods were established for a linearized model of an overhead crane with constant rope length. Especially, in Section 4.4, a minimum-time input shaping-based feedforward controller was formulated for a time-invariant linear dynamics of the overhead crane system. In this chapter, an advanced version of the scheme shown in Section 4.4 will be introduced for a luffing dynamics of a rotary crane system with time-varying rope length. The newly established technique, named model reference input shaping (MRIS) control, is able to completely suppress the residual vibration for a highly nonlinear time-varying system. The basic idea of the proposed approach is to obtain a reference oscillation from a second-order time-invariant linear system, on which the standard input shaping control is applied. The MRIS control law is then designed to exactly match the real vibration of the system with the reference oscillation. By such a means, an exact zero vibration suppression can be achieved for the actual system. The reference command is parameterized to cope with control objectives other than the vibration suppression. Simulation results are provided to verify the superiority of the MRIS controller over the standard robust input shaping control method.

5.1 Introduction

Rotary cranes are extensively used at harbors to transport large payloads—ranging from several hundred kilograms to dozen of tons—one point to another in the workplace. There are three main motions in a rotary crane system: slewing, luffing, and hoisting. The slewing motion rotates the entire base,

whereas the luffing movement lowers/rises the boom. The payload is suspended under the boom tip and its height can be adjusted by the hoisting motion. Both slewing and luffing motions are rotational; thus, the rotary crane is usually described in the spherical coordinate system. The rotary crane can also be considered as a robotic arm with two revolute joints and one prismatic joint. Due to the fact that the rope is flexible, the payload will exhibit a residual vibration. This unwanted vibration substantially lengthens the transportation as well as reduces safety of the system in practice. Since the rotary crane is underactuated, the vibration suppression control of this system poses a significant challenge. Therefore, considerable interests were mounting on vibration controls for rotary crane systems. They can be classified into two main classes: feedback and feedforward controls.

Plenty of studies can be found in the feedback control category. In [144], a delayed feedback controller was established to stabilize the sway angles for a ship-mounted crane. Uchiyama [13] formulated a simple linear model of the 3D rotary crane dynamics and afterward, a constant gain partial state feedback controller was designed to robustly stabilize the system for any rope length. Ouyang et al. [145] proposed a nonlinear controller using only slewing motion to suppress both radial and tangential swing angles. Recently, Sun et al. [146] and Lu et al. [147] introduced passivity-based nonlinear controllers for rotary crane systems subject to roll and heave disturbances. Qian et al. [148] reported a nonlinear controller for an offshore boom crane, which comprises an adaptive robust control law and a learning strategy. To sum up, feedback control techniques demonstrated their excellent properties in dealing with uncertainties and disturbances. However, they require a sophisticated and costly sensor structure, which demands a frequent maintenance. This is the reason that the feedback controllers are still not commonly used in practical cranes. In numerous contexts, feedforward controls are preferable in industry due to their simplicity, ease of implementation, and no additional measurement system being required.

Among the feedforward schemes [60, 68, 149], the input shaping control [43, 48] is the most widely applied method. Its basic idea is to intelligently modulate the original reference command by convolving with a sequence of impulses called input shaper. The input shaper is designed in such a way that the vibration induced by all impulses is self canceled. If the input shaper causes no vibration, its convolution with any reference command also results in a zero vibration for the system. Danielson [150] implemented a non-robust Zero Vibration (ZV) input shaper and two robust ones, including Zero Vibration Derivative (ZVD) and Specified Insensitivity (SI), to a rotary crane with only luffing motion. This study reported that performance of the robust input shapers are better than the ZV input shaper, which is not robust to modeling errors. The same conclusion was made in [151], where a double-pendulum rotary crane was considered. Recently, Newman and Vaughan [152] proposed a specially designed input shaper that can suppress the vibration under non-initial conditions. However,

TABLE 5.1: System parameters.

Parameter	Description	Value
L_B	Boom length (m)	30
d_1	Length of the FJ line (m)	9.157
α_1	Auxiliary angle (rad)	1.45
b_1	Radius of the luffing drum (m)	0.3
g	Gravitational acceleration (m/s^2)	9.81

the above-mentioned studies cannot completely suppress vibration for the rotary crane system, that is to say, only a vibration reduction is guaranteed. Furthermore, the time-varying rope length scenario was not yet considered to an elaborate degree since the standard input shaping control, which is originally designed for a second-order time-invariant linear plant, cannot be trivially applied to a time-varying nonlinear system. Those are the problems needing to be overcome.

In order to address the aforementioned challenges, a new model reference input shaping controller for the luffing motion of the rotary crane will be formulated in this chapter. The proposed technique can handle a highly nonlinear luffing pendulum dynamics with an arbitrary (known) time-varying rope length. The newly established input shaping control law enables us to use the non-robust ZV input shaper to completely suppress the vibration; thus, the transferring time is significantly faster than standard robust input shapers, which are slow and cannot provide an exact zero vibration cancellation.

5.2 Mathematical modeling of luffing dynamics

The swinging motion of the payload induced from the luffing actuation is illustrated in Fig. 5.1, where $\varphi(t)$, $\theta(t)$, and $l(t)$ are the luffing angle, swing angle, and rope length respectively. In order to vary the luffing angle, a servo motor is attached at the point A to rotate the luffing drum, which connects to the points F and T by ropes (see Fig. 5.1). The rotation angle of the luffing motor is denoted as $\varphi_M(t)$. All essential parameters of the system are summarized in Table 5.1.

By using the Euler-Lagrange method, the nonlinear luffing dynamics of the rotary crane system with a time-varying rope length can be described as follows:

$$l\ddot{\theta} + 2\dot{l}\dot{\theta} + g\sin\theta = u(t), \tag{5.1}$$

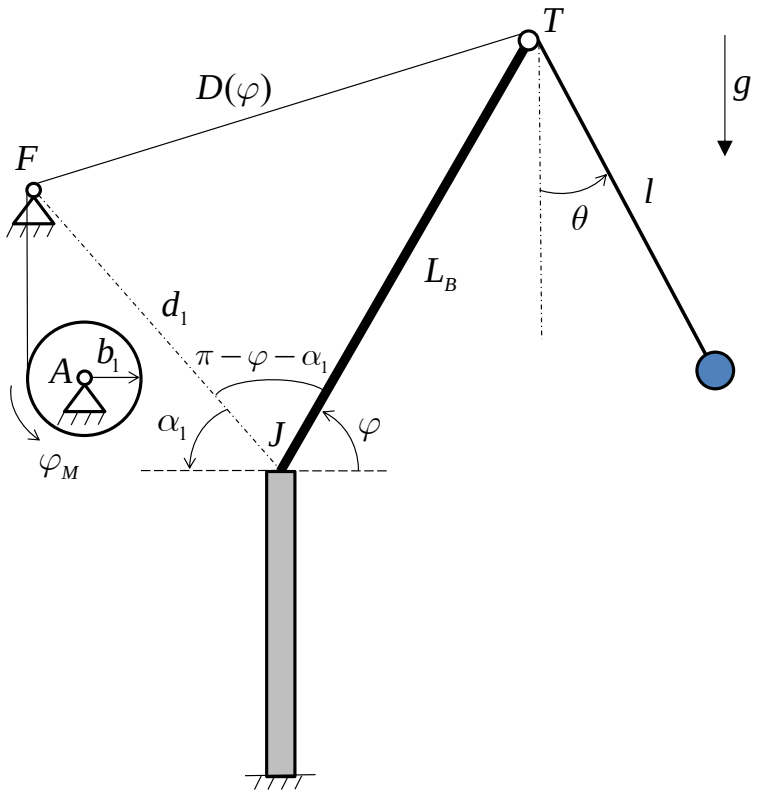

FIGURE 5.1: Mathematical modeling of the luffing dynamics.

where $u(t) = L_B\ddot{\varphi}\sin(\varphi-\theta) + L_B\dot{\varphi}^2\cos(\varphi-\theta)$. The hoisting profile $l(t)$ can be arbitrary. However, $l(t)$ is supposed to be known and $\dot{l}(t)$ is continuous. It is also commonly assumed that the system starts from rest (see [60, 68, 151]), namely $\dot{\varphi}(0) = \dot{l}(0) = \theta(0) = \dot{\theta}(0) = 0$. Furthermore, let $\varphi(0) := \varphi_0$ and $l(0) := l_0$. To obtain vibration-free transport, the following terminal conditions must be achieved in some finite terminal time τ:

$$\varphi(\tau) = \varphi_f,\ l(\tau) = l_f,\ \dot{\varphi}(\tau) = \dot{l}(\tau) = \theta(\tau) = \dot{\theta}(\tau) = 0. \tag{5.2}$$

In (5.2), φ_f and l_f are positive reference values of the luffing angle and the rope length respectively.

The actuator dynamics from the luffing motor to the boom's luffing angle will be presented next. Consider the triangle FTJ in Fig. 5.1, we have

$$D^2(\varphi) = d_1^2 + L_B^2 + 2d_1L_B\cos(\alpha_1+\varphi)\,. \tag{5.3}$$

Denote the initial angle of the luffing motor as $\varphi_{M0} := \varphi_M(0)$. The initial value D_0 of $D(\varphi)$ can be calculated by replacing φ by φ_0 in (5.3). Since the variation of the rope length is constant, it can be

obtained that

$$(\varphi_M - \varphi_{M0})\, b_1 = D_0 - D(\varphi). \tag{5.4}$$

Let $\phi := \alpha_1 + \varphi$. From (5.4), it can be inferred that

$$\varphi_M = \frac{D_0 + b_1\varphi_{M0} - \sqrt{d_1^2 + L_B^2 + 2d_1 L_B \cos\phi}}{b_1}. \tag{5.5}$$

Differentiating (5.3) and (5.4), we have

$$\dot{D}(\varphi) = -\frac{d_1 L_B \sin\phi}{D}\dot{\varphi} \tag{5.6}$$

$$\dot{D}(\varphi) = -b_1\dot{\varphi}_M. \tag{5.7}$$

Comparing (5.6) and (5.7) yields

$$\dot{\varphi}_M = \frac{d_1 L_B}{b_1}\frac{\sin\phi}{D}\dot{\varphi}. \tag{5.8}$$

By taking the derivative of (5.8), it results in

$$\ddot{\varphi}_M = \frac{d_1 L_B}{b_1}\left[\frac{D\left(\ddot{\varphi}\sin\phi + \dot{\varphi}^2\cos\phi\right) - \dot{\varphi}\dot{D}\sin\phi}{D^2}\right]. \tag{5.9}$$

The MRIS control will be designed based on (5.1) where the control input is $u(t)$. Afterward, it can be translated to the real signal commanding the luffing servo motor in the position or velocity level using (5.5) or (5.8) respectively.

The control objective is to design a MRIS control law to bring the system from its initial conditions to the terminal conditions (5.2) in a minimum time, considering the following actuator constraints:

$$|\dot{\varphi}_M| \le \dot{\varphi}_M^{\max}, |\ddot{\varphi}_M| \le \ddot{\varphi}_M^{\max}, |\dot{l}| \le \dot{l}^{\max}, |\ddot{l}| \le \ddot{l}^{\max}. \tag{5.10}$$

For a real-size rotary crane system, $\dot{\varphi}_M^{\max} = 5.47$ rad/s, $\ddot{\varphi}_M^{\max} = 2.73$ rad/s^2, $\dot{l}^{\max} = 1.5$ m/s, and $\ddot{l}^{\max} = 0.6$ m/s^2. The following section will be devoted to the design of the MRIS controller.

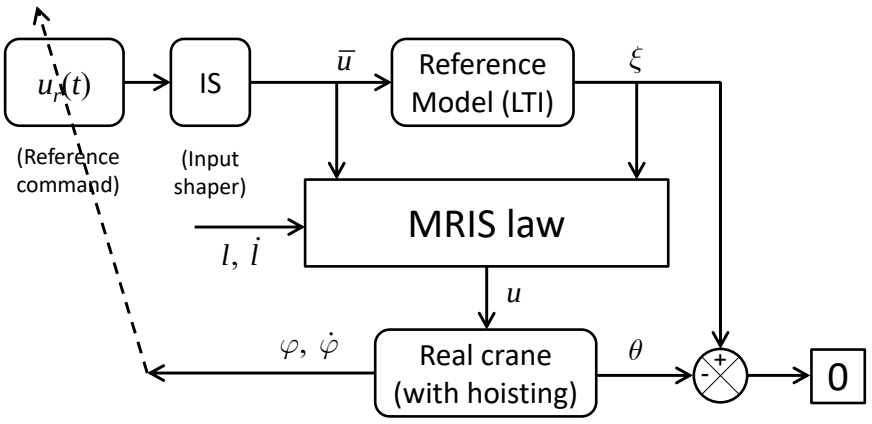

FIGURE 5.2: Basic concept of the MRIS control design.

5.3 MRIS controller design

5.3.1 Design concept

The input shaping control is originally established for a second-order time-invariant linear system. A direct application of the standard input shaping control for a time-varying nonlinear system often results in a poor vibration suppression performance. In order to circumvent this problem, the standard input shaping control law is firstly applied to a reference model, which is a second-order time-invariant linear system. Thus, the oscillation of the reference model (named reference oscillation) can be completely suppressed. The actual control input of the time-varying nonlinear system is then derived to exactly match the vibration of the real system with the reference oscillation. By such a means, a complete vibration suppression can be achieved for the real plant. The aforementioned concept of the MRIS scheme is illustrated in Fig. 5.2. To accomplish the MRIS controller design, the reference command $u_r(t)$ (see Fig. 5.2) must be determined to fulfill control objectives other than the vibration suppression. This can be done by parameterizing $u_r(t)$ in such a way that the number of unknowns in $u_r(t)$ should be (at least) equal to the number of remaining control targets. For instance, $u_r(t)$ should have two to-be-determined variables to realize two remaining objectives $\varphi(\tau) = \varphi_f$ and $\dot{\varphi}(\tau) = 0$ in (5.2).

5.3.2 MRIS control law

The reference model is introduced as follows:

$$\bar{l}\ddot{\xi} + g\xi = \bar{u}(t), \tag{5.11}$$

where $\bar{l}$ is a constant nominal rope length. The natural period of (5.11) is $T = 2\pi\sqrt{\bar{l}/g}$. The control input $\bar{u}(t)$ (see Fig. 5.2) is designed based on the standard input shaping technique

$$\bar{u}(t) = u_r(t) * I(t), \tag{5.12}$$

where $*$ is the convolution operator and $I(t)$ is the ZV input shaper, which has the following expression in time domain [153]:

$$I(t) = 0.5\left[\delta(t) + \delta\left(t - T/2\right)\right]. \tag{5.13}$$

In (5.13), $\delta(.)$ is the Dirac delta generalized function. As discussed earlier at the end of Section 5.3.1, the reference command should have two unknowns. Therefore, it is chosen to be the following bang-off-bang profile:

$$u_r(t) = \begin{cases} a, & 0 \le t \le t_1 \\ -a, & t_1 < t \le t_f \\ 0, & t > t_f, \end{cases} \tag{5.14}$$

where a and t_1 are to-be-determined variables, and t_f will be gradually reduced to obtain a minimum transferring time that meets the actuator limits (5.10) (see [60]).

Under the action of the control input (5.12), the reference oscillation is suppressed, namely

$$\xi\left(t_f + T/2\right) = \dot{\xi}\left(t_f + T/2\right) = 0. \tag{5.15}$$

The next step is to design the real control input $u(t)$ (see Fig. 5.2) to match the actual vibration $\theta(t)$ with the reference oscillation $\xi(t)$, that is to say

$$\theta(t) \equiv \xi(t),\ \dot{\theta}(t) \equiv \dot{\xi}(t),\ \ddot{\theta}(t) \equiv \ddot{\xi}(t),\ \forall t \ge 0. \tag{5.16}$$

By using (5.1) and (5.11), we have

$$\begin{aligned} \ddot{\xi} &= -\frac{g}{\bar{l}}\xi + \frac{\bar{u}(t)}{\bar{l}} \\ \ddot{\theta} &= -2\frac{\dot{l}}{l}\dot{\theta} - \frac{g}{l}\sin\theta + \frac{u(t)}{l}. \end{aligned} \tag{5.17}$$

Applying (5.16) on (5.17) results in

$$-2\frac{\dot{l}}{l}\dot{\xi} - \frac{g}{l}\sin\xi + \frac{u(t)}{l} = -\frac{g}{\bar{l}}\xi + \frac{\bar{u}(t)}{\bar{l}}, \tag{5.18}$$

from which the MRIS law $u(t)$ can be extracted as follows:

$$u(t) = \bar{u}(t)\frac{l}{\bar{l}} + g\left(\sin\xi - \frac{l}{\bar{l}}\xi\right) + 2\dot{l}\dot{\xi}. \tag{5.19}$$

By using the MRIS control law (5.19), the vibration of the time-varying nonlinear system (5.1) is completely suppressed, namely

$$\theta\left(t_f + T/2\right) = \dot{\theta}\left(t_f + T/2\right) = 0. \tag{5.20}$$

Therefore, to accomplish the MRIS controller design, one needs to determine two unknowns a and t_1 in $u_r(t)$ to fulfill the remaining requirements, those are

$$\varphi\left(t_f + T/2\right) = \varphi_f,\ \dot{\varphi}\left(t_f + T/2\right) = 0. \tag{5.21}$$

Comparing the definition of $u(t)$ in (5.1) with (5.19), we have

$$\begin{aligned} &L_B\ddot{\varphi}\sin\left(\varphi - \xi\right) + L_B\dot{\varphi}^2\cos\left(\varphi - \xi\right) \\ &= \left[u_r(t) * I(t)\right]\frac{l}{\bar{l}} + g\left(\sin\xi - \frac{l}{\bar{l}}\xi\right) + 2\dot{l}\dot{\xi}. \end{aligned} \tag{5.22}$$

Two unknowns a and t_1 can be designed based on (5.22) to realize (5.21). However, since (5.22) is a nonlinear differential-integral equation, an analytical solution may not exist. For this reason, the following optimization problem is configured to determine a and t_1:

$$\begin{aligned} \min_{a,t_1} \quad & \omega_1\left[\varphi\left(t_f + T/2\right) - \varphi_f\right]^2 + \omega_2\dot{\varphi}^2\left(t_f + T/2\right) \\ \text{s.t.} \quad & \text{Nonlinear differential-integral equation (5.22).} \end{aligned} \tag{5.23}$$

The weighting coefficients of (5.23) are $\omega_1 = 10^3$ and $\omega_2 = 10^5$. The nonlinear program (5.23) can be solved by the *fmincon* routine of MATLAB.

Note that, for any nonlinear optimization solver, good initial guesses of decisive variables are crucial to ensure that the converged (local) minimum has an acceptable quality. The following subsection

will be devoted to formulating the initial guesses for a and t_1, which are sufficiently close to the true solutions.

5.3.3 Computation of initial guesses for unknown variables

Denote the initial guess of a and t_1 as a_0 and t_{10} respectively. The purpose is to produce reasonable values of a_0 and t_{10} in closed-form. Note that, it is infeasible to obtain an analytical solution of a and t_1 when a full time-varying nonlinear system is used. Therefore, the computation of a_0 and t_{10} will be conducted on a simplified model. This model utilizes the constant nominal rope length $\bar{l}$ and also assumes the swing angle is sufficiently small such that $\sin\theta \approx \theta$ and $\theta \ll \varphi$. Under these assumptions, based on (5.1), the simplified dynamics of the system is given by

$$\bar{l}\ddot{\theta} + g\theta = \psi(t), \tag{5.24}$$

where $\psi(t) = L_B\ddot{\varphi}\sin\varphi + L_B\dot{\varphi}^2\cos\varphi$. The initial conditions of (5.24) are

$$\varphi(0) = \varphi_0,\ \dot{\varphi}(0) = 0,\ \theta(0) = 0,\ \dot{\theta}(0) = 0. \tag{5.25}$$

The present goal is to design the input $\psi(t)$ of the simplified model (5.24) in the form of a standard input shaping control law, that is

$$\psi(t) = \psi_r(t) * I(t), \tag{5.26}$$

where $I(t)$ is the ZV input shaper in (5.13) and $\psi_r(t)$ is a bang-off-bang profile similarly to (5.14), that is to say

$$\psi_r(t) = \begin{cases} a_0, & 0 \le t \le t_{10} \\ -a_0, & t_{10} < t \le t_f \\ 0, & t > t_f \end{cases}. \tag{5.27}$$

Note that, the initial guesses a_0 and t_{10} are present in (5.27) and their values must be determined to fulfill the conditions $\varphi(t_f + T/2) = \varphi_f$ and $\dot{\varphi}(t_f + T/2) = 0$ in (5.21). Let us denote $z := -L_B\cos\varphi + L_B\cos\varphi_0$. The terminal conditions (5.21) can be translated to the z-coordinate as follows:

$$z\,(t_f + T/2) = z_f,\ \dot{z}\,(t_f + T/2) = 0, \tag{5.28}$$

where $z_f = -L_B \cos\varphi_f + L_B \cos\varphi_0$. Taking the first and second derivatives of z results in

$$\dot{z} = L_B \dot{\varphi} \sin\varphi \tag{5.29}$$

$$\ddot{z} = L_B \ddot{\varphi} \sin\varphi + L_B \dot{\varphi}^2 \cos\varphi. \tag{5.30}$$

From (5.30), we have $\psi(t) = \ddot{z}(t)$. From (5.26), it yields

$$\ddot{z}(t) = \psi_r(t) * I(t). \tag{5.31}$$

Note that, unlike (5.22), (5.31) is a linear differential-integral equation, which admits an analytical solution. To solve (5.31), the Laplace transformation method can be used. Taking the Laplace transform for both sides of (5.31), we have

$$s^2 z(s) = \psi_r(s) I(s). \tag{5.32}$$

From (5.27) and (5.13), the Laplace transforms of $\psi_r(t)$ and $I(t)$ can be easily obtained by

$$\psi_r(s) = -\frac{a_0}{s}\left(2e^{-st_{10}} - e^{-st_f} - 1\right) \tag{5.33}$$

$$I(s) = 0.5\left(1 + e^{-0.5Ts}\right). \tag{5.34}$$

Plugging (5.33) and (5.34) into (5.32) and taking the inverse Laplace transform of $z(s)$, we can obtain a closed-form expression of $z(t)$ and $\dot{z}(t)$ in terms of a_0 and t_{10} as shown in (5.35), where $H(.)$ is the Heaviside function:

$$\begin{aligned}
z(t) = -\frac{1}{2}a_0 \Big[&(t-t_{10})^2 H(t-t_{10}) + (t-t_{10}-T/2)^2 H(t-t_{10}-T/2) - 0.5(t-t_f)^2 H(t-t_f) \\
&-0.5(t-t_f-T/2)^2 H(t-t_f-T/2) - 0.5(t-T/2)^2 H(t-T/2) - 0.5t^2\Big]. \\
\dot{z}(t) = -\frac{1}{2}a_0 \Big[&2(t-t_{10}) H(t-t_{10}) + (t-t_{10})^2 \delta(t-t_{10}) + 2(t-t_{10}-T/2) H(t-t_{10}-T/2) \\
&+ (t-t_{10}-T/2)^2 \delta(t-t_{10}-T/2) - (t-t_f) H(t-t_f) - 0.5(t-t_f)^2 \delta(t-t_f) \\
&- (t-t_f-T/2) H(t-t_f-T/2) - 0.5(t-t_f-T/2)^2 \delta(t-t_f-T/2) \\
&- (t-T/2) H(t-T/2) - 0.5(t-T/2)^2 \delta(t-T/2) - t\Big].
\end{aligned} \tag{5.35}$$

By using (5.28) on (5.35), it can be obtained that

$$a_0 = \frac{4z_f}{t_f^2},\ t_{10} = \frac{t_f}{2}. \tag{5.36}$$

The values of a_0 and t_{10} in (5.36) are the initial guesses of a and t_1 when solving the nonlinear program (5.23).

5.4 Simulation results

This section provides simulation results of the proposed MRIS controller and its comparisons with no-control case and the standard robust input shaper ZVDD [43]. In no-control context, both luffing and hoisting motions use trapezoidal velocities to reach their reference values without considering the vibration suppression. The simulations are conducted for the following two cases with different luffing ranges:

- Case 1: $\varphi_0 = 0.38$ rad (22 degs), $\varphi_f = 0.79$ rad (45 degs), $l_0 = 30$ m, and $l_f = 10$ m.
- Case 2: $\varphi_0 = 0.38$ rad (22 degs), $\varphi_f = 1.22$ rad (70 degs), $l_0 = 30$ m, and $l_f = 10$ m.

The nominal rope length is chosen as $\bar{l} = 0.5\,(l_0 + l_f)$. Note that, t_f is gradually reduced by the bisection method to obtain a minimum value $(t_f)_{\min}$ for which the actuator limitations (5.10) are met. The computational results are summarized as follows:

- Case 1: $a = 0.206$, $t_1 = 5.553$ s, $(t_f)_{\min} = 11.35$ s.
- Case 2: $a = 0.550$, $t_1 = 5.552$ s, $(t_f)_{\min} = 11.35$ s.

The computational times of Case 1 and Case 2 are 10.76 s and 9.53 s respectively on a personal computer with 2.7-GHz Intel Core i5-4310M and 8 GB of RAM. It is remarked that the total transferring time of the MRIS controller is $(t_f)_{\min} + T/2$, where $T/2$ is the delay caused by the ZV input shaper. In two cases, an identical minimum transportation time is obtained due to the actuator limitations of the hoisting motion. It is also important to note that, when initial guesses of a and t_1 are both set to zero, the optimization solver (i.e., *fmincon*) fails to provide a good solution and sometimes, infeasibility is encountered. Thus, the appropriate guesses suggested in Section 5.3.3 are crucial.

A standard robust ZVDD input shaper is employed to compare with the proposed MRIS controller. The formula of the ZVDD input shaper in time domain is given by [153]

$$I_1(t) = \frac{1}{8}\delta(t) + \frac{3}{8}\delta\left(t - \frac{T}{2}\right) + \frac{3}{8}\delta\left(t - T\right) + \frac{1}{8}\delta\left(t - \frac{3T}{2}\right). \tag{5.37}$$

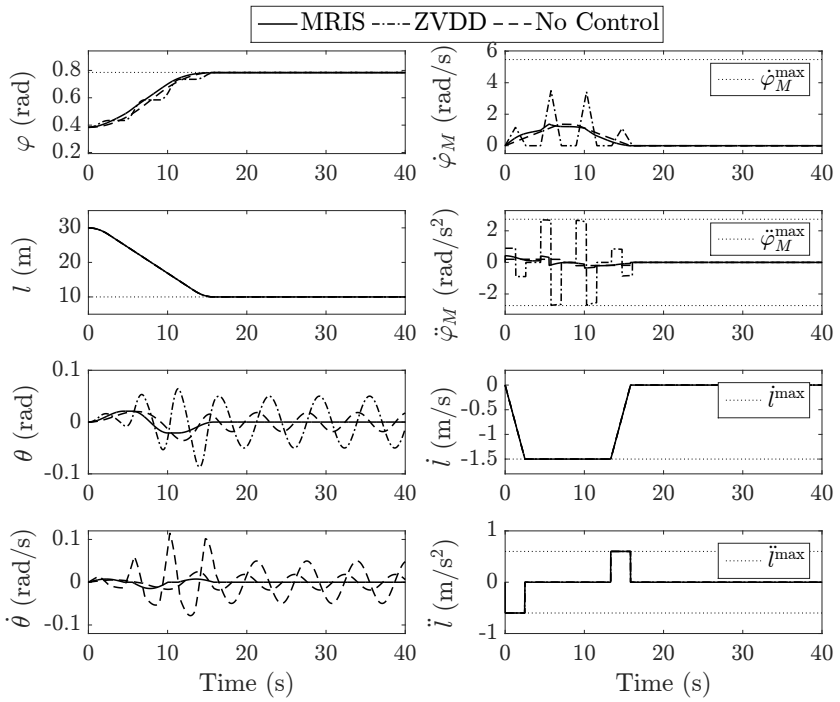

FIGURE 5.3: Comparative simulation result in Case 1.

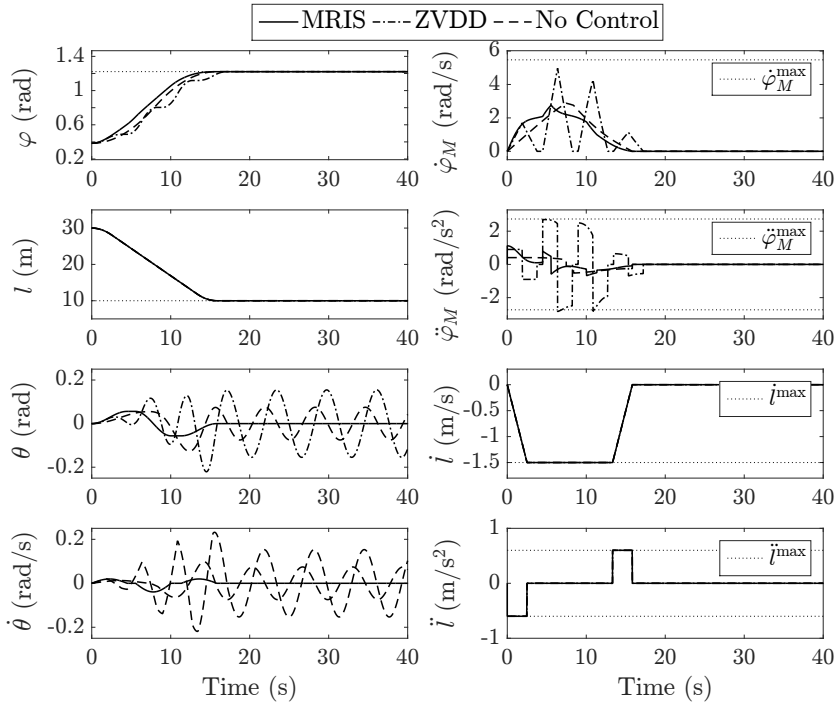

FIGURE 5.4: Comparative simulation result in Case 2.

The comparative simulation results between the MRIS control, a standard robust input shaping control using the ZVDD input shaper (5.37), and a no-control case are given in Figs. 5.3–5.4 for Case 1 and Case 2. Note that, the full time-varying nonlinear system (5.1) is used in the simulations. From Figs. 5.3–5.4, it can be observed that the MRIS control law is able to completely suppress the vibration, whereas there still exists a significant residual oscillation after the motion in the case when the robust ZVDD input shaper is utilized. Furthermore, the control input magnitude of the MRIS controller is considerably smaller than the ZVDD input shaping control. Therefore, it has been shown that, under a relatively similar transportation time, the proposed MRIS scheme is superior than the standard robust input shaping method.

5.5 Summary

This chapter established a model reference input shaping controller—a new scheme to obtain an exact zero vibration suppression for a highly nonlinear time-varying system found in the luffing dynamics of the rotary crane. The performance of the MRIS controller was shown to be superior than the standard robust input shaping control using the ZVDD input shaper.

Chapter 6

Resonance-based Tossing Control

In Chapters 2–5, the vibration was seen as a harmful property that needs to be eliminated, since cranes are assumed to transfer large blocks. For this reason, various vibration suppression control techniques were presented in the previous chapters. The main aim of this chapter is to evidently demonstrate that one can employ the vibration *excitation* control to further shorten the transfer time in the context of bulk material transportation of an overhead crane. As such, it shows that the vibration suppression control is not the best option in all circumstances. In practice, transportation of bulk materials using an overhead crane system possesses a special property, that is, the transferred materials can be dropped/discharged while in the air. In order to exploit such a unique feature, this chapter introduces a new concept, named tossing control methodology, to enhance transportation productivity. A specific type of tossing controller is proposed, which relies on the phenomenon of linear resonance to induce oscillation in periodically increasing amplitude. A novel resonance-based tossing controller—comprising an optimal linearization law and a resonance evoking component—is formulated. It will be shown that, under similar requirements of bulk materials transportation, conditions, and actuator constraints, the resonance-based tossing control can reduce the transferring time up to 26.5% compared with the well-known minimum-time swing suppression controller—the fastest member of the swing suppression control group. The results show that, although it is not always able to obtain a faster transportation using the resonance tossing controller, evidence for breaking the time limitation of the minimum-time swing suppression control is provided. Both simulation and experimental results are presented to verify the effectiveness of the proposed resonance tossing control method.

FIGURE 6.1: An overhead crane is transferring bulk material in a warehouse.[1]

6.1 Introduction

As previously discussed in Chapter 4, overhead cranes are widely used in various places such as factories, storage yards, harbors, etc. to transfer heavy payloads point-to-point. The payload is suspended under the trolley by wire ropes and its height can be adjusted by the hoisting motion. The trolley is actuated to relocate the payload within the workspace. The payloads are usually large blocks or bulk materials (such as sand, cement, etc.). When transferring the bulk materials, the overhead crane must utilize a specially designed grab bucket which can close/open to effectively grasp/drop the materials (see Fig. 6.1). The fundamental property of the bulk materials transportation is that the materials can be dropped/discharged from the air and they naturally fall down toward their intended destination by gravity. This is completely different to a large block transfer, in which the payload must be eventually laid down on the ground by the overhead crane. It is well-known that the payload exhibits vibration during and after transportation. The residual oscillation is usually undesirable when transferring a large block payload, since, for safety, the swinging motion needs to cease before the payload can be safely landed. Therefore, in such circumstances, vibration suppression control (see Chapters 1&4 and references therein) must be emphasized. In the context of bulk materials transportation, its aforementioned unique property, namely that materials can be discharged while in the air, implies a favorable consequence, that is, the zero terminal swing angle constraint as found with the vibration suppression control can be relaxed. As a result, the requirements of bulk materials transportation are stated as

[1]Source: https://www.reel-coh.com

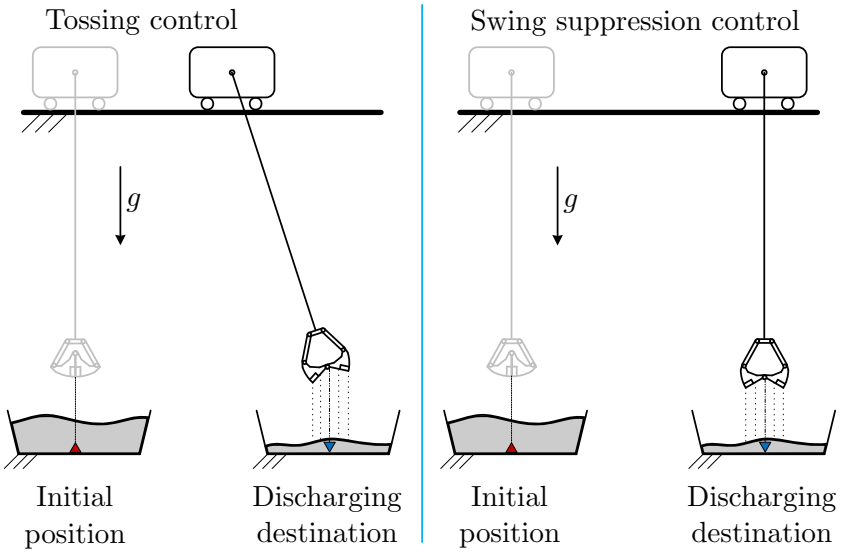

FIGURE 6.2: Difference between (swing) tossing control and swing suppression control.

follows: the payload (grab bucket with materials inside) should be transferred above the discharging destination, at which the payload's horizontal and vertical velocities are zero, meanwhile the trolley must stop[2], and the terminal swing angle is not necessarily zero. The relaxation of the constraint on the zero terminal swing angle indeed offers the possibility of further reducing the transferring time by exciting the payload vibration rather than suppressing/minimizing it. Such a type of control is termed tossing control. Note that, both tossing and swing suppression control methodologies can realize the requirements of bulk materials transportation. The only difference between them is the tossing control aims at achieving a large terminal swing angle, whereas the swing angle must be zero in the swing suppression control. This dissimilarity is illustrated in Fig. 6.2.

This chapter will introduce a resonance-based tossing control for an overhead crane system. The proposed method utilizes the linear resonance phenomenon (see [154, p. 113], [155, p. 162]) to generate a large swing angle with periodically increasing amplitude. Here, the linear resonance is employed instead of the nonlinear one due to the following reasons. First, the linear vibration frequency can be exactly computed, whereas it is generally not possible in the case of the nonlinear vibration [156]. Second, the linear resonance frequency is independent from the magnitude of control input and

[2]These requirements are explained as follows. At the discharging destination, the payload speed in both horizontal and vertical directions must be zero in order to make use of the following advantages. Firstly, it ensures that, in ideal conditions, when the grab opens, the bulk materials fall down along the vertical axis, which prevents spilling. Secondly, the control input for the returning phase can be easily obtained by simply applying the designed control input of the transferring phase backward in time (see Section 6.3.3). Lastly, after discharging, the payload tendency is to swing toward the initial position, which naturally makes the returning phase more time-efficient. In addition, the trolley velocity must also be zero since after discharging the material, to save time, the trolley needs to immediately return to the initial position to supply material for the next transportation cycle.

oscillation itself, whereas such a property may not hold in the nonlinear resonance [157]. Therefore, by using the linear resonance, the controller design can be facilitated. The resonance control law is given by a parameterized composite sine and cosine function, whose frequency is identical with that of the system. By that means, the resonance can be created. Since a large swing angle is supposed to be generated, the nonlinear model of the overhead crane ought to be used. Therefore, in order to obtain the linear resonance for a nonlinear system, an exact linearization law is added to the resonance control input. The technical difficulty in using such a technique is that the control effort for linearizing the system grows rapidly as the swing angle increases, which is even unbounded when the swing angle approaches the singular points at $\pm\pi/2$ if a conventional linearization law is used. To solve that problem, an optimal gain for the linearization law will introduced to minimize its magnitude. A favorable property of the proposed optimal exact linearization law is that its magnitude can be bounded by a known limit for all swing angles in $(-\pi/2,\ \pi/2)$. Essential terminal conditions resulted from the tossing control requirements are employed to determine the unknown parameters of the total resonance control law. Both maximum velocity and maximum acceleration of the actuator are taken into account. To the best of author's knowledge, none of existing researches investigated a similar problem relating to the tossing control methodology.

It is well-known that, among all vibration controllers, the minimum-time (or time-optimal) control universally provides the smallest possible transferring time [57, 59, 139, 158]. Nevertheless, at its best, the proposed resonance-based tossing controller is able to save 26.5% transferring time (or 6.4 seconds in one cycle of transportation, see Section 6.5) compared with the minimum-time swing suppression control. Therefore, this evidence confirms the main aim of the chapter and proves the possibility of breaking the time limitation of the minimum-time swing suppression control in the context of bulk materials transportation.

The remainder of this chapter is organized as follows. In Section 6.2, a mathematical model of the overhead crane system is presented. Moreover, requirements of the bulk materials transferring process are introduced. Section 6.3 is devoted to the design of the resonance-based tossing controller to fulfill the transportation task. Comparative simulation result of the proposed tossing controller and the minimum-time swing suppression control is provided in Section 6.5. Experimental result on a small-scale overhead crane is given in Section 6.6 to verify the effectiveness of the proposed motion planning method. Finally, Section 6.7 draws conclusions of the chapter.

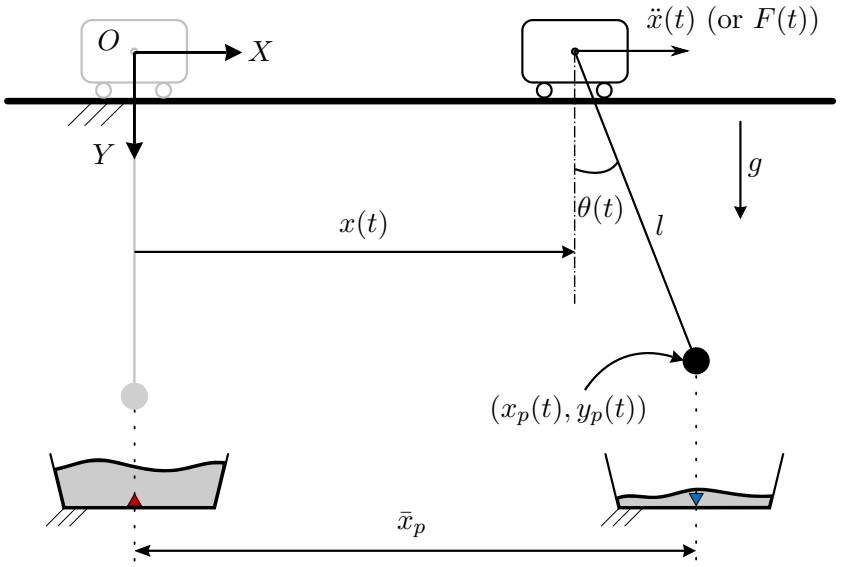

FIGURE 6.3: Mathematical model of the overhead crane system.

6.2 Problem formulation

A mathematical description of the overhead crane system in the case of bulk materials transportation is illustrated in Fig. 6.3, in which $x(t)$ (m) and $\theta(t)$ (rad) are the trolley position and the swing angle. The net force driving the trolley is denoted as $F(t)$. In addition, m (kg), M (kg), l (m), and g ($= 9.81$ m/s^2) represents the payload mass, trolley mass, rope length, and gravitational acceleration respectively. From Fig. 6.3, the horizontal and vertical positions of the payload can be computed by

$$x_p(t) = x(t) - l\sin\theta(t) \tag{6.1}$$

$$y_p(t) = l\cos\theta(t). \tag{6.2}$$

By differentiating (6.1) and (6.2), horizontal and vertical velocities of the payload are

$$\dot{x}_p(t) = \dot{x}(t) - l\dot{\theta}(t)\cos\theta(t) \tag{6.3}$$

$$\dot{y}_p(t) = -l\dot{\theta}(t)\sin\theta(t). \tag{6.4}$$

The dynamics of the overhead crane system in this chapter is similar to that formulated in Section 4.2 of Chapter 4. Therefore, by recalling two equations (4.9) and (4.10), the mathematical model of the

overhead crane system shown in Fig. 6.3 can be described by

$$(M+m)\,\ddot{x} - ml\ddot{\theta}\cos\theta + ml\dot{\theta}^2\sin\theta = F \tag{6.5}$$

$$l\ddot{\theta} + g\sin\theta = \ddot{x}\cos\theta. \tag{6.6}$$

Similarly to Section 4.2, $\ddot{x}(t)$ is chosen to be the control input of the system and only (6.6) is employed in the subsequent tossing control design. Note that, in Section 4.2, a linearized version of (6.6) is utilized to design minimum-time zero-vibration S-curve commands, whereas the nonlinear differential equation (6.6) will directly be employed to design the tossing controller. The reason is that the small angle approximation is not longer valid in the tossing control methodology, as a large swing angle is supposed to be generated. Due to the physical limitation of the trolley actuator, the following maximum velocity and maximum acceleration constraints must be strictly complied:

$$|\dot{x}(t)| \le v_{\max} \text{ and } |\ddot{x}(t)| \le a_{\max}, \tag{6.7}$$

where $v_{\max} > 0$ and $a_{\max} > 0$. By using the information of the servo motor's maximum velocity and maximum torque, as well as the structure of the transmission system, the values of $v_{\max}$ and $a_{\max}$ can easily be estimated [159].

Throughout this chapter, it is also assumed that the payload starts from rest, namely $x(0) = \dot{x}(0) = \theta(0) = \dot{\theta}(0) = 0$ [59, 63, 139, 158, 160, 161]. In order to realize the tossing control requirements (see Section 6.1), the following terminal conditions must be fulfilled

$$\dot{x}(t_f) = \dot{x}_p(t_f) = \dot{y}_p(t_f) = 0,\ x_p(t_f) = \bar{x}_p,\ \theta(t_f) < 0. \tag{6.8}$$

In (6.8), t_f is the terminal time and $\bar{x}_p$ represents the horizontal desired destination of the payload (see Fig. 6.3). By imposing (6.8), the payload is transferred to the discharging destination ($x_p(t_f) = \bar{x}_p$) at zero velocities in both horizontal and vertical directions ($\dot{x}_p(t_f) = \dot{y}_p(t_f) = 0$), the trolley stops ($\dot{x}(t_f) = 0$), and a large terminal swing angle is obtained ($\theta(t_f) < 0$). From (6.3) and (6.4), horizontal and vertical velocities of the payload at the terminal time t_f are

$$\dot{x}_p(t_f) = \dot{x}(t_f) - l\dot{\theta}(t_f)\cos\theta(t_f) \tag{6.9}$$

$$\dot{y}_p(t_f) = -l\dot{\theta}(t_f)\sin\theta(t_f). \tag{6.10}$$

In order to realize the condition $\dot{x}(t_f) = \dot{x}_p(t_f) = \dot{y}_p(t_f) = 0$ of (6.8), we should make $\dot{x}(t_f) = \dot{\theta}(t_f) = 0$. If this condition is strengthened by adding $\theta(t_f) = 0$, it will become the vibration control, which is

not of interest in this chapter. Moreover, by using (6.1), the remaining condition of (6.8), namely $x_p(t_f) = \bar{x}_p$, can be developed to $x(t_f) - l\sin\theta(t_f) = \bar{x}_p$. In summary, the terminal conditions (6.8) are converted to

$$\dot{x}(t_f) = \dot{\theta}(t_f) = 0,\ x(t_f) - l\sin\theta(t_f) = \bar{x}_p,\ \theta(t_f) < 0. \tag{6.11}$$

The following section will be devoted to formulating the resonance tossing control to realize (6.11) while ensuring (6.7).

6.3 Design of resonance-based tossing control

6.3.1 Resonance control with an optimal linearization law

The basic idea of the proposed method (to realize the tossing control requirements) is based on the resonance phenomenon. Mechanical resonance can be evoked by matching the frequency of the control input to that of the oscillation. The main technical difficulty of utilizing the resonance for a nonlinear system is that the frequency of the nonlinear vibration strongly depends on the control input as well as the oscillation amplitude [156, 157]. This creates a dilemma in the control design process, since to generate the resonance, the control input must know the oscillation frequency in advance so that the frequency matching can be done. Furthermore, the calculation of exact vibration frequency for a nonlinear system is not an easy task, or sometimes, is impossible [156]. Therefore, the linear resonance is employed instead of the nonlinear one. In order to generate the linear resonance phenomenon for the nonlinear system (6.6), the following exact linearization resonance control law is proposed

$$\ddot{x}(t) = \underbrace{g\left(\tan\theta - \frac{k\theta}{\cos\theta}\right)}_{:=L(t)} \overbrace{-\frac{a}{\cos\theta}\sin(\omega_0 t) - \frac{b}{\cos\theta}\cos(\omega_0 t)}^{:=R(t)}. \tag{6.12}$$

In (6.12), $L(t)$ is the linearization law to exactly linearize the nonlinear system (6.6) and $R(t)$ is the control input for generating the resonance. The unknown parameters a, b, and ω_0 will be determined in the subsequent deductions by solving a system of nonlinear equations (see (6.55)). Furthermore, the constant k must be designed to minimize the magnitude of the linearization law $L(t)$. This optimal design objective is explained as follows. The methodology of the tossing control is to excite a large swing angle, which entirely depends on the magnitude of $R(t)$. As the swing angle $\theta(t)$ increases, nevertheless, the control effort for linearizing the system (or the magnitude of $L(t)$) rapidly increases

(see Fig. 6.5 with $k = 1$). Moreover, the control input is limited by $|\ddot{x}(t)| \leq a_{\max}$. Thus, no room is left for the (prioritized) resonance generation component $R(t)$. For this reason, maximum value of $|L(t)|$ over a range of operating swing angle $\left(\theta \in \left[-\bar{\theta}, \bar{\theta}\right],\ \bar{\theta} > 0\right)$ needs to be minimized by k. Therefore, k should be a minimizer of the following minimax optimization problem

$$\begin{aligned} \min_{k} \quad & \max_{\theta} \left[f\left(k, \theta\right) = \left(\tan\theta - \frac{k\theta}{\cos\theta} \right)^2 \right] \\ \text{s.t.} \quad & \theta \in \left[-\bar{\theta}, \bar{\theta}\right] \text{ with } \bar{\theta} \in [0, \pi/2) \\ & k \in (0, +\infty)\,. \end{aligned} \tag{6.13}$$

Note that, $\bar{\theta}$ is treated as an unknown, which can be solved together with the parameters a, b, and the terminal time t_f (see (6.55)). The optimal solution of (6.13) is given by Theorem 5.

Theorem 5. The minimizer $k^\star$ of the minimax optimization problem (6.13) is given by

$$k^\star = \frac{1}{\cos\theta^\star + \theta^\star \sin\theta^\star}, \tag{6.14}$$

where $\theta^\star$ is determined by

$$\sin\left(\bar{\theta} + \theta^\star\right) - \theta^\star \cos\left(\bar{\theta} + \theta^\star\right) = \bar{\theta}. \tag{6.15}$$

Proof. Since $f(k, \theta)$ is an even function with respect to θ; hence, it is sufficient to perform the optimization procedure on $\theta \in \left[0, \bar{\theta}\right]$. Flow of the proof is explained as follows. The interest region of k is divided into three sub-intervals, namely $k \in (0, +\infty) = (0, \underline{k}] \cup [\underline{k}, 1] \cup [1, +\infty)$, where $\underline{k} := 1/\left(\cos\bar{\theta} + \bar{\theta}\sin\bar{\theta}\right)$. Firstly, it is proven that for $0 < k \leq \underline{k}$, the minimum value of the function $\max f(k, \theta)$ attains at $k = \underline{k}$. Secondly, for $1 \leq k < +\infty$, the minimum of $\max f(k, \theta)$ is achieved at $k = 1$. Therefore, the whole interest region of k shrinks from $(0, +\infty)$ down to $[\underline{k}, 1]$. Finally, for $\underline{k} \leq k \leq 1$, the optimal solution is determined by the intersection between the critical function and the boundary function.

To begin the proof, the following essential calculus results are provided to facilitate the subsequent presentations

$$\theta - \sin\theta \geq 0,\ \forall\theta \geq 0. \tag{6.16}$$

$$\sin\theta - \theta\cos\theta \geq 0,\ \forall\theta \geq 0. \tag{6.17}$$

Furthermore, the first partial derivative of $f(k,\theta)$ with respect to k is given by

$$\frac{\partial f(k,\theta)}{\partial k} = \frac{2\theta\,(k\theta - \sin\theta)}{\cos^2\theta}. \tag{6.18}$$

A. Interval 1 ($0 < k \leq \underline{k}$)

At first, let us consider a function $q(\theta) = \underline{k}\theta - \sin\theta$. The boundary values of $q(\theta)$ are given by

$$q(\theta)|_{\theta=0} = 0 \tag{6.19}$$

$$q(\theta)|_{\theta=\bar{\theta}} = \frac{\cos\bar{\theta}\left(\bar{\theta}\cos\bar{\theta} - \sin\bar{\theta}\right)}{\cos\bar{\theta} + \bar{\theta}\sin\bar{\theta}}. \tag{6.20}$$

By using the result of (6.17) and note that $\bar{\theta} \geq 0$, we have $q(\theta)|_{\theta=\bar{\theta}} \leq 0$. In summary, we have

$$q(\theta)|_{\theta=0} = 0 \text{ and } \; q(\theta)|_{\theta=\bar{\theta}} \leq 0. \tag{6.21}$$

The critical point θ_s of $q(\theta)$ must satisfy $\partial q(\theta)/\partial\theta|_{\theta=\theta_s} = 0 \Rightarrow \cos\theta_s = \underline{k}$. Therefore, the value of $q(\theta)$ at the critical point θ_s is given by

$$q(\theta_s) = \underline{k}\theta_s - \sin\theta_s = \theta_s\cos\theta_s - \sin\theta_s. \tag{6.22}$$

By using (6.17), it is concluded that $q(\theta_s) \leq 0$. By combining this result and (6.21), we have $q(\theta) \leq 0,\ \forall\theta \in \left[0,\ \bar{\theta}\right]$. Therefore, $\underline{k}\theta - \sin\theta \leq 0,\ \forall\theta \in \left[0,\ \bar{\theta}\right]$. Moreover, in this case, we have $k \leq \underline{k}$; thus, $k\theta - \sin\theta \leq 0$. For this reason, from (6.18), $\partial f(k,\theta)/\partial k \leq 0$ holds. This implies that when θ is held constant, $f(k,\theta)$ decreases as k increases. Therefore

$$\min_{k}\max_{\theta\in\left[0,\,\bar{\theta}\right]} f(k,\theta)\Big|_{0<k\leq\underline{k}} = \max_{\theta\in\left[0,\,\bar{\theta}\right]} f(k,\theta)\Big|_{k=\underline{k}}. \tag{6.23}$$

B. Interval 2 ($1 \leq k < +\infty$)

From (6.16), we have $\sin\theta \leq \theta$, but $k \geq 1$, so $\sin\theta \leq k\theta \Rightarrow k\theta - \sin\theta \geq 0$. By using the condition that $\theta \geq 0$ and $\cos^2\theta > 0$, it can be obtained from (6.18) that $\partial f(k,\theta)/\partial k \geq 0$. This result means that when θ is held constant, $f(k,\theta)$ increases as k increases. Therefore, it can be easily seen that

$$\min_{k}\max_{\theta\in\left[0,\,\bar{\theta}\right]} f(k,\theta)\Big|_{k\geq 1} = \max_{\theta\in\left[0,\,\bar{\theta}\right]} f(k,\theta)\Big|_{k=1}. \tag{6.24}$$

C. Interval 3 ($\underline{k} \leq k \leq 1$)

Since the absolute maximum value of a function is the largest term between its values at the critical points and at the boundaries [162, p. 207]; thus, the critical function and the boundary function should be computed.

The critical function is derived as follows. For each k, a critical point θ_c of $f(k,\theta)$ must satisfy $\partial f(k,\theta)/\partial\theta|_{\theta=\theta_c} = 0$, which can be expanded to

$$(\sin\theta_c - k\theta_c)\cos\theta_c\left[1 - k\left(\cos\theta_c + \theta_c\sin\theta_c\right)\right] = 0. \tag{6.25}$$

The results of (6.25) are

$$\begin{cases} \sin\theta_c = k\theta_c \\ \cos\theta_c = 0 \Rightarrow \theta_c = \pi/2 \Rightarrow \text{(Reject)} \\ 1 - k\left(\cos\theta_c + \theta_c\sin\theta_c\right) = 0. \end{cases} \tag{6.26}$$

In (6.26), when $\sin\theta_c = k\theta_c$, we have $f(k,\theta)|_{\theta=\theta_c} = 0$. Thus, this critical point can be excluded from consideration since $f(k,\theta)$ is always non-negative. For the remaining scenario, namely $1 - k\left(\cos\theta_c + \theta_c\sin\theta_c\right) = 0$, we have $k = 1/\left(\cos\theta_c + \theta_c\sin\theta_c\right)$. Denote $f_c(k)$ as the value of $f(k,\theta)$ at the critical point θ_c. By using the result $k = 1/\left(\cos\theta_c + \theta_c\sin\theta_c\right)$, the critical function $f_c(k)$ can be computed by

$$f_c(k) = \left(\tan\theta_c - \frac{k\theta_c}{\cos\theta_c}\right)^2 = \left(\frac{\sin\theta_c - \theta_c\cos\theta_c}{\cos\theta_c + \theta_c\sin\theta_c}\right)^2. \tag{6.27}$$

The first derivatives of $f_c(k)$ and k with respect to θ_c are

$$\frac{df_c(k)}{d\theta_c} = \frac{2\theta_c^2\left(\sin\theta_c - \theta_c\cos\theta_c\right)}{\left(\cos\theta_c + \theta_c\sin\theta_c\right)^3}. \tag{6.28}$$

$$\frac{dk}{d\theta_c} = \frac{-\theta_c\cos\theta_c}{\left(\cos\theta_c + \theta_c\sin\theta_c\right)^2} \leq 0. \tag{6.29}$$

By using the result of (6.17), it can be concluded that $df_c(k)/d\theta_c \geq 0$. For this reason, $f_c(k)$ increases as θ_c increases. Furthermore, (6.29) implies that k decreases as θ_c increases. Therefore, in summary, we have the critical function $f_c(k)$ decreases with respect to k.

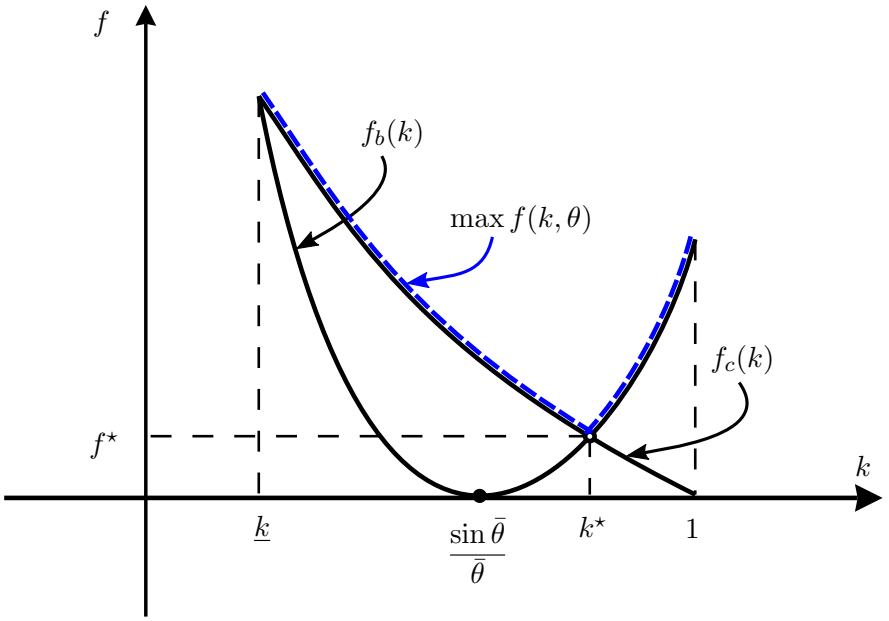

FIGURE 6.4: Illustrations of the critical function $f_c(k)$, the boundary function $f_b(k)$, and the function $\max f(k,\theta)$. The optimal solution is attained at the second intersection between $f_c(k)$ and $f_b(k)$.

Now, we will examine the boundary function. Since $f(k,\theta)|_{\theta=0} = 0$, the only boundary needing to be considered is $\theta = \bar{\theta}$. Denote $f_b(k)$ as the boundary function of $f(k,\theta)$. It can be evaluated as

$$f_b(k) = f(k,\theta)|_{\theta=\bar{\theta}} = \left(\frac{\sin\bar{\theta} - k\bar{\theta}}{\cos\bar{\theta}}\right)^2. \tag{6.30}$$

From (6.30), $f_b(k)$ is a parabolic function with respect to k, which attains zero at $k = \left(\sin\bar{\theta}\right)/\bar{\theta}$. At this point, properties of the critical function $f_c(k)$ and the boundary function $f_b(k)$ are clear. Their illustrations are depicted in Fig. 6.4. Note that $\max f(k,\theta) = \max\{f_b(k), f_c(k)\}$. Therefore, one could sketch the function $\max f(k,\theta)$ by the blue dash curve as shown in Fig. 6.4. The left part of the function $\max f(k,\theta)$ belongs to $f_c(k)$ and the right part belongs to $f_b(k)$. It is immediately recognized that $\max f(k,\theta)$ is a convex function. From that, it is not difficult to see that the minimizer $k^\star$ of the minimax optimization problem (6.13) is attained at the intersection between $f_c(k)$ and $f_b(k)$, namely $k^\star$ must satisfy

$$f_c(k^\star) = f_b(k^\star), \tag{6.31}$$

where $k^\star = 1/\left(\cos\theta_c^\star + \theta_c^\star \sin\theta_c^\star\right)$ and $\theta_c^\star$ is the critical point of $f(k^\star, \theta)$. By using (6.27) and (6.30), the condition in (6.31) can be expanded as follows

$$\left(\frac{\sin\theta_c^\star - \theta_c^\star\cos\theta_c^\star}{\cos\theta_c^\star + \theta_c^\star\sin\theta_c^\star}\right)^2 = \left(\frac{\sin\bar{\theta} - k^\star\bar{\theta}}{\cos\bar{\theta}}\right)^2. \tag{6.32}$$

The result in (6.32) can be further developed to

$$\begin{bmatrix} \sin\left(\theta_c^\star - \bar{\theta}\right) - \theta_c^\star\cos\left(\theta_c^\star - \bar{\theta}\right) = -\bar{\theta} & (6.33) \\ \sin\left(\theta_c^\star + \bar{\theta}\right) - \theta_c^\star\cos\left(\theta_c^\star + \bar{\theta}\right) = \bar{\theta}. & (6.34) \end{bmatrix}$$

It can be seen that (6.33) corresponds to the first intersection point (at $k = \underline{k}$) of $f_c(k)$ and $f_b(k)$ (see Fig. 6.4); hence, it does not indicate the optimal solution. The second intersection point given by (6.34) determines our desirable optimal solution. From this observation as well as the results of (6.23) and (6.24), the minimizer of the optimization problem is given by

$$k^\star = \frac{1}{\cos\theta^\star + \theta^\star\sin\theta^\star}, \tag{6.35}$$

where $\theta^\star$ is computed by $\sin\left(\bar{\theta} + \theta^\star\right) - \theta^\star\cos\left(\bar{\theta} + \theta^\star\right) = \bar{\theta}$. This completes the proof. □

The optimal solution of (6.13) can be found by solving the nonlinear equation (6.15). By using the Intermediate Value Theorem [162, p. 52], it is easy to show that, for all $\bar{\theta} \in [0,\ \pi/2)$, (6.15) has one and only one root $\theta^\star \in \left[0,\ \bar{\theta}\right]$. Therefore, (6.15) can be solved by any one-dimensional root-finding solver. For instance, if a bisection method is employed, the computational complexity for solving the nonlinear equation (6.15) is $\mathcal{O}(n)$ [163] and so is the minimax program (6.13).

Denote $L^\star(t) := L(t)|_{k=k^\star}$ as the optimal linearization law. Some important properties of the optimal solution are presented in the following corollary of Theorem 5.

Corollary 1. The optimal solution (6.14)–(6.15) of the minimax program (6.13) has the following properties:

1) $\lim\limits_{\bar{\theta}\to(\pi/2)^-} \theta^\star = \pi/2.$

2) $\lim\limits_{\bar{\theta}\to(\pi/2)^-} k^\star = 2/\pi.$

3) $\lim\limits_{\bar{\theta}\to(\pi/2)^-} \max\limits_{\theta\in[-\bar{\theta},\bar{\theta}]} |L^\star(t)| = 2g/\pi.$

Proof. Taking the limit as $\bar{\theta} \to (\pi/2)^-$ for both sides of (6.15) results in

$$\lim_{\bar{\theta}\to(\pi/2)^-} \left[\sin\left(\bar{\theta}+\theta^\star\right) - \theta^\star \cos\left(\bar{\theta}+\theta^\star\right)\right] = \pi/2. \tag{6.36}$$

By using the sum law, multiplication law, and the composite function law of the limit computation [162, p. 35] on (6.36), it can be obtained that

$$\cos z + z \sin z = \pi/2, \tag{6.37}$$

where $z = \lim_{\bar{\theta}\to(\pi/2)^-} \theta^\star$. It can be easily seen that (6.37) has only one solution, that is $z = \pi/2$. Therefore, $\lim_{\bar{\theta}\to(\pi/2)^-} \theta^\star = \pi/2$, which proves the property 1).

For the proof of the property 2), we can take the limit as $\bar{\theta} \to (\pi/2)^-$ for both sides of (6.14), which yields

$$\lim_{\bar{\theta}\to(\pi/2)^-} k^\star = \frac{1}{\cos z + z \sin z}. \tag{6.38}$$

By using the property 1), we have $\lim_{\bar{\theta}\to(\pi/2)^-} k^\star = 2/\pi$.

At the optimal solution, from (6.31), we have

$$\max_{\theta\in[-\bar{\theta},\bar{\theta}]} |L^\star(t)| = g\sqrt{f_c(k^\star)} = g\sqrt{f_b(k^\star)}. \tag{6.39}$$

Taking the limit as $\bar{\theta} \to (\pi/2)^-$ on (6.30) yields

$$\lim_{\bar{\theta}\to(\pi/2)^-} \sqrt{f_b(k^\star)} = \lim_{\bar{\theta}\to(\pi/2)^-} \frac{\sin\bar{\theta} - k^\star\bar{\theta}}{\cos\bar{\theta}}. \tag{6.40}$$

From the property 2), we have $\lim_{\bar{\theta}\to(\pi/2)^-} k^\star = 2/\pi$. Therefore, the limit in (6.40) is in a $0/0$ indeterminate form. Applying the L'Hôpital rule [162, p. 192] on (6.40) results in

$$\lim_{\bar{\theta}\to(\pi/2)^-} \sqrt{f_b(k^\star)} = \lim_{\bar{\theta}\to(\pi/2)^-} \frac{\cos\bar{\theta} - k^\star}{-\sin\bar{\theta}} = \frac{2}{\pi}. \tag{6.41}$$

Therefore, the result $\lim_{\bar{\theta}\to(\pi/2)^-} \max_{\theta\in[-\bar{\theta},\bar{\theta}]} |L^\star(t)| = 2g/\pi$ follows, which proves the property 3). □

Note that, the property 3) implies that the optimal linearization law is bounded for all swing angles $\theta \in (-\pi/2,\ \pi/2)$ by $2g/\pi$ if the gain $k^\star = 2/\pi$ is utilized. Let $L_1(t) := L(t)|_{k=1}$ be the conventional

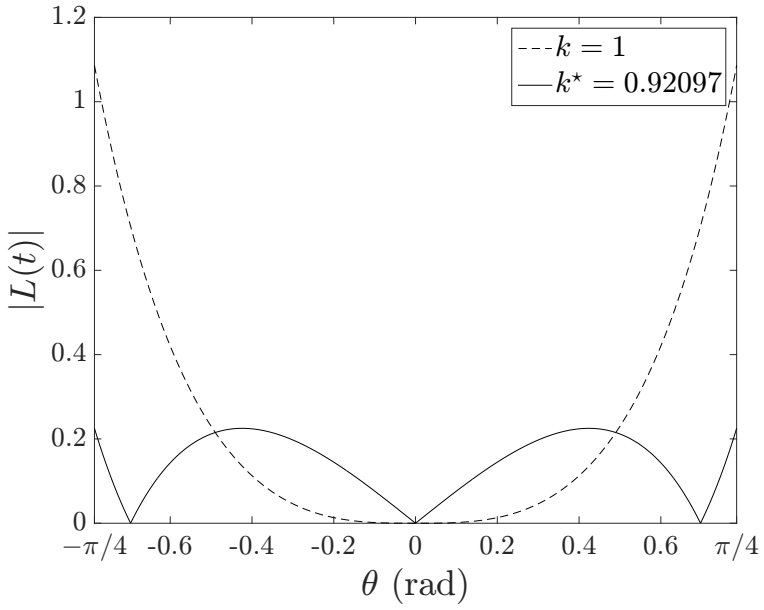

FIGURE 6.5: Magnitude comparison between the optimal linearization law ($k^\star = 0.92097$) and the non-optimal one ($k = 1$) with $\bar{\theta} = \pi/4$.

linearization law. It can be easily shown that when $\theta = \pm\bar{\theta}$, we have $\lim_{\bar{\theta}\to(\pi/2)^-} |L_1(t)| = +\infty$, which is unbounded. Therefore, the optimal linearization law is more favorable than the conventional one.

As an illustrative example, the optimization problem (6.13) will be solved by means of Theorem 5 with $\bar{\theta} = \pi/4$ rad. In the first step, $\theta^\star$ can be computed from (6.15) by *fzero* routine of MATLAB. Then, $k^\star$ can be easily determined by (6.14). The resultant optimal solution is $k^\star = 0.92097$. According to Fig. 6.5, the maximum magnitude of the optimal linearization law is only 0.225, which is significantly smaller than that of the conventional linearization law with $k = 1$, whose maximum value is 1.086.

So far, the optimal value $k^\star$ of k can be calculated by (6.14) and (6.15). Substituting the control law (6.12) (with a replacement of k by $k^\star$) into (6.6), the closed loop system is governed by

$$l\ddot{\theta}(t) + k^\star g\theta(t) = -a\sin(\omega_0 t) - b\cos(\omega_0 t). \tag{6.42}$$

In order to generate the resonance, it must be chosen that $\omega_0 = \sqrt{k^\star g/l}$. Note that, (6.42) is a second order differential equation under the excitation of a biased sinusoidal input; thus, it has an analytical solution. The solution of (6.42) can be derived by using the method of undetermined coefficients [155]. A summation of the homogeneous solution and the particular solution of (6.42) gives us:

$$\theta(t) = c_1\cos(\omega_0 t) + c_2\sin(\omega_0 t) + \frac{a}{2l\omega_0}t\cos(\omega_0 t) - \frac{b}{2l\omega_0}t\sin(\omega_0 t)\,, \tag{6.43}$$

where c_1 and c_2 are to-be-determined coefficients. By taking the first derivative of $\theta(t)$ in (6.43), it is obtained that

$$\begin{aligned}\dot{\theta}(t) = &- c_1\omega_0 \sin(\omega_0 t) + c_2\omega_0 \cos(\omega_0 t) + \frac{a}{2l\omega_0}\cos(\omega_0 t) \\ &- \frac{a}{2l}t\sin(\omega_0 t) - \frac{b}{2l\omega_0}\sin(\omega_0 t) - \frac{b}{2l}t\cos(\omega_0 t)\,. \end{aligned} \tag{6.44}$$

The initial conditions $\theta(0) = 0$ and $\dot{\theta}(0) = 0$ are respectively applied on (6.43) and (6.44) to solve for two unknowns c_1 and c_2. Consequently, we have $c_1 = 0$ and $c_2 = -a/\left(2l\omega_0^2\right)$. In summary, the solution of (6.42) can be expressed by

$$\begin{aligned}\theta(t) &= -\frac{a}{2l\omega_0^2}\sin(\omega_0 t) + \frac{a}{2l\omega_0}t\cos(\omega_0 t) - \frac{b}{2l\omega_0}t\sin(\omega_0 t) \\ \dot{\theta}(t) &= -\frac{b}{2l\omega_0}\sin(\omega_0 t) - \frac{a}{2l}t\sin(\omega_0 t) - \frac{b}{2l}t\cos(\omega_0 t)\,. \end{aligned} \tag{6.45}$$

By summing three sinusoidal functions with an identical frequency, $\theta(t)$ can be rewritten in a more compact form

$$\theta(t) = \Gamma(t)\sin(\omega_0 t + \Phi(t))\,. \tag{6.46}$$

In (6.46), $\Gamma(t)$ and $\Phi(t)$ are given by

$$\begin{aligned}\Gamma(t) &= \sqrt{\left(\frac{\gamma t}{2l\omega_0}\right)^2 + \left(\frac{a}{2l\omega_0^2}\right)^2 - \frac{\gamma a t\cos\varphi}{2l^2\omega_0^3}} \\ \Phi(t) &= \tan^{-1}\left[\frac{\gamma t\sin\varphi}{(-a/\omega_0) + \gamma t\cos\varphi}\right], \end{aligned}$$

where $\gamma = \sqrt{a^2 + b^2}$ and $\varphi = \tan^{-1}(-a/b)$. From (6.46), it is recognized that amplitude of the oscillation is $\Gamma(t)$. Furthermore, if $\gamma \neq 0$, we have

$$\begin{aligned}\lim_{t\to+\infty}\Gamma(t) &= \lim_{t\to+\infty}\sqrt{\left(\frac{\gamma t}{2l\omega_0}\right)^2 + \left(\frac{a}{2l\omega_0^2}\right)^2 - \frac{\gamma a t\cos\varphi}{2l^2\omega_0^3}} \\ &= +\infty. \end{aligned} \tag{6.47}$$

The result in (6.47) implies that the amplitude of $\theta(t)$ will approach to infinity as $t \to +\infty$, which clearly indicates the resonance phenomenon. In the following subsection, all of the unknowns a, b, $\bar{\theta}$, $\theta^\star$, and t_f will be determined to fulfill the tossing control requirements.

6.3.2 Embedding the tossing control requirements

In order to solve for five unknown parameters a, b, $\bar{\theta}$, $\theta^\star$, and t_f, the tossing control requirements (6.11) need to be employed. For the sake of clear presentation, denote $h(a, b, \bar{\theta}, \theta^\star, t) := \ddot{x}(t)$, where $\ddot{x}(t)$ is given by (6.12) with a replacement of k by $k^\star$. With the initial conditions $x(0) = \dot{x}(0) = 0$ (see Section 6.2), it can be easily obtained that

$$\dot{x}(t) = \int_0^t h(a, b, \bar{\theta}, \theta^\star, \sigma) d\sigma \tag{6.48}$$

$$x(t) = \int_0^t \int_0^\sigma h(a, b, \bar{\theta}, \theta^\star, \rho) d\rho d\sigma. \tag{6.49}$$

The double integration in (6.49) can be reduced to a single one by using the Cauchy' formula for repeated integral [164, p. 193], which results in

$$x(t) = \int_0^t (t - \sigma) h(a, b, \bar{\theta}, \theta^\star, \sigma) d\sigma. \tag{6.50}$$

From (6.48), the condition on zero trolley speed at t_f—$\dot{x}(t_f) = 0$—can be rewritten by

$$\int_0^{t_f} h(a, b, \bar{\theta}, \theta^\star, t) dt = 0. \tag{6.51}$$

By using (6.50), the condition on the target payload position at t_f—$x(t_f) - l \sin\theta(t_f) = \bar{x}_p$—can be exploited as below

$$-l \sin\theta(t_f) + \int_0^{t_f} (t_f - t) h(a, b, \bar{\theta}, \theta^\star, t) dt = \bar{x}_p. \tag{6.52}$$

The zero swing rate condition $\dot{\theta}(t_f) = 0$ can be developed by using (6.45), whose result is

$$-\frac{b}{2l\omega_0} \sin(\omega_0 t_f) - \frac{a}{2l} t_f \sin(\omega_0 t_f) - \frac{b}{2l} t_f \cos(\omega_0 t_f) = 0. \tag{6.53}$$

Now, we have four equations (6.15), (6.51)–(6.53) to solve for five unknowns. Thus, one missing equation can be filled in by setting $\theta(t_f) = -\bar{\theta}$. By using (6.45), it can be rewritten as

$$\frac{-a}{2l\omega_0^2} \sin(\omega_0 t_f) + \frac{t_f}{2l\omega_0} [a \cos(\omega_0 t_f) - b \sin(\omega_0 t_f)] = -\bar{\theta}. \tag{6.54}$$

In summary, to solve for five unknowns a, b, $\bar{\theta}$, $\theta^\star$, and t_f, we have the following set of five nonlinear equations

$$\begin{cases} \dfrac{-a}{2l\omega_0^2}\sin(\omega_0 t_f) + \dfrac{t_f}{2l\omega_0}\left[a\cos(\omega_0 t_f) - b\sin(\omega_0 t_f)\right] = -\bar{\theta} \\ -\dfrac{b}{\omega_0}\sin(\omega_0 t_f) - at_f\sin(\omega_0 t_f) - bt_f\cos(\omega_0 t_f) = 0 \\ \displaystyle\int_0^{t_f} h(a,b,\bar{\theta},\theta^\star,t)dt = 0 \\ l\sin\bar{\theta} - \displaystyle\int_0^{t_f} h(a,b,\bar{\theta},\theta^\star,t)tdt = \bar{x}_p \\ \sin\left(\bar{\theta}+\theta^\star\right) - \theta^\star\cos\left(\bar{\theta}+\theta^\star\right) = \bar{\theta}. \end{cases} \tag{6.55}$$

The MATLAB routine *fsolve* can be utilized to solve (6.55). Initial guesses of unknowns (for feeding to the *fsolve* solver) are $a_0 = 0$, $b_0 = 0$, $\bar{\theta}_0 = \pi/12$, $\theta_0^\star = \bar{\theta}_0/2$, and $t_{f0} = 2n\pi/\omega$ $(n = 1, 2, 3, \ldots)$ where $\omega = \sqrt{g/l}$. Note that, in order to ensure the maximum velocity and maximum acceleration constraints are strictly complied, namely $\max|\dot{x}(t)| \leq v_{\max}$ and $\max|\ddot{x}(t)| \leq a_{\max}$, the index n of t_{f0} can be gradually increased until those inequalities are met.

Remark 17. Since $\bar{\theta}$, $\theta^\star$, and t_f are required to be positive, in (6.55), the following changes of variables should be performed to ensure *fsolve* routine run properly: $\bar{\theta} = z_1^2$, $\theta^\star = z_2^2$, and $t_f = z_3^2$. Moreover, for safety, the payload should remain underneath the trolley, namely that magnitude of the terminal swing angle should not exceed $\pi/2$. In other words, it requires that $\bar{\theta} < \pi/2$. To guarantee such a condition for the resultant solution, the following auxiliary barrier equation is added to (6.55):

$$z_4 := \ln\left(\pi/2 - \bar{\theta}\right) = \ln\left(\pi/2 - z_1^2\right). \tag{6.56}$$

Therefore, at present, six unknowns need to be solved are a, b, z_i $(i = 1, \ldots, 4)$. Initial guesses for z_i $(i = 1, \ldots, 4)$ are made at $z_{10} = \sqrt{\bar{\theta}_0}$, $z_{20} = \sqrt{\theta_0^\star}$, $z_{30} = \sqrt{t_{f0}}$, and $z_{40} = \ln\left(\pi/2 - \bar{\theta}_0\right)$.

It is also worth noting that the resonance-based tossing controller only utilizes the rope length l in its design, which can be easily measured in practice. Therefore, parametric uncertainty is not a significant issue for the proposed method.

6.3.3 Transferring and returning phases

An entire cycle of the transportation is explained as follows. In the first half (or transferring phase), by employing the control law (6.12), the payload is transferred from the initial position to the discharging destination, at which the grab opens to drop down the materials. The second half (or returning

phase) starts immediately after the first half, where the trolley returns to the initial position to supply materials for the next cycle. Note that, at the end of the second half, the trolley speed must be zero and there should be no residual vibration. Since the controller (6.12) is independent of the payload mass m, one simple way to realize the above requirement is to apply $\ddot{x}(t)$ (in (6.12)) backward in time as the control input for the returning phase. The proof of this claim is provided as follows. Recall the dynamical model of the overhead crane in the transferring phase as below (see (6.6)):

$$l\ddot{\theta}(t) + g\sin\theta(t) = \cos\theta(t)\ddot{x}(t),\ t \in [0,\ t_f], \tag{6.57}$$

where, by assumption, the system starts from rest (see Section 6.2). Namely, the initial conditions of (6.57) are

$$x(0) = \dot{x}(0) = \theta(0) = \dot{\theta}(0) = 0. \tag{6.58}$$

Denote $\bar{x}$ as the terminal position of the trolley at the end of the transferring phase, that is to say, $\bar{x} = \bar{x}_p - l\sin\bar{\theta}$. Since the transferring phase employs the resonance-based tossing controller, the following terminal conditions of (6.57) are realized:

$$x(t_f) = \bar{x},\ \dot{x}(t_f) = 0,\ \theta(t_f) = -\bar{\theta},\ \dot{\theta}(t_f) = 0. \tag{6.59}$$

Now consider the model of the overhead crane system in the returning phase as below:

$$l\ddot{\theta}_r(\mu) + g\sin\theta_r(\mu) = \cos\theta_r(\mu)\ddot{x}_r(\mu),\ \mu \in [t_f,\ 2t_f]. \tag{6.60}$$

In (6.60), to draw a distinction with the transferring phase, the swing angle and the control input of the returning phase are denoted as θ_r and $\ddot{x}_r$ respectively. Since the returning phase starts immediately after the transferring phase, to realize the differentiable continuity condition of the solution, it requires that $\theta_r(t_f) = \theta(t_f)$, $\dot{\theta}_r(t_f) = \dot{\theta}(t_f)$, $x_r(t_f) = x(t_f)$, and $\dot{x}_r(t_f) = \dot{x}(t_f)$, namely that the initial conditions of (6.60) are assumed to be

$$x_r(t_f) = \bar{x},\ \dot{x}_r(t_f) = 0,\ \theta_r(t_f) = -\bar{\theta},\ \dot{\theta}_r(t_f) = 0. \tag{6.61}$$

The assumption of (6.61) will be checked at the end of the proof. Since the control input $\ddot{x}_r(\mu)$ is a backward-in-time version of the input $\ddot{x}(t)$, the following relation holds:

$$\ddot{x}_r(\mu) = \ddot{x}(2t_f - \mu),\ \forall \mu \in [t_f,\ 2t_f]. \tag{6.62}$$

By substituting (6.62) to (6.60), we have

$$l\ddot{\theta}_r(\mu) + g\sin\theta_r(\mu) = \cos\theta_r(\mu)\ddot{x}(2t_f - \mu),\ \mu \in [t_f,\ 2t_f]. \tag{6.63}$$

Performing the following time-reversing transformation without shifting/scaling the magnitude of the variable θ_r:

$$\tau = 2t_f - \mu,\ \psi = \theta_r. \tag{6.64}$$

From (6.64), the following results can be obtained:

$$d\tau = -d\mu,\ d\tau^2 = d\mu^2,\ d\psi = d\theta_r. \tag{6.65}$$

Applying the transformations of (6.64) and (6.65) on (6.63) results in the following differential equation:

$$l\ddot{\psi}(\tau) + g\sin\psi(\tau) = \cos\psi(\tau)\ddot{x}(\tau),\ \tau \in [0,\ t_f], \tag{6.66}$$

with the subsequent terminal conditions

$$x(t_f) = \bar{x},\ \dot{x}(t_f) = 0,\ \psi(t_f) = -\bar{\theta},\ \dot{\psi}(t_f) = 0. \tag{6.67}$$

After the transformation, the differential equation (6.66) (describing the returning phase dynamic) is identical with (6.57), which represents the dynamic of the transferring phase. Furthermore, their terminal conditions are also similar (see (6.59) and (6.67)). Hence, the conclusion is

$$\psi(\tau) = \theta(\tau),\ \dot{\psi}(\tau) = \dot{\theta}(\tau),\ \forall\tau \in [0,\ t_f]. \tag{6.68}$$

From (6.64), we have $\psi = \theta_r$ and by using $d\tau = -d\mu$ from (6.65), the result of (6.68) gives us

$$\theta_r(\mu) = \theta(\tau),\ \dot{\theta}_r(\mu) = -\dot{\theta}(\tau),\ \forall\tau \in [0,\ t_f]. \tag{6.69}$$

By employing the relation between two time frames $\tau = 2t_f - \mu$ on (6.69), we have

$$\theta_r(2t_f) = \theta(0) = 0,\ \dot{\theta}_r(2t_f) = -\dot{\theta}(0) = 0. \tag{6.70}$$

Furthermore, from (6.62), we have $\ddot{x}_r(\mu) = \ddot{x}(\tau)$, therefore

$$x_r(\mu) = x(\tau),\ \dot{x}_r(\mu) = -\dot{x}(\tau),\ \forall\tau \in [0,\ t_f]. \tag{6.71}$$

By using the relation $\tau = 2t_f - \mu$, (6.71) gives us

$$x_r(2t_f) = x(0) = 0,\ \dot{x}_r(2t_f) = -\dot{x}(0) = 0. \tag{6.72}$$

The results in (6.70) and (6.72) show that, at the end of the returning phase, the trolley returns to the initial position at zero speed and no residual vibration occurs. In order to finish the proof, the assumption on the differentiable continuity of the solution must be checked. From (6.69) and (6.71), by utilizing $\tau = 2t_f - \mu$, the following can be obtained:

$$x_r(t_f) = \bar{x},\ \dot{x}_r(t_f) = 0,\ \theta_r(t_f) = -\bar{\theta},\ \dot{\theta}_r(t_f) = 0, \tag{6.73}$$

which verifies (6.61). Consequently, the continuity assumption is satisfied. This completes the proof.

Remark 18. The tossing control requirement (6.11) implies that, at the discharging destination, only when all materials can be fully discharged from the grab bucket *instantaneously*, the positioning accuracy of the falling materials is perfectly ensured. Given that a 4-ton capacity grab bucket needs two seconds to drop its entire load, an absolute positioning accuracy may not be possible in reality. However, when the tossing control is applied, it can be guaranteed that the velocities of the payload (i.e., the grab bucket with materials inside) in both horizontal and vertical directions are zero at the discharging destination (see (6.11)). Consequently, in the neighborhood of the dropping point, the payload's velocities are sufficiently small for a discharge with an acceptable accuracy. Furthermore, the contact forces between particles of the granular materials as well as between particles and the inner wall of the grab bucket will make the stream of the dropping materials nearly vertical, despite having slight initial velocities. According to the above discussions, therefore, the grab can prematurely open one second (half of the grab's fully discharging time) before reaching the discharging destination, by which a satisfactory positioning accuracy is ensured. By using such a discharging operation, we can effectively prevent the falling materials spilling over the container without slowing down the transportation. The above discharging process can be observed in the operation of experienced crane operators. In summary, the discharging period is two seconds, whose center is the terminal time t_f obtained by solving (6.55).

6.4 Review of the minimum-time swing suppression control

In similarity to the resonance-based tossing control, the minimum-time swing suppression control is designed only for the transferring phase. Control input for the returning phase can be obtained by

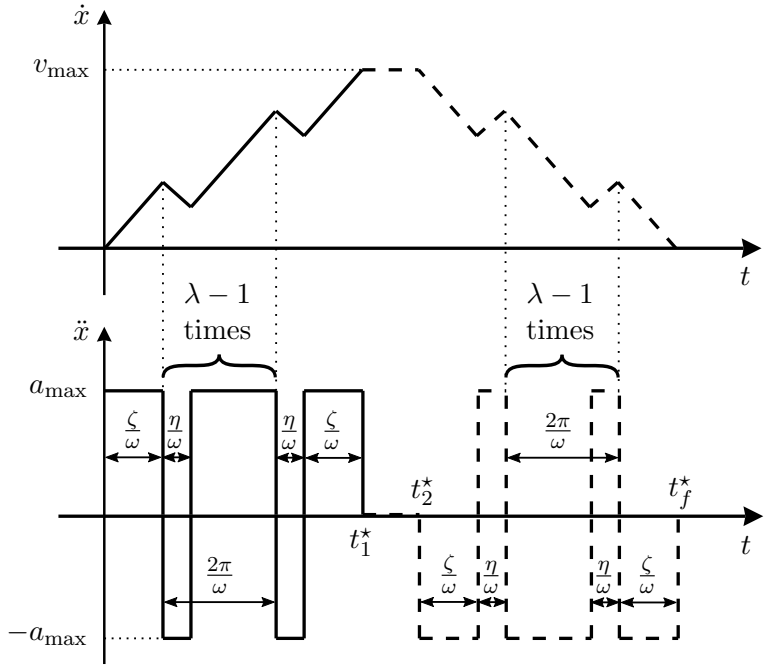

FIGURE 6.6: Minimum-time swing suppression control profile of the transferring phase. Note that 2λ is the switching numbers (between $a_{\max}$ and $-a_{\max}$) of the control input segment spanning from $t = 0$ to $t = t_1^\star$, which is represented by the solid line.

simply applying the computed input of the transferring phase backward in time.

In the transferring phase, the objective of the minimum-time swing suppression control is to transfer the payload to the discharging destination without vibration (i.e., $x(t_f^\star) = \bar{x}_p$, $\dot{x}(t_f^\star) = \dot{\theta}(t_f^\star) = 0$, *and* $\theta(t_f^\star) = 0$) in a minimum time $t_f^\star$. Note that $\omega = \sqrt{g/l}$. For a sufficient large transferring distance, a version of the minimum-time swing suppression control profile under the maximum velocity and maximum acceleration constraints is illustrated in Fig. 6.6, where a bang-bang control input suggested by the Pontryagin Minimum Principle is observed. Specifically, the dimensionless durations ζ and η are computed by [158, 160, 161]

$$\begin{aligned} K_m &= 2\zeta - (2\lambda - 1)\eta + 2(\lambda - 1)\pi \\ \eta &= 2\tan^{-1}\left(\frac{\sin\zeta}{2\lambda - \cos\zeta}\right), \end{aligned} \tag{6.74}$$

where $K_m := (\omega v_{\max})/a_{\max}$, $0 \leq \zeta \leq \pi$, $0 \leq \eta \leq \pi/2$, and the index $\lambda \in \mathbb{N}^+$ is chosen such that following condition must be fulfilled

$$2\pi\lambda > K_m > 2(\lambda - 1)\pi. \tag{6.75}$$

In addition, the important switching instants of the bang-bang control input in Fig. 6.6 are given by

$$\begin{aligned} t_1^\star &= \frac{2\zeta + \eta + 2(\lambda - 1)\pi}{\omega} \\ t_2^\star &= \frac{\bar{x}_p - 2\int_0^{t_1^\star}\int_0^t \ddot{x}(\sigma)d\sigma dt}{v_{\max}} + t_1^\star. \end{aligned} \tag{6.76}$$

The minimum transferring time is $t_f^\star = t_1^\star + t_2^\star$.

The computation process of the minimum-time swing suppression control is explained as follows. Firstly, the index λ should be determined by using (6.75). Then, ζ and η can be calculated by solving the system of two nonlinear equations (6.74) through, for instance, *fsolve* routine of MATLAB. Next, the time instants $t_1^\star$, $t_2^\star$, and $t_f^\star$ can be computed by using (6.76). From the above information, the minimum-time swing suppression control profile can be established as suggested by Fig. 6.6.

6.5 Simulation result: comparison with minimum-time swing suppression control

A real gantry crane in use at the harbor is utilized in the simulation study. It has a capacity of $\sim 65\%$ compared with the Sepetiba crane introduced in [63]. The maximum velocity and maximum acceleration are $v_{\max} = 1.5$ m/s and $a_{\max} = 0.6$ m/s^2. The rope length is $l = 20$ m. The resonance-based tossing control will be compared with the minimum-time swing suppression control in various discharging destination $\bar{x}_p$ ranging from 9 m to 20 m. Therefore, a discrete-value simulation test is configured as follows. Let Σ be the range of the discharging distance $\bar{x}_p$ as below:

$$\Sigma := \left\{ \bar{x}_p \in \mathbb{R}^+ : d \le \bar{x}_p \le D, d = 9 \text{ m}, D = 20 \text{ m} \right\}, \tag{6.77}$$

where $\mathbb{R}^+$ is the set of positive real numbers. The set Σ is uniformly discretized into $N = 1100$ points to form the following subset $\Sigma_D \subset \Sigma$:

$$\Sigma_D = \left\{ \bar{x}_p \in \Sigma : \bar{x}_p = d + i\frac{D-d}{N}, i \in \mathbb{N}, 0 \le i \le N \right\}. \tag{6.78}$$

Note that $\mathbb{N}$ is the natural numbers set. For each point of Σ_D, the solution of the concerning (tossing or vibration) controller will be solved by using the results in Section 6.3.2 and Appendix 6.4 respectively. The controller gives a positive result to the test if a solution exists for very member of Σ_D and satisfies the velocity constraint $|\dot{x}(t)| \le v_{\max}$ and the acceleration constraint $|\ddot{x}(t)| \le a_{\max}$ simultaneously.

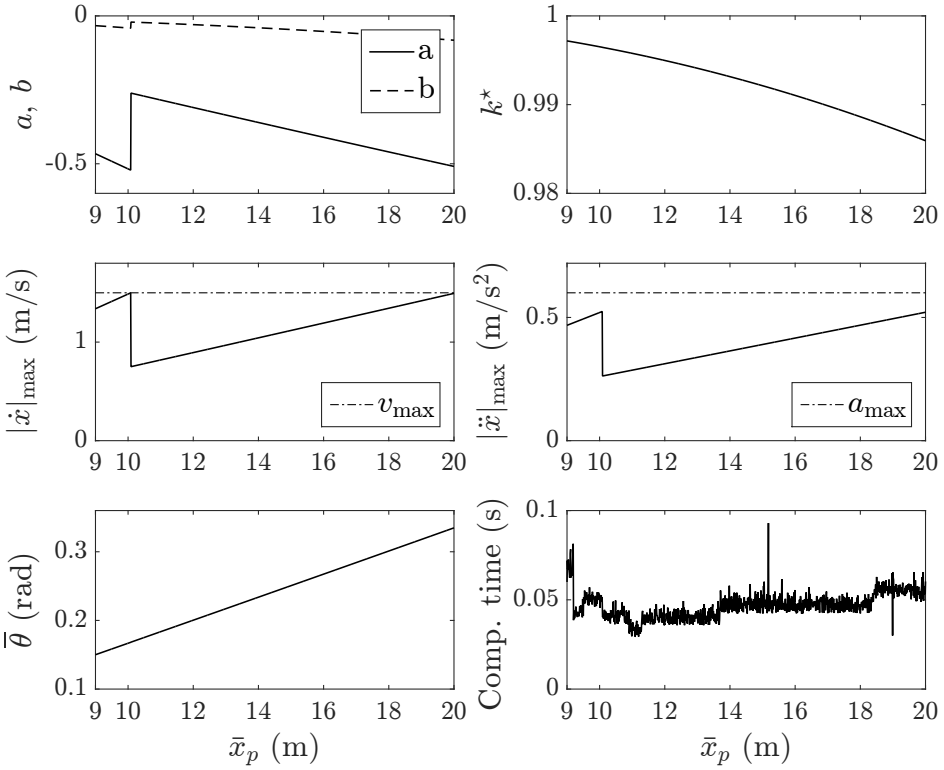

FIGURE 6.7: Computational result of the resonance-based tossing controller in the discrete-value simulation test.

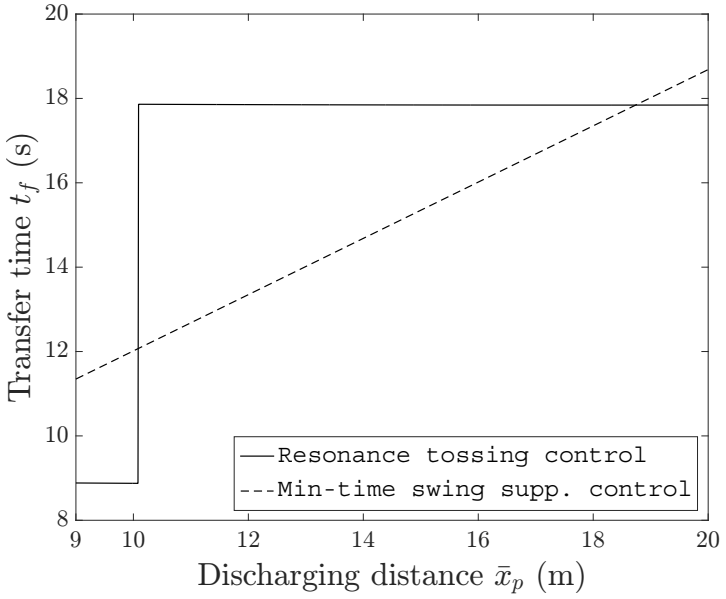

FIGURE 6.8: Comparison of the transferring time between the resonance-based tossing and the minimum-time swing suppression controls in the discrete-value simulation test.

TABLE 6.1: Computational results of the resonance-based tossing control and the minimum-time swing suppression control ($\bar{x}_p = 10$ m).

Proposed resonance-based tossing control							Minimum-time swing suppression control						
a	b	$\bar{\theta}$	$\theta^\star$	$k^\star$	t_f	$2t_f$	λ	ζ	η	$t_1^\star$	$t_2^\star$	$t_f^\star$	$2t_f^\star$
-0.517	-0.041	0.167 rad	0.084 rad	0.997	**8.86 s**	**17.72 s**	1	1.373	0.996	5.344 s	6.671 s	**12.01 s**	**24.02 s**

Firstly, the test will be applied to the resonance tossing control. The result is positive. The control parameters as well as the computational results of the test are shown in Fig. 6.7. It can be seen that the magnitude of the terminal swing angle $\bar{\theta}$ increases as the transferring distance increases, which agrees well with the physical intuition. Furthermore, $\bar{\theta}$ is always less than $\pi/2$, thus the safety condition is ensured. The maximum and average computational time are 0.093 second and 0.0467 second respectively on a personal computer with an Intel Core i5-3210M and 8 GB of RAM. Therefore, the applicability of the resonance tossing controller is verified.

The discrete-value simulation test is then carried out on the minimum-time swing suppression control. The transferring time comparison of the resonance tossing control and the minimum-time swing suppression control are shown in Fig. 6.8. According to Fig. 6.8, the resonance tossing control can provide a significantly faster transferring time than the minimum-time swing suppression control when $\bar{x}_p \in [9,\ 10.08]$ m, namely in configurations with short discharging destination. At its peak, for the discharging distance $\bar{x}_p = 10.08$ m, the transferring time of the resonance tossing control is 8.87 seconds, whereas the minimum-time swing suppression control needs 12.07 seconds. Therefore, by using the tossing control method, one can reduce the transferring time by 3.2 seconds (or 6.4 seconds in one transportation cycle). Thus, productivity can be enhanced up to 26.5%. This evidence confirms the main purpose of this chapter, and proves the possibility of breaking the time limitation of the minimum-time swing suppression control. For the long transferring distance contexts, the resonance tossing control is not able to produce a similar result. Here, the characteristic of the proposed tossing controller, which is inherited from the resonance behavior, can be clearly observed, namely that its transferring time lies in the neighborhood of $T, 2T, \ldots$, where T is the natural frequency of the closed-loop system.

In order to demonstrate a whole transportation process including both transferring and returning phases, two controllers are computed for the desired discharging distance $\bar{x}_p = 10$ m. The resultant control parameters of two controllers are aggregated in Table 6.1. Simulation results of two controllers are shown in Fig. 6.9. It can be seen that, at the center of the materials dropping/discharging period (represented by the solid blue line and the dash red line for the resonance-based tossing control and the minimum-time swing suppression control respectively), the payload reaches the target destination at

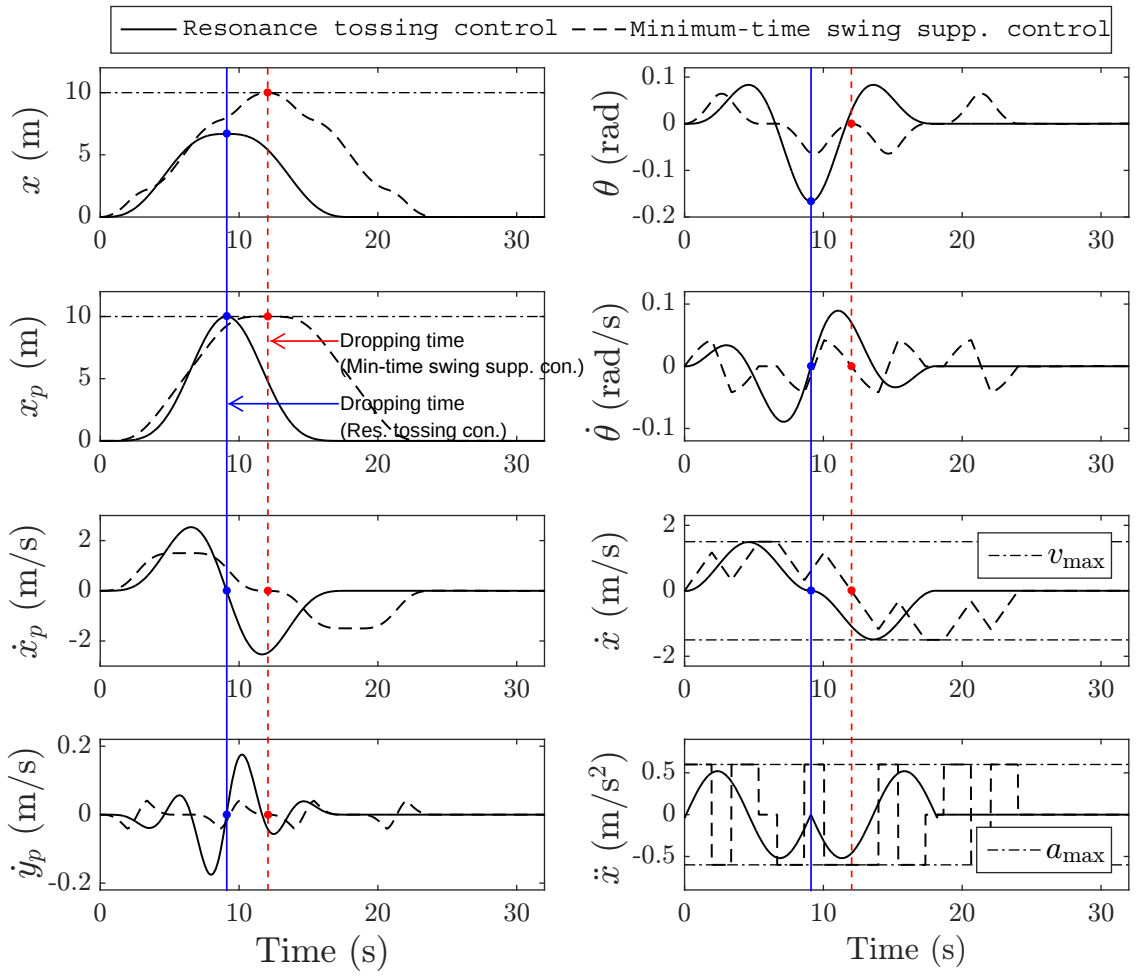

FIGURE 6.9: Comparative simulation results of the proposed resonance-based tossing control and the minimum-time swing suppression control.

zero horizontal and vertical velocities, whereas the trolley completely stops. Therefore, requirements of the transferring phase are fulfilled by both controllers. Moreover, at the end of the returning phase, in both control schemes, the vibration is completely suppressed. To sum up, two controllers satisfy the necessary conditions of the bulk materials transportation. The main difference between the proposed resonance-based tossing control and the minimum-time swing suppression control is explained as follows. At the dropping time, the swing angle in the case of tossing controller is $-\bar{\theta} = -0.167$ rad (or -9.57 degrees), whereas it is 0 degree when the minimum-time swing suppression control is employed (see θ graph in Fig. 6.9). This characteristic leads to the fact that, at the discharging point, the payload must not be exactly under the trolley in the tossing control case, which is completely in contrast to the minimum-time swing suppression control (see x and x_p graphs of Fig. 6.9). For this reason, if the actuator limits are sufficiently large (or the discharging distance is short), the tossing

controller can take full advantage of the long rope length to save the transferring time since the trolley is not required to travel a full distance as it does in the case of vibration controller (see subfigure x).

6.6 Experimental result

The proposed resonance-based tossing control now will be implemented on the same experimental overhead crane system shown in Section 4.5 of Chapter 4, which is illustrated in Fig. 4.11. The rope length used in this chapter is $l = 1.4$ m. Based on specifications of the servo motor and the transmission system, values of the maximum velocity and the maximum acceleration are given by $v_{\max} = 0.8$ m/s and $a_{\max} = 1$ m/s^2 respectively. The target horizontal position of the payload is $\bar{x}_p = 1.2$ m. According to the result of Section 6.3, parameters of the resonance tossing control for the experimental configuration can be computed as $a = -0.8763$, $b = -0.1187$, $\bar{\theta} = 0.2861$ rad, $\theta^\star = 0.1444$ rad, $k^\star = 0.9897$, and $t_f = 2.336$ seconds. The computational time is only 0.14 second; thus, online command generation is feasible. Note that, the resonance-based tossing controller is realized as a feedforward scheme, namely that it is offline computed and integrated twice to obtain a control law in the position level, which is equivalent to (6.50). This position command will be realized by a built-in motion controller of the servo driver to drive the trolley motion. For clarification, the measured swing angle is recorded for a sole purpose of verifying the validity of the proposed controller in practice. To illustrate the independence (or robustness) of the proposed resonance tossing control law with respect to the payload mass, two experiments with a 25 kg and a 30 kg payload are conducted. In both cases, the same controller parameters computed as above are employed. Fig. 6.10 depicts the experimental results of the resonance tossing controller. The system responses in two cases (25 kg and 30 kg payload) are almost identical, which indicates that the proposed controller is robust against the change of the payload mass. The payload is precisely transferred to the destination with zero horizontal and vertical velocities; afterward, it is brought back to the initial position with no residual vibration. Note that, the noise level of the experimental acceleration signal, which is obtained by differentiating the measured position (from an encoder attached at the end of the servo motor) twice, is very high even though a low-pass filter is employed; hence, it is not present in Fig. 6.10. Such an observation noise has no effect to the system performance. The experimental data completely agrees with the simulation result, which verifies the effectiveness of the proposed resonance-based tossing control system.

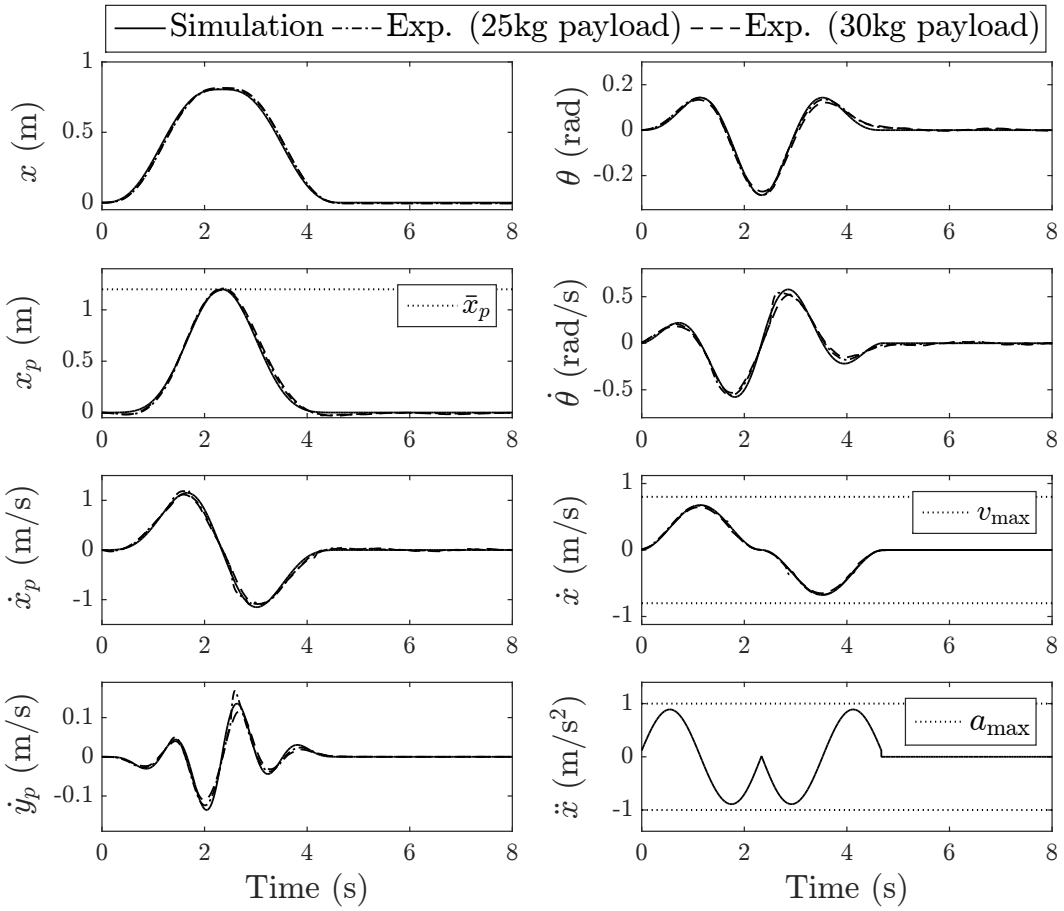

FIGURE 6.10: Experiment (Exp.) results of the resonance tossing control. They are in a complete agreement with the simulation result.

6.7 Summary

This chapter proposed a resonance-based tossing controller for an overhead crane to suit the context of bulk materials transportation. The analysis showed that both tossing control and vibration control groups can realize the requirements of the bulk materials transferring process. The crucial conclusion of the chapter emphasizes on the result that there are possibilities to break the time limitation of the minimum-time vibration controller—the fastest member of the vibration control family—by using the tossing control methodology. Both simulation and experimental results are provided to clarify the effectiveness of the proposed method and they are in a complete agreement. Possible developments will be elaborated in Chapter 7 to further enhance productivity of the bulk materials transportation in future.

Chapter 7

Conclusions and Recommendations for Future Work

7.1 Conclusions

This thesis proposed a number of control schemes to address both skew and swing vibration control problems of cranes. Most of the theoretical results of the thesis were verified by actual experiments. Also, the simulation results resembled well with the experimental data, showing that the entire modelings and control designs are correct, and that the proposed approaches are sufficiently practical. The detailed summary of each chapter is elaborated as follows.

Part I (Skew vibration control of cranes):

- Chapter 2 established robust controllers to address the robust skew vibration control problem. The results indicated that the integral sliding mode controller outperformed the dynamic output feedback H_∞ controller. This can be explained by the fact that the structure of the integral sliding mode controller enables the payload to track its reference *and* reference rate. The H_∞ controller does not possess such a capability.
- Chapter 3 investigated the possibility of reducing energy consumption without trading-off the sub-optimal transfer time for the skew rotation process of cranes. This objective was achieved using a switched optimal control scheme with the aid of an additional binary actuator, which is an electro-mechanical clutch. In the same minimum transfer time, the switched optimal control

system can save 25.49% and 61.70% of the consumed energy in the medium and long transfer cases, respectively, in comparison with the no-switched time-optimal control system. Also, compared with the input shaping and integral sliding mode controllers, the switched optimal controller can significantly reduce both transfer time and total energy consumption.

Part II (Swing vibration control of cranes):

- Chapter 4 established minimum-time zero-vibration S-curve commands for an overhead crane system with actuator limits, including maximum allowable acceleration and velocity. A parameterized bang-off-bang acceleration profile was used in both the embedding and shaping techniques to formulate constrained (discrete) nonlinear programs. These optimization problems can be solved in an online fashion, and thus online command generation was feasible. It was also shown that the proposed minimum-time S-curve commands are faster than those of the relevant studies [140, 141] in terms of transfer time.
- Chapter 5 introduced a model reference input shaping control design for the luffing dynamics of a rotary crane. The newly established technique can completely suppress the swing oscillation for a highly nonlinear time-varying system. This cannot be achieved if standard input shaping controllers were employed.
- Chapter 6 pursued a different direction of vibration suppression control, i.e., the use of vibration excitation control to further reduce the transfer time in the context of bulk material transport. In such a framework, a resonance-based tossing control law was proposed, and it was shown that both the vibration suppression and excitation controls can accomplish the task. However, under the same conditions and actuator constraints, the resonance tossing control can reduce the transfer time up to 26.5% compared with the well-known minimum-time swing suppression controller, which is the fastest member of the swing suppression control group. Therefore, it was found that the vibration suppression control is not always the best option in every situation.

To sum up, various vibration control schemes for crane systems have been formulated in this thesis. A general remark on the usage of the proposed controllers is explained as follows. For the large blocks transport, the vibration suppression controls (i.e., integral sliding mode control, H_∞ control, switched optimal control, minimum-time S-curve commands, and model reference input shaping control) should be utilized, whereas the vibration excitation control using resonance-based tossing controller (Chapter 6) can be employed in the case of bulk material transport to enhance the transfer productivity. Among the established skew vibration suppression schemes, the integral sliding mode control and H_∞

control should be used when severe parametric uncertainties and disturbances are present. It was also shown in Chapter 2 that the integral sliding mode control is a more preferable candidate. For indoor environments, where the disturbance is less harsh, the switched optimal control (Chapter 3) can be used to reduce both transfer time and energy consumption. In regard to the swing suppression control, the minimum-time S-curve commands (Chapter 4) are most suitable for a transfer process with a constant rope length due to their simplicity and ease of implementation. In the case of time-varying rope length, the model reference input shaping control (Chapter 5) should be employed.

7.2 Recommendations for Future Work

A number of possible future developments can be drawn from the thesis, and they are summarized as follows.

Part I (Skew vibration control of cranes):

- More diverse types of controls should be applied to address the robust skew vibration control problem of cranes. In Chapter 2, only non-adaptive integral sliding mode and H_∞ controllers were formulated. In the future, adaptive robust controls should be investigated to deal with not only parametric uncertainties but also external disturbances caused by wind, sea heaves, etc.
- The computational time of the switched optimal controller in Chapter 3 should be improved to enhance the practicability of the switched optimal control system. The fast nonlinear model predictive control technique is a promising solution.

Part II (Swing vibration control of cranes):

- In Chapter 4, the minimum-time zero-vibration S-curve commands of a two-dimensional overhead crane were derived under actuator limitation constraints and the constant rope length assumption. This result can be extended to three-dimensional gantry/rotary crane systems with time-varying rope lengths and by adding state constraints (e.g., maximum allowable swing angle and swing rate). Furthermore, the nonlinear transverse flexibility of the rope, which appears when the payload is very light and/or when disturbances (e.g., wind) exert on the cable, should be considered in the control design process.
- In Chapter 5, only the luffing dynamics of the rotary crane with a time-varying rope length was considered. In the future, the model reference input shaping control design presented in

Chapter 5 should be extended to a complete three-dimensional rotary crane system with a full set of simultaneous motions, including luffing, skewing, and hoisting.

- In Chapter 6, it has been shown that, compared with the classical minimum-time vibration suppression control, it is possible to reduce the transfer time for the transportation of bulk materials by using the tossing control methodology. This result, therefore, indicates the importance of further research on the topic. A specific type of tossing controller, which is based on the phenomenon of mechanical resonance, was introduced in Chapter 6 to realize the transportation requirements. Nevertheless, in some configurations, the transfer time using the resonance-based tossing controller is slower than the minimum-time vibration control. Note that the objective of both tossing and vibration controls is to reduce the transferring time as much as possible. As a result, the use of a particular controller varies according to the circumstances. In order to address this issue, a *unified minimum-time controller*, which satisfies the requirements of the bulk materials transfer process (stated in Section 6.1) in minimum-time, should be formulated in the future. Also, actuator limits, including the maximum velocity and maximum acceleration, must be taken into account. The Pontryagin Minimum Principle is the main tool for designing such a controller. There may have two important points. First, the terminal swing angle $\theta(t_f)$ should be free rather than constrained by $\theta(t_f) = 0$ as in the case of vibration control. If the time-optimal solution requires that $\theta(t_f) \neq 0$, then the unified minimum-time control is actually a minimum-time tossing controller; otherwise, it is a minimum-time vibration controller. Thus, it is guaranteed that the unified minimum-time controller is the best choice among the tossing and vibration control groups. Second, since a large swing angle may occur, a nonlinear model must be utilized, and therefore an analytical solution of the unified minimum-time control might not be possible. As a result, a computational nonlinear optimal control scheme may be needed. Additionally, in order to increase the maneuverability, time-varying rope lengths and a unified minimum-time control design for three-dimensional crane systems should be considered.

Moreover, the swing and skew dynamics of crane systems were independently treated in this thesis. Therefore, it is interesting to investigate the interference between the swing and skew dynamics in future works. As such, simultaneous swing and skew vibration controllers should be established to concurrently achieve precise position and orientation controls for crane systems.

Finally, the proposed controllers in this thesis were applied only on laboratory systems. Therefore, they should be implemented on real-size cranes, as this is the ultimate goal of any research and development activities. We are preparing to install some of the controllers introduced in this thesis on gigantic cranes as part of the joint research project with Iknow Machinery, Co., Ltd., Japan.

Appendix A

General Solution

This appendix provides detail of the extended CG scheme, which is used by the general solution described in Section 3.6.3 to solve the switched optimal control seeking stage (stage (a) of Algorithm 4).

In the first step, necessary conditions of optimality will be derived by means of the following lemma.

Lemma 2. Consider the optimal control problem (3.31). Assuming that the switching instants are now fixed. The necessary conditions for optimality are given as

$$\dot{\boldsymbol{x}} = \begin{cases} \boldsymbol{f}_k(\boldsymbol{x}) + \boldsymbol{b}_k(\boldsymbol{x})u_k & (k=1,3) \\ \boldsymbol{f}_k(\boldsymbol{x}) & (k=2) \end{cases}, \text{ if } t \in \mathbb{T}_k. \tag{A.1}$$

$$\dot{\boldsymbol{\lambda}}(t) = -\left(\frac{\partial H_k}{\partial \boldsymbol{x}}\right)^\top \quad (k=1,2,3), \text{ where} \tag{A.2}$$

$$H_k \triangleq \begin{cases} L(\boldsymbol{x}) + \boldsymbol{\lambda}^\top \left(\boldsymbol{f}_k(\boldsymbol{x}) + \boldsymbol{b}_k(\boldsymbol{x})u_k\right) & (k=1,3) \\ L(\boldsymbol{x}) + \boldsymbol{\lambda}^\top \boldsymbol{f}_k(\boldsymbol{x}) & (k=2) \end{cases},$$

$$\boldsymbol{\lambda}(t_f) = \left(\frac{\partial \phi_g\left(\boldsymbol{x}(t_f)\right)}{\partial \boldsymbol{x}(t_f)}\right)^\top, \tag{A.3}$$

$$\boldsymbol{\lambda}(t_k^+) = \boldsymbol{\lambda}(t_k^-) \quad (k=1,2), \tag{A.4}$$

$$u_k = \begin{cases} u_{\max} & \text{if } \dfrac{\partial H_k}{\partial u_k} < 0 \\ -u_{\max} \le u_k \le u_{\max} & \text{if } \dfrac{\partial H_k}{\partial u_k} = 0 \\ -u_{\max} & \text{if } \dfrac{\partial H_k}{\partial u_k} > 0 \end{cases}, \ (k=1,3). \tag{A.5}$$

The proof of Lemma 2 is conducted in a similar manner with [130, p.73], and therefore it is omitted here. Note that in Lemma 2, (A.1) represents the switched system dynamic in each time interval. Conditions of the costate vector $\boldsymbol{\lambda}(t)$ are given in (A.2)–(A.4). The bounded optimal control input of each interval must satisfy (A.5).

Based on Lemma 2, the following extended clipping-off CG algorithm is proposed to solve the switched optimal control problem subject to the fixed switching instants posed in the stage (a). From (A.5), it is motivated to define 2 sub-interval point sets, "unsaturated-control sub-interval points" $\mathbb{U}_j^i$ and "saturated-control sub-interval points" $\mathbb{S}_j^i$ of jth interval ($j = 1, 3$) at ith iteration, as follows.

$$\mathbb{S}_j^i = \left\{ t \in \mathbb{T}_j : \left| u_j^i(t) \right| = u_{\max} \text{ and } \operatorname{sgn}(u_j^i(t)) = -\operatorname{sgn}(g_j^i(t)) \right\}, \tag{A.6}$$

$$\mathbb{U}_j^i = \mathbb{T}_j - \mathbb{S}_j^i, \tag{A.7}$$

where $g_j^i(t) \triangleq \partial H_j^i / \partial u_j^i$ and "sgn" represents a usual signum function. In Algorithm 5, the notation $(.)_j^i(t)$ denotes the value of the function $(.)$ at ith iteration and in jth interval.

Algorithm 5: Extended clipping-off CG algorithm for solving the bounded optimal control input in respect of fixed switching instants and fixed terminal time.

Step 1 At every time step $t \in \mathbb{T}_1 \cup \mathbb{T}_3$, giving an an admissible initial guess of the optimal control input $\boldsymbol{u}^0(t) = \left[u_1^0(t),\ u_3^0(t)\right]^\top \in \Omega$. Solving the state equation (A.1) forward and costate equation (A.2) backward in time. Compute $\boldsymbol{g}^0(t) = \left[g_1^0(t),\ g_3^0(t)\right]^\top = \left[\dfrac{\partial H_1^0}{\partial u_1^0},\ \dfrac{\partial H_3^0}{\partial u_3^0}\right]^\top$ by employing the continuity condition in (A.4). Let the initial search direction as $\boldsymbol{p}^0(t) \triangleq \left[p_1^0(t),\ p_3^0(t)\right]^\top = -\boldsymbol{g}^0(t)$.

Step 2 Choose a scalar step-size α^0 such that $J_g\left(\left\{\boldsymbol{u}^0 + \boldsymbol{\varepsilon}^0 \boldsymbol{p}^0\right\}_{\boldsymbol{s}}\right)$ is minimized by means of any one dimensional linesearch, where the value of $\boldsymbol{\varepsilon}^0$ at the time step t is given as $\boldsymbol{\varepsilon}^0(t) = \left[\varepsilon_1^0(t),\ \varepsilon_3^0(t)\right]^\top$ and

$$\varepsilon_j^0(t) = \begin{cases} 0 & \text{if } t \in \mathbb{S}_j^0 \\ \alpha^0 > 0 & \text{if } t \in \mathbb{U}_j^0 \end{cases}, \ (j = 1, 3). \tag{A.8}$$

For clarification, $\left\{\boldsymbol{u}^0 + \boldsymbol{\varepsilon}^0 \boldsymbol{p}^0\right\}_{\boldsymbol{s}}$ at t is given by

$$\left\{\boldsymbol{u}^0 + \boldsymbol{\varepsilon}^0 \boldsymbol{p}^0\right\}_{\boldsymbol{s}} = \begin{bmatrix} \left\{u_1^0(t) + \varepsilon_1^0(t) p_1^0(t)\right\}_s \\ \left\{u_3^0(t) + \varepsilon_3^0(t) p_3^0(t)\right\}_s \end{bmatrix}, \tag{A.9}$$

and

$$\{(.)\}_s = \begin{cases} (.) & \text{if } |(.)| \le u_{\max} \\ u_{\max} & \text{if } (.) > u_{\max} \\ -u_{\max} & \text{if } (.) < -u_{\max}. \end{cases} \tag{A.10}$$

Let $\boldsymbol{u}^1 = \left\{\boldsymbol{u}^0 + \boldsymbol{\varepsilon}^0\boldsymbol{p}^0\right\}_{\boldsymbol{s}}$ and $i = 1$.

Step 3 At each t, determine the next search direction $\boldsymbol{p}^i(t) = \left[p_1^i(t),\ p_3^i(t)\right]^\top$ as follows

$$p_j^i(t) = \begin{cases} -g_j^i(t) + \beta_j^i p_j^{i-1}(t) & \text{if } t \in \mathbb{U}_j^i, \\ -g_j^i(t) & \text{if } t \in \mathbb{S}_j^i, \end{cases} \tag{A.11}$$

where $j = 1, 3$ and

$$\beta_j^i = \begin{cases} (\beta_0^i)_j & \text{if } (\beta_0^i)_j < (\beta_m^i)_j \\ \gamma^i(\beta_m^i)_j & \text{if } (\beta_0^i)_j \ge (\beta_m^i)_j,\ 0 < \gamma^i < 1 \\ 0 & \text{if } (I_2^i)_j = 0 \text{ or } (I_3^i)_j = 0, \end{cases} \tag{A.12}$$

with $(\beta_0^i)_j \triangleq \dfrac{(I_1^i)_j}{(I_2^i)_j},\ (I_2^i)_j \neq 0;\ (\beta_m^i)_j \triangleq \dfrac{(I_1^i)_j}{(I_3^i)_j},\ (I_3^i)_j \neq 0$, and

$$\begin{aligned} (I_1^i)_j &= \int\limits_{t\in\mathbb{U}_j^i} g_j^i(t) g_j^i(t) dt \\ (I_2^i)_j &= \int\limits_{t\in\mathbb{U}_j^i} g_j^{i-1}(t) g_j^{i-1}(t) dt \\ (I_3^i)_j &= \int\limits_{t\in\mathbb{U}_j^i} g_j^i(t) p_j^{i-1}(t) dt. \end{aligned} \tag{A.13}$$

Step 4 Choose a step-size α^i to minimize $J_g\left(\left\{\boldsymbol{u}^i + \boldsymbol{\varepsilon}^i\boldsymbol{p}^i\right\}_{\boldsymbol{s}}\right)$ in the similar manner with Step 2, then let $\boldsymbol{u}^{i+1} = \left\{\boldsymbol{u}^i + \boldsymbol{\varepsilon}^i\boldsymbol{p}^i\right\}_{\boldsymbol{s}}$ and $i \leftarrow i + 1$. Go to Step 5.

Step 5 Repeat Step 3 and Step 4 until $\left|J_g(\boldsymbol{u}^{i+1}) - J_g(\boldsymbol{u}^i)\right| < \delta\left|J_g(\boldsymbol{u}^{i+1})\right|$ or $J_g(\boldsymbol{u}^{i+1}) < J_{tol}$ where $\delta > 0$ regards to tolerance at which the algorithm is said to be converged. Here, the tolerance δ is chosen as $\delta = 10^{-6}$.

In Steps 2 and 4 of Algorithm 5, the minimizer α^i of $J_g\left(\left\{\boldsymbol{u}^i + \boldsymbol{\varepsilon}^i\boldsymbol{p}^i\right\}_{\boldsymbol{s}}\right)$ can be obtained by any 1D linesearch algorithm, e.g., the golden section method [165]. Specifically, a high–low–high geometry pattern of the cost functional J_g with respect to α^i should be found beforehand to determine the feasible searching interval. The convergence analysis of Algorithm 5 is shown in Appendix B.

Appendix B

Convergence Analysis of Algorithm 5

In this appendix, inspired from [128], a convergence analysis is carried out for Algorithm 5 of Appendix A. By means of the one-dimensional linesearch in Step 4, variation of the control input u_j^i in jth interval at ith iteration is given as follows

$$\delta u_j^i = \begin{cases} \alpha^i p_j^i(t) & \text{if } t \in \mathbb{U}_j^i \\ 0 & \text{if } t \in \mathbb{S}_j^i \cup \mathbb{T}_2 \end{cases}, (j = 1, 3). \tag{B.1}$$

Due to (B.1) and (A.2)-(A.4), variation of the cost functional J_g^i at ith iteration is described by

$$\delta J_g^i = \int_{t_0}^{t_f} \frac{\partial H}{\partial u} \delta u \Big|^i dt = \sum_{j=1,3} \int_{t_{j-1}}^{t_j} \frac{\partial H}{\partial u} \delta u \Big|_j^i dt \tag{B.2}$$

$$= \alpha^i \sum_{j=1,3} \int_{\mathbb{U}_j^i} g_j^i(t) p_j^i(t) dt. \tag{B.3}$$

It is noted that $t_3 \triangleq t_f$. Substituting (A.11) into (B.3) results in

$$\delta J_g^i = \alpha^i \sum_{j=1,3} \int_{\mathbb{U}_j^i} \left[-g_j^i(t) g_j^i(t) + \beta_j^i g_j^i(t) p_j^{i-1}(t) \right] dt \tag{B.4}$$

$$= \alpha^i \sum_{j=1,3} \left[-(I_1^i)_j + \beta_j^i (I_3^i)_j \right] \tag{B.5}$$

According to (A.12)–(A.13), $-(I_1^i)_j + \beta_j^i (I_3^i)_j < 0$ can always be guaranteed and by $\alpha^i > 0$ thus $\delta J_g^i < 0$. Therefore, it can be obtained that $J_g(\boldsymbol{u}^{i+1}) < J_g(\boldsymbol{u}^i)$, $i = 0, 1, 2, \ldots$ From this, Algorithm 5

will converge to a local minimum $J_g(\boldsymbol{u}^\star)$. When a local minimum $J_g(\boldsymbol{u}^\star)$ is reached as $i \to \infty$, the following conditions hold

$$g_j^i(t) = g_j^{i-1}(t) \text{ and } p_j^i(t) = p_j^{i-1}(t),\ (j = 1, 3). \tag{B.6}$$

Furthermore, since $\delta J_g^i = 0$, from (B.3) and (B.4), it results in

$$\begin{cases} \sum\limits_{j=1,3} \int\limits_{\mathbb{U}_j^i} g_j^i(t) p_j^i(t) dt = 0 \\ \sum\limits_{j=1,3} \int\limits_{\mathbb{U}_j^i} \left[-g_j^i(t) g_j^i(t) + \beta_j^i g_j^i(t) p_j^{i-1}(t) \right] dt = 0. \end{cases} \tag{B.7}$$

In (B.7), by employing (B.6) and substituting the upper equation into the lower equation, it can be reduced to

$$\sum_{j=1,3} \int_{\mathbb{U}_j^i} g_j^i(t) g_j^i(t) dt = 0, \tag{B.8}$$

which results in

$$g_j^i(t) \equiv 0 \text{ for every } t \text{ in } \mathbb{U}_j^i,\ (j = 1, 3). \tag{B.9}$$

By the constructions of "saturated-control sub-interval points" as in (A.6) and the result in (B.9), necessary conditions of an optimal control input for the switched system in the stage (a) (as found in (A.5)) are now fulfilled. This completes the proof.

References

[1] L. Shapiro and J. Shapiro, *Cranes and Derricks*, 4th ed. New York: McGraw-Hill Education, 2010.

[2] A. Arena, A. Casalotti, W. Lacarbonara, and M. P. Cartmell, "Dynamics of container cranes: three-dimensional modeling, full-scale experiments, and identification," *Int. J. of Mechanical Sciences*, vol. 93, pp. 8 – 21, 2015.

[3] N. Q. Hieu and K. S. Hong, "Skew control of a quay container crane," *J. of Mechanical Science and Technology*, vol. 23, no. 12, pp. 3332–3339, Dec 2009.

[4] L. Morrish, M. P. Cartmell, and A. J. Taylor, "Geometry and kinematics of multicable spreader lifting gear," *Proc. Inst. of Mech. Eng., Part C: J. of Mech. Eng. Sci.*, vol. 211, no. 3, pp. 185–194, 1997.

[5] E. M. Rahman, A. H. Nayfeh, and Z. N. Masoud, "Dynamics and control of cranes: A review," *J. of Vibration and Control*, vol. 9, no. 7, pp. 863–908, 2003.

[6] L. Ramli, Z. Mohamed, A. M. Abdullahi, H. I. Jaafar, and I. M. Lazim, "Control strategies for crane systems: A comprehensive review," *Mechanical Systems and Signal Processing*, vol. 95, pp. 1 – 23, 2017.

[7] K. Yoshida and H. Kawabe, "A design of saturating control with a guaranteed cost and its application to the crane control system," *IEEE Trans. on Automatic Control*, vol. 37, no. 1, pp. 121–127, Jan 1992.

[8] G. Corriga, A. Giua, and G. Usai, "An implicit gain-scheduling controller for cranes," *IEEE Trans. on Control Systems Technology*, vol. 6, no. 1, pp. 15–20, Jan 1998.

[9] M. A. Karkoub and M. Zribi, "Robust control schemes for an overhead crane," *J. of Vibration and Control*, vol. 7, no. 3, pp. 395–416, 2001.

[10] A. D. G. Hazlerigg, "Automatic control of crane operations," *IFAC Proc. Volumes*, vol. 5, no. 1, Part 1, pp. 250 – 258, 1972.

[11] H. H. Lee, "Modeling and control of a three-dimensional overhead crane," *J. of Dynamic Systems, Measurement, and Control*, vol. 120, no. 4, pp. 471–476, Dec 1998.

[12] O. Sawodny, H. Aschemann, and S. Lahres, "An automated gantry crane as a large workspace robot," *Control Engineering Practice*, vol. 10, no. 12, pp. 1323 – 1338, 2002.

[13] N. Uchiyama, "Robust control of rotary crane by partial-state feedback with integrator," *Mechatronics*, vol. 19, no. 8, pp. 1294 – 1302, 2009.

[14] Y. Mori and Y. Tagawa, "Vibration controller for overhead cranes considering limited horizontal acceleration," *Control Engineering Practice*, vol. 81, pp. 256 – 263, 2018.

[15] J. Lévine, *Analysis and Control of Nonlinear Systems: A Flatness-based Approach.* Berlin, Heidelberg: Springer-Verlag, 2009.

[16] G. G. Rigatos, *Nonlinear Control and Filtering Using Differential Flatness Approaches.* Cham, Switzerland: Springer, 2015.

[17] F. Boustany and B. d'Andrea-Novel, "Adaptive control of an overhead crane using dynamic feedback linearization and estimation design," in *Proc. of the IEEE Int. Conf. on Robotics and Automation*, vol. 3, May 1992, pp. 1963–1968.

[18] L. A. Tuan, G. H. Kim, M. Y. Kim, and S. G. Lee, "Partial feedback linearization control of overhead cranes with varying cable lengths," *Int. J. of Precision Engineering and Manufacturing*, vol. 13, no. 4, pp. 501–507, Apr 2012.

[19] L. A. Tuan, S. G. Lee, D. V. Hung, S. C. Moon, and B. S. Kim, "Partial feedback linearization control of a three-dimensional overhead crane," *Int. J. of Control, Automation and Systems*, vol. 11, no. 4, pp. 718–727, Aug 2013.

[20] X. Wu and X. He, "Partial feedback linearization control for 3-d underactuated overhead crane systems," *ISA Trans.*, vol. 65, pp. 361 – 370, 2016.

[21] Y. Qian and Y. Fang, "A learning strategy based partial feedback linearization control method for an offshore boom crane," in *54th IEEE Conf. on Decision and Control (CDC)*, 2015, pp. 6737–6742.

[22] G. Bartolini, A. Pisano, and E. Usai, "Second-order sliding-mode control of container cranes," *Automatica*, vol. 38, no. 10, pp. 1783 – 1790, 2002.

[23] N. B. Almutairi and M. Zribi, "Sliding mode control of a three-dimensional overhead crane," *J. of Vibration and Control*, vol. 15, no. 11, pp. 1679–1730, 2009.

[24] N. Q. Hieu and K. S. Hong, "Sliding-mode antisway control of an offshore container crane," *IEEE/ASME Trans. on Mechatronics*, vol. 17, no. 2, pp. 201–209, Apr 2012.

[25] Y. Fang, B. Ma, P. Wang, and X. Zhang, "A motion planning-based adaptive control method for an underactuated crane system," *IEEE Trans. on Control Systems Technology*, vol. 20, no. 1, pp. 241–248, Jan 2012.

[26] J. H. Yang and S. H. Shen, "Novel approach for adaptive tracking control of a 3-d overhead crane system," *J. of Intelligent & Robotic Systems*, vol. 62, no. 1, pp. 59–80, Apr 2011.

[27] N. Sun, Y. Fang, H. Chen, and B. He, "Adaptive nonlinear crane control with load hoisting/lowering and unknown parameters: Design and experiments," *IEEE/ASME Trans. on Mechatronics*, vol. 20, no. 5, pp. 2107–2119, Oct 2015.

[28] M. Zhang, X. Ma, X. Rong, R. Song, X. Tian, and Y. Li, "A partially saturated adaptive learning controller for overhead cranes with payload hoisting/lowering and unknown parameters," *Nonlinear Dynamics*, vol. 89, no. 3, pp. 1779–1791, Aug 2017.

[29] D. Chwa, "Nonlinear tracking control of 3-d overhead cranes against the initial swing angle and the variation of payload weight," *IEEE Trans. on Control Systems Technology*, vol. 17, no. 4, pp. 876–883, Jul 2009.

[30] N. Sun and Y. Fang, "New energy analytical results for the regulation of underactuated overhead cranes: An end-effector motion-based approach," *IEEE Trans. on Industrial Electronics*, vol. 59, no. 12, pp. 4723–4734, Dec 2012.

[31] N. Sun, Y. Fang, and X. Zhang, "Energy coupling output feedback control of 4-dof underactuated cranes with saturated inputs," *Automatica*, vol. 49, no. 5, pp. 1318 – 1325, 2013.

[32] X. Wu and X. He, "Nonlinear energy-based regulation control of three-dimensional overhead cranes," *IEEE Trans. on Automation Science and Engineering*, vol. 14, no. 2, pp. 1297–1308, Apr 2017.

[33] H. Chen, Y. Fang, and N. Sun, "An adaptive tracking control method with swing suppression for 4-dof tower crane systems," *Mechanical Systems and Signal Processing*, vol. 123, pp. 426 – 442, 2019.

[34] N. Sun, Y. Fu, T. Yang, J. Zhang, Y. Fang, and X. Xin, "Nonlinear motion control of complicated dual rotary crane systems without velocity feedback: Design, analysis, and hardware experiments," *IEEE Trans. on Automation Science and Engineering*, vol. 17, no. 2, pp. 1017–1029, 2020.

[35] B. Käpernick and K. Graichen, "Model predictive control of an overhead crane using constraint substitution," in *2013 American Control Conf.*, 2013, pp. 3973–3978.

[36] M. Böck and A. Kugi, "Real-time nonlinear model predictive path-following control of a laboratory tower crane," *IEEE Trans. on Control Systems Technology*, vol. 22, no. 4, pp. 1461–1473, 2014.

[37] Š. Ileš, J. Matuško, and F. Kolonić, "Sequential distributed predictive control of a 3d tower crane," *Control Engineering Practice*, vol. 79, pp. 22 – 35, 2018.

[38] G. Galuppini, L. Magni, and D. M. Raimondo, "Model predictive control of systems with dead-zone and saturation," *Control Engineering Practice*, vol. 78, pp. 56 – 64, 2018.

[39] M. Park, D. Chwa, and S. Hong, "Antisway tracking control of overhead cranes with system uncertainty and actuator nonlinearity using an adaptive fuzzy sliding-mode control," *IEEE Trans. on Industrial Electronics*, vol. 55, no. 11, pp. 3972–3984, Nov 2008.

[40] Y. Zhao and H. Gao, "Fuzzy-model-based control of an overhead crane with input delay and actuator saturation," *IEEE Trans. on Fuzzy Systems*, vol. 20, no. 1, pp. 181–186, Feb 2012.

[41] C. Chang, "Adaptive fuzzy controller of the overhead cranes with nonlinear disturbance," *IEEE Trans. on Industrial Informatics*, vol. 3, no. 2, pp. 164–172, May 2007.

[42] L. H. Lee, P. H. Huang, Y. C. Shih, T. C. Chiang, and C. Y. Chang, "Parallel neural network combined with sliding mode control in overhead crane control system," *J. of Vibration and Control*, vol. 20, no. 5, pp. 749–760, 2014.

[43] N. C. Singer and W. P. Seering, "Preshaping command inputs to reduce system vibration," *ASME J. of Dynamic Systems, Measurement, and Control*, vol. 112, no. 1, pp. 76–82, Mar 1990.

[44] N. Singer, W. Singhose, and E. Kriikku, "An input shaping controller enabling cranes to move without sway," United States, Tech. Rep., 1997, wSRC-TR–97-0049.

[45] C. F. Cutforth and L. Y. Pao, "Control using equal length shaped commands to reduce vibration," *IEEE Trans. on Control Systems Technology*, vol. 11, no. 1, pp. 62–72, Jan 2003.

[46] W. Singhose, L. Porter, M. Kenison, and E. Kriikku, "Effects of hoisting on the input shaping control of gantry cranes," *Control Engineering Practice*, vol. 8, no. 10, pp. 1159 – 1165, 2000.

[47] A. Tzes and S. Yurkovich, "An adaptive input shaping control scheme for vibration suppression in slewing flexible structures," *IEEE Trans. on Control Systems Technology*, vol. 1, no. 2, pp. 114–121, Jun 1993.

[48] W. Singhose, "Command shaping for flexible systems: A review of the first 50 years," *Int. J. of Precision Engineering and Manufacturing*, vol. 10, no. 4, pp. 153–168, Oct 2009.

[49] E. Pereira, J. R. Trapero, I. M. Díaz, and V. Feliu, "Adaptive input shaping for single-link flexible manipulators using an algebraic identification," *Control Engineering Practice*, vol. 20, no. 2, pp. 138 – 147, 2012.

[50] D. Blackburn, W. Singhose, J. Kitchen, V. Patrangenaru, J. Lawrence, T. Kamoi, and A. Taura, "Command shaping for nonlinear crane dynamics," *J. of Vibration and Control*, vol. 16, no. 4, pp. 477–501, 2010.

[51] J. Lawrence and W. Singhose, "Command shaping slewing motions for tower cranes," *J. of Vibration and Acoustics*, vol. 132, no. 1, Jan 2010.

[52] J. Vaughan, D. Kim, and W. Singhose, "Control of tower cranes with double-pendulum payload dynamics," *IEEE Trans. on Control Systems Technology*, vol. 18, no. 6, pp. 1345–1358, 2010.

[53] L. Ramli, Z. Mohamed, and H. I. Jaafar, "A neural network-based input shaping for swing suppression of an overhead crane under payload hoisting and mass variations," *Mechanical Systems and Signal Processing*, vol. 107, pp. 484 – 501, 2018.

[54] L. S. Pontryagin, *Mathematical Theory of Optimal Processes.* CRC Press, 1987.

[55] A. E. Bryson and Y. C. Ho, *Applied Optimal Control: Optimization, Estimation and Control.* CRC Press, 1975.

[56] D. E. Kirk, *Optimal Control Theory: An Introduction.* Dover Publications, 2004.

[57] M. Athans and P. L. Falb, *Optimal Control: An Introduction to the Theory and Its Applications.* Dover Publications, 2006.

[58] Y. Sakawa and Y. Shindo, "Optimal control of container cranes," *Automatica*, vol. 18, no. 3, pp. 257 – 266, 1982.

[59] J. W. Auernig and H. Troger, "Time optimal control of overhead cranes with hoisting of the load," *Automatica*, vol. 23, no. 4, pp. 437 – 447, 1987.

[60] K. Terashima, Y. Shen, and K. Yano, "Modeling and optimal control of a rotary crane using the straight transfer transformation method," *Control Engineering Practice*, vol. 15, no. 9, pp. 1179 – 1192, 2007.

[61] Z. Wu and X. Xia, "Optimal motion planning for overhead cranes," *IET Control Theory Applications*, vol. 8, no. 17, pp. 1833–1842, 2014.

[62] X. Zhang, Y. Fang, and N. Sun, "Minimum-time trajectory planning for underactuated overhead crane systems with state and control constraints," *IEEE Trans. on Industrial Electronics*, vol. 61, no. 12, pp. 6915–6925, 2014.

[63] J. J. D. Cruz and F. Leonardi, "Minimum-time anti-swing motion planning of cranes using linear programming," *Optimal Control Applications and Methods*, vol. 34, no. 2, pp. 191–201, 2013.

[64] B. Kolar, H. Rams, and K. Schlacher, "Time-optimal flatness based control of a gantry crane," *Control Engineering Practice*, vol. 60, pp. 18 – 27, 2017.

[65] P. H. Meckl and P. B. Arestides, "Optimized s-curve motion profiles for minimum residual vibration," in *Proc. of the American Control Conf.*, vol. 5, Jun 1998, pp. 2627–2631.

[66] H. Li, M. D. Le, Z. M. Gong, and W. Lin, "Motion profile design to reduce residual vibration of high-speed positioning stages," *IEEE/ASME Trans. on Mechatronics*, vol. 14, no. 2, pp. 264–269, Apr 2009.

[67] W. Singhose, R. Eloundou, and J. Lawrence, "Command generation for flexible systems by input shaping and command smoothing," *ASME J. of Guidance, Control, and Dynamics*, vol. 33, no. 6, pp. 1697–1707, Nov 2010.

[68] N. Uchiyama, H. Ouyang, and S. Sano, "Simple rotary crane dynamics modeling and open-loop control for residual load sway suppression by only horizontal boom motion," *Mechatronics*, vol. 23, no. 8, pp. 1223 – 1236, 2013.

[69] R. Béarée and A. Olabi, "Dissociated jerk-limited trajectory applied to time-varying vibration reduction," *Robotics and Computer-Integrated Manufacturing*, vol. 29, no. 2, pp. 444 – 453, 2013.

[70] R. Béarée, "New damped-jerk trajectory for vibration reduction," *Control Engineering Practice*, vol. 28, pp. 112 – 120, 2014.

[71] K. A. Alghanim, K. A. Alhazza, and Z. N. Masoud, "Discrete-time command profile for simultaneous travel and hoist maneuvers of overhead cranes," *J. of Sound and Vibration*, vol. 345, pp. 47 – 57, 2015.

[72] H. Chen, Y. Fang, and N. Sun, "Optimal trajectory planning and tracking control method for overhead cranes," *IET Control Theory Applications*, vol. 10, no. 6, pp. 692–699, 2016.

[73] M. Fliess, J. Lévine, P. Martin, and P. Rouchon, "On differentially flat nonlinear systems," *IFAC Proc. Volumes*, vol. 25, no. 13, pp. 159 – 163, 1992.

[74] ——, "Flatness and defect of non-linear systems: introductory theory and examples," *Int. J. of Control*, vol. 61, no. 6, pp. 1327–1361, 1995.

[75] J. Neupert, E. Arnold, K. Schneider, and O. Sawodny, "Tracking and anti-sway control for boom cranes," *Control Engineering Practice*, vol. 18, no. 1, pp. 31 – 44, 2010.

[76] T. Yang, N. Sun, H. Chen, and Y. Fang, "Motion trajectory-based transportation control for 3-d boom cranes: Analysis, design, and experiments," *IEEE Trans. on Industrial Electronics*, vol. 66, no. 5, pp. 3636–3646, 2019.

[77] T. Gustafsson, "Modelling and control of rotary crane systems," Ph.D. dissertation, Div. of Automat. Control, Lulea Univ. of Tech., Lulea, Sweden, 1993.

[78] K. Terashima and M. Suzuki, "Path planning and navigation of overhead traveling crane with three-dimensional transport based on a diffusion equation strategy," in *Advances in Manufacturing*. London: Springer London, 1999, pp. 335–347.

[79] U. Schaper, C. Dittrich, E. Arnold, K. Schneider, and O. Sawodny, "2-dof skew control of boom cranes including state estimation and reference trajectory generation," *Control Engineering Practice*, vol. 33, pp. 63 – 75, 2014.

[80] V. Utkin and J. Shi, "Integral sliding mode in systems operating under uncertainty conditions," in *Proc. of 35th IEEE Conf. on Decision and Control*, vol. 4, Dec 1996, pp. 4591–4596.

[81] S. Kamal, A. Raman, and B. Bandyopadhyay, "Finite-time stabilization of fractional order uncertain chain of integrator: An integral sliding mode approach," *IEEE Trans. on Automatic Control*, vol. 58, no. 6, pp. 1597–1602, Jun 2013.

[82] P. R. Kumar, A. Chalanga, and B. Bandyopadhyay, "Smooth integral sliding mode controller for the position control of stewart platform," *ISA Trans.*, vol. 58, pp. 543 – 551, 2015.

[83] R. Pradhan and B. Subudhi, "Double integral sliding mode mppt control of a photovoltaic system," *IEEE Trans. on Control Systems Technology*, vol. 24, no. 1, pp. 285–292, Jan 2016.

[84] A. Ferrara and G. P. Incremona, "Design of an integral suboptimal second-order sliding mode controller for the robust motion control of robot manipulators," *IEEE Trans. on Control Systems Technology*, vol. 23, no. 6, pp. 2316–2325, Nov 2015.

[85] Q. Shen, D. Wang, S. Zhu, and E. K. Poh, "Integral-type sliding mode fault-tolerant control for attitude stabilization of spacecraft," *IEEE Trans. on Control Systems Technology*, vol. 23, no. 3, pp. 1131–1138, May 2015.

[86] S. L. Chen and K. C. Wu, "Contouring control of smooth paths for multiaxis motion systems based on equivalent errors," *IEEE Trans. on Control Systems Technology*, vol. 15, no. 6, pp. 1151–1158, Nov 2007.

[87] F. Castanos and L. Fridman, "Analysis and design of integral sliding manifolds for systems with unmatched perturbations," *IEEE Trans. on Automatic Control*, vol. 51, no. 5, pp. 853–858, May 2006.

[88] L. Fridman, J. Moreno, and R. Iriarte, Eds., *Sliding Modes after the First Decade of the 21st Century: State of the Art*. Berlin, Germany: Springer Berlin Heidelberg, 2011.

[89] S. Dadras and H. R. Momeni, "Fractional terminal sliding mode control design for a class of dynamical systems with uncertainty," *Comm. in Non. Sci. and Num. Sim.*, vol. 17, no. 1, pp. 367 – 377, 2012.

[90] S. Dadras and H. R. Momeni, "Passivity-based fractional-order integral sliding-mode control design for uncertain fractional-order nonlinear systems," *Mechatronics*, vol. 23, no. 7, pp. 880 – 887, 2013.

[91] W. J. Cao and J. X. Xu, "Nonlinear integral-type sliding surface for both matched and unmatched uncertain systems," *IEEE Tran. on Automatic Control*, vol. 49, no. 8, pp. 1355–1360, Aug 2004.

[92] J. X. Xu, Z. Q. Guo, and T. H. Lee, "A synthesized integral sliding mode controller for an underactuated unicycle," in *2010 11th Int. Workshop on Variable Structure Systems (VSS)*, Jun 2010, pp. 352–357.

[93] J. X. Xu and Z. Q. Guo and T. H. Lee, "Design and implementation of integral sliding-mode control on an underactuated two-wheeled mobile robot," *IEEE Trans. on Industrial Electronics*, vol. 61, no. 7, pp. 3671–3681, Jul 2014.

[94] K. Zhou and J. C. Doyle, *Essentials of Robust Control*. Upper Saddle River, N.J., USA: Practice Hall, 1998.

[95] U. Mackenroth, *Robust Control System - Theory and case studies*. Berlin, Germany: Springer-Verlag, 2004.

[96] D. W. Gu, P. H. Petkov, and M. M. Konstantinov, *Robust Control Design with MATLAB*. London, UK: Springer-Verlag, 2013.

[97] L. T. Aguilar and Y. V. Orlov, *Advanced H_∞ Control - Towards Nonsmooth Theory and Applications*. New York, USA: Birkhauser, 2014.

[98] D. Lefebvre, P. Chevrel, and S. Richard, "An H_∞-based control design methodology dedicated to the active control of vehicle longitudinal oscillations," *IEEE Trans. on Control Systems Technology*, vol. 11, no. 6, pp. 948–956, Nov 2003.

[99] I. U. Ponce, J. Bentsman, Y. Orlov, and L. T. Aguilar, "Generic nonsmooth mathcal H_∞ output synthesis: Application to a coal-fired boiler/turbine unit with actuator dead zone," *IEEE Trans. on Control Systems Technology*, vol. 23, no. 6, pp. 2117–2128, Nov 2015.

[100] M. Alma, J. J. Martinez, I. D. Landau, and G. Buche, "Design and tuning of reduced order H_∞ feedforward compensators for active vibration control," *IEEE Trans. on Control Systems Technology*, vol. 20, no. 2, pp. 554–561, Mar 2012.

[101] J. Jayender, R. V. Patel, S. Nikumb, and M. Ostojic, "Modeling and control of shape memory alloy actuators," *IEEE Trans. on Control Systems Technology*, vol. 16, no. 2, pp. 279–287, Mar 2008.

[102] K. Yano and K. Terashima, "Robust liquid container transfer control for complete sloshing suppression," *IEEE Trans. on Control Systems Technology*, vol. 9, no. 3, pp. 483–493, May 2001.

[103] I. N. Kar, K. Seto, and F. Doi, "Multimode vibration control of a flexible structure using H_∞-based robust control," *IEEE/ASME Trans. on Mechatronics*, vol. 5, no. 1, pp. 23–31, Mar 2000.

[104] J. E. McInroy, J. F. O. Brien, and A. A. Allais, "Designing micromanipulation system for decoupled dynamics and control," *IEEE/ASME Trans. on Mechatronics*, vol. 20, no. 2, pp. 553–563, Apr 2015.

[105] Y. K. Yong, K. Liu, and S. O. R. Moheimani, "Reducing cross-coupling in a compliant xy nanopositioner for fast and accurate raster scanning," *IEEE Trans. on Control Systems Technology*, vol. 18, no. 5, pp. 1172–1179, Sep 2010.

[106] B. Robu, L. Baudouin, C. Prieur, and D. Arzelier, "Simultaneous H_∞ vibration control of fluid/plate system via reduced-order controller," *IEEE Trans. on Control Systems Technology*, vol. 20, no. 3, pp. 700–711, May 2012.

[107] Y. Li and Q. Xu, "Design and robust repetitive control of a new parallel-kinematic xy piezostage for micro/nanomanipulation," *IEEE/ASME Trans. on Mechatronics*, vol. 17, no. 6, pp. 1120–1132, Dec 2012.

[108] J. J. E. Slotine and W. Li, *Applied Nonlinear Control*. Englewood Cliffs, N.J., USA: Prentice Hall, 1991.

[109] B. L. Zhang, Q. L. Han, X. M. Zhang, and X. Yu, "Integral sliding mode control for offshore steel jacket platforms," *J. of Sound and Vibration*, vol. 331, no. 14, pp. 3271 – 3285, 2012.

[110] D. P. Bertsekas, *Nonlinear Programming*, 3rd ed. USA: Athena Scientific, 2016.

[111] R. C. M. Gen, *Genetic Algorithms and Engineering Optimization*. USA: John Wiley & Sons, 2007.

[112] M. Clerc, *Particle Swarm Optimization*. USA: John Wiley & Sons, 2010.

[113] R. Hassan, B. Cohanim, O. Weck, and G. Venter, "A comparison of particle swarm optimization and the genetic algorithm," in *46th AIAA/ASME/ASCE/AHS/ASC Structures, Structural Dynamics and Materials Conference*, Apr 2005, pp. 1–13.

[114] S. Panda and N. P. Padhy, "Comparison of particle swarm optimization and genetic algorithm for facts-based controller design," *Applied Soft Computing*, vol. 8, no. 4, pp. 1418 – 1427, 2008.

[115] M. G. Safonov, *Modelling, Robustness and Sensitivity Reduction in Control Systems*, 4th ed. New York, USA: Springer-Verlag, 1987.

[116] K. Z. Liu and Y. Yao, *Robust Control: Theory and Applications*. Singapore: John Wiley & Sons, 2016.

[117] K. A. Stroud and D. J. Booth, *Advanced Engineering Mathematics*, 4th ed. New York, USA: Palgrave Macmillan, 2003.

[118] M. Montanari, F. Ronchi, C. Rossi, A. Tilli, and A. Tonielli, "Control and performance evaluation of a clutch servo system with hydraulic actuation," *Control Engineering Practice*, vol. 12, no. 11, pp. 1369 – 1379, 2004, mechatronic Systems.

[119] P. Giani, M. Tanelli, S. M. Savaresi, and M. Santucci, "Launch control for sport motorcycles: A clutch-based approach," *Control Engineering Practice*, vol. 21, no. 12, pp. 1756 – 1766, 2013.

[120] K. V. Berkel, T. Hofman, A. Serrarens, and M. Steinbuch, "Fast and smooth clutch engagement control for dual-clutch transmissions," *Control Engineering Practice*, vol. 22, pp. 57 – 68, 2014.

[121] K. D. Mishra and K. Srinivasan, "Robust control and estimation of clutch-to-clutch shifts," *Control Engineering Practice*, vol. 65, pp. 100 – 114, 2017.

[122] J. T. Betts, *Practical Methods for Optimal Control and Estimation Using Nonlinear Programming*. Cambridge University Press, USA, 2009.

[123] J. A. Snyman, C. Frangos, and Y. Yavin, "Penalty function solutions to optimal control problems with general constraints via a dynamic optimisation method," *Computers & Mathematics with Applications*, vol. 23, no. 11, pp. 47 – 55, 1992.

[124] A. Al-Garni, K. Moustafa, and S. J. Nizami, "Optimal control of overhead cranes," *Control Engineering Practice*, vol. 3, no. 9, pp. 1277 – 1284, 1995.

[125] V. M. Becerra, "Solving optimal control problems with state constraints using nonlinear programming and simulation tools," *IEEE Trans. on Education*, vol. 47, no. 3, pp. 377–384, Aug 2004.

[126] L. Lasdon, S. Mitter, and A. Waren, "The conjugate gradient method for optimal control problems," *IEEE Trans. on Automatic Control*, vol. 12, no. 2, pp. 132–138, Apr 1967.

[127] L. Lasdon, "Conjugate direction methods for optimal control," *IEEE Trans. on Automatic Control*, vol. 15, no. 2, pp. 267–268, Apr 1970.

[128] V. H. Quintana and E. J. Davison, "Clipping-off gradient algorithms to compute optimal controls with constrained magnitude," *Int. J. of Control*, vol. 20, no. 2, pp. 243–255, 1974.

[129] A. V.Rao, "A survey of numerical methods for optimal control," *Advances in the Astronautical Sciences*, vol. 135, no. 1, pp. 497–528, Oct 2009.

[130] S. Lenhart and J. T. Workman, *Optimal Control Applied to Biological Models*. Boca Raton, Florida: Chapman and Hall/CRC, 2007.

[131] X. Xu and P. J. Antsaklis, "Optimal control of switched systems based on parameterization of the switching instants," *IEEE Transaction on Automatic Control*, vol. 49, no. 1, pp. 2–16, Jan 2004.

[132] F. Zhu and J. P. Antsaklis, "Optimal control of hybrid switched systems: A brief survey," *Discrete Event Dynamic Systems*, vol. 25, no. 3, pp. 345–364, Sep 2015.

[133] P. Schlott, A. Geise, G. Grabmair, T. Fritzel, and O. Sawodny, "A crane-based five-axis manipulator for antenna tests," *Control Engineering Practice*, vol. 85, pp. 149 – 162, 2019.

[134] Y. L. Yang, Y. D. Wei, J. Q. Lou, L. Fu, S. Fang, and T. H. Chen, "Dynamic modeling and adaptive vibration suppression of a high-speed macro-micro manipulator," *J. of Sound and Vibration*, vol. 422, pp. 318 – 342, 2018.

[135] N. Sun, T. Yang, Y. Fang, Y. Wu, and H. Chen, "Transportation control of double-pendulum cranes with a nonlinear quasi-pid scheme: Design and experiments," *IEEE Trans. on Systems, Man, and Cybernetics: Systems*, vol. 49, no. 7, pp. 1408–1418, Jul 2019.

[136] B. Lu, Y. Fang, and N. Sun, "Nonlinear control for underactuated multi-rope cranes: Modeling, theoretical design and hardware experiments," *Control Engineering Practice*, vol. 76, pp. 123 – 132, 2018.

[137] L. H. Lee, P. H. Huang, Y. C. Shih, T. C. Chiang, and C. Y. Chang, "Parallel neural network combined with sliding mode control in overhead crane control system," *J. of Vibration and Control*, vol. 20, no. 5, pp. 749–760, 2014.

[138] Z. C. Qiu and W. Z. Zhang, "Trajectory planning and diagonal recurrent neural network vibration control of a flexible manipulator using structural light sensor," *Mechanical Systems and Signal Processing*, vol. 132, pp. 563 – 594, 2019.

[139] X. Zhang, Y. Fang, and N. Sun, "Minimum-time trajectory planning for underactuated overhead crane systems with state and control constraints," *IEEE Trans. on Industrial Electronics*, vol. 61, no. 12, pp. 6915–6925, Dec 2014.

[140] N. Sun, Y. Fang, X. Zhang, and Y. Yuan, "Transportation task-oriented trajectory planning for underactuated overhead cranes using geometric analysis," *IET Control Theory Applications*, vol. 6, no. 10, pp. 1410–1423, Jul 2012.

[141] N. Q. Hoang, S. G. Lee, H. Kim, and S. C. Moon, "Trajectory planning for overhead crane by trolley acceleration shaping," *J. of Mechanical Science and Technology*, vol. 28, no. 7, pp. 2879–2888, Jul 2014.

[142] W. Rudin, *Principles of mathematical analysis*, 3rd ed. USA: McGraw-Hill, 1976.

[143] S. K. Cho and H. H. Lee, "An anti-swing control of a 3-dimensional overhead crane," in *Proc. of the American Control Conf.*, vol. 2, Jun 2000, pp. 1037–1041.

[144] Z. N. Masoud, A. H. Nayfeh, and D. T. Mook, "Cargo pendulation reduction of ship-mounted cranes," *Nonlinear Dynamics*, vol. 35, no. 3, pp. 299–311, Feb 2004.

[145] H. Ouyang, N. Uchiyama, and S. Sano, "Suppression of two-dimensional load-sway in rotary crane control using only horizontal boom motion," *J. of System Design and Dynamics*, vol. 5, no. 4, pp. 535–546, 2011.

[146] N. Sun, Y. Fang, H. Chen, Y. Fu, and B. Lu, "Nonlinear stabilizing control for ship-mounted cranes with ship roll and heave movements: Design, analysis, and experiments," *IEEE Trans. on Systems, Man, and Cybernetics: Systems*, vol. 48, no. 10, pp. 1781–1793, Oct 2018.

[147] B. Lu, Y. Fang, N. Sun, and X. Wang, "Antiswing control of offshore boom cranes with ship roll disturbances," *IEEE Trans. on Control Systems Technology*, vol. 26, no. 2, pp. 740–747, Mar 2018.

[148] Y. Qian, Y. Fang, and B. Lu, "Adaptive repetitive learning control for an offshore boom crane," *Automatica*, vol. 82, pp. 21–28, 2017.

[149] G. G. Parker, K. Groom, J. E. Hurtado, J. Feddema, R. D. Robinett, and F. Leban, "Experimental verification of a command shaping boom crane control system," in *Proc. of the 1999 American Control Conf.*, vol. 1, Jun 1999, pp. 86–90.

[150] J. Danielson, "Mobile boom cranes and advanced input shaping control," Master's thesis, School of Mechanical Engineering, Georgia Institute of Technology, Georgia, USA, 2008.

[151] E. Maleki and W. Singhose, "Dynamics and zero vibration input shaping control of a small-scale boom crane," in *Proc. of the 2010 American Control Conf.*, Jun 2010, pp. 2296–2301.

[152] D. Newman and J. Vaughan, "Command shaping of a boom crane subject to nonzero initial conditions," in *2017 IEEE Conf. on Control Technology and Applications (CCTA)*, Aug 2017, pp. 1189–1194.

[153] E. Pereira, J. Trapero, I. Díaz, and V. Feliu, "Adaptive input shaping for maneuvering flexible structures using an algebraic identification technique," *Automatica*, vol. 45, no. 4, pp. 1046 – 1051, 2009.

[154] C. Constanda, *Differential Equations: A Primer for Scientists and Engineers*, 2nd ed. New York: Springer, 2017.

[155] W. E. Boyce, R. C. DiPrima, and D. B. Meade, *Elementary Differential Equations and Boundary Value Problems*, 11th ed. New Jersey: John Wiley & Sons, 2017.

[156] E. Kartashova, *Nonlinear Resonance Analysis: Theory, Computation, Applications*. New York: Cambridge University Press, 2010.

[157] A. L. Fradkov, "Feedback resonance in nonlinear oscillators," in *1999 European Control Conf. (ECC)*, Aug 1999, pp. 3599–3604.

[158] K. S. Hong and U. H. Shah, *Dynamics and Control of Industrial Cranes*. Singapore: Springer, 2019.

[159] G. W. Younkin, *Industrial Servo Control Systems: Fundamentals And Applications, Revised And Expanded*, 2nd ed. New York: CRC Press, 2002.

[160] K. Furuta, N. Kawaji, T. Yoshio, and T. Hara, *Control of mechanical systems*. Tokyo: Ohmsha, 1984, in Japanese.

[161] Y. Yoshida and H. Tabata, "Visual feedback control of an overhead crane and its combination with time-optimal control," in *2008 IEEE/ASME Int. Conf. on Advanced Intelligent Mechatronics*, Jul 2008, pp. 1114–1119.

[162] J. Stewart, *Essential Calculus: Early Transcendentals*, 2nd ed. Belmont, CA: Brooks/Cole, 2012.

[163] A. Gil, J. Segura, and N. M. Temme, *Numerical Methods for Special Functions*, 1st ed. Philadelphia: SIAM, 2007.

[164] G. B. Folland, *Advanced Calculus*, 1st ed. Upper Saddle River, NJ: Pearson, 2002.

[165] W. Sun and Y. Yuan, *Optimization Theory and Methods: Nonlinear Programming*. Springer, USA, 2006.

Acknowledgements

I owe my most sincere gratitude to my principal supervisor, Prof. Kazuhiko Terashima. He is one of the greatest people I have had the privilege of working with. He had a unique and firmly grounded view toward the system and control theory. I am always amazed at his novel ideas, his strong sense of intuition, and his clear vision for the academia–industry collaboration. He is my constant source of motivation. With his endless energy, encouragement, and wholehearted attentions, he helped me overcome the toughest times of my PhD. This thesis would not exist and/or complete at all without his support. I know appreciative words are not enough for me to thank him. To me, he is more than an academic supervisor.

I would also like to express my gratefulness to my co-supervisor, Prof. Naoki Uchiyama, for his excellent advice and kind support. I learned from him professionalism, critical thinking, and thoughtfulness. Thank you for allowing me to attend your weekly group meetings for international students. These seminars were truly open and helpful.

I would like to deliver my great appreciation to Prof. Takanori Miyoshi and Assoc. Prof. Ryosuke Tasaki. I am very thankful for your fruitful discussions, your sincere advice, and your valuable helps.

Sincere thanks are given to the Reviewers, Prof. Hideki Yanada and Assoc. Prof. Tomoaki Mashimo, for taking your precious time and effort to evaluate my thesis, especially for your nice comments and suggestions.

I wish to thank Assoc. Prof. Nguyen Quoc Chi, who greatly inspired me to pursue the path of academic research.

Many thanks go to the Amano Institute of Technology for providing valuable financial support for my PhD.

I would also like to acknowledge Sinfonia Technology Co., Ltd. and Iknow Machinery Co., Ltd. for allowing me to join the collaboration project on crane controls. Helpful discussions at research report meetings have greatly forced me to look at the problem at hand in different and fresh perspectives.

I wish to thank all the members of the System and Control Laboratory (especially Dr. Ito, Dr. Halim, Sasatake-san, Yuki-san, Shoji-san, Taniguchi-san, Suzuki-san, Dung-san, Kim-san, Philipp, and Janik) and the Systems Engineering Laboratory (especially Tobias, Martin, Bernd, Dr. Farrage, Mathew, Enock, Min, Noki, Shogo-san, Sato-san, and Arai-san). I cherish all the beautiful moments and memories that I shared with all of you guys.

Finally, I want to express my deepest indebtedness to my Grandmother, Father, Mother, Sister, and Little Niece for their continuous encouragement and love. They are always the most precious gifts of my life.

Publications

Journals (peer-reviewed)

- **H. D. Tho**, A. Kaneshige, and K. Terashima, "Minimum-time s-curve commands for vibration-free transportation of an overhead crane with actuator limits," *Control Engineering Practice (IF: 3.193)*, vol. 98, 2020.
- **H. D. Tho**, N. Uchiyama, and K. Terashima, "Resonance-based tossing control for bulk materials transportation of an overhead crane," *IEEE Trans. on Industrial Electronics (IF: 7.515)*, 2020, to appear.
- **H. D. Tho**, K. Suzuki, M. Tsume, R. Tasaki, T. Miyoshi, and K. Terashima, "A switched optimal control approach to reduce transferring time, energy consumption, and residual vibration of payload's skew rotation in crane systems," *Control Engineering Practice (IF: 3.193)*, vol. 84, pp. 247–260, 2019.
- **H. D. Tho** and K. Terashima, "Robust control designs of payload's skew rotation in a boom crane system," *IEEE Trans. on Control Systems Technology (IF: 5.312)*, vol. 27, no. 4, pp. 1608–1621, 2019.

International Conferences (peer-reviewed)

- **H. D. Tho**, N. Uchiyama, and K. Terashima, "Model reference input shaping control of a nonlinear rotary crane with time-varying rope length," in *7th IEEE Int. Conf. on Control, Decision and Info. Tech. (CoDIT)*, 2020, to appear.
- **H. D. Tho**, N. Uchiyama, and K. Terashima, "A minimum-time zero vibration s-curve command for an overhead crane with actuator limits," in *58th IEEE Conf. on Decision and Control (CDC)*, 2019, pp. 7963–7969.
- **H. D. Tho**, R. Tasaki, T. Miyoshi, and K. Terashima, "Optimal control of payload's skew rotation in crane systems with state and control input constraints," *in 2nd IEEE Conf. on Control Tech. and Applications (CCTA)*, 2018, pp. 729–735.
- **H. D. Tho**, R. Tasaki, A. Kaneshige, T. Miyoshi, and K. Terashima, "Robust sliding mode control with integral sliding surface of an underactuated rotary hook system," in *IEEE Int. Conf. on Advanced Intelligent Mechatronics (AIM)*, 2017, pp. 998–1003.
- **H. D. Tho**, R. Tasaki, K. Terashima, M. Tsume, and K. Suzuki, "Robust sliding mode control of a rotary hook," *IFAC-PapersOnLine*, vol. 50, no. 1, pp. 6060–6066, 2017, 20th IFAC World Congress.
- **H. D. Tho**, K. Takemori, R. Tasaki, T. Miyoshi, and K. Terashima, "Adaptive input shaping control of a rotary hook," in *55th Annual Conf. of the Soc. of Instrument and Control Engineers of Japan (SICE)*, 2016, pp. 596–602.